Rita Esposito The Deteriorating Impact of Alkali-Silica Reaction on Concrete. Expansion and Mechanical Properties

The Deteriorating Impact of Alkali-Silica Reaction on Concrete

Rita Esposito

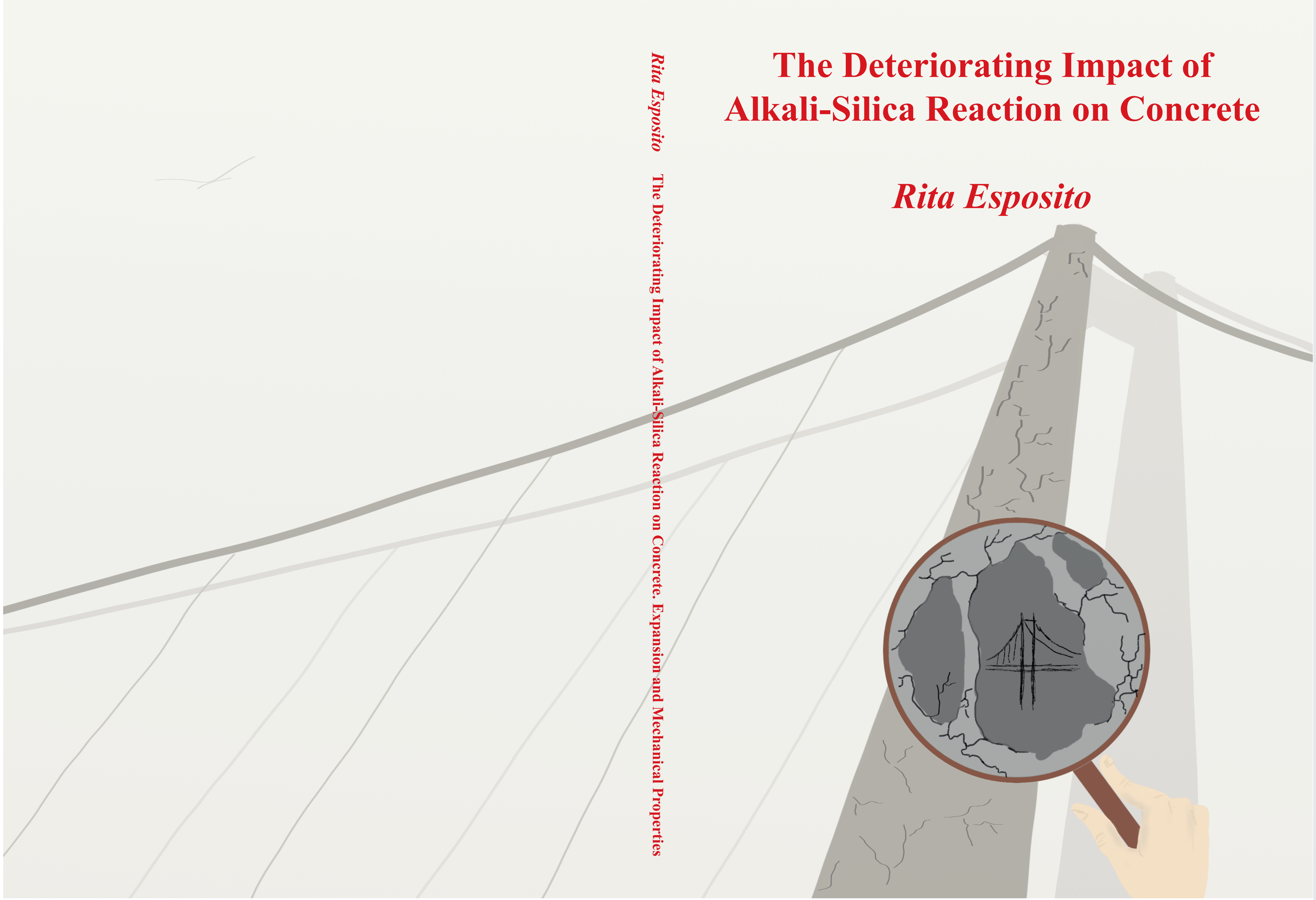

INVITATION

You are kindly invited to
attend the public defence of
my Ph.D. thesis

**THE
DETERIORATING
IMPACT OF
ALKALI-SILICA
REACTION
ON CONCRETE
Expansion and
Mechanical Properties**

The defence will take place on
Wednesday, 6 January 2016 at
10:00 in the Senaatszaal in the
Aula of Delft University of
Technology, Mekelweg 5,
Delft.

A brief introduction to the
thesis will precede the defence,
at 9:30.

The defence will be followed
by a reception to which you
are cordially invited.

RITA ESPOSITO

The Deteriorating Impact of Alkali-Silica Reaction on Concrete

Expansion and Mechanical Properties

Rita ESPOSITO

The Deteriorating Impact of Alkali-Silica Reaction on Concrete

Expansion and Mechanical Properties

Proefschrift

ter verkrijging van de graad van doctor
aan de Technische Universiteit Delft,
op gezag van de Rector Magnificus prof. ir. K.C.A.M. Luyben,
voorzitter van het College voor Promoties,
in het openbaar te verdedigen op woensdag 6 januari 2016 om 10:00 uur

door

Rita ESPOSITO

Civiel ingenieur,
Universiteit Parma, Parma, Italië,
geboren te Cremona, Italië.

Dit proefschrift is goedgekeurd door de

promotor: Prof. dr. ir. M.A.N. Hendriks

Samenstelling promotiecommissie:

Rector Magnificus,	voorzitter
Prof. dr. ir. M.A.N. Hendriks	Technische Universiteit Delft, Norwegian University of Science & Technology
Onafhankelijke leden:	
Dr. ir. O. Çopuroğlu	Technische Universiteit Delft
Prof. dr. ir. D.A. Hordijk	Technische Universiteit Delft
Prof. dipl.-ing. dr. G. Meschke	Ruhr University Bochum
Dr. dipl.-ing. I. Miahi	Cardiff University
Prof. dr. ir. H.E.J.G. Schlangen	Technische Universiteit Delft
Prof. dr. ir. L.J. Sluys	Technische Universiteit Delft
Prof. dr. ir. J.G. Rots	Technische Universiteit Delft, reservelid

The research described in this thesis was developed within the STW project "Performance Assessment Tool for Alkali-Silica Reaction (PAT-ASR)" (code No. 10977), which is part of the STW program "Integral Solutions for Sustainable Construction (IS2C)".

Keywords: Alkali-Silica Reaction (ASR), Concrete, Mechanical properties, Multiscale material model, Micromechanics

Printed by: Ipskamp Drukkers, Eschede, The Netherlands

Front & Back: Idea by R. Esposito, drawing by Z. Hossain

ISBN 978-94-6259-984-0

An electronic version of this dissertation is available at
`http://repository.tudelft.nl/`.

Summary

The assessment of concrete structures affected by alkali-silica reaction (ASR) is a complex problem due to the multiscale nature of this long-term phenomenon. The reaction starts within the concrete constituents with the formation of an expansive alkali-silica gel at reaction products level. Being the expansive gel confined within the concrete micro-structure, an internal pressure is built up that induces damage at aggregate level. This micro-cracking affects the mechanical characteristics of the material at concrete level. At structural level, the performance of members and of structures itself can thus be compromised by the reaction.

Since the material characterization is one of the main points of attention within a structural assessment, this thesis work aims to study the deteriorating impact of ASR on concrete in terms of both expansion and degradation of the mechanical properties. Both experimental and modelling approaches are followed.

The experimental investigation, which includes laboratory tests supplemented with literature data, shows a statistically relevant relationship between the concrete expansion and the degradation of mechanical properties of ASR-affected concrete specimens stored under free-expansion conditions. Rather than the compressive strength, the elastic modulus results the best indicator of ASR signs in concrete by showing the fastest degradation rate, leading to the lowest residual value. By comparing the behaviour of unaffected and affected concretes in terms of strength-stiffness correlations a substantial difference is observed.

Considering that unaffected and affected concrete experimentally appear as substantially different materials at concrete level, a multiscale modelling approach, ranging between aggregate and concrete level, is adopted to explore the deteriorating impact induced by ASR. An analytically solved micro-poro-fracture-mechanical model, which is based on a limited number of input parameters, is adopted. The approach considers the micro-cracking phenomenon as the common damage mechanism associated to the internal swelling and the external mechanical loading. The model is able to approximate the behaviour of unaffected concrete under uniaxial loading as well as the relation between stiffness and strength of unconstrained ASR-affected concrete. However, the lack of permanent deformation in its formulation results as a limitation.

In conclusion, this thesis work highlights the importance of a multiscale analysis to explore the ASR phenomenon in concrete and concrete structures. The deteriorating impact of ASR on concrete can be correlated to the microcracking phenomenon at aggregate level and should be considered both in terms of expansion and mechanical degradation. The proposed multiscale material modelling approach results as a method for the material characterization, which can be extended to both the reaction products and the structural level.

Samenvatting

De beoordeling van de constructieve veiligheid van betonconstructies die zijn aangetast door alkali-silicareactie (ASR) is een complex probleem vanwege de meerschalige aard van dit lange-termijn fenomeen. De reactie begint in het beton met de vorming van een zwellende alkali-silica-gel. Dit is de schaal van de reactieproducten. Omdat de zwellende gel opgesloten zit binnen de microstructuur van het beton, wordt er een inwendige druk opgebouwd die schade veroorzaakt. Dit is de schaal van de toeslagmaterialen. Deze micro-scheuren beïnvloeden de mechanische eigenschappen van het materiaal. Dit is de schaal van het beton. Op constructie-schaal, kunnen door de reactie de capaciteit van elementen en van de constructie zelf in gevaar komen.

Aangezien de materiaaleigenschappen een van de belangrijkste aandachtspunten van een constructieve beoordeling is, is dit proefschrift gericht op het bestuderen van de negatieve invloed van ASR op beton, in termen van uitzetting en degradatie van de mechanische eigenschappen. Zowel experimentele als modelmatige benaderingen worden gevolgd.

Het experimentele onderzoek bevat laboratoriumproeven, aangevuld met gegevens uit de literatuur. Het toont een statistisch relevante relatie tussen de uitzetting van het beton en de degradatie van de mechanische eigenschappen van door ASR aangetaste betonnen proefstukken die ongehinderd kunnen uitzetten. Niet de druksterkte, maar de elasticiteitsmodulus is de beste indicator van aantasting van het beton door ASR. Het toont de grootste snelheid van degradatie en resulteert in de laagste restwaarde. Bij het vergelijken van het gedrag van onaangetast en aangetast beton in termen van sterkte versus stijfheid is een wezenlijk verschil waargenomen.

Wetende dat onaangetast en aangetast beton experimenteel wezenlijk verschillen op de schaal van beton, wordt een meerschalige aanpak gebruikt, op de schalen van toeslagmaterialen en beton, om de aantasting van ASR te verkennen. Een ana-

lytisch micro-poro-breuk-mechanisch model wordt gebruikt, dat is gebaseerd op een beperkt aantal parameters. Het model houdt rekening met de micro-scheuren als het gemeenschappelijke schademechanisme dat gekoppeld is aan de interne zwelling van de gel en de externe mechanische belasting. Het model is in staat om het gedrag van onaangetast beton onder uniaxiale belasting, als ook de relatie tussen stijfheid en sterkte van ASR-aangetast beton te benaderen. Echter, het gebrek aan permanente vervorming in de formulering blijkt een beperking.

Concluderend, dit proefschrift benadrukt het belang van een meerschalige analyse om het ASR-fenomeen in beton en betonconstructies te verkennen. De degraderende invloed van ASR op beton kan worden gecorreleerd met de micro-scheuren op de schaal van toeslagmaterialen en moet worden beschouwd in termen van uitzetting en mechanische degradatie. De voorgestelde meerschalige materiaalmodellering is een mogelijkheid om het materiaal te karakteriseren. De modellering kan worden uitgebreid naar de schaal van reactieproducten en de structurele schaal.

Symbols and Abbreviations

General notation

z	scalar
$\boldsymbol{z}$, z_i	1st order tensor and its i-th component
$\boldsymbol{Z}$, Z_{ij}	2nd order tensor and its ij-th component
$\mathbb{Z}$, Z_{ijkl}	4th order tensor and its $ijkl$-th component

Roman symbols

a_i	in plane radius of the cracks, which belong to the i-th crack family
c_i	thickness radius of the cracks, which belong to the i-th crack family
c_i^{d}	deformed thickness radius of the cracks, which belong to the i-th crack family
d	size of the local heterogeneity of the REV
$d_{\max}$	maximum aggregate size
d_1, d_2	damage variables in the two branches of the 1D pressure-based model
f	volume fraction of the lower-scale porosity (level I) in the two-scale porosity model
f_{c}	compressive strength
f_{t}	tensile strength
$f_{\mathrm{t,dir}}$	direct tensile strength
$f_{\mathrm{t,sp}}$	splitting tensile strength
g_{f}	microscopic fracture energy (in tension)
h_n, h_t	mapping coefficients for a 2nd order tensor
l	characteristic length of the REV
l_i	additional crack surface related to the i-th crack family

m	number of crack families
m_{l}	gradient of the piecewise linear curve fitting in the low-expansion zone
m_{m}	gradient of the piecewise linear curve fitting in the moderate-expansion zone
m_{h}	gradient of the piecewise linear curve fitting in the high-expansion zone
m_{e}	gradient of the piecewise linear curve fitting in the extreme-expansion zone
n_i	number of cracks per unit of volume of the i-th crack family
$\boldsymbol{n}_i$	normal vector of cracks, which belong to the i-th crack family
q_{l}	constant of the piecewise linear curve fitting in the low-expansion zone
q_{m}	constant of the piecewise linear curve fitting in the moderate-expansion zone
q_{h}	constant of the piecewise linear curve fitting in the high-expansion zone
q_{e}	constant of the piecewise linear curve fitting in the extreme-expansion zone
s_i	stability coefficient of the i-th crack family
$\boldsymbol{u}$	displacement field on the boundary of the inclusion domain $\delta\Omega_i$
t_{c}	characteristic time
t_{l}	latency time
$\boldsymbol{x}$	macroscopic position vector
$\boldsymbol{z}$	microscopic position vector
$\mathbb{A}_i$	strain concentration tensor of the i-th inclusion phase for the Mori-Tanaka scheme
A_{t}	area underneath the stress-strain curve in tension
$\boldsymbol{B}$	Biot tensor
$\mathbb{B}_i$	stress concentration tensor of the i-th inclusion phase for the Mori-Tanaka scheme
$\mathbb{C}$	stiffness tensor
D	characteristic length of the structure
$\dot{D}_i$	dissipation rate associated to the propagation of the i-th crack family
$\mathbb{D}$	compliance tensor
E_{d}, E_{m}	mechanical strains in the two branches of the 1D pressure-based model

E_{if},E_{im}	expansion strains in the two branches of the 1D pressure-based model
E^{I}, E^{II}	total strains in the two branches of the 1D pressure-based model
E^{ASR}	linear expansion strain in the 1D pressure-based model
$E^{\mathrm{ASR}}_{\mathrm{vol}}$	volumetric expansion strain in the 1D pressure-based model
$\boldsymbol{E}$, E_{ij}	macroscopic strain tensor and its *ij*-th component
$\boldsymbol{E}^{\mathrm{applied}}$	macroscopic applied strain tensor
$\boldsymbol{E}^{\mathrm{cr}}$	critical macroscopic strain tensor in the case of zero pressure ($P = 0$)
$\boldsymbol{E}^{P}$	macroscopic strain tensor induced by the pressure P under free-expansion condition ($\boldsymbol{\Sigma} = 0$)
$\boldsymbol{E}^{\mathrm{unit}}$	macroscopic unit strain tensor
$\boldsymbol{E}'$	macroscopic effective strain tensor
$\boldsymbol{E}^{*}$	eigenstrain tensor in the inclusion domain
G_i	energy release rate for the *i*-th crack family
$G_{\mathrm{c},i}$	critical value of the energy release rate for the *i*-th crack family
G_{f}	macroscopic fracture energy (in tension)
H_n, H_t	mapping coefficients for a 4th order tensor
$\boldsymbol{I}$, $\mathbb{I}$	2nd and 4th order identity tensor
L	load case
MOR	modulus of rupture
$1/N_i$	Biot modulus of the *i*-th phase
$\mathbb{O}$	null 4th order tensor
P	pressure generated by the swelling of the expansive alkali-silica gel
P^{cr}	critical pressure for the case of free-expansion condition ($\boldsymbol{\Sigma} = 0$)
$\mathbb{S}_i$	Eshelby tensor of the *i*-th inclusion phase
T, T^{ref}	current and reference temperature
$\mathbb{T}_i$	strain concentration tensor of the *i*-th inclusion phase for the dilute scheme
U_{c}	activation energy related to the characteristic time t_{c}
U_{l}	activation energy related to the latency time t_{l}
$\mathbb{V}_i$	stress concentration tensor of the *i*-th inclusion phase for the self-consistent scheme
W, $\dot{W}$	work and its rate
$\mathbb{W}_i$	stress concentration tensor of the *i*-th inclusion phase for the dilute scheme
X_i	aspect ratio of the cracks, which belong to the *i*-th crack family
Y	elastic modulus. This symbol is used to avoid confusion with the components of the macroscopic strain tensor $\boldsymbol{E}$.

Y_{dyn}	dynamic elastic modulus. This symbol is used to avoid confusion with the components of the macroscopic strain tensor $\boldsymbol{E}$.
Y_{st}	static elastic modulus. This symbol is used to avoid confusion with the components of the macroscopic strain tensor $\boldsymbol{E}$.
Y_1, Y_2	elastic modulus in the two branches of the 1D pressure-based model. This symbol is used to avoid confusion with the components of the macroscopic strain tensor $\boldsymbol{E}$.
$\mathbb{Z}_i$	strain concentration tensor of the i-th inclusion phase for the self-consistent scheme

Greek symbols

α	distribution constant in the 1D pressure-based model
$\boldsymbol{\alpha}$	strain coefficient tensor
$\boldsymbol{\beta}$	stress coefficient tensor
β_0	normalized property value at the zero expansion
β_∞	normalized property value at the asymptotic expansion
β_j	normalized value of the j-th mechanical property
$\overline{\beta_j}$	residual normalized value of the j-th mechanical property
δQ	increment of the variable Q (with the exception of $\delta\Omega$ and $\delta\Omega_i$)
$\delta\Omega$	boundary of the REV domain
$\delta\Omega_i$	boundary of the inclusion domain
ϵ_i	damage variable of the cracks, which belong to the i-th crack family
ε	ASR-induced concrete expansion measured during experiments
ε_{l}	latency expansion in the S-shaped curve fitting
ε_{l}	characteristic expansion in the S-shaped curve fitting
$\boldsymbol{\varepsilon}$,ε_{ij}	microscopic strain tensor and its ij-th component
γ	loading coefficient for the 1D pressure-based model
$\gamma_{\boldsymbol{E}}$	loading coefficient correlating the applied macroscopic strain $\boldsymbol{E}^{\mathrm{applied}}$ to the critical macroscopic strain $\boldsymbol{E}^{\mathrm{cr}}$
γ_P	loading coefficient correlating the pressure P to the critical pressure P^{cr}
ϕ_i	volume fraction of the i-th inclusion phase in a two-phase system
ν	Poisson ratio
$\boldsymbol{\xi}$	displacement field on the boundary of the REV domain $\delta\Omega$
ρ_{s}	solidification ratio
$\boldsymbol{\sigma}$,σ_{ij}	microscopic stress tensor and its ij-th component
$\boldsymbol{\sigma}^P$	microscopic pre-stress tensor induced by the pressure P in the inclusion domain

Φ	volume fraction of all crack families
Ψ_{el}	elastic energy
Ψ_{pot}	potential energy
$\mathbf{\Sigma}$, Σ_{ij}	macroscopic stress tensor and its ij-th component
$\mathbf{\Sigma}^{\mathrm{unit}}$	macroscopic unit stress tensor
Ω_i	domain of the i-th phase

Subscripts and Superscripts

$*$	reference configuration (with the exception of the eigenstrain $\boldsymbol{E}^*$ and the incremental strain $\delta\boldsymbol{E}^*$)
agg	quantity related to the aggregate phase
c	quantity related to the crack phase
cem	quantity related to the cement paste phase
f	quantity related to the fluid gel in the solidification model (with the exception of the macroscopic fracture energy G_{f})
gel	quantity related to the ASR gel phase
in	initial quantity related to the undamaged concrete
m	quantity related to the solid matrix phase
p	quantity related to the pores at level I in the two-scale porosity model
pm	quantity related to the porous matrix phase
s	quantity related to the solidified gel in the solidification model
vol	volumetric
Q_i^j	quantity Q evaluated for the i-th crack radius and j-th volume fraction of the solidified cracks in the solidification model.

Abbreviations

ASR	alkali-silica reaction
ER	extremely reactive concrete
FEA	finite element analysis
FEM	finite element method
ITZ	interfacial transition zone
PR	potentially reactive concrete
REV	representative elementary volume
RR	reactive concrete
XFEM	extended finite element method

Contents

Introduction

1

1.1 Background

The alkali-silica reaction (ASR), within the group of alkali-aggregate reactions, is a harmful long-term deteriorating process that evolves at different scales. The chemical process involves *silica* ions, available in the aggregates, and *alkali* ions, mainly present in pores solution together with *water* (*reaction products level*). The formed alkali-silica gel, when exposed to moisture, tends to swell. Its expansion, while confined in the pore structure of concrete, builds up an internal pressure with the consequent formation of cracks in the aggregates and in the cement paste (*aggregate level*). As a consequence, the concrete is expanding and its mechanical properties are degrading (*concrete level*). The reduction in material resistance compromise the performance of the structure in terms of both capacity and durability (*structural level*).

The interaction of the various phenomena at the different scales is a peculiar characteristic of ASR in concrete structures (Figure 1.1). The applied external load acting on an affected structures can be redistributed due to the differential resistance of the material (structural to concrete level interaction). The stress state of the material influences the redistribution of the gel, thus the expansion and the cracking formation (concrete to aggregate level interaction). Eventually, the redistribution of cracks modifies the equilibrium of the system at the reaction products level (e.g. water ingress), thus the chemical process can be (re)activated or stopped (aggregate to reaction products level interaction).

The concrete degradation is influenced by compressive stresses, resulting in an anisotropic swelling and degradation. In a structure, the confinement effect can be induced passively from the reinforcements and actively from the loads. As

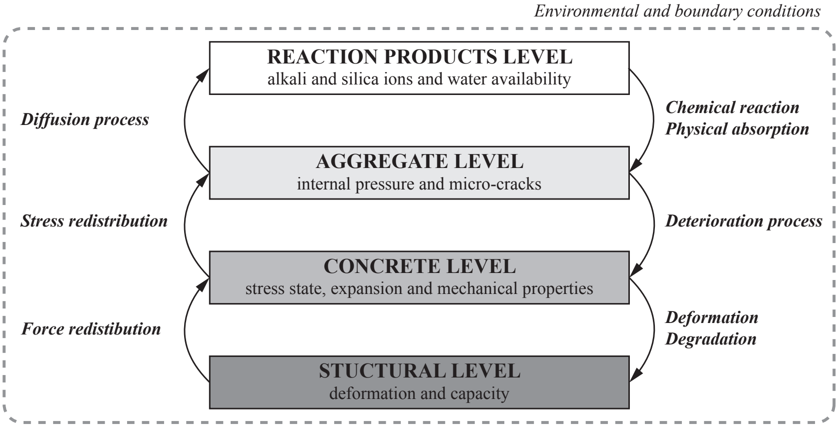

Figure 1.1: The alkali-silica reaction in concrete structures.

a consequence members of the same structure, which are similarly affected, can deteriorate differently.

The degradation of concrete is mainly influenced by the micro-cracking process at aggregates level. The damage present in the aggregates and cement paste can reduce substantially the mechanical properties of the material, even for low expansion values. However, a clear trend in the degradation of engineering properties is still unknown.

The micro-cracking process is correlated to the swelling of the expansive alkali-silica gel, which is influenced by the adopted mix design and the environmental conditions. The proportion between water, alkali ions and silica ions influence the rate of the gel swelling. The amount and the rate of expansion is influenced by the crystalline structure and the size of the aggregates; grains with higher disordered crystalline structure (e.g. opal) or small size aggregates lead to fast reactions and large expansion values. Environmental conditions influence the reaction rate (e.g. the reaction is faster at higher temperature).

Numerous experimental campaigns and various modelling approaches have been developed to understand and predict the effects of ASR on concrete and concrete structures. Due to the multilevel character of the phenomenon, researchers studied the physics from various viewpoints. Engineers mostly investigate the effects induced by the expansive alkali-silica gel on concrete and concrete structures, while geologists and chemists focus on the deteriorating process to determine the kinetics of the reaction of different rock types.

Early approaches experimentally investigated the correlation between gel swelling and concrete expansion, and adopted macro-mechanical material models based on phenomenological relationships for structural analyses. The experiments revealed the importance of environmental conditions and the strong coupling between chemical processed and external boundary conditions. At the beginning, models accounted only for the concrete expansion induced by ASR. Over the years the approaches became more complex with a focus on the coupling effects between the expansion and the mechanical boundary conditions. In the recent period various methods have been developed to describe the interaction between ASR and other long-term phenomena, such as creep.

With technological progress, microscopic investigations were initiated for the identification of the damage process at aggregate level and consequently micro-mechanical material models were developed. The experiments, mostly focussed on free-expansion tests, show the dependence of the microscopic damage process on the adopted mix design. The micro-mechanical models aim to explain the cracking process at aggregate level and the subsequent concrete expansion.

Several investigations are focussed on the kinetics of the reaction and models which describe the flux of ions in the concrete as a porous media are used to define the link between the chemical process and the subsequent expansion. The alkali-silica gel can be present in concrete in an expansive and/or harmless form. The gel, while flowing into the concrete micro-structure, can be in contact with other substances which modify its composition and characteristics, resulting in a different swelling behaviour. The main scope of these models is to explain the evolution of the deteriorating process and the consequent concrete expansion.

The total picture of background and consequences of interactions between the different level is still incomplete. More specifically, at concrete level the evolution of concrete expansion is a well-studied phenomenon. However, the relations between concrete expansion and mechanical degradation is not completely assessed in literature, neither experimentally nor from a modelling point of view. Further, to understand and asses the impact of both expansion and mechanical degradation at structural level, it is necessary to also consider the phenomena at aggregate level (Figure 1.2). This notion determined the scope of this thesis.

1.2 Research scope

The aim of this research is to study the deteriorating impact of alkali-silica reaction considering the correlation between expansion and mechanical degradation of concrete. Both experimental and modelling approaches are followed, analysing the phenomenon at concrete level within the perspective of structural assessments (Figure 1.2).

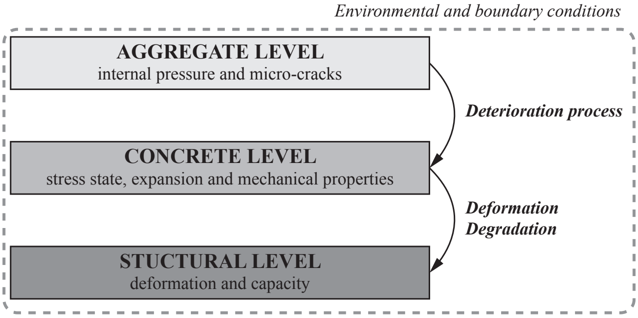

Figure 1.2: Focus of this thesis work.

Experimental tests have been carried out on a reference material, by analysing the evolution of the mechanical properties during the expansion process. These laboratory tests have been conducted as a part of a larger experimental campaign focused on one main case study: the Nautesund bridge (Oslo, Norway). The Nautesund bridge is a unique case, because from construction to demolition, all material and structural details of this bridge were properly documented. Through a collaboration between the Delft University of Technology (TU Delft) and the Norwegian Public Roads Administration (NPRA), a large amount of experimental investigations was conducted on this reference material involving, micro to macroscopic tests as well as laboratory and field analyses.

The experimental results have been statistically analysed in combination with literature data to identify the degradation trend of stiffness and strength of concrete. Correlations between expansion and mechanical properties, tested on specimens under free-expansion conditions, are investigated.

To explore the degradation behaviour induced by ASR on concrete, a multiscale material model, which aims to bridge the gap between micro- and macro-mechanical material models, is adopted. The approach is a micro-poro-fracture-mechanical model which considers affected concrete as a porous material subjected to internal pressure, which is generated by the expansive alkali-silica gel, and external mechanical loading. The aforementioned approach is adopted here mainly to describe the deteriorating impact of ASR on the engineering properties of concrete. However, due to its multiscale formulation, it can be further applied to describe the coupling effects between the internal loading and the external boundary conditions. The model focuses on the relation between aggregate and concrete level. It can be extended to both reaction products and structural levels. In the first case, a kinetic formulation should be introduced to link the expansive pressure to the gel production. In the second case, the model can be either implemented in the finite element method (FEM) or adopted as a complementary tool for the description of the mechanical degradation.

The research has been conducted in the context of a wider project named *performance assessment tool for alkali-silica reaction* (PAT-ASR), which aims to understand the damaging effects of ASR by employing experiments and modelling approaches on various observation scales.

1.3 Research contributions

- The thesis analyses the problem of ASR in concrete structures within a new multiscale perspective by highlighting the need of understanding the deteriorating impact of ASR at concrete level in terms of both expansion and mechanical properties degradation.
- Experimental and literature data are analysed to establish a statistically relevant relationship between the expansion and the degradation of mechanical properties induced by ASR in unconstrained specimens.
- A pressure-based multiscale material model is proposed as a versatile tool for the material characterization of unaffected and ASR-affected concrete.

1.4 Thesis outline

The thesis work is divided into two main branches: one focused on experimental investigations and the other dedicated to the formulation and validation of the proposed multiscale material model (Figure 1.3).

In *Chapter 2* the state-of-the-art in experimental investigations is presented. The scale of observation ranges from microscopic investigation to the analysis of affected concrete elements. The chapter explains the ASR mechanisms in concrete, the induced degradation of the material and the structural effects.

Considering the modelling approaches developed in literature, an overview is given in *Chapter 3*. A comparative analysis is performed by categorizing the input and output parameters of the available literature models. The motivations behind the modelling adopted in this thesis work are presented.

In *Chapter 4* the mechanical degradation of concrete induced by the alkali-silica reaction is investigated. The attention is on the relation between mechanical properties, key parameters within any structural assessment, and concrete expansion due to ASR. Mechanical test results performed on a reference material are presented. Moreover, available literature data, on the evolution of engineering properties of ASR-affected concrete under free-expansion conditions, are collected and statistically analysed.

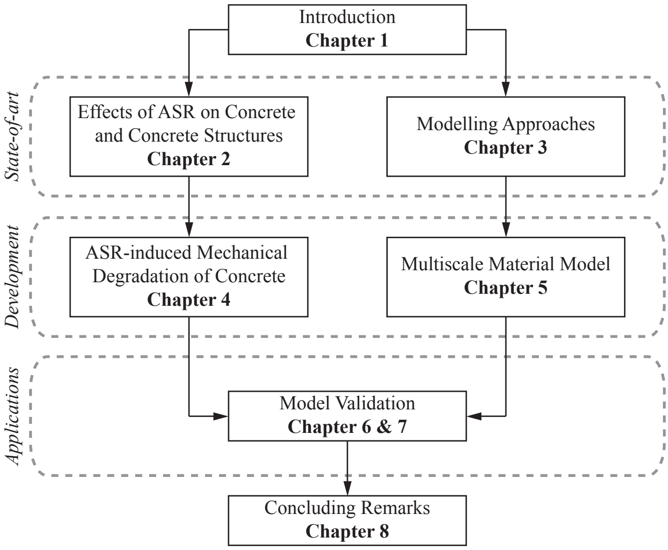

Figure 1.3: Outline of the thesis.

The experimental investigations show that ASR-affected concrete appears as a substantially different material and the known engineering constitutive models, developed for unaffected concrete, cannot be adopted. To simulate its degradation behaviour, a multiscale material model is presented in *Chapter 5*. The model is developed in the context of micro-poro-mechanics theory, which combines micro-mechanics and poro-mechanics approaches. The former determines the macroscopic stiffness of concrete on the basis of its microscopic components at aggregate level and the latter defines the macroscopic state equation of concrete subject to internal and external loading conditions, which act at aggregate and concrete levels, respectively.

In *Chapter 6* the validation of the model is first illustrated for the case of unaffected concrete subjected to external mechanical loading. The calibration procedure for the determination of the micro-mechanical parameters is explained. Afterwards, uniaxial and biaxial loading tests are simulated and model results are compared with literature data. A parametric study is carried out.

In *Chapter 7* the model is validated for the case of ASR-affected concrete. The degradation of engineering properties is studied, making a link with the findings of Chapter 4, by simulating free-expansion tests followed by uniaxial loading tests.

Eventually, conclusions are presented in *Chapter 8*.

Literature Review: Experimental Findings

2

The alkali-silica reaction (ASR) is a harmful long-term deterioration process which, starting within the concrete constituents, produces expansion and damage from aggregate up to structural level. The coupling between the chemical process, the material characteristics and the macroscopic boundary conditions results fundamental in the determination of its deteriorating impact on the concrete material.

To understand the process and its structural consequences, this chapter presents a literature review of the main experimental findings. The ASR mechanisms (Section 2.1) involves *alkali*, present mostly in the cement paste, *silica*, available in the aggregates, and *water* in the pore solution. It generates a hydrophilic expansive gel which deteriorates concrete constituents in terms of expansion and mechanical characteristics (Section 2.2). When the reaction is developed in concrete structures (Section 2.3), its evolution is modified by the confinement effects induced by the reinforcements and loading conditions, which act as restraints. However, different studies have led to diverging conclusions with respect to the effect of this confinement on the loading capacity and ductility of the structures involved. It results that further investigations are needed on the deteriorating impact of ASR on concrete material, especially with respect to the evolution of engineering properties, key parameters in any structural assessment, and on the role of confinement effects (Section 2.4).

Considering that the performance of affected concrete structures are strictly related to the material deterioration, in Chapter 4 the effects of ASR are experimentally studied to establish the relation between concrete expansion and mechanical properties.

2.1 ASR Mechanisms

The alkali-silica reaction in concrete is generally considered as the combination of two distinct stages: in the first stage, the *chemical reaction* forms the reaction products within the boundary of the aggregates, in the second stage, the *physical water absorption* by the reaction products leads to local swelling (Diamond et al., 1981). As reported by Glasser (1992), the kinetics of ASR can be described following Dent-Glasser and Kataoka (1981). First the *silica*, available in aggregates, reacts with the *alkali ions*, present in pore solution, to form the alkali-silica gel:

$$\underbrace{\mathrm{SiO_2}}_{\mathrm{Siloxane}} + \underbrace{\mathrm{R^+OH}}_{\mathrm{Hydroxyli\ ions}} \rightarrow \underbrace{\mathrm{R^+SiO_{(aq)}}}_{\mathrm{Alkali-silica\ gel}} + \underbrace{\mathrm{SiOH}}_{\mathrm{Silicic\ acid}} \tag{2.1}$$

where R^+ denote an alkali ion such as Na^+, K^+ and Ca^+. The production of alkali-silica gel is also provided by the reaction between the produced silicic acid ions and the alkali ions:

$$\underbrace{\mathrm{SiOH}}_{\mathrm{Silicic\ acid}} + \underbrace{\mathrm{R^+OH}}_{\mathrm{Hydroxyli\ ions}} \rightarrow \underbrace{\mathrm{R^+SiO_{(aq)}}}_{\mathrm{Alkali-silica\ gel}} + \underbrace{\mathrm{H_2O}}_{\mathrm{Water}} \tag{2.2}$$

In this first stage, the gel is created in an aqueous form, which is harmless for the material. In the second stage, the exposure to moisture produces an expansive alkali-silica gel:

$$\underbrace{\mathrm{R^+SiO_{(aq)}}}_{\mathrm{Alkali-silica\ gel}} + \underbrace{\mathrm{nH_2O}}_{\mathrm{Water}} \rightarrow \underbrace{\mathrm{R^+SiO\left(H_2O\right)_n}}_{\mathrm{Expansive\ alkali-silica\ gel}} \tag{2.3}$$

During the process, the composition of the gel, which is linked to its swelling power, results influenced by the type of alkali ions R^+. In presence of portlandite, $Ca\left(OH\right)_2$, the first reaction product is a C-S-H gel with a low Ca/Si ratio, having a fluid structure. Afterwards, due to the increase of dissolved silica, the Ca/Si ratio is increasing and consequently the chemical bounded water in the reaction products decreases creating a more dense structure (Leemann et al., 2011). The presence of sodium and potassium ions leads to the formation of a very viscous gel, which governs the swelling process (Hagelia, 2010). It results that the initial presence of portlandite acts as a *buffer* for the reaction (Wang and Gillott, 1991). To account for this phenomenon, the equivalent alkali content Na_2O_{eq} is defined as:

$$\mathrm{Na_2O_{eq}} = \mathrm{Na_2O} + 0.658\mathrm{K_2O} \tag{2.4}$$

where the coefficient 0.658 is the ratio between the molar mass of sodium and potassium oxide.

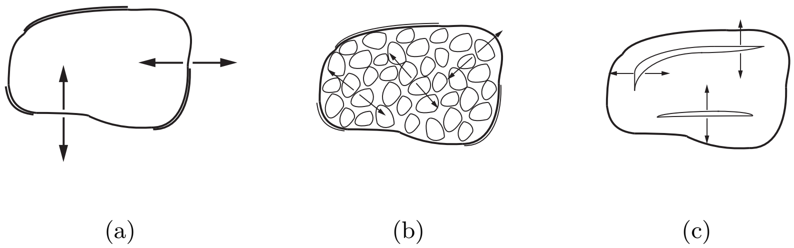

(a) (b) (c)

Figure 2.1: Induced ASR damage mechanisms for different type of aggregates (adapted from Sanchez et al. (2015)).

The development of the reaction products and of the cracking at aggregate level appears different for various aggregate types. Sanchez et al. (2015) reported three different reaction mechanism (Figure 2.1): (1) peripheral reaction rim formation; (2) diffusion reactions in gel pockets within the aggregates and (3) formations of veins within the particles.
The first mechanisms (Figure 2.1a) is observed in quartz-bearing aggregates (e.g. granites, quartzitic diorites and quartzo-feldspathic gneisses),which present a non-porous structure, and can be summarized as proposed by Ichikawa and Miura (2007). At the beginning, the reaction products form a soft reaction rim composed by a fluid hydrated alkali-silica gel. The precipitate Ca_2^+ ions easily penetrates into the rim by making the rim rigid. Afterwards, the alkali ions R^+ fast penetrates the rigid rim and convert the silica products in bulky alkali-silica. The generated pressure induces the cracking of aggregates and surrounding cement paste.
In presence of porous aggregates (e.g. quartzitic sandstones), a thinner reaction rim is observed, but the swelling pressure is stored into the gel pockets (Figure 2.1b). Çopuroğlu (2010) and Rivard et al. (2002) suggest that after the formation of the soft reaction rim, the penetration of the alkali aggressively attacks the aggregates by deteriorating its grain joints. The migration of the alkali within the aggregate produces the densification of the rim, which is thinner than the case of reactive non-porous aggregates. The micro-cracks are first developed in the gravel and radially spread over the cement paste.
The third mechanism (Figure 2.1c) is observed in silica limestone aggregates. The reaction products appear as veins within the aggregates, which follow the original alignment of the rock bedding. The micro-cracks are formed within the aggregates, by following the presence of impure silica, and they become thinner when approaching the cement paste area.

2.2 ASR-induced Concrete Degradation

The deteriorating impact of ASR on concrete is represented by the expansion of the material and the degradation of its mechanical characteristics. The first is directly induced by the swelling of the reaction products, the second is the consequence of the cracks formation within aggregates and/or cement paste.

2.2.1 Expansion

The expansion of unrestrained concrete, which is influenced by the composition of the mix design, the environmental conditions and the casting procedure, is characterized by a sinusoidal evolution in time (Larive, 1998). At the beginning, the chemical reaction develops and no concrete expansion is observed. This stage is characterized by a latency time. Subsequently, the expansion develops fast, within a characteristic time, until an asymptotic value is reached.

Garcia-Diaz et al. (2006) proposed a four-stage mechanism which links the reaction kinetics to the concrete expansion evolution. In the first stage, where no concrete expansion is observed, the chemical reaction takes place with the formation of alkali-silica gel and the precipitation of silicic acid ions. In the second stage, characterized by a rapid concrete expansion, the expansive alkali-silica gel is generated and the precipitation process is slowed down. In the third stage, the dissolution-precipitation process of the first stage starts again, by filling the cracks with reaction products and slow down the concrete expansion. In the last stage, the concrete expansion is asymptotic even if the reaction continues, because the formation of expansive reaction products is counterbalanced by the precipitation process. They propose that the concrete expansion is proportional to the aggregate expansion with an amplification factor of three.

The mix design of concrete results extremely relevant for the amount of expansion developed. Water, alkali and silica ions should be available in a minimum quantity to trigger the reaction, however a *pessimum proportion* exists, which leads to the maximum expansion, influenced by the nature of the reactive aggregates and the mobility of the pore fluids within the concrete (Swamy, 1992). The latter is governed from the porosity of the material, thus from the water to cement ratio (W/C). In fact, the lower the water content available in the system, the lower the probability that the alkali-silica gel forms or becomes expansive. The increase or decrease of supplied water to laboratory specimens showed a similar variation in concrete expansion (Larive, 1998). Similar considerations are concluded with respect to the alkali content of a concrete mix containing potentially reactive aggregates. The maximum expansion is increasing with the increment in alkali content (Multon et al., 2010); however a threshold is still observed in the context of the pessimum proportion effect. Kagimoto et al. (2014)

report that for elevated alkali concentration the gel changes its characteristics limiting its swelling ability.

The aggregate size influences the concrete expansion in terms of rate and maximum value. Experimental tests, performed on aggregates containing quartz (Ben Haha, 2006; Hobbs and Gutteridge, 1979; Zhang et al., 1999), reveal that for grains with sizes between 0.15 and 10 mm, the smaller the aggregate size, the greater the concrete expansion. A similar trend was observed by Andic-Cakir et al. (2009), who reported an increase in expansion when fine reactive aggregate were added to concrete microbar mixtures. Concrete with reactive silica limestone aggregates with sizes between 0.08 to 2.5 mm, present an inverse tendency (Multon et al., 2010). Multon et al. (2010) show that if the concrete contains only large reactive aggregates its expansion will be slower with respect to a concrete with different reactive aggregate sizes; this phenomenon can be explained with the difficulty of the alkali solution to penetrate the aggregates. Moreover, if multiple aggregate sizes are considered the behaviour can be different on the basis of the ratio between the coarse and fine particles. This ratio determines how large the reaction rim around the aggregates is: the larger the rim, the smaller the expansion because the gel has more space before pressurizing the concrete skeleton.

The swelling process is influenced by the environmental conditions (Larive, 1998; Swamy, 1992). Elevated temperatures lead to a faster reaction (Figure 2.2a). The latency period is shortened and the asymptotic value is reached faster. Besides, the moisture content is a relevant parameter. Laboratory tests have shown that if the relative humidity is lower than 50% the concrete does not expand, even if the gel has been formed (Figure 2.2b).

The casting procedure influences the orientation of the concrete expansion and the crack formation. Larive (1998) observed that the gel prefers to swell in the direction parallel to the casting direction; the measured expansion in this direction ranges from 1.3 to 2.8 times the expansion in the perpendicular direction. Comparing vertically cast cylinders and horizontally cast prisms prepared with the same mix and stored in the same condition, their expansion perpendicular to the casting direction resulted similar (Figure 2.3a). Tensile tests on unaffected concrete specimens with the same particle-size show, as is well-known, that the tensile strength is lower along the casting direction. This indicates that the pores distribution determines both the preferred expansion direction and the direction with the weakest tensile strength. This is also confirmed from the tendency of the cracks to orientate the swelling; in fact before cracking occurs, the concrete expansion has an isotropic behaviour (Figure 2.3b). Anisotropic cracking resulting from anisotropic strength properties influence the anisotropic expansion.

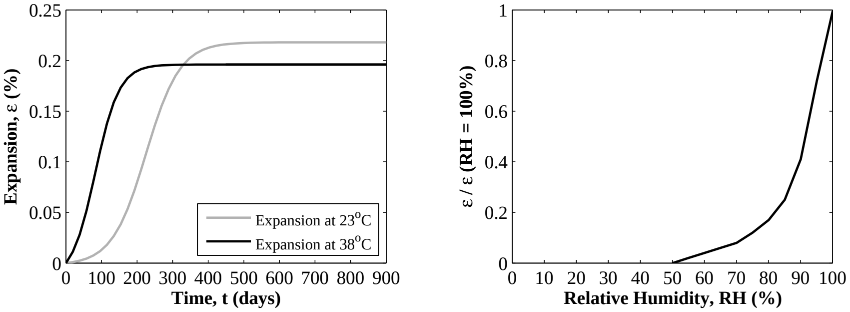

(a) (b)

Figure 2.2: Influence of environmental conditions on concrete expansion: (a) Effect of temperature (adapted from Larive (1998)); (b) Effect of relative humidity (adapted from Swamy (1992)).

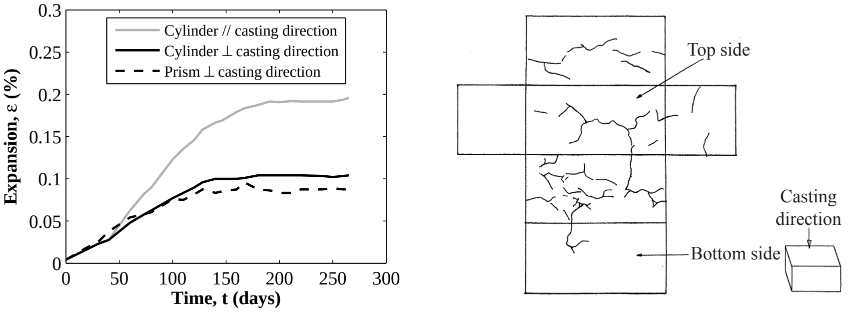

(a) (b)

Figure 2.3: Influence of casting direction on concrete expansion (adapted from Larive (1998)): (a) Expansion of vertically cast cylinders and horizontally cast prisms; (b) Crack pattern of horizontally cast prisms.

Table 2.1: Lower bounds to the residual mechanical properties as percentages of values for unaffected concrete at 28-day (ISE, 1992).

Property	Lower bounds				
Expansion (%)	0.05	0.10	0.25	0.50	1.00
Cubic compressive strength	1.00	0.85	0.80	0.75	0.70
Cylindrical compressive strength	0.95	0.80	0.60	0.60	-
Splitting tensile strength	0.85	0.75	0.55	0.40	-
Elastic modulus	1.00	0.70	0.50	0.35	0.30

2.2.2 Degradation of Mechanical Properties

The formation of cracks at aggregate and concrete level and the swelling process contribute to the degradation of the material. Up to now, the effects of ASR on concrete have been studied mainly with respect to the expansion evolution. Limited research was performed to estimate the degradation of engineering properties leading to controversial results.

The elastic modulus results the most affected property, followed by the tensile strength; while the compressive strength shows a variable trend. Figure 2.4 shows the evolution of expansion and mechanical properties as a function of time, for laboratory specimens stored under free-expansion conditions. All the authors placed the specimens in a high humidity environment. The storing temperature was around $T = 38 - 40°\text{C}$, with the exception of Swamy and Al-Asali (1988), who adopted room temperature ($T = 20°\text{C}$). The specimens reach an asymptotic expansion value between 0.12 to 0.70%, with the exception of an extreme case of the mix B tested by Ahmed et al. (2003), which reached $\varepsilon = 2.70\%$. The elastic modulus Y (Figure 2.4b) substantially degrades up to 90% of its initial value, by presenting an asymptotic residual value (Ahmed et al., 2003; Swamy and Al-Asali, 1988). The compressive strength f_c (Figure 2.4c) does not result as a good indicator for the detection of ASR signs, as already concluded by Swamy and Al-Asali (1988) in earlier studies. In some case, its decreases, similarly to the elastic modulus, down to an asymptotic residual value (Ahmed et al., 2003); other mix designs show an increment (Ben Haha, 2006) or no variations (Multon, 2004). The splitting tensile strength $f_\text{t,sp}$ (Figure 2.4d) degrades similarly to the elastic modulus. Relatively, it reaches higher residual values.

An estimation of the lower bounds to the residual mechanical properties of unrestrained concrete for various ASR free-expansions is proposed by ISE (1992) and reported in Table 2.1.

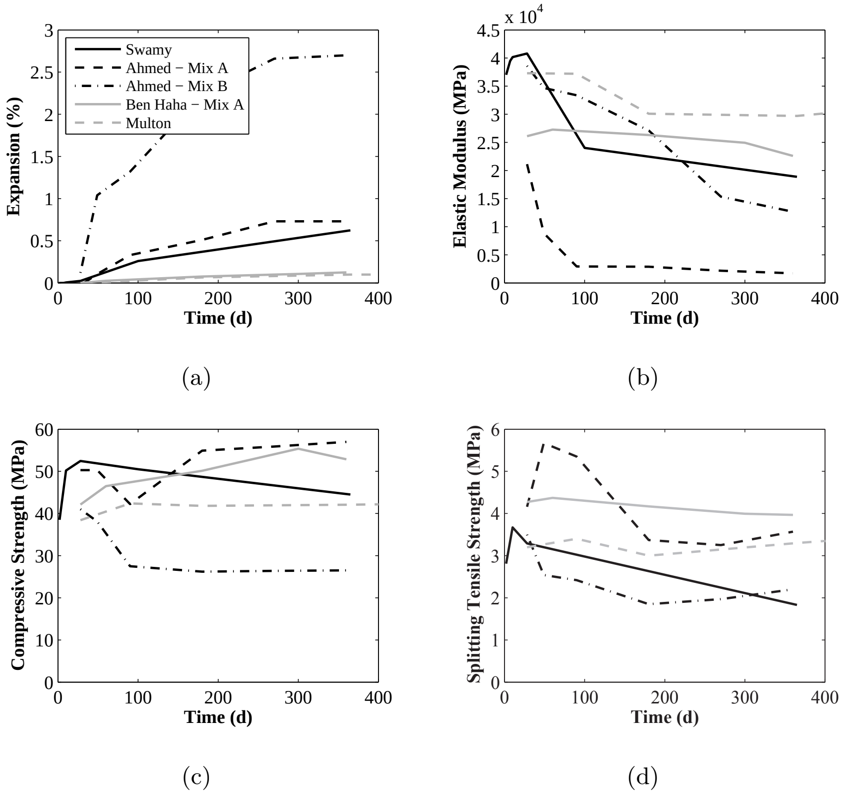

(a) (b)

(c) (d)

Figure 2.4: Mechanical degradation of unconstrained ASR-affected concrete (Ahmed et al., 2003; Ben Haha, 2006; Multon, 2004; Swamy and Al-Asali, 1988): (a) Concrete expansion; (b) Elastic Modulus; (c) Compressive strength; (d) Splitting tensile strength.

2.3 Structural Effects

The damaging process of ASR-affected concrete is strongly correlated to its function within the structure, as it depends on the stress state at which is subjected. As a consequence, the performance of various elements within the same structure may be different.

2.3.1 Confinement Effect

When ASR-affected concrete is subjected to compressive loading, the expansion redistributes along the directions that are less compressed, leading to an anisotropic expansion of the material. This effect is known in literature as the *expansion transfer concept* (Multon, 2004) or *swelling redistribution* (Saouma and Perotti, 2006). Larive (1998) and Dunant (2009) studied the effects of uniaxial compressive loading on affected concrete stored under different environmental conditions. Multon (2004) investigated the expansion evolution in cylindrical specimens subjected to uniaxial compressive loading and confined in radial direction by steel rings. A complete review of these experimental findings can be found in the work by Giorla (2013).

Figure 2.5 shows the evolution of axial and radial expansion strains for affected and unaffected concrete specimens stored under sustained compressive loading. When the affected specimens are sustaining a compressive stresses while expanding, their deformation occurs mainly in the plane perpendicular to the loading direction (Figure 2.5a). In the case of relevant compressive stress, the axial strain results similar to the one of unaffected concrete (Figure 2.5b). The higher the applied load, the higher the expansion redistribution along the radial direction.

2.3.2 Behaviour of Affected Structural Elements

The confinement effect of the concrete expansion plays an important rule on the behaviour of structural elements by redistributing the expansion and pressurizing the member. Several authors investigated the bearing capacity of ASR-affected structural elements with diverging results.

The redistribution of the concrete expansion leads to the orientation of the induced cracks. In unrestrained concrete the crack pattern is irregular presenting intersecting and bifurcating cracks, usually named *map cracks* (Figure 2.6a). Appropriate reinforcements confine the expansion of concrete by orienting the cracks parallel to the direction of the restraint (Figure 2.6b). As a consequence, the concrete expansion is reduced with respect to the case of unrestrained concrete (Section 2.3.1), but the steel bars present tensile stresses, which can lead to

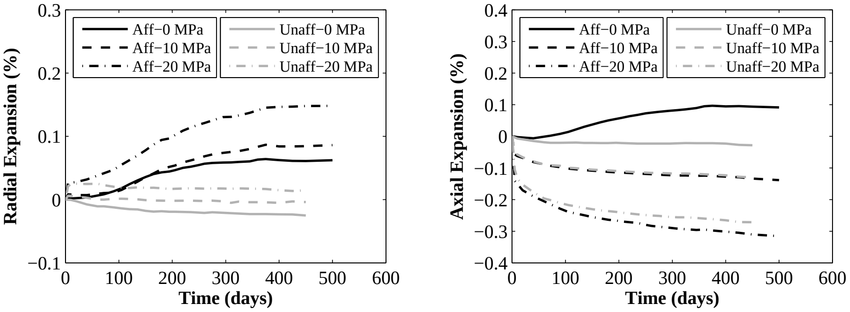

(a) (b)

Figure 2.5: Confinement effect in affected (Aff) and unaffected (Unaff) specimens subjected to 0, 10 and 20 MPa compressive loading (adapted from Multon (2004)): (a) Measured radial strain (perpendicular to the loading direction); (b) Measured axial strain (parallel to the loading direction).

yielding for lower values of external loading. A similar effect is also provided from the application of external compressive loading.

The pressurizing effect induced by the expansive reaction products appears beneficial for the flexural behaviour of reinforced concrete beams, enhancing their capacity and leading to a more ductile behaviour. Giannini (2012) tested full-scale beams exposed to in-situ conditions (Austin, Texas), which presented a maximum expansion of 1.55% along the height, reporting that their bending capacity was slightly increasing. Inoue et al. (2012) observed an increment of 20% flexural capacity of reinforced concrete beams, when companion specimens reached an expansion of 0.44%. In both cases the behaviour of the affected member results more ductile with respect to similar unaffected specimens, showing less deflection under loading. However, the yielding of the bars may occur earlier than in unaffected beams, as reported by Giannini (2012).

The shear capacity of reinforced beams results more dependent from the variation in tensile strength of the concrete. den Uijl et al. (2000) evaluated the behaviour of beams from flat slabs of a bridge having no shear reinforcement. The capacity of the beams was only 75% of the one expected for the unaffected concrete. The beams failed in diagonal shear and not as expected in flexural shear. To account for this modifications, they suggest to evaluate the shear resistance of affected beams on the basis of the tensile strength along the casting direction. Furthermore, the tensile strength variation in affected members influences the bond between steel bars and concrete. ISE (1992) reports a similar degradation

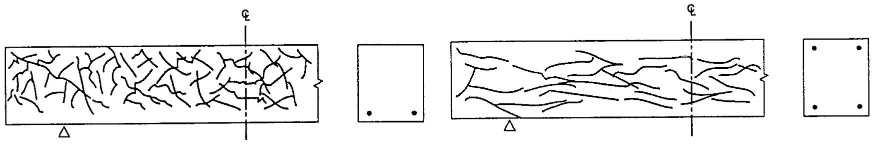

(a)

(b)

Figure 2.6: Behaviour of affected structural elements: (a) Crack pattern in beams with only bottom reinforcements; (b) Crack pattern in beams with equal top and bottom reinforcements (adapted from ISE (1992)).

trend between bond slip and splitting tensile strength for bars that were not restrained by links.

The reduction in compressive strength of affected concrete and the reduction of concrete cover, may compromise the performance of reinforcement columns. The latter is especially relevant for the stability of the structure.

In the case of slabs, a more ductile punching shear mechanisms is reported (ISE, 1992) for concrete expansion values higher than 0.6%. The capacity of the slabs resulted not affected by the reaction (Clark and Ng, 1989); however de-lamination in the reinforcements planes may occur.

Since the behaviour of a concrete member is strictly related to the ability of the reaction products to expand and to the stress state of the material, a different damaging behaviour can be observed for members belonging to the same structure. Stemland (2013) tested beams extracted from the Nautesund bridge (Oslo, Norway) at two locations. It is assumed that the original concrete properties are the same and that the environmental conditions are similar. Members belonging to supporting pillars presented minor signs of ASR, while elements extracted from the tower columns showed significant damage. The difference may be explained by the difference in stress state of the two elements.

2.4 Concluding Remarks

The alkali-silica reaction damages the concrete from aggregate up to structural level. The presence of expansive alkali-silica gel within aggregate boundaries leads to deterioration of the concrete constituents with consequent loss of mechanical characteristics of the material. The performance of structural members and of structures itself can be compromised by the reaction.

At the present time, it is still not completely clear to what extend the ASR compromises the performance of structures and structural members. Contradictory results have been found from several authors who registered no variation, or even an increase, of the capacity of affected members. It appears that the pressurizing effect generated by the expansive alkali-silica gel acts as a beneficial pre-stress within the material, especially if reinforcements and loading condition behave as restraints to the swelling. On the other hand, cracks at the surface of the structures may promote other degradation mechanisms, such as corrosion of the steel bars.

The material deterioration was usually studied with respect to the expansion of unrestrained concrete. The expansion of unrestrained concrete results dependent from the mix design, the environmental conditions and the casting direction. Among others, the silica and alkaline pore solution should be available within a minimum amount to generates the reaction products; a *pessimum proportion* is also defined as the one generating the maximum concrete expansion. The temperature and moisture content of the material influences the rate of expansion; however it should be remarked that the range of these parameters during laboratory tests is much higher than the one experienced by the structures (e.g temperatures higher than 30°C). Eventually, the casting direction may influence the strength distribution in concrete leading to an overall intrinsic anisotropic expansion behaviour. In structures, the intrinsic anisotropy results less relevant with respect to the redistribution of the swelling generated by the confinement effect.

Limited investigations analysed the evolution of engineering properties in ASR-affected concrete specimens stored under free-expansion conditions. The elastic modulus results as the most sensitive property, followed by the tensile strength. On the contrary, contradictory results are reported for the compressive strength.

In conclusion, it appears relevant for the structural assessment to consider the deteriorating impact of ASR on concrete in terms of both expansion and degradation of mechanical characteristics. The latter aspect needs a deeper investigation, which is presented in Chapter 4. Experimental results performed within this thesis work are reported and statistically analysed together with available literature data. The research aims to link the evolution of expansion and engineering properties in free expendable concrete, considering that the latter is a direct consequence of the internal damage generated from the expansive alkali-silica gel.

Literature Review: Modelling Approaches

3

In the previous chapter the main experimental findings regarding the mechanism of alkali-silica reaction in concrete and its structural effects has been presented. In this chapter, the literature review is extended by illustrating the available modelling approaches.

Due to the multiscale nature of the phenomenon, which starts at reaction product level and with possible consequences up to structural level, the problem has been studied by different expertise (e.g. geologists, material engineers, structural engineers) in different fields (e.g. material sciences, structural mechanics). Therefore several modelling approaches were developed with different aims.

An overview of the modelling techniques (Section 3.1) is presented by categorizing the input and output variables of the numerous models. The different methods were classified on the basis of their input parameters as: models based on concrete expansion (Section 3.2), models based on internal pressure (Section 3.3), models based on the gel production (Section 3.4) and models based on the ions diffusion-reaction mechanisms (Section 3.5). The attention is focused on understanding if and how the available models are able to describe the deteriorating impact induced by ASR in concrete material and if the approaches can ultimately be extended to structural analyses.

The description of the coupling between the phenomena at aggregate and concrete level is of importance for the structural assessment (Section 3.6). This is not always a point of attention for the current presented models. To formulate a versatile approach that can be easily down- and up-scaled at reaction products and structural level, an analytically solved multiscale material model is chosen, which is presented in Chapter 5.

3.1 Overview

In general, literature reviewers classify models on the basis of the observed scale (Pan et al., 2012; Saouma and Xi, 2004). The models able to simulate the behaviour of structures are classified as structural or macroscopic. The approaches which investigate the phenomenon at reaction products or aggregate level are defined as microscopic or mesoscopic. It should be noticed that authors adopt different definitions of structural, macro, meso and micro scale; for clarity this terminology is not adopted in the presented classification.

To propose a consistent and comprehensive literature review, the available modelling approaches are subdivided on the basis of their starting scale, which is defined as the level at which the input parameters are defined. Table 3.1 reports an overview of the available models for ASR-affected concrete.

Various models, especially in the early days, have focused on the description of the structural behaviour by imposing an *ASR expansion* at *concrete level.* They form the first category of modelling approaches in Table 3.1. The Finite Element Method (FEM) was employed to couple the imposed expansion with a damage criterion for concrete. The imposed concrete expansion, was first considered in the context of the thermal equivalence. Subsequently, thanks to systematic laboratory campaigns, kinetic laws were formulated considering the thermodynamic aspects, promoting a chemo-mechanical approach. The attention was mainly focused on the dependency of the concrete expansion from the environmental (Section 2.2.1) and boundary (Section 2.3.1) conditions. Attempts were made to correlate the swelling to the potential reactivity of the concrete mix design (e.g. alkali content). Having as an ultimate goal the assessment of affected structures, some researchers formulated the constitutive relationship for concrete considering microscopic phenomena in the context of mixture theory; the idea of ASR developing in a heterogeneous concrete material started to take root.

Thanks to microscopic laboratory observations, which revealed the connection between the *internal pressure* generated by the gel expansion and the consequent concrete behaviour, various models were developed *at aggregate level.* They are listed as the second category of modelling approaches in Table 3.1. The concrete was considered as a heterogeneous multiphase material composed by aggregates and cement paste and in some cases also by pore space. Three techniques could be distinguish in this category. First, mathematical models were employed to describe the correlation between the expansive gel, the internal pressure developed on the concrete constituents and consequent fracture processes. Second, the micro-poro-mechanical theory, which provides an analytical solution method, was employed to define the nature of the mechanisms at aggregates level and to explain the evolution of the observed concrete free-expansion. Third, computational based models, in which the concrete constituents are explicitly modelled by FEM, were

Table 3.1: Overview of modelling approaches for ASR in concrete.

■ Input
░ Scope
▒ Demonstration
▓ Experimental validation

	Reaction Products Level		Aggregate Level		Concrete Level			Structural Level		
	Ions & water	Gel	Swelling	Damage	Swelling	Damage	Mech. Prop.	Lab specimens	Members	Structures
Charlwood (1994)					■			░	░	▓
Léger et al. (1996)					■		■	░	░	▓
Capra and Bournazel (1998)					■	░	░	▒		
Malla and Wieland (1999)					■	░	░	░	░	▓
Ulm et al. (2000)					■	░	░	░	░	▒
Li and Coussy (2002)					■	░	░	░	░	▓
Capra and Sellier (2003)					■	░	░	░	▓	
Farage et al. (2004)					■	░	░	▓		
Bangert et al. (2004)					■	░	░	▓	▓	
Saouma and Perotti (2006)					■		■	░	░	▓
Winnicki and Pietruszczak (2008)					■	░	░	▓	░	▓
Comi et al. (2009)					■	░	░	▓	░	▓
Pesavento et al. (2012)					■	░	░	▓		
Esposito and Hendriks (2012)					■	░	▓			
Bažant et al. (2000)			■	▒						
Dormieux et al. (2004)			■	░	▒	░	░	▒		
Schlangen and Van Breugel (2005)			■	▒	▒	░	▒	▒		
Çopuroğlu and Schlangen (2007)			■	▓	▒	░	░	▓		
Comby-Peyrot et al. (2009)			■	▓	▓	░	▓	▓		
Reinhardt and Mielich (2011)			■	▓						
Anaç et al. (2012b)			■	▓	▓	░	░	▓		
Wu et al. (2014)			■	▒	░	░	░	▒		
This thesis work			■	░	▓	░	▓	▓		
Ulm et al. (2002)		■	░	░	▓	░	░	▓		
Lemarchand (2001)		■	░	░	▓	░	░	▓		
Grimal et al. (2008a,b)		■	░	░	▓	░	░	▓	▓	
Dunant and Scrivener (2010)		■	░	▓	▓	░	▓	▓		
Giorla (2013)		■	░	▓	▓	░	░	▓		
Pignatelli et al. (2013)		■	░	▓	▓	░	░	▓	▓	
Charpin and Ehrlacher (2014)		■	░	░	▓	░	▒	▓		
Bažant and Steffens (2000)	■	░	▒							
Suwito et al. (2002)	■	░	░	░	▓			▓		
Poyet et al. (2007)	■	░	░	░	▓			▓		
Multon et al. (2009)	■	░	░	░	▓	░	▓	▓		
Puatatsananon and Saouma (2013)	■	░	▒	▒	▓	░	░	▓		
Alnaggar et al. (2013)	■	░	░	░	▓	▓	▓	▓		
Liuaudat et al. (2014)	■	▒								
Nguyen et al. (2014)	■	░	░	░	▒			▒		

proposed to investigate the correlation between the induced damaged at aggregate level and the consequent concrete expansion.

To couple the physical chemistry of ASR with the mechanical behaviour of concrete, various modelling approaches were used to study the phenomenon at *reaction products level*. They are listed as the third category of modelling approaches in Table 3.1. The reaction kinetics was expressed as a function of the *change in mass or volume of the gel* (Section 2.1). This approach was first adopted to formulate or further develop models that investigate the phenomenon at aggregate levels. Two schools developed, on using analytical models based on the micro-poro-mechanical theory and one using computational based models. In addition, some authors implemented this type of reaction kinetics in a chemo-mechanical approach to describe the behaviour of affected structural members.

Recently, the investigation at reaction products level have been further improved by the formulation of *diffusion-reaction* models to simulate the chemical process. They are listed as the fourth category of modelling approaches in Table 3.1. First, mathematical models were developed to describe the flux of ions and water and their subsequent reaction, as well as the diffusion and expansion of the produced gel. Afterwards, the models were linked to existing damage model to describe the coupling between the reaction process and the mechanical behaviour of concrete. To date, these models have only been scaled up to concrete level, by describing the expansion phenomenon. Analytical micro-poro-mechanical techniques and computational modelling techniques at aggregate level have been used.

3.2 Models based on Concrete Expansion

A number of modelling approaches have been developed starting at concrete level and focussing on massive structures such as concrete arch-dams. The effects of ASR were modelled by imposing an expansion strain in concrete. The evolution of the strain over time was derived from phenomenological laws or from reaction kinetics laws based on thermodynamic principles. Table 3.2 gives an overview and it may serve as a guideline for this section.

At the beginning, Finite Element Analyses (FEA) of affected structures were performed considering the induced expansion similarly as a thermally induced strain. The numerical results were compared with the in-situ deformation measurements of affected structures, as showed by Malla and Wieland (1999).

Thanks to the large and systematic laboratory campaigns, phenomenological laws were formulated that link the induced concrete expansion to the environmental conditions (Larive, 1998; Swamy, 1992), the stress state of the material (Charlwood, 1994; Multon, 2004) and the reactivity of the material (Léger et al., 1996). Charlwood (1994) has recognized the importance of compressive stress on

Table 3.2: Models based on concrete expansion.

	Model type	Imposed strains dependent on	Validation (V)/ Demonstration (D)
Charlwood (1994); Thompson et al. (1994)	phenomenological	stress state	powerhouse (V)
Léger et al. (1996)	phenomenological with reduction of stiffness and tensile strength	stress state, temperature, moisture, reactivity	2D FEA spillway pier (V)
Capra and Bournazel (1998)	phenomenological with probabilistic fracture mechanics	stress state, temperature, moisture, reactivity	lab specimens (D)
Malla and Wieland (1999)	phenomenological with linear-elastic fracture mechanics	-	3D FEA arch-gravity dam (V)
Ulm et al. (2000)	thermo-chemo-plastic with kinetics law	temperature	2D FEA dam and bridge box girder (D)
Li and Coussy (2002)	thermo-chemo-plastic with kinetics law	temperature, moisture	2D FEA bridge pier (D)
Capra and Sellier (2003)	thermo-hygro-chemo-damage with kinetics law	temperature, moisture, reactivity	2D FEA of lab specimens (V) and of RC beam (D)
Farage et al. (2004); Fairbairn et al. (2004)	thermo-chemo-cracking with kinetics law	temperature	3D FEA lab specimen and dam (V)
Bangert et al. (2004)	thermo-hygro-chemo-damage based on mixture theory	temperature, moisture	2D FEA lab specimens and beam (D)
Saouma and Perotti (2006)	thermo-hygro-chemo with kinetics law and reduction of stiffness and tensile strength	stress state, temperature, moisture	2D FEA lab specimens (V) and dam (D)
Winnicki and Pietruszczak (2008); Winnicki et al. (2014)	thermo-hygro-chemo-plastic for RC with kinetics law	stress state, temperature, moisture	lab specimens (V) and 2D FEA dam (V)
Comi et al. (2009)	thermo-chemo-damage with kinetics law	temperature	2D FEA lab specimens and dam (V)
Pesavento et al. (2012)	thermo-hygro-chemo-damage based on mixture theory	temperature, moisture	2D FEA lab specimens (V)
Esposito and Hendriks (2012)	thermo-chemo-cracking rheological-based	temperature	lab specimens (V)

the anisotropic expansion of affected concrete. He adopted a logarithmic law for the reduction of the concrete expansion on the basis of the compressive stress. This model was adopted by Thompson et al. (1994) and Berra et al. (2010).
Léger et al. (1996) developed a phenomenological model in which the induced concrete expansion was dependent on the stress state of the material following Charlwood (1994), linearly dependent on the temperature and the relative humidity above a certain threshold value and a function of the total alkali content and aggregate type. The tensile strength and the elastic modulus of concrete were degrading on the basis of the imposed expansion. The model was applied to study the behaviour of a spillway pier.
Capra and Bournazel (1998) merged a phenomenological approach with probabilistic cracking theory which aimed to account for the spatial distribution of the reaction sites within the structures. The damage was evaluated with linear fracture mechanics theory. The model was adopted to simulate free and confined concrete expansion tests on laboratory specimens.

Subsequently, the thermo-chemo-mechanical models, which expressed the concrete free-expansion as a function of a thermodynamic kinetics law, were developed following the idea proposed by Ulm et al. (2000). The approach has been based on the large experimental campaign performed by Larive (1998), who tested several concrete mixtures stored under various environmental conditions. A phenomenological sinusoidal law for the evolution of concrete expansion was derived based on three parameters: the latency time, the characteristic time and the asymptotic expansion value (Section 2.2.1). Ulm et al. (2002) explained this behaviour in the context of physical chemistry, considering the concrete as a porous material subjected to an internal pressure and to an external mechanical loading. They adopt a first order reaction kinetics laws, in which the two time parameters depend on the temperature and the activation energies within the Arrhenius concept. The imposed expansion was not dependent on the moisture content and the stress state of the material. The induced damage was evaluated in the framework of a plasticity criterion. The model's abilities were demonstrated with 2D FEA of a gravity dam and a bridge box girder.

The thermo-chemo-mechanical approach proposed by Ulm et al. (2000), based on the thermodynamic reaction law, was further developed and applied in combination with existing damage models.
Li and Coussy (2002) extended the kinetics law by including the dependency of the imposed concrete strain on the moisture content. The damage criterion was formulated within the plasticity theory. The model aimed to be used in a structural assessment strategy; it was tested for bridge components.
Capra and Sellier (2003) adopted a probabilistic approach, following up the work of Capra and Bournazel (1998), to describe the main damage mechanisms in affected

structures. The reaction kinetics was linked to the consumption of alkali and it was dependent on temperature and relative humidity. Three damage variables were identified to describe the probability of cracking due to the ASR-induced concrete expansion, tensile and compressive stresses. The model was able to simulate the anisotropic expansion behaviour observed in constrained laboratory specimens; its abilities were further demonstrated for an affected reinforced concrete beam subjected to a moisture gradient.

Farage et al. (2004) implemented the thermo-chemo-mechanical model proposed by Ulm et al. (2000) within a smeared fixed cracking model. They adopted an ideally plastic stress-strain relationship to describe the behaviour of affected concrete in tension. This ductile post-cracking relation is derived from a back analysis of only one set of experimental tests (Larive, 1998). The model was validated with 3D FEA of laboratory specimens, and further applied by Fairbairn et al. (2004) to a concrete dam.

Saouma and Perotti (2006) mainly focused on the expansion redistribution effect generated by the coupling between internal swelling and stress state of the material (Section 2.3.1). The volumetric imposed strain, which is a function of temperature (Ulm et al., 2002) and moisture content (Capra and Bournazel, 1998), was distributed along the principal stress directions on the basis of the current stress state and the tensile and compressive strength of the material. The induced material deterioration was imposed as a reduction of the stiffness and tensile strength in time following a sinusoidal curve, similarly to Malla and Wieland (1999); no degradation of compressive strength is assumed. The model was validated by simulating the confined expansion tests performed by Multon (2004); subsequently a gravity dam was studied by 2D FEA. This approach meets the needs of practical engineers and it is still widely used (Saouma, 2013). As a consequence, it was initially selected within this Ph.D. work to perform analyses of affected structures and members (Appendix A).

Winnicki and Pietruszczak (2008) described the chemo-mechanical interaction within the framework of a thermo-hygro-chemo-plastic model for reinforced concrete. The imposed concrete strain depended on the compressive stresses following Charlwood (1994), on the temperature following Ulm et al. (2002) and on the relative humidity in agreement with Capra and Bournazel (1998). They have pointed out the importance of an appropriate modelling techniques to describe the coupling between internal swelling and external mechanical loading as well as the mechanical degradation induced in the material. The model was validated against free-expansion and confined expansion tests on laboratory prisms and cylinders. It was further applied to study the crack formation in a gravity dam (Winnicki et al., 2014).

Comi et al. (2009) studied the damaging effects in affected concrete in the context of their fracture energy based bi-dissipative damage model. The model was able to describe the anisotropic swelling behaviour observed in confined expansion tests, by employing two isotropic damage variables for tension and compressive stresses. The model was validated in terms of expansion evolution for confined concrete specimens. It was further employed to investigate the behaviour of a concrete gravity dam.

To link the reaction kinetics to the physics of the phenomenon, Bangert et al. (2004) and Pesavento et al. (2012) adopted mixture theory, considering the concrete as a multiphase reactive porous media composed by a solid skeleton and capillarity porosity. The swelling of reaction products was evaluated as an imposed strain on the concrete skeleton, which depended on the temperature and the degree of saturation of water. The imposed strains were linked to the difference in density between the reactive and unreactive skeleton. They accounted for the coupling between the ASR phenomenon and the pressure exerted by the water in the capillarity porosity and in the skeleton; thus, the thermo-hygro-chemical coupling was formulated. The material model was formulated in the mathematical framework and further implemented in finite element method (FEM).
Bangert et al. (2004) employed a regularized continuum isotropic damage model based on damage variables, which did not account for the cracking induced by the expansive alkali-silica gel at aggregate level. As a results, affected concrete specimens stored under free-expansion conditions do not present any damage; the cracking can occur only in confined affected specimens. The model's abilities were demonstrated by means of 2D FEA of laboratory specimens and of a beam.
Pesavento et al. (2012) adopted a non-local isotropic damage model based on two damage variables related to the external mechanical loading and internal chemical loading. The damage variable associated with the chemical reaction was derived by fitting the experimental results in terms of expansion versus Young's modulus curve. The model was validated by 2D FEA of laboratory specimens; only part of the specimens is meshed, taking advantage of symmetry, due to the heavy computational effort which is needed to solve the complex equation system. The validation procedure analysed specimens subjected to various hygro-thermal conditions and stored under free-expansion conditions. The comparison was made in terms of induced expansion and mass variation of concrete.

Since the assessment of ASR effects in concrete structures is the primary focus of this Ph.D. work, a thermo-chemo-cracking model (Esposito and Hendriks (2012), Appendix B) was first developed to be merged with the approach proposed by Saouma and Perotti (2006). The rheological model aimed to explain the link between the expansion and the degradation of mechanical properties in affected concrete, which is not accounted for in the aforementioned modelling techniques. The reaction kinetics law proposed by Ulm et al. (2000) was adopted. The damage mechanisms was described by two parallel inelastic springs, one of them working

Table 3.3: Models based on internal pressure.

	Model type	Imposed	Validation (V)/ Demonstration (D)
Bažant et al. (2000)	linear-fracture mechanics theory	pressure in particle rim	Idealized one-particle cubic cell (D)
Dormieux et al. (2004)	chemo-poro-micro-elastic	pressure in porosity	lab specimens (D)
Schlangen and Van Breugel (2005)	lattice model with quasi-brittle aggregate, ITZ and matrix phase	strain in aggregate and/or ITZ	2D FEA lab specimens (D)
Çopuroğlu and Schlangen (2007); Schlangen and Copuroğlu (2010)	lattice model with quasi-brittle aggregate, ITZ and matrix phase	strain in aggregate and/or ITZ	2D and 3D FEA lab specimens (V)
Comby-Peyrot et al. (2009)	particle model with linear-elastic aggregate phase and elastic damage matrix phase	strain at aggregates rim	3D FA lab specimens (V)
Reinhardt and Mielich (2011)	linear-elastic fracture mechanics	pressure in aggregates	rock specimens (V)
Anaç et al. (2012b)	lattice model with quasi-brittle aggregate, ITZ and matrix phase	strain in aggregate and/or ITZ	2D FEA lab specimens (V)
Wu et al. (2014)	FE^2 multiscale model	strain in porosity at lower level	3D FEM lab specimens (D)

in series with the imposed expansion. The model aimed to reproduce the stiffness and tensile strength degradation in both unaffected and affected concretes. The validation, against laboratory specimens stored under free-expansion conditions, showed the limitation of the model. It was concluded that further investigations on the deteriorating impact of ASR on concrete material could only be modelled by observing the phenomenon at aggregate level rather than at concrete level.

3.3 Models based on Internal Pressure

Thanks to the technological advancement in microscopic investigation, at the beginning of this century several approaches have investigated the ASR mechanisms at aggregate level, to explain the induced effects at concrete level. The concrete was represented as a heterogeneous material composed primary by aggregates and matrix phases. In the latter, the cement paste and small particles (e.g. sand) were included, while in the former only gravel particles were considered. Some authors have also considered the presence of an Interfacial Transition Zone (ITZ), which surrounds the aggregates to the matrix. The expansion of concrete was obtained as a direct result of the gel swelling. Table 3.3 gives and overview of the proposed models, which start from an assumed internal pressure.

Three typologies of approaches have been developed:(1) mathematical models that describe damage mechanisms at aggregate level, (2) micro-poro-mechanical methods that analytically correlate the local and global quantities at aggregate and concrete level and (3) numerical methods that compute, through FEM techniques, the damage at aggregate level within the different phases of concrete. All the approaches, adopted the concept of representative elementary volume (REV), that has been defined as an infinitesimal portion of the three-dimensional material system under consideration. Denoting by D and l the characteristic length of the structure and of the REV, respectively. The REV results representative of the structure only if its length l is larger than the size d of local heterogeneity (e.g. aggregate and/or pore size) and smaller than the structure dimension D:

$$d \ll l \ll D \tag{3.1}$$

The first typology of approaches includes mathematical models, which adopted linear-fracture mechanics theory to study the cracking phenomenon in reactive particles. Bažant et al. (2000) considered concrete specimens made of waste glass particles. These particles, differently from natural aggregates, consist of pure silica with a ordered crystalline structures; as a consequence the ASR develops fast and the reaction products are uniformly distributed around the particle rim (Figure 2.1a). The analysed REV consisted of idealized periodic cubic cell made of a single spherical particle embedded in the cement paste matrix. The pressure induced by the expansive reaction products was considered as an internal loading. The influence of both external and internal loading on the cracking was accounted in the context of effective stress concept. The relationship between tensile strength and expansion of concrete was established by means of the stress intensity factor; neither a correlation with the compressive strength nor with the Young's modulus was made. The approach was mainly employed to identify the *pessimum size* of aggregates, which leads to the maximum concrete expansion. With a similar focus, Reinhardt and Mielich (2011) investigated the correlation between expansive pressure and cracking for natural rocks. In this case, the internal pressure was applied within the aggregates. Comparison with experimental results on reactive rocks showed that the critical stress intensity factor appears to govern the cracking of the aggregates and to be sensitive to the alkaline environment.

The second typology of approaches adopts the micro-poro-mechanics theory, which blends the concepts of poro-mechanics, micro-mechanics and analytical homogenization approaches. Dormieux et al. (2004) were one of the first research group to treats ASR-affected concrete in the framework of micro-poro-mechanics theory. The concrete was considered as a porous material composed by a pore space, filled by expansive gel products, embedded in a solid matrix, representing the concrete skeleton. The state equations and the mechanical characteristics at the global scale (concrete level) were analytically evaluated on the basis of the quantities at local scale (aggregate level). The ASR phenomenon was simulated by means of cracks growing in the vicinity of the aggregates, which were not explicitly considered. A reaction kinetics was proposed to link the gel mass production and the damage process, but this has not been adopted during the validation process. The approach can be defined as smeared, since the overall behaviour of the material depends only on the elastic properties of the phases and on the shape and volume fraction of the pore space. They showed that the concrete free-expansion results from the crack propagation at aggregate level after saturation of the pore space is reached. The initial delay in concrete expansion is directly related to the filling of initial porosity. This concept has been further developed by Lemarchand et al. (2005), as shown in next section.

The third typology of approaches regards the numerical computation of the phenomenon at aggregate level. The structure of concrete at the local scale was modelled by FEM techniques; this approach allows to compare the damage mechanisms at aggregate level with the one observed on laboratory specimens under microscope (e.g. polished section analysis). The computational effort, which can be quite elevated, depends from the REV dimension and mesh size adopted. Schlangen and Van Breugel (2005) adopted the lattice model, already developed in their research group (Schlangen and Van Mier, 1992). The concrete was considered as a three-phase material composed of aggregates, cement paste and ITZ phases. A peculiar characteristics of this technique was that the aggregates were modelled by using for their real shape and not as spheres. Each phase was meshed by beam elements able to transfer normal forces, shear forces and bending moments. A brittle fracture mechanism was adopted: when an element reached its tensile strength, it was removed from the system. The swelling of the alkali-silica gel was treated as an imposed expansion randomly distributed within the aggregate boundaries. The relation between the location of swelling points and the resulting concrete expansion was investigated in comparison with experimental findings (Çopuroğlu and Schlangen, 2007; Schlangen and Copuroğlu, 2010). The model was able to simulate the ASR-induced damage mechanisms at aggregate level and to approximate the concrete expansion. They evaluated the degradation in terms of tensile strength, but no comparison is made with experiments.
The lattice model has been further applied by Anaç within the PAT-ASR project, as a tool to assess the damage mechanisms of ASR in combination with a large experimental investigation (Anaç et al., 2012b). Microscopic observations from

polished section analyses were adopted both as input to describe the lattice mesh and in comparison with numerical results. The damage, numerically estimated, was compared with damage rating index (DRI), which evaluates the presence of cracks and gel formations correlated to the ASR phenomenon.
Comby-Peyrot et al. (2009) employed a full three-dimensional FE model, in which the aggregate were represented by particles. Only gravels, embedded in a mortar matrix formed by the small size aggregates and the cement paste, were considered. The particles behaved linearly elastic, while a non-local Maziar model was adopted for the mortar phase. Mechanical tests on mortar bars, like Brazilian splitting test and bending test, were used to identify the input parameters. The ASR phenomenon was simulated by swelling of the aggregate rim. The imposed strain was evaluated as an increment of the particles volume, which was input by fitting the expansion evolution of unconstrained concrete specimens. The model was able to reproduce the crack pattern of damaged affected concrete and its Young's modulus degradation.
Wu et al. (2014) proposed a multiscale material model ranging from reaction products to concrete level. The concrete was modelled by aggregates, represented by spherical inclusions, embedded in the cement paste, which was formed by a pore space and the product derived from the cement hydration. The expansive alkali-silica gel was considered, rather than a phase, as an imposed strain in the pore space of the matrix, at one scale lower than the aggregates. The imposed strain depended from the moisture content and from the temperature, following the same kinetics law proposed by Ulm et al. (2000). The behaviour of concrete was determined by a numerical two-scale homogenization approach, which solves the boundary values problem for the REV employing the FEM at both scales. The aggregates were considered as elastic phase, while the cement paste followed a visco-plastic behaviour. The isotropic damage criterion was formulated only at aggregate scale, but the effects of reaction products, within the cement paste phase, was accounted via the deterioration of its mechanical properties. The model's abilities were demonstrated for two specimens subjected to different environmental conditions; only the damage pattern at aggregate level is shown.

3.4 Models based on Gel Production

To couple the physical chemistry of ASR with the mechanical behaviour of concrete, various modelling approaches have studied the phenomenon at reaction products level. The reaction kinetics was expressed as a function of the change in mass or volume of the expansive alkali-silica gel, which was subsequently translated into an imposed strain or pressure at aggregate level. Depending on the complexity of the adopted methods, different output levels were reached. In the majority of the cases, the ASR effects were described at concrete level and the approach was

Table 3.4: Models based on gel production.

	Model type	Variation of gel	Validation (V)/ Demonstration (D)
Ulm et al. (2002)	chemo-micro-poro-plastic	mass	lab specimens (D)
Lemarchand (2001); Lemarchand et al. (2003, 2005)	chemo-micro-poro-elastic	mass	lab specimens (V)
Grimal et al. (2008a,b)	thermo-hygo-chemo-damage rheological-based	mass	lab specimens (V) and 3D FEA RC beams (V)
Dunant and Scrivener (2010)	XFEM with quasi-brittle aggregate and cement paste phases, elastic gel pockets	surface	2D FA lab specimens (V)
Giorla (2013); Giorla et al. (2015)	XFEM with quasi-brittle visco-elastic cement paste phase, quasi-brittle aggregates and elastic gel pockets	surface	2D FA lab specimens (V)
Pignatelli et al. (2013)	chemo-micro-poro-damage	mass	lab specimens (V) and 2D FEA beams (V)
Charpin and Ehrlacher (2014)	chemo-micro-poro-fracture	volume	lab specimens (V)

proposed as a complementary tool to be adopted in the structural assessment. Table 3.4 gives an overview of models based on the gel production.

In the framework of micro-poro-mechanical theory, Ulm et al. (2002) and Lemarchand et al. (2005) have investigated the connection between the swelling of reaction products at aggregate level and the consequent concrete expansion. They both considered the swelling of the reaction products as a pressure, exerted within the porosity space, on the concrete skeleton.
Ulm et al. (2002) have demonstrated that "the swelling pressure activates the same fractional-dilatation mechanisms" at aggregate level, which are present during concrete cracking by external applied loading. The initial delay between the activation of ASR and the concrete expansion, was obtained from the reaction products filling the existing pore space. The stress induced anisotropy expansion, observed in confined concrete, was considered as a result of the chemo-poro-plastic dilatation, in which the compressive stresses pressurize the solid matrix and delay the occurrence of irreversible deformations.
Lemarchand et al. (2005) applied chemo-poro-elastic theory to identify the nature of the free-expansion behaviour of concrete between the topochemical or the through-solution nature mechanism. In the topochemical mechanism the reaction products uniformly fill the porosity, following the reaction kinetics related to the dissolution of silica, while in the through-solution mechanism the ASR phenomenon is described by the cracking process around the aggregates. They have concluded that both mechanisms were able to describe the sinusoidal free-expansion curve; however the characteristic time, within which the expansion is developed, resulted a function of the reaction kinetics.
Charpin (2013) have studied the induced anisotropic expansive behaviour in confined concrete specimens by employing a chemo-micro-poro-fracture model. The concrete was composed of aggregate, ITZ and cement paste phases, which behaved elastically. The expansive alkali-silica gel was formed at the aggregate rim and it flowed within the ITZ porosity. The overall concrete properties were analytically evaluated. The internal pressure, exerted by the gel in the cement paste, was evaluated as a function of the change in gel volume. The damage at aggregate level was represented by three orthogonal penny-shaped cracks, saturated by the gel, formed around the spherical aggregates. The damage criterion, based on energy approach, accounted for two mechanisms: the de-cohesion of aggregate and ITZ phases and the cracking of the cement paste. The model was validated for confined laboratory specimens in terms of concrete expansion. Good agreement with experimental results was obtained for concrete specimens under compressive loading up to 10 MPa. For higher compressive stresses, the de-cohesive mechanisms was not activate, thus the model underestimated the expansion values. The author reports an overestimation of the stiffness degradation, but no comparison is made with experimental findings.

Some authors have analysed the ASR-induced damage at aggregate level adopting computational methods in combination with microscopic observations.
Dunant and Scrivener (2010) employed the extended finite element method (XFEM) to model the evolution of concrete structure at aggregate level induced by the formation of the reaction products. In a two-dimensional system, circular inclusions represented the aggregates embedded in the cement past matrix. The reaction products were accounted, within the aggregates, with randomly distributed gel pocket phases. The gel's stiffness was calibrated by fitting the free-expansion curve of concrete at early stage. The swelling process was simulated by grow of the gel pockets until a pre-set percentage of the aggregate has reacted. To consider the heterogeneity of the material, the mechanical properties of the phases were distributed according to a Weibull law. A non-local continuum damage model was adopted where each phase had an elastic-brittle behaviour. The comparison of experimental and numerical results, obtained by 2D analyses, besides describing the damage at aggregate level, was able to reproduce the behaviour of concrete in terms of expansion and stiffness degradation. The latter was justified by the author as a consequence of the cracking in the aggregates and not in the cement paste, which is prevented by compressive stresses.
The model proposed by Dunant and Scrivener (2010) was further developed by Giorla (2013), by considering the coupling between ASR and creep phenomena. This can explain the different damage process which results limited in the cement paste with respect to the aggregate phase. Being the ASR a long-term process, the internal pressure can induce permanent deformation within the cement paste that behaves as a visco-elastic material. The model was able to simulate the behaviour of affected concrete under multi-axial stress state. However, the comparison with experimental findings is performed only in terms of concrete expansion.

In the framework of thermo-chemo-mechanical model for structural analyses, some researchers have formulated a constitutive model for affected concrete to be used in FEA.
Grimal et al. (2008a,b) extended the model proposed by Capra and Sellier (2003) including a reaction kinetics law, which depended on the variation of gel mass on the basis of saturation degree of the concrete porosity; the combined effects of creep, shrinkage and ASR was considered. The material degradation was described by a probabilistic-based orthotropic damage model, which accounted for the damage induced by expansion, tension and compressive stresses (Capra and Sellier, 2003). The model was calibrated and validated, in terms of concrete expansion, by adopting a set of tests on unaffected and affected concrete under various confinement degree. Subsequently, it was applied to the simulation of reinforced concrete beams partially immersed in water (Multon, 2004). The model is based on a large number of input parameters, which calibration requires a relevant number of experimental results on the same concrete mix design.

Pignatelli et al. (2013) further developed the model proposed by Comi et al. (2009), making the connection between reaction product and aggregate level. The concrete was modelled as a two-phase material, composed by a wet gel and concrete skeleton. The swelling pressure resulted from the change in mass of the wet gel phase, which depended from temperature and saturation degree through the reaction extend (reaction kinetics law). The damage of concrete induced by ASR was evaluated with a simplified micro-mechanical model, in which the unaffected skeleton and the gel phase work in series and in parallel with the damaged skeleton. The damage induced by tension and compressive stress was evaluated separately, with two isotropic damage variables (Comi et al., 2009). The model was able to predict the expansion behaviour of concrete laboratory specimens under free and confined expansion conditions. It was further applied to the simulation of concrete beams subjected to wetting conditions.

3.5 Models based on Ions Diffusion-Reaction

Recently, researchers have studied the chemical process at reaction products level in terms of ions dissolution-reaction mechanisms. In some cases, these mathematical approaches have been implemented in computational models for the description of the mechanical consequences of ASR in concrete. Table 3.5 gives an overview.

The chemical process has been first described in a mathematical framework, which allowed scaling up to aggregate level. Bažant and Steffens (2000) adopted a mathematical model to describe the reaction kinetics in affected concrete specimens made of waste glass particles. This work was developed in combination, but separated, with Bažant et al. (2000), who have investigated the induced fracture mechanisms at aggregate level. Due to the employment of pure silica particles with an ordered crystalline structure, the reaction products formed a rim around the grains. The grow of the rim around the particle was associated with the diffusion of the water within the reaction products and the dissolution of the silica, while the swelling of the reactive rim was correlated to the water imbibation from the capillarity porosity. The model was applied to study the influence of particle size on the swelling pressure generated by the reaction products.

Suwito et al. (2002) investigated the pessimum aggregate size effect in ultra-accelerated mortar bar tests adopting an analytically solved micro-poro-mechanical model. The concrete was represented by a three-phase material composed by a spherical domain embedded in the homogenized matrix, which has the same mechanical characteristics of the concrete. The spherical domain was formed by the aggregate, centrally placed, surrounded by the cement paste phase. The reaction products were considered placed on the particle rim; they were assumed as a part of the aggregates and not as a separated phase. A linear-elastic beha-

Table 3.5: Models based on ions diffusion-reaction mechanisms.

	Model type	Diffusion-reaction mechanism	Validation (V)/ Demonstration (D)
Bažant and Steffens (2000)	mathematical	dissolution silica, water diffusion within gel rim, water imbibation from porosity	Idealized one-particle cubic cell (D)
Suwito et al. (2002)	chemo-micro-poro-elastic	diffusion alkali ions, diffusion of gel in cement paste	lab specimens (V)
Poyet et al. (2007)	chemo-micro-poro-elastic	diffusion-reaction of sodium and calcium ions within gel rim	Idealized one-particle cubic cell (V)
Multon et al. (2009); Sanchez et al. (2014b)	chemo-micro-poro-damage	diffusion-reaction of sodium and calcium ions within gel rim	lab specimens (V)
Puatatsananon and Saouma (2013)	computational multiscale	diffusion alkali ions, diffusion of gel in cement paste	lab specimens (V)
Alnaggar et al. (2013)	lattice discrete particle	dissolution silica, water diffusion within gel rim, water imbibation from porosity	3D FEA lab specimens (V)
Liuaudat et al. (2014)	mathematical model	forward and backward diffusion-reaction of alkali and silica ions in the rim	1D interface system between aggregate and cement paste (D)
Nguyen et al. (2014)	chemo-elastic	diffusion-reaction of sodium ions	1D penetration of NaCl ions in concrete beam (D)

viour of the phases was considered and the effective properties of concrete were analytical determined. The reaction kinetics was represented by two diffusion processes: first the alkali ions flow within the aggregates and react with the silica ions, second the expansive alkali-silica gel, formed at the rim of the aggregates, flows in the cement paste porosity. The reaction products, which were defined as a viscous gel, generate expansion only when flowing in the cement paste porosity; no swelling power was assumed for the gel saturating the reaction rim. The model was validated by simulating the expansion of mortar bars with different aggregate size.

Poyet et al. (2007) described the reaction kinetics for the case of spherical aggregates embedded in the cement paste, assuming that the reaction products are situated at the rim. The model accounted for the transport of sodium and calcium ions in the aggregates and for the equilibrium of their concentrations outside the particles. The stechiometric proportion between the alkali and silica ions involved in the reaction was assumed fixed. The diffusion process was considered dependent also from the precipitation of portlandite, which influence the expansion rate of concrete (Section 2.2.1). They assumed that the chemical reaction generates two products with fix composition: the C-S-H gel, that is a harmless species and a natural constituent of the cement paste, and the expansive alkali-silica gel. The variation in molar volume of the reaction products was considered as the cause of the damage at aggregate level, which was assumed isotropic, and consequently of the concrete expansion. The approach was validated, in terms of concrete free-expansion, for laboratory specimens, which differentiate only in aggregate grading.

Liuaudat et al. (2014) proposed a diffusion-reaction model, in which the chemical reaction generates, at the aggregate rim, two types of reactive products with different density. The approach was adopted to study the mechanisms for a single interface system between aggregate and cement paste. The model was able to explain the relationship between swelling power and compositions of reaction products, as well as the effect of portlandite on the silica dissolution (Section 2.1). At the moment, it is not applied for the description of the behaviour of affected concrete.

Nguyen et al. (2014), similarly to Poyet et al. (2007), have correlated the induced concrete expansion to the diffusion of the alkali ions, which leading to dissolution of the silica, forms the expansive reactive products. The approach accounted for the tortuosity of undamaged porous material, which can influence the diffusion process. The concrete was considered as a linear-elastic material. The approach was able to reproduce the kinetics law between concrete expansion and time, which are usually used as input constitutive relationship for the approaches discussed in Section 3.2.

Some of the aforementioned mathematical approaches have been further implemented in existing damage models. Alnaggar et al. (2013) have adopted a lattice discrete particle model, which simulates the concrete at the scale of coarse aggregates. The gravel were represented by spherical particles, subjected to a rigid body kinetics. The ASR was modelled as an erosion of the aggregates with the subsequent formation of a reaction rim; the amount of formed gel mass was computed by following Bažant and Steffens (2000). The generated local swelling was governed by water imbibition and it was imposed as internal strain on the aggregates. The shrinkage and creep phenomena were also accounted as imposed strain on the particle, by applying the superposition effect. The behaviour of concrete specimens stored under free-expansion and under confinement was well reproduced, in terms of expansion and cracking in concrete. The degradation of mechanical properties, which was found within the bounds proposed by ISE (1992) (Chapter 2), is estimated, for the same concrete mixture adopted in the validation procedure, by modifying two input parameters correlated to the reaction kinetics. The approach adopts a heavy computational procedure and it is based on large number of input parameters.

Multon et al. (2009) have adopted a mathematical chemo-damage model, in which the reaction kinetics was described in agreement with Poyet et al. (2007). The concrete was modelled by a single-aggregate REV composed by a particle surrounded by reactive products and embedded in the cement paste. The diffusion-reaction process was located at the rim and it generates variation in molar volume of the reaction products, which leads to an expansion of the aggregates. Considering the expansive alkali-silica gel as incompressible, its swelling was accounted as an isotropic imposed strain in the aggregates. The Young's modulus of the REV was reduced, considering an isotropic damage variable, due to the tensile stresses produced by the expansive aggregates in the surrounding cement paste. The model was based on a limited number of input parameters, among which only the ones related to the diffusion-reaction process need calibration. The validation was performed on mortar bar specimens, stored under free-expansion condition, with different aggregate size and alkali content. The comparison with experimental results was reported in terms of expansion. Sanchez et al. (2014b) have adopted the model proposed by Multon et al. (2009) to simulate the evolution of mechanical properties versus expansion in concrete specimens stored under free-expansion condition. The model overestimated the degradation in terms of Young's modulus and tensile strength. The evolution of compressive strength was reasonable represented by introducing an additional damage variable in compression, empirically correlated to the one in tension.

Puatatsananon and Saouma (2013) have further developed, in a numerical framework, up to structural level the mathematical model proposed by Suwito et al. (2002), which ranged from reaction products to concrete level. The two diffusion problems of the alkali ions and of the gel, which were previously solved analytically (Suwito et al., 2002), were obtained with a finite difference analysis of a single-aggregate REV. A one-way coupling between the diffusion processes and the stress analysis was evaluated with FEA. The damage was considered only at aggregate level, by introducing interface elements between the particle and the cement paste in the single-aggregate REV. As a consequence, the predicted internal pressure was more realistic with respect to the one found by Suwito et al. (2002). The approach was validated, in terms of concrete free-expansion, for mortar specimens, which differentiate only in aggregate grading.

3.6 Concluding Remarks

Due to the interactive multiscale nature of ASR in concrete structures, various modelling approaches have been developed. Their starting points were formulated at different scales. Considering the adopted techniques, different scopes could be reached, not always allowing an analysis at structural level.

To select an appropriate modelling approach for ASR-affected structures, a review of the available models was performed following an alternative approach, in which the models were categorized on the basis of their input scale. The scope of the models was specified for each approach. In each group, the models were divided, on the basis of the solution techniques, including mathematical, analytical and computational methods.

It results that the nature of the phenomenon at aggregate level and its interaction at concrete level must be considered in the formulation of a model suitable for the structural assessment. Excluding this interaction and considering the ASR-induced concrete expansion as an input variable would lead to the use of phenomenological approaches, which are not available for the great variety of concrete mixtures, environmental conditions ad confinement states. Moreover, the use of phenomenological approaches is dangerous as long as the interactive multiscale nature of ASR is not yet understood. The first attempts to consider the interaction between phenomena at aggregate and concrete level were chemo-mechanical models. The definition of a kinetics law linking the concrete expansion to the chemical process is of practical use, but it still needs a more sophisticated formulation used in structural analysis. On the contrary, if the emphasis is only on the chemical mechanisms, the focus is easily narrowed down to the reaction products level and far from the structural one. Considering complex models for the ions diffusion-reaction processes limits the up-scaling.

The attention should be focused not only on the ASR-induced concrete expansion, but also to the material degradation, as already discussed in Chapter 2. This aspect received limited attention in the literature models, which are mainly validated in terms of concrete expansion.

A selected technique, even if primarily developed for the aggregate-concrete level interaction, should facilitate down- and up-scaling to reaction products and structural level, respectively. Theoretical approaches are often employed to describe a particular mechanism, such as the flux of ions or the cracking in aggregates induced by the expansive alkali-silica gel. By their own, they are not able to describe the material and structural effects, but they can smoothly be implemented in other techniques. Computational approaches, which discretize the concrete constituents with FEM, perform detailed simulation of the damage at aggregate level, which can be compared with microscopic observations. Their computational effort is substantial and often are based on a relevant number of input parameters. They can be easily augmented with additional and refined modelling concepts, but their abilities to up-scale to structures appear limited. Micro-poro-mechanical models provides an analytically solved approach which accounts for the microscopic aspects at the macroscopic scale. The approach results in a three-dimensional smeared model, which correlates the aggregates and concrete level. The micro-structure of concrete is idealized and no direct comparison can be made with laboratory observation. It is a versatile techniques, which can cooperate with theoretical models, for the description of the ASR mechanisms, and with FEM, for the structural analysis.

In conclusion, to describe the deteriorating impact of ASR on concrete and concrete structures a micro-poro-fracure-mechanical model is selected to describe the interaction of the phenomena between aggregate and concrete level. The versatility of the techniques, which is analytically solved, allows to account for the expansion of the reaction products at aggregate level and its coupling with the external loading imposed on the material. The model, which is described in Chapter 5, is validated against the behaviour of unaffected (Chapter 6) and affected concrete (Chapter 7). For the validation in Chapter 7, the experimental findings of Chapter 4 are used.

Experimental Research on the ASR-induced Concrete Degradation[1]

4

In Chapter 2 the deteriorating effects of the ASR on concrete and concrete structures were presented considering the main experimental evidences. In this chapter the focus is on the evolution of engineering properties (i.e., elastic modulus, compressive and tensile strengths) in ASR-affected concrete specimens stored under free-expansion conditions. The correlation between concrete expansion and material degradation has been made. Usually the evolution of mechanical properties is expressed as a function of time; as a consequence, deviating results are observed.

First, new experimental results on two comparable concrete mixtures containing Dutch and Norwegian aggregates are presented (Section 4.1 and Section 4.2). The latter is the reference material recovered from the highly affected Nautesund bridge (Oslo, Norway) and employed in the context of a wider experimental campaign, which aimed to study the effects induced by ASR at aggregate and concrete levels. Afterwards, available literature data, on the mechanical degradation of ASR-affected concrete under free-expansion, are collected (Section 4.3) and statistically analysed (Section 4.4) to clarify the deteriorating impact of ASR on concrete. The elastic modulus results one of the most degraded property together with the splitting tensile strength, while the compressive strength is less influenced by the process. The known engineering strength-stiffness relations employed for unaffected concrete under mechanical loading result not applicable to ASR-affected concrete (Section 4.5).

These findings will be further adopted in Chapter 6 for the validation of the proposed multiscale material model (Chapter 5). Details on the experimental tests are available in Appendix C.

---

[1] This chapter is based on Esposito et al. (2015)

Table 4.1: Mixture proportions.

Material	Amount kg/m^3	Density kg/m^3	ASG m^2/kg	Absorption %	Moisture w.%
RR1 mix design (natural Dutch aggregates)					
Cement	380	3,160			
Water	175				
Aggregate 0-2 mm	581	2,551	5.36	0.77	0.26
Aggregate 2-4 mm	269	2,551	1.95	0.77	0.26
Aggregate 4-8 mm	264	2,582	0.52	0.41	0.07
Aggregate 8-16 mm	443	2,598	0.31	0.23	0.04
Aggregate 16-22 mm	195	2,599	0.23	0.49	0.27
RR2 mix design (crushed Norwegian aggregates)					
Cement	380	3,160			
Water	171				
Aggregate 0-2 mm	601	2,651	5.36	0.28	0.03
Aggregate 2-4 mm	278	2,651	1.95	0.28	0.03
Aggregate 4-8 mm	273	2,691	0.52	0.28	0.07
Aggregate 8-16 mm	460	2,718	0.31	0.12	0.06
Aggregate 16-22 mm	200	2,688	0.23	0.17	0.07

4.1 Material and Test Methods

In 2010 a large experimental campaign was begun at the Delft University of Technology (TU Delft) under the framework of the PAT-ASR project (Anaç et al., 2012a). The scope of this research was to investigate the damage effects induced by the ASR in concrete on various scales: from microscopic to macroscopic level.

Here, the results for the macroscopic scale on the deteriorating impact of ASR on concrete in terms of expansion and the degradation of mechanical properties are reported. The experimental results are evaluated in a statistical context through the introduction of a classification and a normalisation procedure. Each concrete mix design is classified on the basis of the expansion value obtained in a prescribed testing duration. Their mechanical properties are normalised to identify a degradation trend.

Two comparable concrete mixtures were adopted throughout this study using Dutch and Norwegian aggregates. The latter represents the concrete mix design used in the Nautesund bridge (Oslo, Norway), which exhibited severe ASR damage. The Nautesund bridge is a unique case, because from construction to demolition, all materials and structural details were properly documented. Through a collaboration between the Delft University of Technology (TU Delft) and the Norwegian Public Roads Administration (NPRA), concrete specimens of this structure were used in the PAT-ASR project for verification purposes.

Table 4.2: Physical and chemical characteristics of cement.

Property	Value	Unit
Physical properties (cf. EN 196)		
Particle analysis +90 μm	0	%
Particle analysis +64 μm	0	%
Particle analysis -24 μm	88.6	%
Particle analysis -30 μm	94.3	%
Specific surface Blaine	565	m^2/kg
Compressive strength 1 d	29.7	MPa
Compressive strength 2 d	39.0	MPa
Compressive strength 7 d	47.9	MPa
Compressive strength 28 d	57.0	MPa
Chemical properties (cf. EN 196-2)		
Loss on ignition (L.O.I.)	2.21	%
Free lime	2.08	%
Tot. Chloride	0.05	%
Sulphur Trioxide SO_3	3.34	%
Silica SiO_2	19.88	%
Alumina Al_2O_3	4.85	%
Ferric Oxide Fe_2O_3	3.76	%
Lime CaO	61.71	%
Magnesia MgO	2.43	%
Phosphorus Pentoxide P_2O_5	0.15	%
Potassium Oxide K_2O	1.02	%
Sodium Oxide Na_2	0.50	%
Alkali Na_2O_{eq}	1.17	%

Table 4.3: Concrete properties for each cast.

Property	Unit	Value					
Cast		1	2	3	4	5	6
Mix design		RR1	RR1	RR2	RR1	RR2	RR2
Specific weight	kg/m^3	2,340	2,386	2,389	2,382	2,450	2,434
Air content	%	4.8	2.7	3.6	2.4	3.3	3.8
Slump H	mm	100	-	90	215	165	120
Slump d	mm	345	565	355	427.5	462.5	407.5
28-d compressive strength	MPa	60.40	67.95	62.44	62.14	68.10	61.80

Table 4.4: Storage conditions of RR1 and RR2 concrete specimens.

	Unit	ε	Y_{st}, f_{c}, ν	$f_{\mathrm{t,sp}}$	Control
Specimen size	mm	75x75x280	100x100x400	150x150x150	150x150x150
No. specimens		6	42	42	18
			After casting		
Time	d	1	1	1	1
Temperature	^{o}C	20	20	20	20
RH	%	98	98	98	98
			Pre-treatment		
Time	d	No	No	No	28
Temperature	^{o}C	No	No	No	20
RH	%	No	No	No	98
			ASR treatment		
Time	d	365	up to 365	up to 365	No
Temperature	^{o}C	38	38	38	No
RH	%	96	96	96	No
			Before testing		
Time	h	24	> 2	> 2	> 2
Temperature	^{o}C	20	20	20	20
RH	%	50	50	50	50

Concrete mixtures cast with Dutch and Norwegian aggregates are respectively classified as RR1 and RR2 mixtures, as clarified in Section 4.2. Norwegian aggregates in the RR2 mix design were primarily composed of coarse-grained quartz, quartzite, gneiss, metarhyolite and other minor rock types. By implementing the point count method (Anaç, 2013), it was estimated that 33% of aggregates with a size of 0-8 mm and 36% of coarse gravel were potentially alkali reactive. Dutch aggregates in the RR1 mix design were primarily composed of quartzite, quartz, (calcareous) chert, volcanic rock fragments and other minor rock types. Thus far no alkali reactivity has been reported for these aggregates. The adopted mixture proportions of cement/fine aggregates/coarse aggregates/water were 1:2.93:1.68:0.46 for the RR1 mix design and 1:3.03:1.74:0.45 for the RR2 mix design by weight. NORCEM Industri (CEM I 42.5R) cement with a dosage of 380 kg/m^3 and an equivalent $\mathrm{Na_2O_{eq}}$ content of 1.17% was used. The two concrete mixtures were designed to have a similar aggregate gradation and a comparable 28-day compressive strength. Therefore, to properly define the mix design, the density, the apparent specific gravity (ASG), the water absorption and the moisture of aggregates were identified following ASTM C127 (2012a) and ASTM C128 (2012b). Table 4.1 and Table 4.2 list the characteristics of the concrete mixtures and cement, respectively.

Due to the large number of specimens needed, they were cast in six sessions; in each session, control casting cubes, which were not subjected to ASR treatment, were prepared. Table 4.3 lists the concrete properties for each cast. Cube specimens with sides of 150 mm were stored for 28 days at 20°C in a fog room and subsequently tested under uniaxial compressive loading following NEN-EN 12390-3:2002 (2002). The load was applied at a constant rate of 0.60 MPa/s. To determine the evolution of the mechanical properties of ASR-affected concrete, expansion and mechanical tests were performed on prisms and cubes stored at 38°C and a relative humidity of greater than 96%. An overview of the storage conditions and specimen sizes is given in Table 4.4. The specimens were placed on top of a metallic grid in plastic boxes; 2 cm of water at the bottom of the box ensured high humidity. The plastic boxes were placed in custom plastic reactors containing water, in which the plastic boxes were immersed 10 cm in water. The reactors included built-in heating elements to heat the water. During the storage period temperature sensors were placed inside the boxes and in the reactors to control the temperature, whereas humidity sensors were installed only in the reactors. The specimens were tested at 14, 28, 49, 91, 182, 252 and 365 days.

The expansion values were measured on 75x75x280-mm prisms according to the procedure proposed by RILEM recommendation AAR-3 (2011). Tests for for determining the static elastic modulus were performed on 100x100x400-mm prisms in agreement with ISO 1920-10:2010(E) (2010). Linear Variable Differential Transformers (LVDTs) were employed to measure vertical and horizontal displacements. The vertical LVDTs were centrally placed on each side of the specimen over a length of 200 mm. The strain and stress on the test specimen were continuously measured during the loading cycle. First, a basic stress of 0.50 MPa was applied for 60 s; afterwards, the strain was constantly increased until the peak was reached. The static elastic modulus Y_{st} and the Poisson ratio ν were determined in the elastic phase of the curve, between the basic stress level and one third of the peak stress. The peak stress was chosen as a measure of the compressive strength f_{c}. The splitting tensile strength $f_{\mathrm{t,sp}}$ was measured for cubes with sides of 150 mm, which is in agreement with EN 13290-6:2009 (2009). The load was applied with a constant increase of 0.05 MPa/s.

4.2 Experimental Results

Table 4.5 lists the results from the expansion and the mechanical tests for both mixtures. Each result was determined as the average of three measurements performed on specimens of the same cast. The number of the cast from which each set of three specimens was prepared is listed, thereby making a distinction between specimens employed for the expansion and mechanical tests (e.g., 4 - 1 means that the expansion measurements were performed on specimens prepared in cast number 4, while the corresponding mechanical tests refer to specimens prepared in cast number 1). The mix design, the properties of fresh concrete and the 28-day cubic compressive strength of each cast are presented in Table 4.1 and Table 4.3. The coefficients of variation of 28-day cubic compressive strength for the RR1 and RR2 concrete mixtures were found to be 5.1 and 4.4%, respectively.

The asymptotic expansion obtained after one year was 0.11% for the RR1 mix design and 0.18% for the RR2 mix design (Figure 4.1a). Both mixtures appeared reactive according to the RILEM recommendation AAR-0 (Sims and Nixon, 2003) and exceeded the recommendation expansion threshold values of 0.05 and 0.1%. The classification proposed by RILEM recommendation AAR-0 (Sims and Nixon, 2003) has been extended and further applied in the next section. Three classes of mixtures were defined on the basis of the maximum concrete expansion reached within the testing time. The concrete mixtures were classified as potentially reactive mixtures (PR) if their expansion was $0.05\% \leq \varepsilon \leq 0.10\%$, or as reactive mixtures (RR) if their expansion was $0.10\% < \varepsilon < 0.50\%$, or as extremely reactive mixtures (ER) if their expansion was greater than 0.50%. If the concrete expansion was found to be $\varepsilon \leq 0.05\%$, the mix design was considered to be non-reactive.

In Figure 4.1b-d, the degradation of the mechanical properties is reported in terms of normalised values versus expansion. Each normalised value β was obtained as the ratio between the current property value and its reference one. The latter was estimated at a reference expansion of 0.05%, which is the value used to discriminate between non-reactive and potentially reactive concrete. This normalisation procedure is also adopted in the next sections, in which available literature data are compared and analysed to describe the degradation behaviour.

The mechanical properties exhibited a slight increase during the first 90 days, followed by a degradation trend. The static elastic modulus (Figure 4.1b) of concrete mixture RR1 exhibited minor variations and ranged between 99 and 107% of its reference value. Conversely, the concrete mixture RR2 exhibited a maximum degradation of 35%. The normalised compressive strength (Figure 4.1c) exhibited a pronounced initial increase from 0.76 to 0.90 for RR1 concrete and from 0.88 to 0.97 for RR2 concrete. After both concrete mixtures tend to the asymptotic value of 1. The splitting tensile strength (Figure 4.1d) gives a similar trend for both mixtures. After a relatively small initial increment a degradation was observed, which obtained a maximum value of 23% for concrete mixture RR1 and of 26% for concrete mixture RR2.

Figure 4.2 reports the evolution of normal and volumetric strains developed during the uniaxial compressive tests for affected concrete stored for 91, 182 and 364 days. The RR1 concrete mix design exhibits a lower stiffness degradation due to ASR with respect to the RR2 concrete mix design, as already presented in Figure 4.1b. For increasing expansion value, the RR1 concrete exhibits an increase in compressive strength (Figure 4.2a), while RR2 concrete shows a similar peak stress but a substantial increase in peak strain (Figure 4.2b). Considering the

Table 4.5: Experimental results and calculated reference values.

Time d	Cast	ε %	Y_{st} GPa	ν	f_{c} MPa	$f_{\mathrm{t,sp}}$ MPa
RR1 mix design (natural Dutch aggregates)						
14	4-4	-0.003	42.1	0.19	45.67	3.92
28	4-1	0.002	42.7	0.20	50.58	3.85
49	4-1	0.005	43.1	0.26	54.20	4.28
91	4-1	0.009	43.1	0.20	53.61	4.38
182	4-2	0.036	38.9	0.28	59.30	3.85
252	4-2	0.079	40.7	0.18	61.79	3.57
364	4-2	0.112	40.1	0.18	62.98	3.27
Calc. ref. value		0.05	39.5	0.24	60.11	3.76
RR2 mix design (crushed Norwegian aggregates)						
14	5-5	0.001	29.2	0.20	53.61	4.44
28	5-3	0.004	30.5	0.21	58.41	4.28
49	5-3	0.010	33.0	0.29	59.67	4.20
91	5-3	0.018	27.4	0.24	63.72	4.53
182	5-6	0.067	25.5	0.25	59.95	3.51
252	5-6	0.123	17.0	0.27	60.03	3.46
364	5-6	0.178	17.4	0.25	59.41	3.25
Calc. ref. value		0.05	26.1	0.25	61.23	3.85

volumetric strains under the uniaxial compressive test, it can be observed that the higher is the concrete expansion due to ASR, the lower is the load at which the maximum volumetric reduction is obtained (Figure 4.2c and Figure 4.2d), which is a sign of accumulated plastic deformation. Similar results were also reported by Pantazopoulou and Thomas (1999).

In conclusion, the studied RR1 and RR2 mixtures were both classified as reactive, which is in agreement with the proposed classification procedure. The RR2 concrete presented highest expansion, and it showed a relevant degradation in terms of its static elastic modulus and splitting tensile strength. The RR1 concrete, which presented lower expansion, showed a nearly constant static elastic modulus; however, its degradation in terms of splitting tensile strength follows the same trend as that for the RR2 concrete. Both concrete mixtures showed an initial increase in compressive strength, which was followed by a nearly constant progression when the reference value was approached.

4.3 Literature Data

Over the past 30 years, various authors have tested the degradation of mechanical properties induced by ASR in concrete specimens stored under free-expansion conditions. In this overview the results obtained by Swamy and Al-Asali (1988),

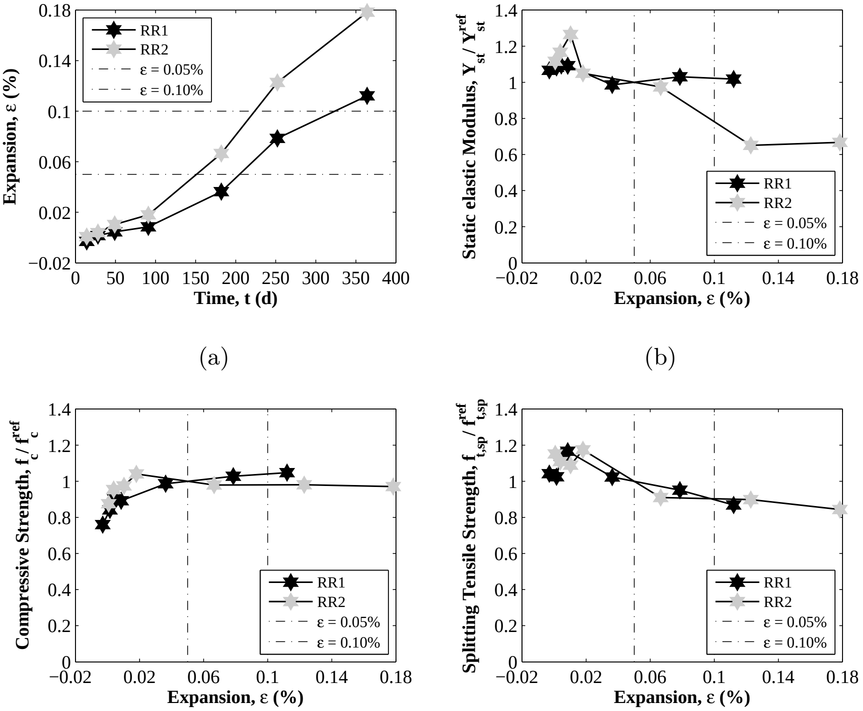

(a) (b)

(c) (d)

Figure 4.1: Experimental results for RR1 and RR2 concretes: (a) Concrete expansion; (b) Static elastic modulus; (c) Compressive strength; (d) Splitting tensile strength.

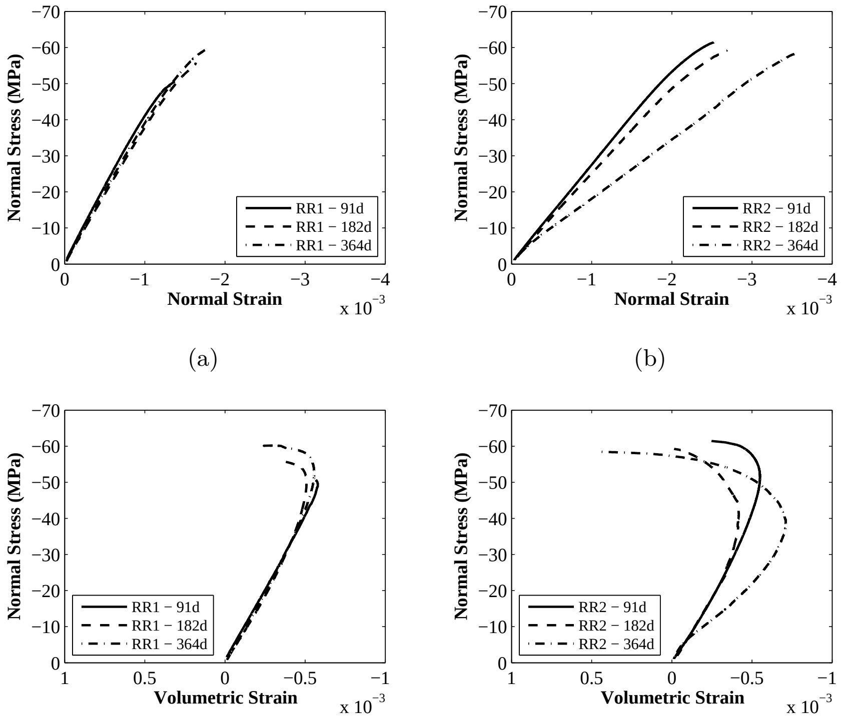

(a) (b)

(c) (d)

Figure 4.2: Experimental results for for RR1 and RR2 concretes subject to uniaxial compressive tests after 91, 182 and 364 days of exposure to the ASR treatment: (a)-(c) Stress-strain relationship in normal direction; (b)-(d) Volumetric strain.

Table 4.6: Literature data: concrete properties.

Author	Data set	Aggregate Type	Cem kg/m^3	W/C	Na_2O_{eq} %
Swamy	ER1	amorphous fused silica (fine)	520	0.44	1.00
	ER2	Beltane opal (fine)	520	0.44	1.00
Larive	RR	Tournaisis limestone (fine and coarse)	410	0.44	1.25
Monette	RR	siliceous limestone (fine and coarse)	423	0.61	1.25
Ahmed	RR	limestone (fine and coarse)	400	0.50	1.75
	ER1	Thames Valley sand (fine) and limestone (coarse)	400	0.50	1.75
	ER2	Thames Valley sand (fine), fused silica (fine) and limestone (coarse)	400	0.50	1.75
Multon	PR	calcareous stones with siliceous inclusions	410	0.50	1.25
Ben Haha	PR1ia-b	chlorite interleaved with layers of quartz and feldspar (fine and coarse)	-	0.46	0.40
	PR1iia-b-c		-	0.46	0.80
	PR1iiia-b-c		-	0.46	1.20
	PR2ia-b	biotitic schist containing phyllosilicates (fine and coarse)	-	0.46	0.40
	PR2iia-b-c		-	0.46	0.80
	PR2iiia-b-c		-	0.46	1.20
Giaccio	PR	granitic stone with feldspars, quartz, micas, epidote, zircon	420	0.42	1.24
	RR1	siliceous orthoquartzite with opal, quartz, chalcedony, microcrystalline	420	0.42	1.24
	RR2	opal, chalcedony	420	0.42	1.24
Sargolzahi	RR	Spratt limestone	345	0.50	1.25
Giannini	RR1	rhyolite and other volcanics (coarse)	420	0.42	1.25
	RR2	quartz, feldspars, siliceous volcanics, chert (fine)	420	0.42	1.25
Lindgård	PR1a	Ottersbo cataclasite with crypto- to microcystalline quartz (coarse)	400	0.45	2.25
	PR2a		550	0.30	0.67
	RR1a		315	0.60	1.17
	RR2a		400	0.45	0.93
	PR1b		400	0.45	2.25
	PR2b		550	0.30	0.67
	RR1b		315	0.60	1.17
	RR2b		400	0.45	0.93
	PR1c		400	0.45	2.25
	PR2c		550	0.30	0.67
	RR1c		315	0.60	1.17
	RR2c		400	0.45	0.93
Sanchez	RR1i	mixed volcanics and chert (fine)	314	0.61	1.25
	RR1ii		370	0.47	1.25
	RR1iii		424	0.37	1.25
	RR2i	mixed volcanics and chert (coarse)	314	0.61	1.25
	RR2ii		370	0.77	1.25
	RR2iii		424	0.37	1.25
Esposito	RR1	quartzite, quartz, (calcareous) chert, volcanic rock fragments (fine and coarse)	380	0.45	1.17
	RR2	coarse grained quartz, quartzite, gneiss, metarhyolite (fine and coarse)	380	0.45	1.17

Larive (1998), Ahmed et al. (2003), Monette (1997), Multon (2004), Ben Haha (2006), Giaccio et al. (2008), Sargolzahi et al. (2010), Giannini and Folliard (2012), (Lindgård, 2013) and Sanchez et al. (2014a), as well as the results presented earlier in this chapter are used.

Table 4.6 and Table 4.7 list the concrete properties and storage conditions employed by the various authors. A variety of natural aggregates was used. In a few cases (Swamy and Ahmed) non-natural aggregates were adopted to accelerate the reaction. This practice, although often criticised, is still sometimes used to understand the ASR mechanism in concrete (Bažant et al., 2000). The water-to-cement ratio, W/C, chosen in these studies varied between 0.30 and 0.61, and the equivalent alkali content ranged between 0.40 and 2.25%. The majority of the authors stored their specimens at 38°C, ensuring a high relative humidity or placing the specimens in water. These storage conditions are now prescribed by current standards and recommendations (e.g., RILEM recommendation AAR-3 (2011) and ASTM C1293 (2001)). In general, the specimens were not wrapped and stored in plastic or metal boxes. Pre-treatment was applied by 6 of 12 authors, who primarily kept the specimens at 20°C in fog room. The specimens were demoulded after one day, with the exception of Larive, who kept the specimens in moulds for three days.

To analyse the data, mixtures were classified on the basis of the asymptotic expansion value obtained within the prescribed testing time (Table 4.8). If a test was terminated before the prescribed testing duration had elapsed (Monette and Giannini), the asymptotic expansion was chosen at the end of the test. In contrast, when the test went beyond the testing duration (Larive and Sargolzahi), the asymptotic expansion was calculated by interpolation. In the cases where different storage conditions were used (Ben Haha and Lindgård), the asymptotic expansion was defined for the condition closest to the one proposed by RILEM recommendation AAR-3 (2011). The classification procedure presented in the previous section was adopted, and the concrete mixtures were divided into potentially reactive (PR, $0.05\% \leq \varepsilon \leq 0.10\%$), reactive (RR, $0.10\% < \varepsilon < 0.50\%$) and extremely reactive (ER, $\varepsilon \geq 0.50\%$). Non-reactive mixtures ($\varepsilon \leq 0.05\%$) were not considered. To distinguish between the different data sets, the name of the first author was indicated. If the same authors tested more than one mix design in the same reactivity class, an Arabic number was added to the data set name (e.g., Swamy-ER1 and Swamy-ER2). If an author tested the same mix design with different proportions, a Roman numeral between i and iii was added to the data set name (e.g., Ben Haha-PR1ia, Ben Haha-PR1iia and Ben Haha-PR1iiia). If an author tested the same mix design under different storage conditions, the letters a, b and c were added to the data set name (e.g., Lindgård-PR1a, Lindgård-PR1b and Lindgård-PR1c). To compare the results, the normalisation procedure presen-

Table 4.7: Literature data: storage conditions.

Author		Pre-treatment				ASR development			
		Time d	Wrap.	Temp. °C	Moist.	Time d	Wrap.	Temp. °C	Moist.
Swamy		No	No	No	No	365	No	20	96%
Larive		11	Al-foil	23	98%	546	No	38	97%
Monette		28	No	20	96%	147	No	38	1N NaOH sol.
Ahmed		28	No	20	in water	365	No	38	in water
Multon		28	Al-foil	20	N/A	730	Al-foil	38	in box
Ben Haha	a	No	No	No	No	365	No	20	in box on water
	b	No	No	No	No	365	No	40	
	c	No	No	No	No	365	No	60	
Giaccio		No	No	No	No	721/904	cotton	38	plastic bag with 5 mL water
Sargolzahi		7	No	20	97%	700	No	38	in plastic box on water
Giannini		No	No	No	No	120/270	No	38	95%
Lindgård	a	1/7/28	No	20	96%	365/784	No	38	in plastic box
	b	1/7/28	No	20	in water (0.5hrs)	273	cotton	60	in metal box on water
	c	1/7/28	No	20	in water (0.5hrs)	365/273	cotton	38	in plastic box with lining
Sanchez		No	No	No	No	63/182	No	38	100%
Esposito		No	No	No	No	365	No	38	96%

Table 4.8: Literature data: asymptotic expansion and calculated reference values.

Author	Data set[#]		Expansion		Calculated reference value at $\varepsilon = 0.05\%$					
			Time d	ε %	Y_{st} GPa	Y_{dyn} GPa	f_{c} MPa	$f_{\mathrm{t,sp}}$ MPa	MOR MPa	$f_{\mathrm{t,dir}}$ MPa
Swamy	ER1	+	365	0.62	-	39.0	52.53	3.24	4.08	-
	ER2	×	365	1.64	-	34.3	43.08	-	-	-
Larive	RR	∗	365	0.21”	33.9	-	52.64	3.93	-	-
Monette	RR	×	147	0.35	18.8	38.2	27.51	-	5.87	-
Ahmed	RR	□ w	365	0.15	32.7	-	51.15	4.74	5.37	4.80
	ER1	□ g	365	0.73	36.3	-	50.30	5.05	6.76	2.60
	ER2	□ b	365	2.70	22.1[†]	-	41.22[†]	3.57[†]	5.26[†]	1.42[†]
Multon	PR	+	365	0.10	32.6	-	42.01	3.14	-	-
Ben Haha	PR1ia	▽w	365	0.05	24.8	-	63.86	4.35	-	-
	PR1iia	▽g	365	0.07	24.8	-	51.43	3.81	-	-
	PR1iiia	▽b	365	0.08	25.2	-	53.62	4.05	-	-
	PR1ib‡	△w	365	0.05	21.8	-	51.09	4.39	-	-
	PR1iib‡	△g	365	0.12	26.8	-	48.27	4.27	-	-
	PR1iiib‡	△b	365	0.14	25.0	-	46.15	4.25	-	-
	PR1iic	◇g	365	0.14	25.0	-	46.15	4.25	-	-
	PR1iiic	◇b	365	0.16	26.5	-	47.53	4.36	-	-
	PR2ia	▽w	365	0.05	26.4	-	34.26	4.25	-	-
	PR2iia	▽g	365	0.07	25.7	-	55.72	3.81	-	-
	PR2iiia	▽b	365	0.07	24.9	-	54.73	3.93	-	-
	PR2ib‡	△w	365	0.12	26.7	-	50.47	4.22	-	-
	PR2iib‡	△g	365	0.14	26.0	-	48.98	4.33	-	-
	PR2iiib‡	△b	365	0.14	25.8	-	47.93	4.25	-	-
	PR2iic	◇g	365	0.14	25.5	-	49.21	4.37	-	-
	PR2iiic	◇b	365	0.16	26.2	-	47.47	4.37	-	-
Giaccio	PR	○w	365	0.08	38.1	-	36.50	-	-	-
	RR1	○g	365	0.21	24.1[†]	-	30.20[†]	-	-	-
	RR2	○b	365	0.28	32.0	-	27.80	-	-	-
Sargolzahi	PR	*	365	0.08”	32.5	20.9	43.02	-	-	-
Giannini	RR1	□ w	120	0.14	25.5	-	36.82	-	-	-
	RR2	□ b	270	0.42	25.4	-	34.52	-	-	-
Lindgård	PR1a‡	◁g	365	0.05	-	44.7	-	-	-	-
	PR2a‡	◁w	365	0.08	-	51.6	-	-	-	-
	RR1a‡	▷g	365	0.21	-	36.5	-	-	-	-
	RR2a‡	▷w	365	0.26	-	42.1	-	-	-	-
	PR1b	◁g	273	0.14	-	43.2	-	-	-	-
	PR2b	◁w	273	0.17	-	47.6	-	-	-	-
	RR1b	▷g	273	0.18	-	34.7	-	-	-	-
	RR2b	▷w	273	0.23	-	38.7	-	-	-	-
	PR1c	◁g	273	0.04	-	40.3[†]	-	-	-	-
	PR2c	◁w	273	0.06	-	49.1	-	-	-	-
	RR1c	▷g	273	0.28	-	37.8	-	-	-	-
	RR2c	▷w	365	0.27	-	42.7	-	-	-	-
Sanchez	RR1i	○w	63	0.30	-	21.0	-	-	-	-
	RR1ii	○g	63	0.30	-	29.5	-	-	-	-
	RR1iii	○b	63	0.30	-	28.0	-	-	-	-
	RR2i	○w	182	0.20	-	23.2	-	-	-	-
	RR2ii	○g	182	0.20	-	30.9	-	-	-	-
	RR2iii	○b	182	0.20	-	29.3	-	-	-	-
Esposito	RR1	⋆b	365	0.11	39.5	-	60.11	3.76	-	-
	RR2	⋆g	365	0.18	26.1	-	61.23	3.85	-	-

‡ Specimen used for the classification (for authors who tested the same mix design in different storage conditions).

” Interpolated expansion value. [†] Extrapolated reference value.

[#] For repeated symbol the marker size is decreased. The filler can be white (w), grey (g) or black (b).

ted in the previous section was adopted. The reference values at an expansion of $\varepsilon = 0.05\%$ were generally interpolated and they are listed in Table 4.8.

The majority of the authors studied the degradation of the compressive strength f_c (10 of 12 authors) and of the static elastic modulus Y_st (9 of 12 authors), as shown in Table 4.8. The tensile behaviour was studied by 7 of 12 authors, who preferred the use of the splitting tensile strength $f_\mathrm{t,sp}$ above the modulus of rupture MOR and the direct tensile strength $f_\mathrm{t,dir}$. Non-destructive tests for determining the dynamic elastic modulus Y_dyn were chosen by 5 of 12 authors.

Figure 4.3 and Figure 4.5 report the variations in the mechanical properties as functions of the concrete expansion. Four zones were defined: the low-expansion zone ($\varepsilon < 0.05\%$), the moderate-expansion zone ($0.05\% \leq \varepsilon \leq 0.10\%$), the high-expansion zone ($0.10\% < \varepsilon < 0.50\%$) and the extreme-expansion zone ($\varepsilon \geq 0.50\%$). Each data point is an average of the results obtained from testing three specimens, with the exception of Swamy, who used two specimens. For clarity, the figures show a non-uniformly scaled expansion axis and the legend is reported in Table 4.8. Figure 4.6 and Figure 4.7, which will be discussed in the next subsection, show the data with a uniformly scaled expansion axis.

It was found that the elastic modulus is subjected to a significant degradation (Figure 4.3a and Figure 4.3b). Both the static and dynamic elastic moduli marginally increase for expansion values up to 0.03%. Subsequently, a slight degradation is observed in the low- and moderate-expansion zones; however their mean values remain close to unity in these zones. For expansion values greater than 0.10%, both of the stiffness properties decreased at similar rate. The maximum degradation was obtained in the extreme-expansion zone, with a reduction of 92% for the static elastic modulus and of 86% for the dynamic one. The non-destructive test provided a more dense data cluster with respect to the destructive test.

The compressive strength was extensively investigated by many authors, although Swamy and Al-Asali stated in 1988, *ipse dixit* "compressive strength is not a good indicator of the initiation or progress of ASR". Figure 4.3c confirms this tendency. In the low-expansion zone, the normalised value of compressive strength ranged between 0.59 and 1.62, with an average of 0.92. The data sets that obtained the lowest and highest normalised compressive strength values are the mixtures PR1ia and PR2ia, respectively, (both tested by Ben Haha (2006)), which contained the lowest alkali content ($\mathrm{Na_2O_{eq}} = 0.4\%$) and were stored at a temperature of 20°C under high humidity. Due to the low alkali content and the non-accelerated storage conditions, it can be hypothesised that the ASR did not lead to a significant concrete expansion and that the increase in strength can be attributed to the hydration process. Excluding these data sets, the maximum normalised value in the low-expansion zone equals 1.04. In the moderate-expansion zone, the data cluster narrows, and the normalised value of the compressive strength increases to 1.28. For expansion values greater than 0.15% the majority

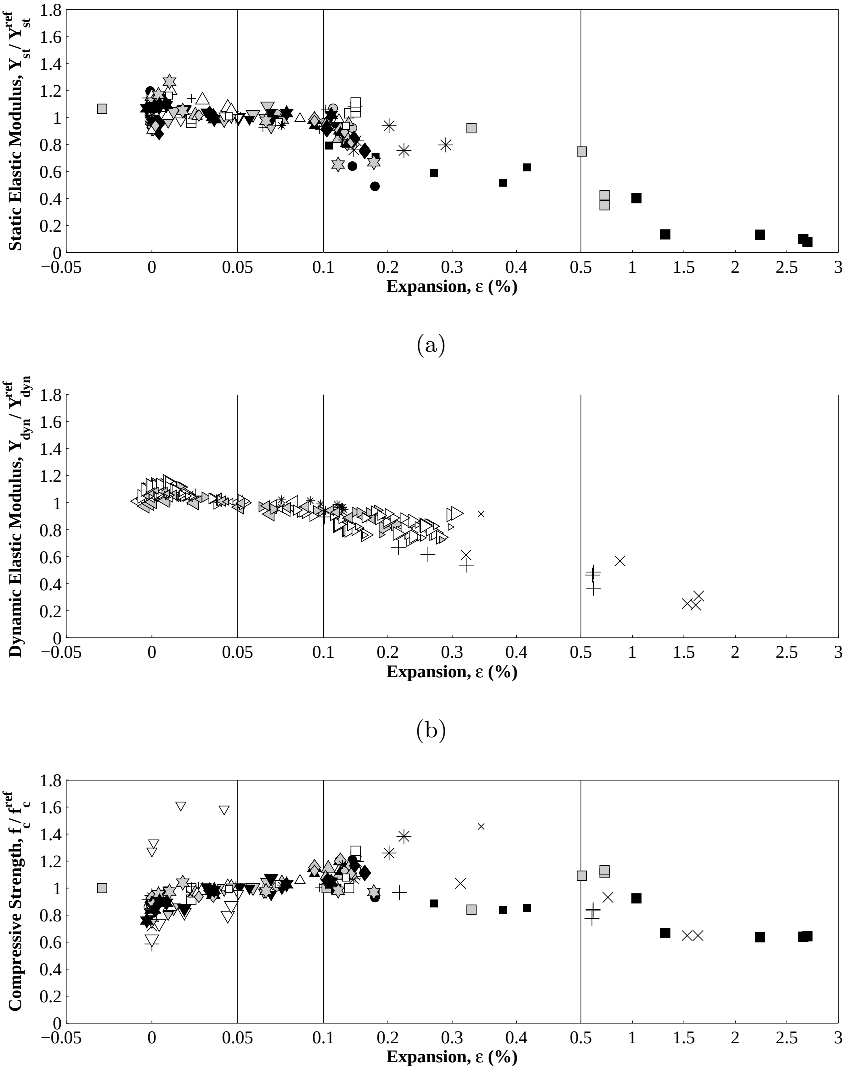

(a)

(b)

(c)

Figure 4.3: Experimental data from the literature: (a) Static elastic modulus; (b) Dynamic elastic modulus; (c) Compressive strength. A non-uniform scale for the expansion axis is used. For the legend see the description in Table 4.8.

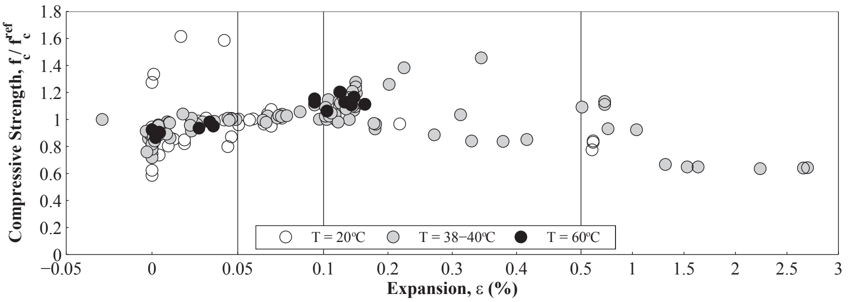

Figure 4.4: Experimental data from the literature: Compressive strength data grouped on the basis of storage temperature.

of the concrete mixtures exhibit a degradation in term of strength; however, the data show a substantial number of exceptions. The maximum degradation is obtained in the extreme-expansion zone, with a reduction of 46%.

To exclude a possible correlation between the initial increment in compressive strength and the hydration process, Figure 4.4 groups the data of Figure 4.3c on the basis of the storage temperature. Specimens stored in different temperature show a similar trend in the moderate-expansion zone. As a results, the increment in strength cannot be addressed to the difference in hydration process. On the contrary, the presence of the gel swelling, which pressurizes the porosity space, acts as a counter load during the compressive test, resulting in a strength increment.

The tensile behaviour of ASR-affected concrete (Figure 4.5) was found to be sensitive to the test method, as previously observed for unaffected concrete. Whereas the splitting (Figure 4.5a) and flexural (Figure 4.5b) tests show an important decrease in the strength for high-expansion values, the direct tensile strength (Figure 4.5c) appears to be less sensitive. In the low-expansion zone, the normalised values of all three tensile strengths are close to unity. After the data clusters spread out, and both the splitting tensile strength and the modulus of rupture drastically decrease. The direct tensile strength exhibits a relevant degradation only in the extreme-expansion zone. However, the data are limited to only three concrete mixtures tested by the same author (Ahmed et al., 2003), which are classified as reactive and extremely reactive. The few data points are spread over an expansion scale that ranges between -0.03 and 2.70%; therefore, a detailed picture of the degradation trend is missing, which can strongly influence the estimation of the reference values. The three strengths exhibit a maximum degradation in the extreme-expansion zone, with a reduction of 53% for the splitting tensile strength (Figure 4.5a), 89% for the modulus of rupture (Figure 4.5b), and 38% for the direct tensile strength (Figure 4.5c).

4.4 Statistical Analysis

To determine the degradation behaviour of the mechanical properties induced by the alkali-silica reaction under free-expansion specimens, a statistical analysis was performed. The normalised data were fitted on the basis of two formulations: an S-shaped curve and a piecewise linear curve. The four zones (low-, moderate-, high- and extreme-expansion zones) were considered to define the weights of each data point. Within each zone data points have the same weight, whereas the sum of the weights for each zone is equal within a weighted least squares fitting process. In this way a bias resulting from an unequal distribution of data points along the expansion axis is limited.

The S-shaped curve is a revised version of the degradation law proposed by Saouma and Perotti (2006) and expresses the normalised value of each property β as a function of the expansion ε, whereby four parameters are employed:

$$\beta = \beta_0 - (\beta_0 - \beta_\infty) \frac{1 - \exp\left(-\frac{\varepsilon}{\varepsilon_c}\right)}{1 + \exp\left(-\frac{\varepsilon - \varepsilon_l}{\varepsilon_c}\right)} \tag{4.1}$$

where β_0 and β_∞ are the normalised property values at zero expansion and at the asymptotic expansion, respectively; and ε_l and ε_c are the latency and characteristic expansion values, respectively. The latency expansion ε_l defines the delay before a relevant degradation of the mechanical property is observed: the lower the latency expansion, the earlier the degradation is observed. The characteristic expansion ε_c contributes to the degradation rate, which is defined as the average decrease between ε_l and $\varepsilon_l + 2\varepsilon_c$.

Figure 4.6 shows the resulting S-shaped curves along with the experimental data. The fitting coefficients and the estimation errors, in terms of standard deviation, are reported in Table 4.9.

In Figure 4.6a the elastic modulus data are denoted by grey dots for destructive tests and by white dots for non-destructive tests. The fitting was formulated by considering all the data (thick continuous line) or by distinguishing between static (thick dash-dot line) and dynamic (thin continuous line) elastic modulus data. The curves exhibit a minor difference only in the extreme-expansion zone. Therefore, all the data can be considered to be representative of the stiffness degradation in concrete subjected to the ASR. The estimation error is 7%. The resulting latency time ε_l is extremely small (on the order of 10^{-14}), which confirms the fast stiffness degradation starting in the low-expansion zone. The maximum,

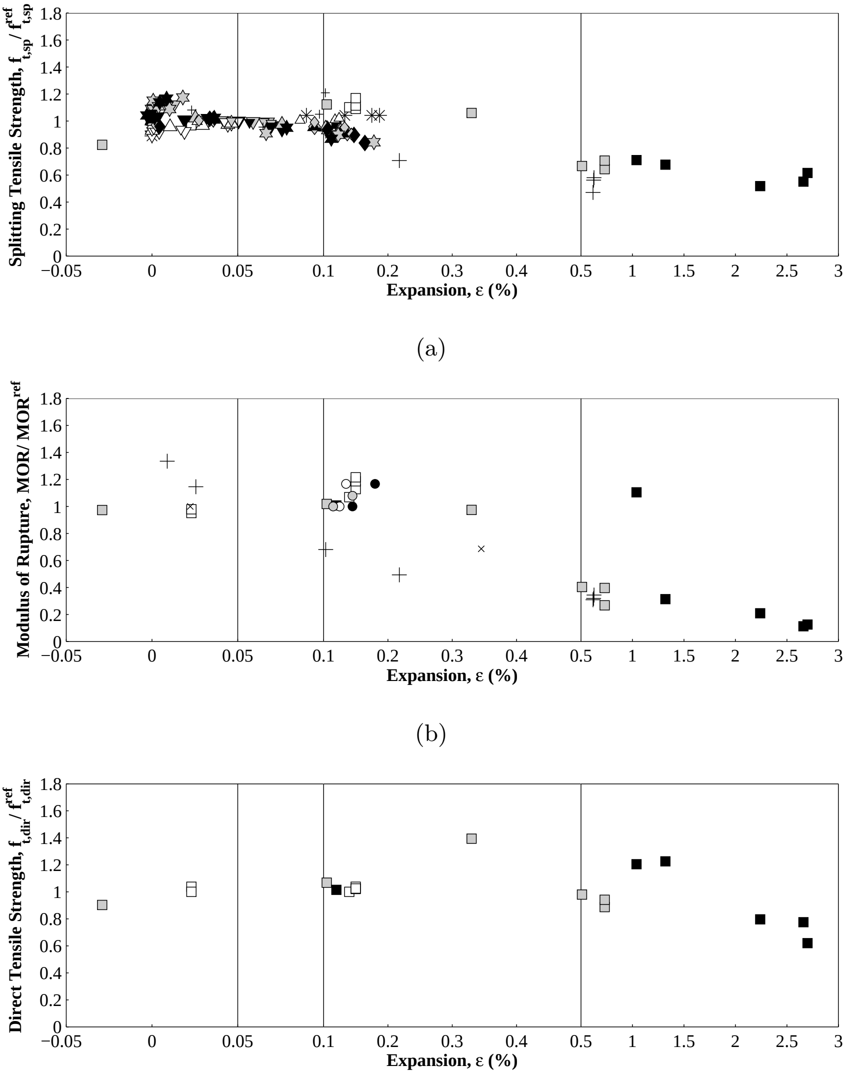

(a)

(b)

(c)

Figure 4.5: Experimental data from the literature: (a) Splitting tensile strength; (b) Modulus of rupture; (c) Direct tensile strength. A non-uniform scale for the expansion axis is used. For the legend see the description in Table 4.8.

β_0, and the minimum, β_∞, normalised values of the elastic modulus equal 1.06 and 0.19.
Figure 4.6b shows the degradation S-shaped curve for the compressive strength. Due to the nature of the formulation, the initial increase in strength cannot be captured; as a result the maximum normalised value β_0 is equal to 1.00 and the latency expansion ε_l is 0.51%. The S-shaped curve exhibits an asymptote at 0.64. The estimation error is 15%.
In Figure 4.6c, the tensile strength data are denoted by grey, white and black dots to indicate the splitting, flexural and direct tensile tests, respectively. The fitting was formulated by considering all the data (thick continuous line) or by distinguishing between the three test methods. As previously mentioned, the test type has a strong influence on the resulting strength. Consequently, it is more appropriate to consider each test method separately. The curve based on the splitting tensile strength data (thick dash-dot line) provides the best fitting with an error of 8%. Its normalised value can range between 1.01 and 0.60. The degradation becomes pronounced after a latency expansion ε_l of 0.35%. The modulus of rupture (thin continuous line) begins to degrade at approximately the same expansion level ($\varepsilon_\mathrm{l} = 0.37\%$); it can reach a maximum deterioration of 76%. The estimation error is 20%, which is relatively high. The direct tensile strength (thin dash-dot line) exhibits a maximum degradation of 30%. The degradation starts at a latency expansion ε_l of 2.15%, meaning that the fitting mainly follows the behaviour of the concrete mix design Ahmed-ER2. The estimation error is 12%.

The statistical analysis was extended by considering a continuous piecewise linear function. This choice was made to allow for an increase in the mechanical properties, e.g., as observed for the compressive strength. The continuity points are represented by the expansion values that delimit the four zones; the formulation is as follows:

$$\beta = \begin{cases} q_\mathrm{l} + m_\mathrm{l}\varepsilon & \varepsilon \leq 0.05\% \\ q_\mathrm{m} + m_\mathrm{m}\varepsilon & 0.05\% < \varepsilon \leq 0.1\% \\ q_\mathrm{h} + m_\mathrm{h}\varepsilon & 0.1\% < \varepsilon \leq 0.5\% \\ q_\mathrm{e} + m_\mathrm{e}\varepsilon & \varepsilon > 0.5\% \end{cases} \tag{4.2}$$

where q and m the linear coefficients for each zone. Due to the continuity condition, the number of unknown coefficients reduces to five; three of the coefficients can be determined as follows:

$$q_\mathrm{m} = q_\mathrm{l} + (m_\mathrm{l} - m_\mathrm{m})\,0.05; \;\; q_\mathrm{h} = q_\mathrm{m} + (m_\mathrm{m} - m_\mathrm{h})\,0.1; \;\; q_\mathrm{e} = q_\mathrm{h} + (m_\mathrm{h} - m_\mathrm{e})\,0.5 \tag{4.3}$$

Figure 4.7 shows the resulting piecewise linear curve along with the experimental data. The fitting coefficients and the estimation errors, in terms of

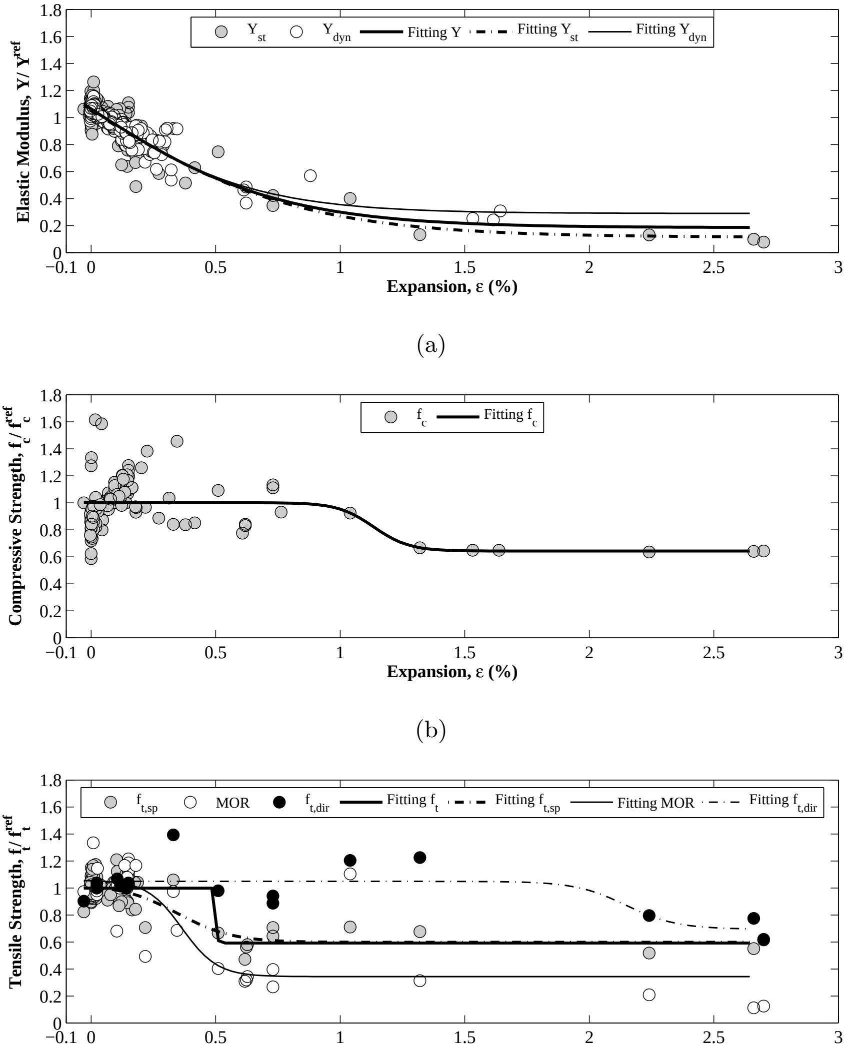

(a)

(b)

(c)

Figure 4.6: Fitting adopting the S-shaped curve (Equation (4.1)): (a) Elastic modulus; (b) Compressive strength; (c) Tensile strength.

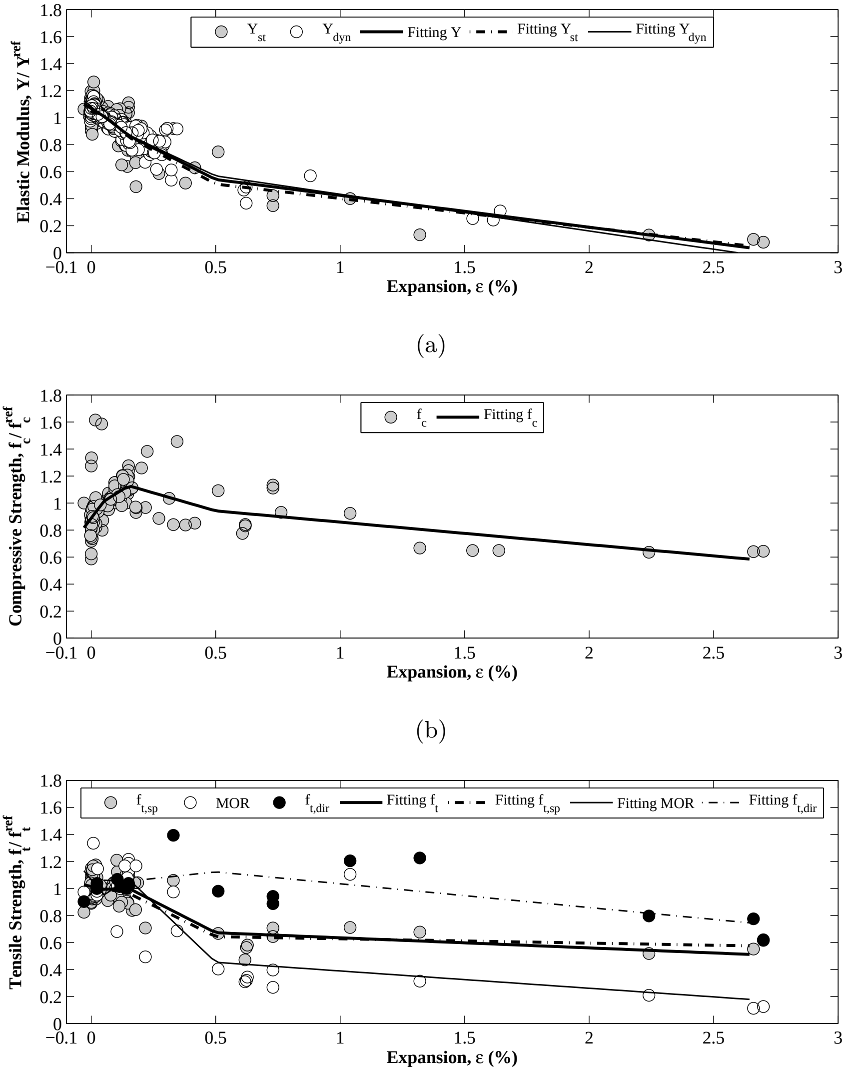

(a)

(b)

(c)

Figure 4.7: Fitting adopting the piecewise linear curve (Equation (4.2)): (a) Elastic modulus; (b) Compressive strength; (c) Tensile strength.

standard deviation, are reported in Table 4.9.
The elastic modulus degradation (Figure 4.7a) was well described by the piecewise linear curve. The estimation error and the degradation rate, which were evaluated in the high-expansion zone, provide results that are similar to those obtained from the S-shaped curve fitting. For expansion values greater than 2.60% this formulation provides unrealistic negative normalised values for the elastic modulus; therefore, zero residual stiffness should be considered after this limit.
The piecewise linear curve better described the behaviour of the compressive strength (Figure 4.7b), which shows an increase in the moderate-expansion zone. The total estimation error is slightly decreased to 13%. However, considering the moderate-expansion zone only, the estimation error is reduced from 20 to 13%.
The piecewise linear curve exhibited similar trend and estimation error with respect to the S-shaped curve for the splitting tensile strength (Figure 4.7c). This formulation is able to capture the slight increase in strength observed for the modulus of rupture in the moderate-expansion zone.

In Figure 4.8a, the best curve fitting results are presented along with an error band equal to 2σ. The piecewise linear curve was chosen to describe the compressive strength behaviour, whereas the S-shaped curve was chosen to describe the other properties. The tensile strength behaviour has been reported in terms of the splitting test results. Both static and dynamic elastic modulus data were considered for describing the stiffness degradation. According to the curve fitting studies, the elastic modulus was found to be the best indicator of ASR signs in concrete. The data show a relevant degradation, already at early expansion, which is characterized by the highest rate. For high-expansion values ($\varepsilon > 2.00\%$) the residual stiffness is 20% of the reference value. Conversely, the compressive strength behaviour is described with an initial gain of 15% and a maximum reduction of 46%. However, the estimation error is high, approximately 13%. The tensile behaviour appears to be well described by the splitting test results. In the high-expansion zone the tensile strength degrades at a similar rate as the elastic modulus, but its deterioration is delayed. The residual value is 46%.

Alternately, Figure 4.8b shows the differences in degradation behaviour from comparing the stiffness and strength properties. When the elastic modulus reaches 85% of its original value, both strengths decrease at a similar rate but still slower than the degradation rate of the elastic modulus. At a normalised value of $\beta_Y = 0.50$ for the elastic modulus, the normalised splitting strength obtains an asymptotic value of $\beta_{f_{\mathrm{t,sp}}} = 0.60$. The compressive strength experiences a drastic deterioration to a normalised value of the elastic modulus of $\beta_Y = 0.20$.

In engineering, it is common practice to express the stiffness Y and tensile strength f_{t} of unaffected concrete as a function of its compressive strength f_{c}. Using the strength-stiffness relationships proposed by Model Code 2010 (CEB-FIP, 2011), the degradation rate of the compressive and tensile strength of unaffected

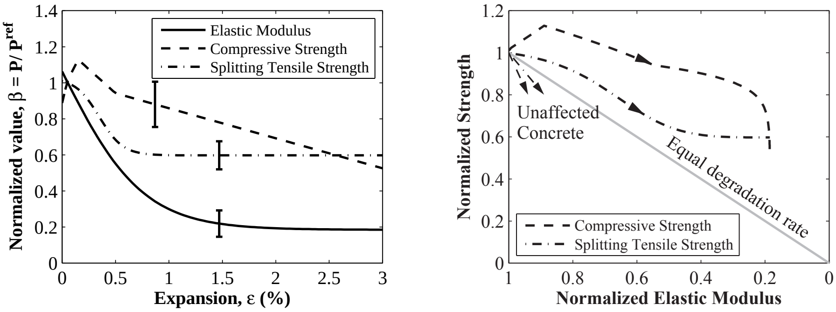

(a) (b)

Figure 4.8: Best curve fitting results: (a) Relation between normalised properties and concrete expansion; (b) Relation between normalised elastic modulus and normalised strengths.

concrete shown to be lower than that for the elastic modulus (Figure 4.8b). To demonstrate this, ASR-affected concrete with a compressive strength reduction of 20% ($\beta_{f_\mathrm{c}} = 0.80$) is considered. Adopting the Model Code formulation, the estimated normalised values of the elastic modulus and tensile strength are 0.94 and 0.86, respectively. Considering the proposed curves, the degradation of the stiffness and tensile strength are substantially different; the normalised values are $\beta_Y = 0.35$ and $\beta_{f_\mathrm{t,sp}} = 0.60$. This demonstrates that for ASR-affected concrete, the engineering strength-stiffness relationships cannot be used to determine the elastic modulus and the tensile strength from the measured compressive strength.

Table 4.9: Fitting coefficients and standard deviation.

Data	S-curve					Piecewise linear curve					
	ε_c	ε_l	β_0	β_∞	σ	q_l	m_l	m_m	m_h	m_e	σ
	%	%			%						%
E	0.37	1.13 10^{-9}	1.06	0.19	7	1.07	-1.06	-1.78	-0.98	-0.23	7
E_st	0.42	2.27 10^{-14}	1.05	0.11	9	1.04	-0.46	-1.89	-1.08	-0.21	9
E_dyn	0.31	6.89 10^{-12}	1.07	0.29	6	1.08	-1.43	-1.75	-0.91	-0.26	6
f_c	0.07	1.13	1.00	0.64	15	0.89	2.36	2.06	-0.37	-0.18	13
f_t	5.24 10^{-04}	0.51	1.00	0.59	15	1.01	-0.15	0.20	-0.83	-0.08	15
$f_\mathrm{t,sp}$	0.11	0.35	1.01	0.60	8	1.01	-0.25	-0.15	-0.86	-0.04	8
MOR	0.07	0.37	1.05	0.34	20	1.06	0.53	0.04	-1.54	-0.14	20
$f_\mathrm{t,dir}$	0.10	2.15	1.05	0.70	12	0.97	2.23	-0.68	0.20	-0.18	13

4.5 Concluding remarks

This chapter attempted to clarify the relationship between concrete expansion due to the ASR and consequent degradation (or enhancement) of engineering properties. From investigations on structures and concrete members down to the microscopic level, numerous researchers have attempted to describe the structural consequences of ASR-induced concrete expansion with varying success. Although a literature survey shows that there is a strong coupling between concrete expansion and the degradation of mechanical properties, numerous findings have never led to a widely agreed upon picture.

First, the laboratory tests performed within this thesis work were presented. The authors investigated the evolution of the static elastic modulus, compressive strength and splitting tensile strength in two comparable reactive concrete mixtures composed of Dutch and Norwegian aggregates. These tests belong to an extensive research project that aims to study the ASR degradation effects on various scales, from micro to macro, to better understand the phenomenon.

Second, available literature data, which focus on the evolution of engineering properties of ASR-affected concrete under free-expansion conditions, were collected and statistically analysed. When expressing the data as a function of the concrete expansion, a clear trend could be observed. The concrete mixtures were categorised into four reactivity classes: non-reactive ($\varepsilon < 0.05\%$), potentially reactive ($0.05\% \leq \varepsilon \leq 0.10\%$), reactive ($0.10\% < \varepsilon < 0.50\%$) and extremely reactive ($\varepsilon \geq 0.50\%$). A normalisation procedure was adopted: each normalised value was obtained as the ratio between the current value of the property and its (calculated) reference value, which corresponds to an expansion of 0.05%. The statistical analysis considered two fitting laws: an S-shaped curve and an piecewise linear curve.

The elastic modulus was identified as the best indicator of ASR signs in concrete, showing relevant degradation already at small expansion values. A deterioration of up to 90% could be observed. Both static and dynamic elastic modulus tests can contribute to the definition of the residual stiffness in the material. The curve fitting provides good results for both laws, with an estimation error of 7%.

The influence of the ASR on the compressive strength has been widely investigated. This test method is one of the principal techniques adopted in structural assessments. However, this method was determined to be the worst indicator in terms of monitoring the ASR. The compressive strength exhibits an initial gain of approximately 15% in the low- and moderate-expansion zones and a subsequent decreases to 46% of its original value. The piecewise linear curve provides the best fitting, thereby allowing the description of a non-monotonic trend. The estimation error is approximately 13%.

The splitting test best captured the influence of the ASR on the tensile behaviour of concrete. The data show an initial delay with respect to the degradation of the elastic modulus but a similar deterioration rate in the high-expansion zone. The splitting tensile strength eventually decreases to 64%. The S-shaped curve provided the best fitting with an estimation error of 8%.

When comparing the degradation behaviour of compressive and splitting tensile strengths with respect to the elastic modulus, a non-linear relation was observed. The ASR-affected concrete appears to be substantially different material and the known engineering strength-stiffness relationships, developed for unaffected concrete, cannot be applied.

The correlation between mechanical degradation and concrete expansion, which appears fundamental to the assessment of ASR-affected concrete structures, should be further investigated systematically to obtain narrowed bounds. Various parameters such as the specimen size, the storage conditions, the type of aggregates and the confinement of the specimens, can play an important role in this phenomenon. To obtain statistically relevant data sets, additional experimental campaigns are necessary.

Pressure-based Multiscale Material Modelling

5

Due to the multiscale nature of the alkali-silica reaction (ASR) in concrete structures, different modelling approaches have been developed on different scales and with various scopes, as presented in Chapter 3. Models ranging at structural level are often case-dependent, because they employ phenomenological laws based on experimental findings. On the contrary, models which act at aggregate or reaction products levels aim to explain the fundamentals of the phenomenon, but they are often too detailed for structural applications. In both cases, they are commonly used to describe the problem in terms of concrete expansion and limited attention is paid to the material degradation.

In the wider framework of structural analyses for ASR-affected concrete structures, a multiscale material model is adopted to understand the deteriorating impact of ASR on concrete. The model aims to bridge the gap between the micro- and macro-mechanical modelling techniques, by studying the interaction of the phenomenon between aggregate and concrete level.

This chapter presents the formulation of the state equations and the damage propagation criterion for the model in the framework of micro-poro-mechanics theory for saturated media and analytical homogenization (Section 5.1). Modifications of the model are discussed (Section 5.2). The model results in a versatile approach which can be extended to the reaction product and structural levels or it can be used as a complementary tool for the mechanical characterization (Section 5.3).

The model is validated for the case of unaffected and ASR-affected concrete in Chapter 6 and Chapter 7, respectively. In the former case, simulation of the laboratory tests on the reference material, studied in Chapter 4, are performed. Further details regarding the analytical solution of the model are given in Appendix D.

5.1 A Micro-poro-fracture-mechanical Model

To study the behaviour of concrete as a porous medium, the micro-poro-mechanics theory, which blends the concepts of poro-mechanics and micro-mechanics approaches, is adopted. The poro-mechanics theory studies the interaction between fluid and solid phases in a porous medium subjected to external loading. Its importance was first recognized in the soil consolidation process, where the entrapped water may exert a relevant pressure on the material. The micro-mechanics theory is employed to determine the macroscopic behaviour of an heterogeneous material considering the events which are happening at the level of its component (micro scale). It takes advantages of homogenization techniques which determine the macroscopic mechanical properties of a composite material on the basis of its constitutive phases.

The concrete is modelled at the aggregate level by means of a representative elementary volume (REV) composed by the solid matrix and the porosity space, modelled as cracks (Figure 5.1a). In case of ASR-affected concrete, it is assumed that the expansive alkali-silica gel saturates the entire porosity space and exerts a pressure on the solid matrix phase. By adopting the terminology commonly used in micro-mechanics, the quantities at aggregate level are name as microscopic, while the one at concrete level are defined as macroscopic.

The porosity space is composed by three orthogonal families of cracks ($m = 3$). Within each family the cracks are aligned in one plane with normal $\boldsymbol{n}_i$. Algorithmically, there is no limit to the number of planes (e.g. Bažant and Oh (1996) considered 21 families in a refined version of their microplane models). The cracks of the i-th family are represented by penny-shaped inclusions, with radius a_i in the inclusion's plane and radius c_i in thickness direction. Their aspect ratio X_i and volume fraction $\phi_{\mathrm{c}i}$ are defined as:

$$X_i = \frac{c_i}{a_i} \tag{5.1a}$$

$$\phi_{\mathrm{c}i} = \frac{4}{3}\pi c_i n_i a_i^2 \tag{5.1b}$$

where n_i is the number of cracks per unit of volume. All the crack families contribute to the porosity of concrete, which has a volume fraction equal to:

$$\Phi = \sum_{i=1}^{m} \phi_{\mathrm{c}i} \tag{5.2}$$

The solid matrix is considered an homogenized material, which properties are related to mechanical characteristics of the aggregates and the cement paste (Figure 5.1b). Consequently, no explicit distinction is made between cracks in

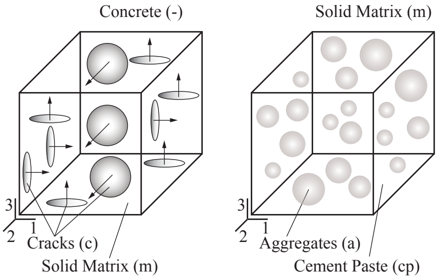

(a) (b)

Figure 5.1: Micro-mechanical model: (a) Concrete; (b) Solid matrix.

the aggregates or in the cement paste. The aggregates are modelled as spherical inclusions, having a volume fraction ϕ_{agg}, embedded in the cement paste matrix.

The state equations, presented in Section 5.1.1, are based on the linear poro-elasticity theory for saturated media. They are solved by taking advantage of the analytical homogenization method illustrated in Section 5.1.2 and Appendix D. The damage propagation is formulated in the framework of linear fracture mechanics theory, as described in Section 5.1.3.

5.1.1 State Equations

The state equations are formulated in the context of saturated porous medium theory. A full description can be found in the work by (Dormieux et al., 2006, Chapter 5); for completeness the main equations are reported in this section. The concrete, occupying a domain Ω, is composed by the solid matrix (Ω_{m}) and the pore space (Ω_{c}); the external boundary of the system is located in the solid phase ($\delta\Omega \in \Omega_{\mathrm{m}}$). The expansive alkali-silica gel is considered as a fluid saturating the entire porosity space. As a consequence, the domain of the fluid corresponds to the domain of the pore space Ω_{c}. The main microscopically mechanical effect of the alkali-silica gel on the solid matrix is identified with a pressure; viscosity effects are neglected. Consequently, the pressure's gradient at microscopic and macroscopic level are of the same order of magnitude. The porosity space is assumed interconnected, thus the fluid pressure can be considered as a single parameter. As a consequence, the macroscopic loading parameters are defined by the macroscopic uniform strain $\boldsymbol{E}$ and the pressure P developed in the porosity space. The state equation of the system describe the evolution of the macroscopic stress and the change in pore space due to these two loading parameters.

The state equations are determined by solving the following boundary value problem:

$$L = L(\boldsymbol{E}, P) \quad \Rightarrow \left\{ \begin{array}{cc} div\boldsymbol{\sigma} = 0 & \Omega \\ \boldsymbol{\sigma} = \mathbb{C}\left(\boldsymbol{z}\right) : \boldsymbol{\varepsilon} + \boldsymbol{\sigma}^P\left(\boldsymbol{z}\right) & \Omega \\ \boldsymbol{\xi} = \boldsymbol{E} \cdot \boldsymbol{z} & \partial\Omega \end{array} \right. \tag{5.3}$$

where $\boldsymbol{z}$ is the position vector at the microscopic scale $\boldsymbol{\sigma}$ and $\boldsymbol{\varepsilon}$ are the microscopic stress strain tensors, respectively, $\mathbb{C}$ is the stiffness tensor of the homogenized material, $\boldsymbol{\sigma}^P$ is the pre-stress tensors due to the pressure P and $\boldsymbol{\xi}$ is the displacement field on the external boundary $\delta\Omega$. The stiffness and the pre-stress tensors are defined as:

$$\mathbb{C}\left(\boldsymbol{z}\right) = \left\{ \begin{array}{cc} \mathbb{C}_{\mathrm{m}} & \Omega_{\mathrm{m}} \\ 0 & \Omega_{\mathrm{c}} \end{array} \right. \tag{5.4a}$$

$$\boldsymbol{\sigma}^P\left(\boldsymbol{z}\right) = \left\{ \begin{array}{cc} 0 & \Omega_{\mathrm{m}} \\ -P\boldsymbol{I} & \Omega_{\mathrm{c}} \end{array} \right. \tag{5.4b}$$

A linear elastic behaviour of the solid matrix is considered:

$$\boldsymbol{\sigma} = \mathbb{C}_{\mathrm{m}} : \boldsymbol{\varepsilon} \tag{5.5a}$$

$$\boldsymbol{\varepsilon} = \mathbb{D}_{\mathrm{m}} : \boldsymbol{\sigma} \tag{5.5b}$$

where $\boldsymbol{\sigma}$ and $\boldsymbol{\varepsilon}$ are the microscopic stress and strain in the solid matrix, respectively, $\mathbb{C}_{\mathrm{m}}$ and $\mathbb{D}_{\mathrm{m}} = \mathbb{C}_{\mathrm{m}}^{-1}$ are the stiffness and compliance tensors of the solid matrix, respectively.

In order to describe the evolution of the pore space during the loading, the Lagrangian definition of the porosity is adopted:

$$\Phi = \frac{|\Omega_{\mathrm{c}}|}{|\Omega^{*}|} \tag{5.6}$$

where Ω^* is the REV volume in the reference configuration, which represents the state of the system prior loading. In the framework of poro-elasticity theory the reference configuration corresponds to the initial status of the system.

The state equations for the entire REV are derived by extending the definition of the microscopic stress, strain and displacement from the domain of the solid matrix Ω_{m} to the domain of the fluid, which corresponds to the one of the pore space Ω_{c} for the case of saturated porous medium. Considering the linearity of the problem, the effect of the two loading parameters can be analysed separately and the state equation can be derived by applying the superposition principle.

The first load case $L' = L\left(\boldsymbol{E}, 0\right)$ considers only the application of macroscopic uniform strain $\boldsymbol{E}$, while the pre-stress induced by the pressure P is zero ($\boldsymbol{\sigma}^P = 0$).

The boundary value problem in Equation (5.3) results:

$$L' = L(\boldsymbol{E}, 0) \quad \Rightarrow \begin{cases} div\boldsymbol{\sigma}' = 0 & \Omega \\ \boldsymbol{\sigma}' = \mathbb{C}\left(\boldsymbol{z}\right) : \boldsymbol{\varepsilon}' & \Omega \\ \boldsymbol{\xi}' = \boldsymbol{E} \cdot \boldsymbol{z} & \partial\Omega \end{cases} \tag{5.7}$$

Being the problem linear, the microscopic, $\boldsymbol{\varepsilon}$, and macroscopic, $\boldsymbol{E}$, strain tensors can be correlated by the 4^{th} order strain concentration tensor $\mathbb{A}$:

$$\boldsymbol{\varepsilon}\left(\boldsymbol{z}\right) = \mathbb{A}\left(\boldsymbol{z}\right) : \boldsymbol{E} \quad \forall \boldsymbol{z} \in \Omega \tag{5.8}$$

The strain concentration tensor includes all the information related to the microstructure, such as the shape, the orientation and the volume fraction of the inclusions as well as the stiffness tensors of each phase in the system. In this work, the strain concentration tensor is estimated by the Mori-Tanaka homogenization method, as described Section 5.1.2. More information on other classic mean-field homogenization methods can be found in Appendix D.

To ensure the compatibility between the microscopic and macroscopic definitions of the rate of mechanical energy, the strain average rule is adopted:

$$\boldsymbol{E} = \overline{\boldsymbol{\varepsilon}} \approx \frac{1}{|\Omega\left(\boldsymbol{x}\right)|} \int\limits_{\Omega(\boldsymbol{x})} \boldsymbol{\varepsilon}\left(\boldsymbol{z}\right) dV_z \tag{5.9}$$

where $\bar{\cdot}$ is the volume average operator and $\boldsymbol{x}$ is the position vectors at the macroscopic scale.

Considering Equation (5.8) and Equation (5.9), the following consistency condition holds:

$$\overline{\mathbb{A}} = \Phi^* \overline{\mathbb{A}}^{\mathrm{c}} + \left(1 - \Phi^*\right) \overline{\mathbb{A}}^{\mathrm{m}} = \mathbb{I} \tag{5.10}$$

where $\overline{\mathbb{A}}^{\mathrm{c}}$ and $\overline{\mathbb{A}}^{\mathrm{m}}$ are the average strain concentration tensors evaluated in the pore space domain and in the solid matrix domain, respectively, and Φ^* is the volume fraction of the pore space in the reference configuration.

Combining Equation (5.7) and Equation (5.8), the microscopic stress results:

$$\boldsymbol{\sigma}'\left(\boldsymbol{z}\right) = \mathbb{C}\left(\boldsymbol{z}\right) : \boldsymbol{\varepsilon}'\left(\boldsymbol{z}\right) = \mathbb{C}\left(\boldsymbol{z}\right) : \mathbb{A}\left(\boldsymbol{z}\right) : \boldsymbol{E} \quad \forall \boldsymbol{z} \in \Omega \tag{5.11}$$

To ensure the compatibility between the microscopic and the macroscopic momentum balance equation, the stress average rule is adopted:

$$\boldsymbol{\Sigma} = \overline{\boldsymbol{\sigma}} \approx \frac{1}{|\Omega\left(\boldsymbol{x}\right)|} \int\limits_{\Omega(\boldsymbol{x})} \boldsymbol{\sigma}\left(\boldsymbol{z}\right) dV_z \tag{5.12}$$

By considering Equation (5.12) and the definition of the stiffness tensor as in Equation (5.4a), the macroscopic stress $\boldsymbol{\Sigma}'$ associated to the first load case $L' = L(\boldsymbol{E}, 0)$ results:

$$\boldsymbol{\Sigma}' = \overline{\boldsymbol{\sigma}'} = \overline{\mathbb{C}(\boldsymbol{z}) : \mathbb{A}(\boldsymbol{z}) : \boldsymbol{E}} = (1-\Phi^*)\,\mathbb{C}_\mathrm{m} : \overline{\mathbb{A}}^\mathrm{m} : \boldsymbol{E} = \mathbb{C} : \boldsymbol{E} \tag{5.13}$$

where $\mathbb{C}$ is the drained stiffness tensor of the homogenized material, which, with the help of Equation (5.10), can be defined as:

$$\mathbb{C} = (1-\Phi^*)\,\mathbb{C}_\mathrm{m} : \overline{\mathbb{A}}^\mathrm{m} = \Phi^*\mathbb{C}_\mathrm{m} : \overline{\mathbb{A}}^\mathrm{c} \tag{5.14}$$

The change in pore space associated to the first load case can be defined as the evolution of the microscopic strain field $\boldsymbol{\varepsilon}'$ (Equation (5.8)) in the pore space:

$$(\Phi - \Phi^*)' = \Phi^*\boldsymbol{I} : \overline{\boldsymbol{\varepsilon}'}^\mathrm{c} = \Phi^*\boldsymbol{I} : \overline{\mathbb{A}}^\mathrm{c} : \boldsymbol{E} = \boldsymbol{B} : \boldsymbol{E} \tag{5.15}$$

where $\boldsymbol{B}$ is the Biot tensor that, with the help of the consistency condition of Equation (5.10), can be defined as:

$$\boldsymbol{B} = \Phi^*\boldsymbol{I} : \overline{\mathbb{A}}^\mathrm{c} = \Phi^*\boldsymbol{I} + (1-\Phi^*)\,\boldsymbol{I} : \overline{\mathbb{A}}^\mathrm{m} \tag{5.16}$$

Introducing Equation (5.14) in Equation (5.16), the Biot tensor $\boldsymbol{B}$ can be expressed as a function of the stiffness tensor $\mathbb{C}$:

$$\boldsymbol{B} = \boldsymbol{I} - \mathbb{D}_\mathrm{m} : \mathbb{C} : \boldsymbol{I} = \boldsymbol{I} - \boldsymbol{I} : \mathbb{C} : \mathbb{D}_\mathrm{m} \tag{5.17}$$

The second load case $L'' = L(0, P)$ considers only the loading defined by the pressure P in terms of the pre-stress $\boldsymbol{\sigma}^P$, while the macroscopic strain is zero ($\boldsymbol{E}'' = 0$). This load case corresponds to the application of a zero microscopic displacement on the REV boundary. The boundary value problem in Equation (5.3) results:

$$L'' = L(0, P) \quad \Rightarrow \begin{cases} div\boldsymbol{\sigma}'' = 0 & \Omega \\ \boldsymbol{\sigma}'' = \mathbb{C}(\boldsymbol{z}) : \boldsymbol{\varepsilon}'' + \boldsymbol{\sigma}^\mathrm{P}(\boldsymbol{z}) & \Omega \\ \boldsymbol{\xi}'' = 0 & \partial\Omega \end{cases} \tag{5.18}$$

To ensure a correspondence between the volume average of the microscopic strain energy and the macroscopic strain energy, the Hill lemma is applied. Considering the microscopic stress field $\boldsymbol{\sigma}''$ of the second load case, which satisfies the momentum balance equation, and the geometrically compatible strain field $\boldsymbol{\varepsilon}'$ of the first load case, the Hill lemma reads:

$$\overline{\boldsymbol{\sigma}'' : \boldsymbol{\varepsilon}'} = \overline{\boldsymbol{\sigma}''} : \overline{\boldsymbol{\varepsilon}'} \tag{5.19}$$

Substituting Equation (5.18) in the left-hand side of Equation (5.19), it results:

$$\overline{\boldsymbol{\sigma}'' : \boldsymbol{\varepsilon}'} = \overline{\boldsymbol{\varepsilon}'' : \mathbb{C}(\boldsymbol{z}) : \boldsymbol{\varepsilon}'} + \overline{\boldsymbol{\sigma}^\mathrm{P}(\boldsymbol{z}) : \boldsymbol{\varepsilon}'} = \overline{\boldsymbol{\sigma}^\mathrm{P}(\boldsymbol{z}) : \boldsymbol{\varepsilon}'} \tag{5.20}$$

in which the conditions $\boldsymbol{E}'' = \overline{\boldsymbol{\varepsilon}''} = 0$, imposed by the loading definition, is used. Introducing Equation (5.8) in Equation (5.20), it results:

$$\overline{\boldsymbol{\sigma}'' : \boldsymbol{\varepsilon}'} = \overline{\boldsymbol{\sigma}^{\mathrm{P}}(\boldsymbol{z}) : \boldsymbol{\varepsilon}'} = \overline{\boldsymbol{\sigma}^{\mathrm{P}}(\boldsymbol{z}) : \mathbb{A}(\boldsymbol{z}) : \boldsymbol{E}} = \overline{\boldsymbol{\sigma}^{\mathrm{P}}(\boldsymbol{z}) : \mathbb{A}(\boldsymbol{z})} : \boldsymbol{E} \tag{5.21}$$

Applying the strain average rule (Equation (5.9)) and the stress average rule (Equation (5.12)) to the right-hand side of Equation (5.19), it results:

$$\overline{\boldsymbol{\sigma}''} : \overline{\boldsymbol{\varepsilon}'} = \boldsymbol{\Sigma}'' : \boldsymbol{E} \tag{5.22}$$

Combining Equation (5.19), Equation (5.21) and Equation (5.22), the following relationship is obtained:

$$\boldsymbol{\Sigma}'' = \overline{\boldsymbol{\sigma}^{\mathrm{P}}(\boldsymbol{z}) : \mathbb{A}(\boldsymbol{z})} \tag{5.23}$$

Introducing the definition of the pre-stress $\boldsymbol{\sigma}^{\mathrm{P}}$ (Equation (5.4b)) in Equation (5.23), the macroscopic stress associated to the second load case $L'' = L(0, P)$ results:

$$\boldsymbol{\Sigma}'' = -P\Phi^{*}\boldsymbol{I} : \overline{\mathbb{A}}^{\mathrm{c}} = -P\boldsymbol{B} \tag{5.24}$$

where $\boldsymbol{B}$ is the Biot tensor of Equation (5.16).
The change in pore space associated to the second load case can be defined as the evolution of the microscopic strain field $\boldsymbol{\varepsilon}''$ (5.8) in the pore space. Considering that the macroscopic strain associate to the second load case is zero ($\boldsymbol{E}'' = \overline{\boldsymbol{\varepsilon}''} = 0$), the following relation holds:

$$\Phi^{*}\overline{\boldsymbol{\varepsilon}''}^{\mathrm{c}} = -\left(1 - \Phi^{*}\right)\overline{\boldsymbol{\varepsilon}''}^{\mathrm{m}} \tag{5.25}$$

where $\overline{\boldsymbol{\varepsilon}''}^{\mathrm{m}}$ is the average strain filed in the solid matrix domain, which is correlated to the average stress in the matrix according to Equation (5.5):

$$\left(1 - \Phi^{*}\right)\overline{\boldsymbol{\varepsilon}''}^{\mathrm{m}} = \left(1 - \Phi^{*}\right)\mathbb{D}_{\mathrm{m}} : \overline{\boldsymbol{\sigma}''}^{\mathrm{m}} \tag{5.26}$$

Considering that the macroscopic stress generated by the pressure P can be defined as in Equation (5.24) and applying the stress average rule Equation (5.12), the average micro stress in the solid matrix can be defined as:

$$\left(1 - \Phi^{*}\right)\overline{\boldsymbol{\sigma}''}^{\mathrm{m}} = \Phi^{*}P\boldsymbol{I} - P\boldsymbol{B} = P\left(\Phi^{*}\boldsymbol{I} - \boldsymbol{B}\right) \tag{5.27}$$

Substituting Equation (5.27) in Equation (5.26) and subsequently in Equation (5.25), it results:

$$\Phi^{*}\overline{\boldsymbol{\varepsilon}''}^{\mathrm{c}} = P\mathbb{D}_{\mathrm{m}} : \left(\boldsymbol{B} - \Phi^{*}\boldsymbol{I}\right) \tag{5.28}$$

As a consequence, the change in porosity associate to second load case $L'' = L(0, P)$ is defined as:

$$\left(\Phi - \Phi^{*}\right)'' = \Phi^{*}\boldsymbol{I} : \overline{\boldsymbol{\varepsilon}''}^{\mathrm{c}} = P\boldsymbol{I} : \mathbb{D}_{\mathrm{m}} : \left(\boldsymbol{B} - \Phi^{*}\boldsymbol{I}\right) = \frac{P}{N} \tag{5.29}$$

where $\frac{1}{N}$ is the Biot modulus defined as:

$$\frac{1}{N} = \boldsymbol{I} : \mathbb{D}_{\mathrm{m}} : (\boldsymbol{B} - \Phi^* \boldsymbol{I}) = (\boldsymbol{B} - \Phi^* \boldsymbol{I}) : \mathbb{D}_{\mathrm{m}} : \boldsymbol{I} \tag{5.30}$$

Applying the superposition principle to the solution of the two load cases $L' = L(\boldsymbol{E}, 0)$ and $L'' = L(0, P)$, *the state equation of poro-elasticity* are recovered:

$$\boldsymbol{\Sigma} = \mathbb{C} : \boldsymbol{E} - \boldsymbol{B}P \tag{5.31a}$$

$$\Phi - \Phi^* = \boldsymbol{B} : \boldsymbol{E} + \frac{P}{N} \tag{5.31b}$$

5.1.2 Analytical Homogenization

To determine the drained stiffness tensor $\mathbb{C}$ the homogenization theory, which evaluates the properties of the overall material on the basis of its components, is applied. For the presented model, the Mori-Tanaka homogenization scheme (Benveniste, 1987) is considered. More details related to the adopted homogenization technique and to its application in the present modelling approach are given in Appendix D. Considering now that the porosity space is formed by three orthogonal cracking planes ($m = 3$), where each of them is composed of aligned identical penny-shaped inclusions, or cracks, (Figure 5.1), the stiffness tensors $\mathbb{C}$ reads:

$$\mathbb{C} = \mathbb{C}_{\mathrm{m}} + \sum_{i=1}^{m} \phi_{\mathrm{c}i} \left(\mathbb{C}_{\mathrm{c}i} - \mathbb{C}_{\mathrm{m}} \right) : \mathbb{A}_{\mathrm{c}i} \tag{5.32}$$

where $\mathbb{C}_{\mathrm{c}i}$ and $\mathbb{A}_{\mathrm{c}i}$ are the stiffness and the strain concentration tensors of the i-th crack family, respectively. The latter is estimated by the Mori-Tanaka method as follows:

$$\mathbb{A}_{\mathrm{c}i} = \mathbb{T}_{\mathrm{c}i} : \left(\phi_{\mathrm{m}} + \sum_{j=1}^{m} \phi_{\mathrm{c}j} \mathbb{T}_{\mathrm{c}j} \right)^{-1} \tag{5.33}$$

with $\mathbb{T}_{\mathrm{c}i}$ equal to its dilute estimation:

$$\mathbb{T}_{\mathrm{c}i} = \left[\mathbb{I} + \mathbb{S}_{\mathrm{c}i} : \mathbb{D}_{\mathrm{m}} : (\mathbb{C}_{\mathrm{c}i} - \mathbb{C}_{\mathrm{m}}) \right]^{-1} \tag{5.34}$$

being $\mathbb{S}_{\mathrm{c}i}$ the Eshelby tensor, which depends on the aspect ratio of the cracks X_i on the orientation of the cracks and on the Poisson ratio of the solid matrix ν_{m} (Mura, 1987), as described in Appendix D. It is noted that the resulting stiffness tensor does not depend on the position and the size of the inclusions. Being the cracks empty inclusions, their stiffness tensor $\mathbb{C}_{ci}$ is equal to the null tensor $\mathbb{O}$ and Equation (5.32) can be defined similarly to Equation (5.14):

$$\mathbb{C} = \mathbb{C}_{\mathrm{m}} : \left(\mathbb{I} - \sum_{i=1}^{m} \phi_{ci} \mathbb{A}_{ci}\right) \tag{5.35}$$

The solid matrix is considered as an homogenized material with respect to the cracks (Figure 5.1a). However, at a lower scale more phases are considered: the aggregates and the cement paste. To account for their effects, the mechanical properties of the solid matrix are linked to their characteristics. The aggregates are modelled as spherical inclusions having a volume fraction ϕ_{agg} and embedded in the cement paste (Figure 5.1b). The stiffness tensor of the solid matrix is evaluated likewise Equation (5.32):

$$\mathbb{C}_{\mathrm{m}} = \mathbb{C}_{\mathrm{cem}} + \phi_{\mathrm{agg}} \left(\mathbb{C}_{\mathrm{agg}} - \mathbb{C}_{\mathrm{cem}}\right) : \mathbb{A}_{\mathrm{agg}} \tag{5.36}$$

where $\mathbb{C}_{\mathrm{cem}}$ is the stiffness tensor of the cement paste, $\mathbb{C}_{\mathrm{agg}}$ and $\mathbb{A}_{\mathrm{agg}}$ are the stiffness and strain concentration tensor of the aggregate, respectively. The stiffness tensor of the solid matrix $\mathbb{C}_{\mathrm{m}}$ is kept constant during the crack propagation. As a consequence, no distinction is made between damage propagation in the aggregates and in the cement paste and *the micro-mechanical formulation is a one-scale single porosity model.*

The approach results in a *three-dimensional smeared* model where the macroscopic stress and strain are obtained as an average of the microscopic quantities. The *loading parameters* are identified by *the macroscopic uniform imposed strain* $\boldsymbol{E}$ *and by the pressure* P exerted by the entrapped expansive alkali-silica gel. *A linear elastic behaviour of the solid matrix is adopted.*

5.1.3 Damage Criterion

The damage criterion for a saturated porous medium is formulated in the framework of linear fracture mechanics theory, on the basis of thermodynamic concepts (Dormieux et al., 2006, Chapter 10). The rate of mechanical work $\dot{W}$ developed by the loading increment $\left(\dot{\boldsymbol{E}}, \dot{P}\right)$ on the porous medium, having reference volume Ω^*, is defined as:

$$\dot{W} = |\Omega^*| \left(\boldsymbol{\Sigma} : \dot{\boldsymbol{E}} + P\dot{\Phi}\right) \tag{5.37}$$

Under the assumption of *elastic behaviour of the solid matrix*, the rate of mechanical work $\dot{W}$ can be translated into the rate of elastic energy density $\dot{W} = |\Omega^*|\dot{\Psi}_{\mathrm{el}}$. The rate of potential energy density $\dot{\Psi}_{\mathrm{pot}}$ can be defined as:

$$\dot{\Psi}_{\mathrm{pot}} = \dot{\Psi}_{\mathrm{el}} - \dot{P}\left(\Phi - \Phi^*\right) = \boldsymbol{\Sigma} : \dot{\boldsymbol{E}} - \dot{P}\left(\Phi - \Phi^*\right) \tag{5.38}$$

The potential energy density Ψ_{pot}, being the macroscopic thermodynamic potential, depends on the loading conditions $L\left(\boldsymbol{E},P\right)$. As a consequence, the state equations (Equation (5.31)) can be defined as follows:

$$\dot{\Psi}_{\text{pot}} = \boldsymbol{\Sigma} : \dot{\boldsymbol{E}} - \dot{P}\left(\Phi - \Phi^*\right) \quad \Rightarrow \quad \begin{cases} \boldsymbol{\Sigma} = \dfrac{\partial \Psi_{\text{pot}}}{\partial \boldsymbol{E}} \\ \left(\Phi - \Phi^*\right) = \dfrac{\partial \Psi_{\text{pot}}}{\partial P} \end{cases} \tag{5.39}$$

Since the state equations are linear functions of the loading parameters $(\boldsymbol{E}, P)$, the potential energy density Ψ_{pot} results a quadratic function:

$$\Psi_{\text{pot}} = \frac{1}{2}\boldsymbol{E} : \mathbb{C} : \boldsymbol{E} - \frac{P^2}{2N} - P\boldsymbol{B} : \boldsymbol{E} \tag{5.40}$$

Considering the crack propagation for the i-th family within the elastic solid matrix, the damage state is identified by adopting the crack density variable ϵ_i (Budiansky and O'Connell, 1976):

$$\epsilon_i = n_i a_i^3 \tag{5.41}$$

For the current damage state, the macroscopic thermodynamic potential related to the i-th family of cracks is a function of the loading parameters and of the crack density variable, $\Psi_{\text{pot},i} = \Psi_{\text{pot},i}\left(\boldsymbol{E}, P, \epsilon_i\right)$. This dependency emerges from Equation (5.40) by noting that the stiffness tensor $\mathbb{C}$, the Biot tensor $\boldsymbol{B}$ and the Biot moduli $1/N$ depend on the crack density variable ϵ_i. The energy dissipation occurs due to the formation of additional crack surface l_i, which is evaluated as:

$$l_i = \pi a_i^2 = \pi\left(\frac{\epsilon_i}{n_i}\right)^{\frac{2}{3}} \tag{5.42}$$

The dissipation rate associated to the i-th family $\dot{D}_i$ is defined as:

$$\frac{\dot{D}_i}{|\Omega^*|} = -\frac{\partial \Psi_{\text{el}}}{\partial l_i}\dot{l}_i = -\frac{\partial \Psi_{\text{el}}}{\partial \epsilon_i}\dot{\epsilon}_i \geq 0 \tag{5.43}$$

where l_i and ϵ_i are interchangeable state variables. *The damage criterion* can be thus formulated in the framework of linear fracture mechanics theory:

$$G_i - G_{\text{c}i} \leq 0; \quad \dot{\epsilon}_i \geq 0; \quad \left(G_i - G_{\text{c}i}\right)\dot{\epsilon}_i = 0 \tag{5.44}$$

where G_i is the energy release rate and $G_{\text{c}i}$ its critical value. The energy release rate G_i is the driving force of the damage process and it is related to the potential energy density of the corresponding i-th family $\Psi_{\mathrm{pot},i}$:

$$G_i\left(\boldsymbol{E},P,\epsilon_i\right)=\frac{\partial\Psi_{\mathrm{pot},i}}{\partial\epsilon_i}=\frac{\partial}{\partial\epsilon_i}\left(\frac{1}{2}\boldsymbol{E}:\mathbb{C}\left(\epsilon_i\right):\boldsymbol{E}-\frac{P^2}{2N\left(\epsilon_i\right)}-P\boldsymbol{B}\left(\epsilon_i\right):\boldsymbol{E}\right)= \\ =-\frac{1}{2}\langle\boldsymbol{E}+P\mathbb{D}_{\mathrm{m}}:\boldsymbol{I}\rangle:\frac{\partial\mathbb{C}}{\partial\epsilon_i}:\langle\boldsymbol{E}+P\mathbb{D}_{\mathrm{m}}:\boldsymbol{I}\rangle \tag{5.45}$$

The strain quantity $\boldsymbol{E}'=\boldsymbol{E}+P\mathbb{D}_{\mathrm{m}}:\boldsymbol{I}$ results as an effective strain, which controls the damage evolution. To make a distinction between the damage evolution under tensile and compressive loading conditions, only the positive part of the effective strain $\langle\boldsymbol{E}'\rangle$ is adopted, as inspired by Mazars (1986). The validation of this assumption is shown in Section 6.3.
The critical energy release rate $G_{\mathrm{c}i}$ is related to the microscopic fracture energy g_{f} and to the current damage state ϵ_i. Considering that the i-th family is composed of n_i cracks per unit of volume, the propagation of each crack will contribute to the definition of the dissipation rate $\dot{D}_i$:

$$\frac{\dot{D}_i}{|\Omega^*|}=g_{\mathrm{f}}n_i\dot{l}_i=G_{\mathrm{c}i}\dot{\epsilon}_i \tag{5.46}$$

Combining Equation (5.42) and Equation (5.46), the critical energy release rate is defined as $G_{\mathrm{c}i}$:

$$G_{\mathrm{c}i}\left(\epsilon_i\right)=\frac{2\pi}{3}g_{\mathrm{f}}\left(\frac{n_i}{\epsilon_i}\right)^{1/3}=\frac{2\pi}{3}\frac{g_{\mathrm{f}}}{a_i} \tag{5.47}$$

Eventually, the stability of damage propagation is considered. The crack propagation of the i-th crack family is stable only if for an increment of crack surface $l_i+\delta l$ the energy release rate $G_i\left(\boldsymbol{E},P,l_i\right)$ is increasing. In terms of the crack density variable ϵ_i, the damage propagation results stable only if the increment of energy release rate is smaller than the increment of its threshold value $G_i\left(\boldsymbol{E},P,\epsilon_i+d\epsilon\right)<G_{\mathrm{c}i}\left(\epsilon_i+d\epsilon\right)$. *The stable damage propagation criterion* for the i-th crack family, is defined, through the stability coefficient s_i, as:

$$s_i=\frac{\partial G_i}{\partial\epsilon_i}\left(\boldsymbol{E},P,\epsilon_i\right)-\frac{\partial G_{\mathrm{c}i}}{\partial\epsilon_i}\left(\epsilon_i\right)<0 \tag{5.48}$$

Substituting Equation (5.45) and Equation (5.47) in Equation (5.48), it is obtained:

$$s_i=-\frac{1}{2}(\boldsymbol{E}+P\mathbb{D}_{\mathrm{m}}:\boldsymbol{I}):\frac{\partial^2\mathbb{C}}{\partial\epsilon_i^2}:(\boldsymbol{E}+P\mathbb{D}_{\mathrm{m}}:\boldsymbol{I})+\frac{2}{9}\pi\frac{g_{\mathrm{f}}}{na^4}<0 \tag{5.49}$$

Noting that *nucleation and opening/closing of cracks are not accounted for*, the crack radius a_i results as a state variable of the problem, equivalently to the crack density variable ϵ_i. In fact, ignoring the nucleation process, the number of cracks per unit of volume n_i within each family is constant during the damage evolution. Similarly, not including the opening/closing of the cracks, the crack radius in the thickness direction c_i is not varying during cracking.

5.2 Model Modifications

The heterogeneity of concrete is accounted differently in various material models available in literature on the basis of the observation point of view. From a structural point of view concrete is considered as an homogeneous material, but at concrete level it commonly described as composed by various heterogeneous phases, such as cement paste, aggregates, pores and cracks. At a lower scale named aggregate level, many imperfection of concrete constituents can be observed. The aggregates are composed by different minerals and the cement paste, which contains different hydration products like the C-S-H gel, can present pores of different sizes.

Due to the interaction between the reaction products of ASR and the structure of concrete at aggregate level, in this section model modifications are proposed to understand the limitation of the one-scale single porosity model. Two variations are considered: one involving a more complex micro-structure of concrete, the other considering the change in phase of the expansive alkali-silica gel from fluid to solid.

First, the concrete is modelled with a two-scale double porosity approach, as described in Section 5.2.1. Now, the crack propagation at a higher scale develops in a porous medium, which is composed by the solid matrix and a lower-scale porosity. The effect of the expansive alkali-silica gel is considered in terms of a saturating pressure, similarly as in Section 5.1.

Second, the evolution in phase of the ASR products is accounted in Section 5.2.2, distinguishing between fluid and solid gel phases. A one-scale single porosity model, similar to the one proposed in Section 5.1, is used as a framework.

5.2.1 Two-Scale Double Porosity

Microscopic investigation of concrete showed that the pore space of concrete is developed at different levels including capillarity pores and C-S-H gel pores. Following the classification reported by Jennings et al. (2008), the former contains large (10μm $-$ 50nm) and medium (50nm $-$ 10nm) pores, which influence the permeability and the strength of the material. The latter considers small (10nm $-$ 2.5nm) and micro-pores (2.5nm $-$ 0.5nm), which are responsible for the shrinkage and creep effects. It can be considered that only the capillarity porosity will contribute to the cracking formation.

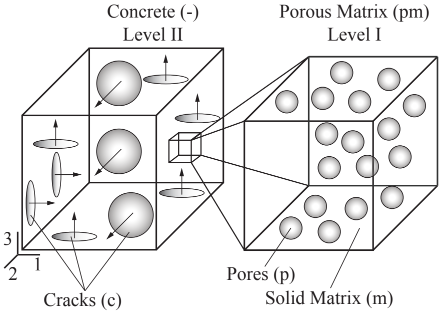

Figure 5.2: Two-scale double porosity model.

The influence on the concrete behaviour of a second porosity system at a lower scale than the cracks is investigated in this section. This approach is adopted in refined literature models, such as Ulm et al. (2014) and Pichler and Hellmich (2011), to estimate the evolution of stiffness properties during the hydration process of concrete.

The concrete is here modelled by a two-scale double porosity model (Figure 5.2). The state equations and the damage criterion are derived similarly to Section 5.1 in agreement with Dormieux et al. (2006) and Ulm (2014). At higher scale (level II), the REV is composed by a porous matrix (Ω_{pm}) and by cracks (Ω_{c}). At lower scale (level I), the porous matrix is constituted by the solid matrix (Ω_{m}) and the C-S-H gel pore space (Ω_{p}). The macroscopic loading parameters are defined by the macroscopic uniform strain $\boldsymbol{E}$, the pressure in the lower-scale porosity P_{p} and the pressure in the higher-scale porosity P_{c}.

The state equations related to level I, are defined, in analogy with Section 5.1.1, under the assumptions of poro-elasticity theory:

$$\boldsymbol{\sigma} = \mathbb{C}_{\mathrm{pm}} : \boldsymbol{\varepsilon} - \boldsymbol{B}_{\mathrm{p}}^{\mathrm{pm}} P_{\mathrm{p}} \tag{5.50a}$$

$$f_{\mathrm{p}} - f_{\mathrm{p}}^{*} = \boldsymbol{B}_{\mathrm{p}}^{\mathrm{pm}} : \boldsymbol{\varepsilon} + \frac{P_{\mathrm{p}}}{N_{\mathrm{pp}}^{\mathrm{pm}}} \tag{5.50b}$$

where $\mathbb{C}_{\mathrm{pm}}$, $\boldsymbol{B}_{\mathrm{p}}^{\mathrm{pm}}$, and $1/N_{\mathrm{pp}}^{\mathrm{pm}}$ are, respectively, the stiffness tensor, the Biot tensor and modulus of the porous matrix, which can be calculated with Equation (5.32), Equation (5.17) and Equation (5.30) considering spherical inclusions. The lower-scale porosity has a volume fraction equal to f_{p} and it is subjected to an uniform pressure P_{p}.

Considering that the stresses are continues at level II, the state equation are derived, by employing Levin's theorem, subdividing the problem in two sub-problems each of them considers the presence of only one loading parameter. The first sub-problem evaluates the system for the case in which both the pressure in the cracks, P_p, and in the spherical pores, P_c, are zero ($L' = L\left(\boldsymbol{E}, 0, 0\right)$). The macroscopic stress $\boldsymbol{\Sigma}$ depends only from the macroscopic uniform strain tensor $\boldsymbol{E}$:

$$\boldsymbol{\Sigma}' = \overline{\boldsymbol{\sigma}'} = \mathbb{C} : \boldsymbol{E} \tag{5.51}$$

The change in porosity, with respect to the undeformed porous matrix, is defined for the first sub-problem as:

$$\left(\phi_\mathrm{p} - \phi_\mathrm{p}^*\right) = \left(1 - \Phi\right) \overline{\left(f_\mathrm{p} - f_\mathrm{p}^*\right)'}^{\mathrm{pm}} = \left(1 - \Phi\right) \boldsymbol{B}_\mathrm{p}^{\mathrm{pm}} : \overline{\boldsymbol{\varepsilon}'}^{\mathrm{pm}} = \boldsymbol{B}_\mathrm{p} : \boldsymbol{E} \tag{5.52a}$$

$$\left(\Phi - \Phi^*\right)' = \boldsymbol{B}_\mathrm{c} : \boldsymbol{E} \tag{5.52b}$$

where the Biot tensor associate to the lower-scale porosity ϕ_p and higher-scale porosity Φ (Equation (5.2)) can be evaluated as a function of the drained stiffness tensor $\mathbb{C}$, considering Equation (5.14):

$$\boldsymbol{B}_\mathrm{p} = \boldsymbol{B}_\mathrm{p}^{\mathrm{pm}} : \mathbb{D}_{\mathrm{pm}} : \mathbb{C} \tag{5.53a}$$

$$\boldsymbol{B}_\mathrm{c} = \boldsymbol{I} + \left(1 - \Phi^*\right) \boldsymbol{I} : \overline{\mathbb{A}}^{\mathrm{pm}} = \boldsymbol{I} - \boldsymbol{I} : \mathbb{D}_{\mathrm{pm}} : \mathbb{C} \tag{5.53b}$$

The second sub-problem is defined as a zero-displacement boundary problem ($L'' = L\left(0, P_\mathrm{p}, P_\mathrm{c}\right)$). The macroscopic stress $\boldsymbol{\Sigma}$ is defined as:

$$\boldsymbol{\Sigma}'' = -\boldsymbol{B}_\mathrm{p} P_\mathrm{p} - \boldsymbol{B}_\mathrm{c} P_\mathrm{c} \tag{5.54}$$

The change in porosity for the second sub-problem results

$$\left(\phi_\mathrm{p} - \phi_\mathrm{p}^*\right)'' = \left(1 - \Phi\right) \left(\boldsymbol{B}_\mathrm{p}^{\mathrm{pm}} : \overline{\boldsymbol{\varepsilon}''}^{\mathrm{pm}} + \frac{P_\mathrm{p}}{N_{\mathrm{pp}}^{\mathrm{pm}}}\right) \tag{5.55a}$$

$$\left(\Phi - \Phi^*\right)'' = \Phi \boldsymbol{I} : \overline{\boldsymbol{\varepsilon}''}^{\mathrm{c}} = -\left(1 - \Phi\right) \boldsymbol{I} : \overline{\boldsymbol{\varepsilon}''}^{\mathrm{pm}} \tag{5.55b}$$

To eliminate from Equation (5.55) the average of the strain over the domain of the porous matrix $\overline{\boldsymbol{\varepsilon}''}^{\mathrm{pm}}$ the stress average rule (Equation (5.12)) is applied:

$$-\boldsymbol{B}_\mathrm{p} P_\mathrm{p} - \boldsymbol{B}_\mathrm{c} P_\mathrm{c} = \left(1 - \Phi\right) \overline{\boldsymbol{\sigma}''}^{\mathrm{pm}} + \Phi \overline{\boldsymbol{\sigma}''}^{\mathrm{c}} \tag{5.56}$$

It results that:

$$\left(1 - \Phi\right) \overline{\boldsymbol{\varepsilon}''}^{\mathrm{pm}} = \mathbb{D}_{\mathrm{pm}} : \left[\left(\left(1 - \Phi\right) \boldsymbol{B}_\mathrm{p}^{\mathrm{pm}} - \boldsymbol{B}_\mathrm{p}\right) P_\mathrm{p} + \left(\Phi \boldsymbol{I} - \boldsymbol{B}_\mathrm{c}\right) P_\mathrm{c}\right] \tag{5.57}$$

Introducing Equation (5.57) in Equation (5.55), it is obtained:

$$\left(\phi_\mathrm{p} - \phi_\mathrm{p}^*\right)'' = \frac{P_\mathrm{p}}{N_{\mathrm{pp}}} + \frac{P_\mathrm{c}}{N_{\mathrm{cp}}} \tag{5.58a}$$

$$(\Phi - \Phi^*)'' = \frac{P_\mathrm{p}}{N_\mathrm{cp}} + \frac{P_\mathrm{c}}{N_\mathrm{cc}} \tag{5.58b}$$

where the Biot moduli are defined as:

$$\frac{1}{N_\mathrm{pp}} = \boldsymbol{B}_\mathrm{p}^\mathrm{pm} : \left[(1-\Phi)\,\boldsymbol{B}_\mathrm{p}^\mathrm{pm} - \boldsymbol{B}_\mathrm{p}\right] + \frac{1-\Phi^*}{N_\mathrm{pp}^\mathrm{pm}} \tag{5.59a}$$

$$\frac{1}{N_\mathrm{pc}} = -\boldsymbol{B}_\mathrm{p}^\mathrm{pm} : \mathbb{D}_\mathrm{pm} : (\boldsymbol{B}_\mathrm{c} - \Phi^* \boldsymbol{I}) \tag{5.59b}$$

$$\frac{1}{N_\mathrm{cp}} = \boldsymbol{I} : \mathbb{D}_\mathrm{pm} : \left[\boldsymbol{B}_\mathrm{p} - (1-\Phi^*)\,\boldsymbol{B}_\mathrm{p}^\mathrm{pm}\right] \tag{5.59c}$$

$$\frac{1}{N_\mathrm{cc}} = (\boldsymbol{B}_\mathrm{c} - \Phi^* \boldsymbol{I}) : \mathbb{D}_\mathrm{pm} : \boldsymbol{I} \tag{5.59d}$$

Applying the superposition of the two problems *the state equations of a two-scale double porosity system* result:

$$\boldsymbol{\Sigma} = \mathbb{C} : \boldsymbol{E} - \boldsymbol{B}_\mathrm{p} P_\mathrm{p} - \boldsymbol{B}_\mathrm{c} P_\mathrm{c} \tag{5.60a}$$

$$\phi_\mathrm{p} - \phi_\mathrm{p}^* = \boldsymbol{B}_\mathrm{p} : \boldsymbol{E} + \frac{P_\mathrm{p}}{N_\mathrm{pp}} + \frac{P_\mathrm{c}}{N_\mathrm{cp}} \tag{5.60b}$$

$$\Phi - \Phi^* = \boldsymbol{B}_\mathrm{c} : \boldsymbol{E} + \frac{P_\mathrm{p}}{N_\mathrm{cp}} + \frac{P_\mathrm{c}}{N_\mathrm{cc}} \tag{5.60c}$$

The damage criterion is evaluated at the crack scale (level II) , accounting for the interaction between the pressure in the pores, P_p, and in the cracks, P_c. It takes the form of Equation (5.44). Following Section 5.1.3, the potential energy density Ψ_pot results:

$$\Psi_\mathrm{pot} = \frac{1}{2}\boldsymbol{E} : \mathbb{C} : \boldsymbol{E} - \frac{1}{2}\left[\left(\frac{1}{N_\mathrm{pp}} + \frac{1}{N_\mathrm{cp}}\right) P_\mathrm{p} + \left(\frac{1}{N_\mathrm{pc}} + \frac{1}{N_\mathrm{cc}}\right) P_\mathrm{c}\right] - (\boldsymbol{B}_\mathrm{p} P_\mathrm{p} + \boldsymbol{B}_\mathrm{c} P_\mathrm{c}) : \boldsymbol{E} \tag{5.61}$$

and the energy release rate G_i of the i-th crack family can thus be derived as:

$$\begin{aligned} G_i = & -\frac{1}{2}\langle \boldsymbol{E} \rangle \frac{\partial \mathbb{C}}{\partial \epsilon_i} : \langle \boldsymbol{E} \rangle + \left(\boldsymbol{B}_\mathrm{p}^\mathrm{m} : \mathbb{D}_\mathrm{pm} : \frac{\partial \mathbb{C}}{\partial \epsilon_i} P_\mathrm{p} - \boldsymbol{I} : \mathbb{D}_\mathrm{pm} : \frac{\partial \mathbb{C}}{\partial \epsilon_i} P_\mathrm{c}\right) : \langle \boldsymbol{E} \rangle + \\ & - \boldsymbol{B}_\mathrm{p}^\mathrm{m} : \mathbb{D}_\mathrm{pm} : \frac{\partial \mathbb{C}}{\partial \epsilon_i} : \mathbb{D}_\mathrm{pm} : \boldsymbol{B}_\mathrm{p}^\mathrm{m} \frac{P_\mathrm{p}^2}{2} - \boldsymbol{I} : \mathbb{D}_\mathrm{pm} : \frac{\partial \mathbb{C}}{\partial \epsilon_i} : \mathbb{D}_\mathrm{pm} : \boldsymbol{I} \frac{P_\mathrm{c}^2}{2} + \\ & + \left(\boldsymbol{B}_\mathrm{p}^\mathrm{m} : \mathbb{D}_\mathrm{pm} : \frac{\partial \mathbb{C}}{\partial \epsilon_i} : \mathbb{D}_\mathrm{pm} : \boldsymbol{I} + \boldsymbol{I} : \mathbb{D}_\mathrm{pm} : \frac{\partial \mathbb{C}}{\partial \epsilon_i} : \mathbb{D}_\mathrm{pm} : \boldsymbol{B}_\mathrm{p}^{I}\right) P_\mathrm{p} P_\mathrm{c} \end{aligned} \tag{5.62}$$

The critical energy release rate G_{ci} is determined with Equation (5.47). The stability of the crack propagation should obey to the criterion of Equation (5.48).

The two-scale double porosity model aims to account for the different pore sizes that are observed in concretes, making the distinction between capillarity pores and C-S-H gel pores. The expansive alkali-silica gel is exerting a pressure in both porosities, thus at both scales; but the damage process is related only to the larger sized capillarity porosity. To understand the importance of this hierarchical structure of concrete with respect to the ASR phenomenon, this model is employed in Chapter 7 to describe the behaviour of ASR-affected concrete under free-expansion condition.

5.2.2 Solidification

Experimental investigations on ASR-affected concrete revealed that the viscoelastic properties of the gel play an important role (Hagelia, 2010; Kawamura and Iwahori, 2004). It can be hypothesized that during the process the gel is changing in phase (Chapter 2) and increasing its mechanical contribution to the overall concrete material behaviour. Furthermore, in structures with major signs of deterioration, expulsion of a dense material was found on their surfaces.

Inspired by the work of Coussy (2005) for freezing materials, a model modification is presented to describe the possible contribution of coexisting fluid and solid gel phases to the overall stiffness of the material. The ASR damage process is simulated by means of two subsequent phenomena: swelling and solidification of the gel. The first process defines the macroscopic expansion of concrete, while the second delays the deterioration. At the beginning, the cracks are saturated by a fluid exerting a pressure P on the material. The concrete is modelled as a one-scale single porosity system and its state equations are described by Equation (5.31). Afterwards, the cracks become partially filled by a solid gel phase, characterized by an elastic modulus Y_{gel}. The i-th crack family is composed by n_{f} pressurized cracks, with volume fraction $\phi_{\text{f}i}$, and n_{s} solidified cracks, with volume fraction $\phi_{\text{s}i}$, where $n = n_{\text{f}} + n_{\text{s}}$ and $\phi_{\text{c}i} = \phi_{\text{f}i} + \phi_{\text{s}i}$. During both processes it is assumed that each family has the same crack radii a, the same volume fraction ϕ_{c} and the same solidification ratio $\rho_{\text{s}} = \phi_{\text{s}}/\phi_{\text{c}}$.

For a certain value of damage a and of solidification ratio ρ_{s}, *the state equations for the solidification model* are:

$$\boldsymbol{\Sigma} = \mathbb{C} : \boldsymbol{E} - \boldsymbol{B}_{\text{f}} P \tag{5.63a}$$

$$\Phi_{\text{f}} - \Phi_{\text{f}}^{*} = \boldsymbol{B}_{\text{f}} : \boldsymbol{E} + \frac{P}{N_{\text{f}}} \tag{5.63b}$$

$$\Phi_{\text{s}} - \Phi_{\text{s}}^{*} = \boldsymbol{B}_{\text{s}} : \boldsymbol{E} \tag{5.63c}$$

where $\Phi_{\mathrm{f}} - \Phi_{\mathrm{f}}^{*}$ and $\Phi_{\mathrm{s}} - \Phi_{\mathrm{s}}^{*}$ are, respectively, the elastic deformations of the total pressurized and solidified porosities:

$$\Phi_{\mathrm{f}} = \sum_{i=1}^{m} \phi_{\mathrm{f}i} = \frac{4}{3}\pi \sum_{i=1}^{m} \left(1 - \rho_{\mathrm{s}i}\right) c_i n_{\mathrm{f}i} a_i^2 \tag{5.64a}$$

$$\Phi_{\mathrm{s}} = \sum_{i=1}^{m} \phi_{\mathrm{s}i} = \frac{4}{3}\pi \sum_{i=1}^{m} \rho_{\mathrm{s}i} c_i n_{\mathrm{s}i} a_i^2 \tag{5.64b}$$

The overall stiffness tensor $\mathbb{C}$ is evaluated with Equation (5.32), but now accounting for the stiffness of the solid gel phase ($\mathbb{C}_{\mathrm{f}i} = \mathbb{O}$ and $\mathbb{C}_{\mathrm{s}i} = \mathbb{C}_{\mathrm{gel}}$):

$$\mathbb{C} = \mathbb{C}_{\mathrm{m}} : \left(\mathbb{I} - \sum_{i=1}^{m} \phi_{\mathrm{f}i} \mathbb{A}_{\mathrm{f}i}\right) + \sum_{i=1}^{m} \phi_{\mathrm{s}i} \left(\mathbb{C}_{\mathrm{gel}} - \mathbb{C}_{\mathrm{m}}\right) : \mathbb{A}_{\mathrm{s}i} \tag{5.65}$$

where $\mathbb{A}_{\mathrm{f}i}$ and $\mathbb{A}_{\mathrm{s}i}$ are evaluated with Equation (5.33) adopting:

$$\mathbb{T}_{\mathrm{f}i} = \left(\mathbb{I} - \mathbb{S}_{\mathrm{f}i}\right)^{-1} \tag{5.66a}$$

$$\mathbb{T}_{\mathrm{s}i} = \left[\mathbb{I} + \mathbb{S}_{\mathrm{s}i} : \mathbb{D}_{\mathrm{m}} : \left(\mathbb{C}_{\mathrm{gel}} - \mathbb{C}_{\mathrm{m}}\right)\right]^{-1} \tag{5.66b}$$

The Biot tensors, $\boldsymbol{B}_{\mathrm{f}}$ and $\boldsymbol{B}_{\mathrm{s}}$, and modulus, $1/N_{\mathrm{f}}$, are evaluated as a function of the strain concentration tensor (Equation (5.16), Equation (5.30)):

$$\boldsymbol{B}_{\mathrm{j}} = \sum_{i=1}^{m} \phi_{\mathrm{j}i} \boldsymbol{I} : \mathbb{A}_{\mathrm{j}i} \quad \text{with} \quad \mathrm{j} = \mathrm{f}, \mathrm{s} \tag{5.67a}$$

$$\frac{1}{N_{\mathrm{f}}} = \left(\boldsymbol{B}_{\mathrm{f}} - \Phi_{\mathrm{f}}^{*} \boldsymbol{I}\right) : \mathbb{D}_{\mathrm{m}} : \boldsymbol{I} \tag{5.67b}$$

The damage evolution of the i-th family is governed by the energy release rate G_i and its critical value $G_{\mathrm{c}i}$, which are evaluated by Equation (5.45) and Equation (5.47), respectively.

Considering a porous medium, subjected to an internal pressure P in which the empty cracks are transformed in solid inclusions, an incremental formulation is needed to evaluate the state equations. In absence of external loading ($\boldsymbol{\Sigma} = 0$, $P > 0$), the total macroscopic strain $\boldsymbol{E} = \boldsymbol{E}^{P} = \mathbb{D} : \boldsymbol{B} P$, corresponding to a crack radius $a + \delta a$ and volume fraction of solidified cracks $\Phi_{\mathrm{s}} + \delta\Phi_{\mathrm{s}}$, can be defined as:

$$\begin{aligned} \boldsymbol{E}_{a+\delta a}^{\Phi_{\mathrm{s}}+\delta\Phi_{\mathrm{s}}} &= \left(\mathbb{D}_a^{\Phi_{\mathrm{s}}} + \delta\mathbb{D}\right) : \left(\boldsymbol{B}_a^{\Phi_{\mathrm{s}}} + \delta\boldsymbol{B}\right) \left(P_a + \delta P\right) + \\ &\quad - \underbrace{\left[\delta\mathbb{D}_a^{\delta\Phi_{\mathrm{s}}} : \boldsymbol{B}_a^{\Phi_{\mathrm{s}}} + \delta\boldsymbol{B}_a^{\delta\Phi_{\mathrm{s}}} : \left(\mathbb{D}_a^{\Phi_{\mathrm{s}}} + \delta\mathbb{D}_a^{\delta\Phi_{\mathrm{s}}}\right)\right] P_a}_{\delta\boldsymbol{E}^{*}} = \\ &= \mathbb{D}_a^{\Phi_{\mathrm{s}}} : \boldsymbol{B}_a^{\Phi_{\mathrm{s}}} P_a + \delta\widehat{\boldsymbol{E}} - \delta\boldsymbol{E}^{*} = \boldsymbol{E}_a^{\Phi_{\mathrm{s}}} + \delta\widehat{\boldsymbol{E}} - \delta\boldsymbol{E}^{*} \end{aligned} \tag{5.68}$$

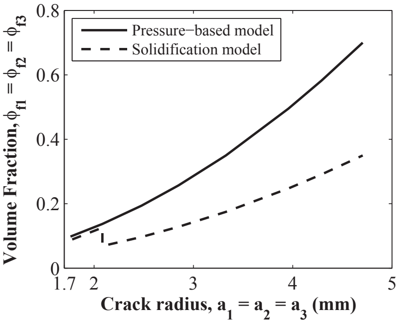

Figure 5.3: Comparison between pressure-based and solidification model: Evolution of pressurized cracks' space, ϕ_f assuming an instantaneous solidification with ratio $\rho_\mathrm{s} = 0.5$.

where $\mathbb{D}_a^{\Phi_\mathrm{s}}$ and $\boldsymbol{B}_a^{\Phi_\mathrm{s}}$ are the compliance and Biot tensors of the overall material in the previous stage (a and Φ_s), while $\delta\mathbb{D}$ and $\delta\boldsymbol{B}$ are their increments due to solidification and cracking processes, which are defined as:

$$\begin{aligned}\delta\mathbb{D} &= \left(\mathbb{D}_a^{\Phi_\mathrm{s}+\delta\Phi_\mathrm{s}} - \mathbb{D}_a^{\Phi_\mathrm{s}}\right) + \left(\mathbb{D}_{a+\delta a}^{\Phi_\mathrm{s}+\delta\Phi_\mathrm{s}} - \mathbb{D}_a^{\Phi_\mathrm{s}+\delta\Phi_\mathrm{s}}\right) = \\ &= \delta\mathbb{D}_a^{\delta\Phi_\mathrm{s}} + \delta\mathbb{D}_{\delta a}^{\Phi_\mathrm{s}+\delta\Phi_\mathrm{s}}\end{aligned} \tag{5.69a}$$

$$\begin{aligned}\delta\boldsymbol{B} &= \left(\boldsymbol{B}_a^{\Phi_\mathrm{s}+\delta\Phi_\mathrm{s}} - \boldsymbol{B}_a^{\Phi_\mathrm{s}}\right) + \left(\boldsymbol{B}_{a+\delta a}^{\Phi_\mathrm{s}+\delta\Phi_\mathrm{s}} - \boldsymbol{B}_a^{\Phi_\mathrm{s}+\delta\Phi_\mathrm{s}}\right) = \\ &= \delta\boldsymbol{B}_a^{\delta\Phi_\mathrm{s}} + \delta\boldsymbol{B}_{\delta a}^{\Phi_\mathrm{s}+\delta\Phi_\mathrm{s}}\end{aligned} \tag{5.69b}$$

The strain increment is denoted by $\delta\widehat{\boldsymbol{E}} - \delta\boldsymbol{E}^*$, where the strain $\delta\boldsymbol{E}^*$ refers only to the stiffening effect due to the solid inclusions. The strain $\delta\boldsymbol{E}^*$ is introduced because the solidification is assumed as a strain-free process:

$$\boldsymbol{E}_a^{\Phi_\mathrm{s}+\delta\Phi_\mathrm{s}} := \boldsymbol{E}_a^{\Phi_\mathrm{s}} := \boldsymbol{E}_a^{\Phi_\mathrm{s}=0} \tag{5.70}$$

Figure 5.3 illustrates the evolution of pressurized cracks space ϕ_f as a function of the resulting crack radius a, for the pressure-based model, described in Section 5.1, and the solidification model. In the former case, the entire porosity results pressurized ($\Phi_\mathrm{f} = \Phi$). In the latter case, an instantaneous solidification ($\rho_\mathrm{s} = 0.5$) is assumed at the moment the crack radius reaches an (arbitrary) value of $a = 2.08$ mm.

Like for the two-scale double porosity model presented in the previous section, the solidification model is explored in Chapter 7 to study the relation between expansion and damage process.

5.3 Concluding Remarks

To understand the deteriorating impact of ASR on concrete, in this chapter a multiscale material model, which evaluates the interaction of the phenomenon between aggregate and concrete level, is presented. The micro-poro-fracture-mechanical approach follows the theory developed by Dormieux et al. (2006) and has been inspired by the work of Lemarchand et al. (2005), Charpin and Ehrlacher (2012) and partially by Mazars (1986).

The concrete is modelled as a porous medium composed by cracks embedded in a solid matrix, formed by aggregates and cement paste. The expansive alkali-silica gel is considered as a fluid saturating the pore space. Its mechanical effect is translated in a macroscopic uniform pressure P, which together with the macroscopic uniform imposed strain $\boldsymbol{E}$ defines the loading parameters of the system. A linear elastic behaviour of the solid matrix is assumed. The state equation of the problem can be derived taking advantage of the poro-elasticity theory, while the damage criterion is formulated in agreement with linear fracture mechanics approach. The overall properties of concrete are determined adopting the analytical Mori-Tanaka homogenization method.

Considering that the interaction between the reaction products of the ASR and the micro-structure of concrete is relevant for the overall response of the material and of the structure, model modifications, which account for more complex definition of the problem, are presented. First, a modification including the hierarchical pore structure of concrete is considered, by adopting a two-scale double porosity model. The crack propagation at higher scale is developed in a porous matrix, which is composed by the solid matrix and a lower-scale porosity. Secondly, the evolution in phase of the ASR products is accounted, considering coexisting fluid and the solid gel phases. A solidification model is developed on the base of a one-scale single porosity system.

The multiscale material model results in a three-dimensional smeared approach based on a micro-mechanical elastic damage formulation. Two extensions are foreseen. First, a kinetic formulation can be introduced to link the expansive pressure to the gel production and appropriate relationship can be adopt to describe the flux of the gel into the porosity space. Second, due to the analytical solution of the model and the definition of macroscopic loading parameters, the model can be either implemented in a displacement-based finite element framework or adopted as a complementary tool to derive the evolution of mechanical characteristics as a function of concrete expansion.

Model Validation for Unaffected Concrete

6

In the previous chapter the proposed multiscale material model, which aims to describe the concrete behaviour on the basis of micro-mechanical quantities at aggregate level, was introduced by presenting the fundamental state equations, the homogenization approach and the damage propagation criterion. In this chapter the model is validated for the case of unaffected concrete, which is considered as a drained porous medium, subject to external mechanical boundary conditions.

First, the solution of the model is presented for the case of uniaxial and biaxial loading conditions (Section 6.1). Second, the attention is focused on the determination of the initial parameters, limited in number, which are divided in input and calibrated parameters (Section 6.2). Input parameters (e.g. the initial porosity) are directly established by macroscopic to microscopic experimental investigations (e.g. the porosity measurements) or by known correlations (e.g. the Power's law for porosity vs. W/C ratio and hydration degree of concrete). Calibrated parameters (e.g. the microscopic fracture energy) are derived from the macroscopic mechanical properties of undamaged concrete. The simulation of uniaxial tensile and compressive tests (Section 6.3) are followed by a concise sensitive study (Section 6.4). Eventually, the behaviour of concrete under biaxial stress state is investigated (Section 6.5). The performances of the model result satisfactory within the adopted linear elastic approach (Section 6.6).

The validation of the model will be continued in Chapter 7 to determine the deteriorating impact of ASR on concrete, by simulating free-expansion tests and subsequent uniaxial loading tests.

6.1 Uniaxial and Biaxial Loading

In the framework of the micro-poro-fracture-mechanical model described in Section 5.1, the unaffected concrete is modelled as a drained material ($P = 0$) subjected to a macroscopic uniform imposed strain $\boldsymbol{E} = \boldsymbol{E}^{\text{applied}}$. The state equations (Equation (5.31)) can then be reduced to:

$$\boldsymbol{\Sigma} = \mathbb{C} : \boldsymbol{E} \tag{6.1a}$$

$$\Phi - \Phi^{*} = \boldsymbol{B} : \boldsymbol{E} \tag{6.1b}$$

The damage criterion for the i-th crack family takes the form (Equation (5.44)):

$$G_i - G_{\text{c}i} \leq 0; \quad \dot{\epsilon_i} \geq 0; \quad (G_i - G_{\text{c}i})\, \dot{\epsilon_i} = 0 \tag{6.2}$$

where the energy release rate G_i (Equation (5.45)) reads:

$$G_i\left(\boldsymbol{E}, P = 0, \epsilon_i\right) = -\frac{1}{2}\langle \boldsymbol{E} \rangle : \frac{\partial \mathbb{C}}{\partial \epsilon_i} : \langle \boldsymbol{E} \rangle \tag{6.3}$$

with $\langle \boldsymbol{E}' \rangle = \langle \boldsymbol{E} \rangle$ the positive part of the macroscopic effective strain tensor $\boldsymbol{E}'$ which in this case is equal to the macroscopic strain tensor $\boldsymbol{E}$. The critical energy release rate $G_{\text{c}i}$ is evaluated by Equation (5.47):

$$G_{\text{c}i}\left(\epsilon_i\right) = \frac{2\pi}{3} g_{\text{f}} \left(\frac{n_i}{\epsilon_i}\right)^{1/3} = \frac{2\pi}{3} \frac{g_{\text{f}}}{a_i} \tag{6.4}$$

To solve the state equations in a general manner, two orthogonal coordinate systems are defined: the global coordinate system (123) aligned with the normal axes of the three crack families and the loading coordinate system (xyz) defining the normal loading directions. A direct correspondence exists between the two coordinate systems that are superimposed (e.g. x → 1, y → 2, z → 3). Moreover, the x-axis is defined as the one where the highest (in absolute sense) load is occurring. The components of the macroscopic strain tensor $\boldsymbol{E}$ can be associated to the strain in this direction E_{xx}:

$$\boldsymbol{E} = \boldsymbol{\alpha} E_{\text{xx}} \tag{6.5}$$

where $\boldsymbol{\alpha}$ is the strain coefficient tensor, with non-zero components:

$$\alpha_{\text{xx}} = 1; \quad \alpha_{\text{yy}} = \frac{E_{\text{yy}}}{E_{\text{xx}}}; \quad \alpha_{\text{zz}} = \frac{E_{\text{zz}}}{E_{\text{xx}}} \tag{6.6}$$

and E_{yy} and E_{zz} denote the strain components along the y- and z-axis. A similar relationship links the macroscopic stress components, which read:

$$\boldsymbol{\Sigma} = \boldsymbol{\beta} \Sigma_{\text{xx}} \tag{6.7}$$

where $\boldsymbol{\beta}$ is the stress coefficient tensor, with non-zero components:

$$\beta_{\mathrm{xx}} = 1; \quad \beta_{\mathrm{yy}} = \frac{\Sigma_{\mathrm{yy}}}{\Sigma_{\mathrm{xx}}}; \quad \beta_{\mathrm{zz}} = \frac{\Sigma_{\mathrm{zz}}}{\Sigma_{\mathrm{xx}}} \tag{6.8}$$

The first state equation can thus be written as:

$$\boldsymbol{\beta}\Sigma_{\mathrm{xx}} = \mathbb{C} : \boldsymbol{\alpha} E_{\mathrm{xx}} \tag{6.9}$$

For the considered uniaxial and biaxial loading cases the stress coefficient tensor $\boldsymbol{\beta}$ is supposed to be known.

A direct method can be derived to solve the damage propagation problems for drained porous media subjected to uniaxial and biaxial loading, in which porosity is composed by three orthogonal crack families. First, the crack family which is propagating should be identified. Second, an (arbitrary) increment in crack damage variable $\delta\epsilon$ is applied and the new stress and strain states are determined.

Considering the reference configuration characterized by the set of crack density variables ϵ_1^* ϵ_2^* and ϵ_3^*, the critical k-th family can be identified by the one which propagate for the lowest value of the larger macroscopic strain component E_{xx}. Not accounting for the nucleation and opening/closing of the cracks, the evolution of the crack density variables ϵ corresponds to the evolution of the crack radii a (Section 5.1). Applying an unit stress along the x-axis $\Sigma_{\mathrm{xx}}^{\mathrm{unit}} = 1$, the macroscopic unit stress tensor $\boldsymbol{\Sigma}^{\mathrm{unit}}$ is determined via the known stress coefficient tensor $\boldsymbol{\beta}$ (Equation (6.7)), which depends from the specific imposed boundary conditions. The corresponding macroscopic strain tensor $\boldsymbol{E}^{\mathrm{unit}}$ is evaluated with Equation (6.9):

$$\boldsymbol{E}^{\mathrm{unit}} = \mathbb{D}^* : \boldsymbol{\Sigma}^{\mathrm{unit}} \tag{6.10}$$

where $\mathbb{D}^* = (\mathbb{C}^*)^{-1}$ is the compliance tensor evaluated for the reference configuration, which depends from the elastic constants of the solid matrix, Y_{m} and ν_{m}, the aspect ratio X_i^* and the volume fraction $\phi_{\mathrm{c,i}}^*$ of the three crack families (Equation (5.35)). To identify the critical k-th family, the critical macroscopic strain tensors $\boldsymbol{E}^{\mathrm{cr},1}$, $\boldsymbol{E}^{\mathrm{cr},2}$ and $\boldsymbol{E}^{\mathrm{cr},3}$, which leads to the propagation of each crack family, are calculated imposing that the energy release rate is equal to its threshold value (Equation (6.3) and Equation (6.4)):

$$-\frac{1}{2}\langle\boldsymbol{\alpha}\rangle\frac{\partial\mathbb{C}^*}{\partial\epsilon_i^*}\langle\boldsymbol{\alpha}\rangle|E_{\mathrm{xx}}^{\mathrm{cr},i}|^2 := \frac{2}{3}\pi\frac{g_{\mathrm{f}}}{a_i^*} \tag{6.11}$$

where $E_{\mathrm{xx}}^{\mathrm{cr},i}$ is the larger component (in absolute sense) of the critical macroscopic strain $\boldsymbol{E}^{\mathrm{cr},i}$ which leads to the propagation of the i-th family. The positive part of the strain coefficient tensor $\langle\boldsymbol{\alpha}\rangle$ is defined similarly as the positive part of the macroscopic unit strain tensor $\langle\boldsymbol{E}^{\mathrm{unit}}\rangle$. It correlates the positive part of the macroscopic imposed strain tensor $\langle \boldsymbol{E} \rangle$ to the absolute value of its larger component $|E_{\mathrm{xx}}|$:

$$\langle \boldsymbol{E} \rangle = \langle \boldsymbol{\alpha} \rangle |E_{\mathrm{xx}}| \tag{6.12}$$

Considering in absolute sense the minimum value of the largest component of the critical strain, the k-th direction of damage propagation can be identified:

$$|E_{\mathrm{xx}}^{\mathrm{cr},k}| = \min \left\{ |E_{\mathrm{xx}}^{\mathrm{cr},1}|, |E_{\mathrm{xx}}^{\mathrm{cr},2}|, |E_{\mathrm{xx}}^{\mathrm{cr},3}| \right\} \tag{6.13}$$

After the identification of the critical k-th family, the analysis is continued by imposing the (arbitrary) increment in crack density variable:

$$\begin{cases} \epsilon_i = \epsilon_i^* + \delta\epsilon & i = k \\ \epsilon_i = \epsilon_i^* & i \neq k \end{cases} \tag{6.14}$$

The macroscopic strain $\boldsymbol{E}$, which is calculated with Equation (6.5), has as larger component $E_{\mathrm{xx}} = E_{\mathrm{xx}}^{\mathrm{cr},k}$ and it is proportion to the coefficient tensor $\boldsymbol{\alpha}$. The macroscopic stress tensor $\boldsymbol{\Sigma}$ is calculated with Equation (6.9), which accounts for stiffness tensor evaluated in the current damage situation.

In conclusion, the analysis of a drained porous medium subjected to uniaxial and biaxial loading, which pore space is composed by three orthogonal crack families aligned within the loading coordinate system, can be directly solved thanks to the relationship between normal components of the strain/stress tensor. The method results in a sequence of linear analyses. A similar method has been advised for analyses at structural level (De Jong et al., 2009).

6.2 Input and Calibrated Parameters

The model is based on a limited number of initial variables, divided in input and calibrated parameters, which define the initial micro-structure of the concrete, the elastic constants of each phase and the fracture properties (Figure 6.1).

The input parameters can be classified in three categories, which are related to: the mechanical properties of undamaged concrete (Y_{in}, $f_{\mathrm{t,in}}$), the elastic constants of the solid matrix (Y_{m}, ν_{m}) function of the cement paste and aggregates' characteristics (Y_{cem}, Y_{agg}, $\nu_{\mathrm{cem}} = \nu_{\mathrm{agg}}$, ϕ_{agg}) and the initial status of the cracks (Φ_{in}, c). They can be determined by macro and microscopic investigation or considering well-known properties correlation (e.g. Power's law for the determination of the capillarity porosity from W/C ratio and hydration degree or Eurocode 2 formulas for correlation between 28-day mechanical properties).

A two-step calibration procedure (Figure 6.1) is adopted to determine the initial aspect ratio of the cracks X_{in} and the microscopic fracture energy g_{f} on the basis of the macroscopic stiffness Y_{in} and tensile strength $f_{\mathrm{t,in}}$ of undamaged

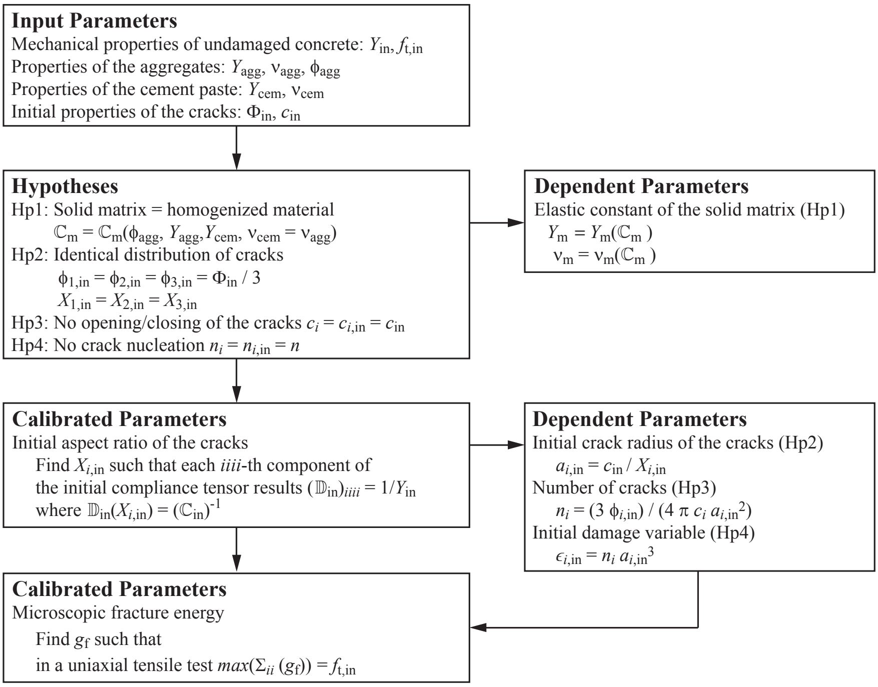

Figure 6.1: Input, calibrated and dependent parameters of the model.

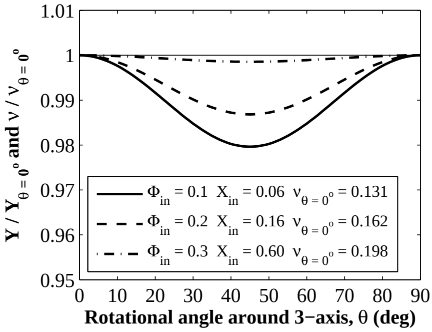

Figure 6.2: Variation of the elastic modulus Y and Poisson ratio ν in the 1-2 plane for different combination of initial volume fraction of the cracks Φ_{in} and initial aspect ratio X_{in} calibrated against $Y_{\text{in}} = 36.3$ GPa. The angles $\theta = 0^o$ and $\theta = 90^o$ identify the 1- and 2-axis, respectively.

Table 6.1: Input parameters for the simulation of uniaxial loading tests.

Property	Value	Unit
Input parameters		
Concrete Young's modulus, Y_{in}	36.3*	GPa
Concrete tensile strength, $f_{\text{t,in}}$	2.97*	MPa
Young's modulus of cement paste, Y_{cem}	43.3	GPa
Young's modulus of aggregates, Y_{agg}	86.5	GPa
Poisson ratio, $\nu_{\text{cem}} = \nu_{\text{agg}}$	0.200	
Volume fraction of aggregate, ϕ_{agg}	0.680	
Initial volume fraction of cracks, $\Phi_{\text{in}} = 3\phi_{ci,\text{in}}$	0.098	
Crack thickness, c_i $(i = 1, 2, 3)$	0.100	mm
Calibrated parameters		
Initial aspect ratio, $X_{i,\text{in}}$ $(i = 1, 2, 3)$	0.057	
Microscopic fracture energy, g_{f}	$3.48\ 10^{-4}$	N/mm
Dependent parameters		
Young's modulus of solid matrix, Y_{m}	68.6	GPa
Poisson ratio of solid matrix, ν_{m}	0.200	
No. of cracks n_i $(i = 1, 2, 3)$	0.025	mm^{-3}
Initial crack radius, $a_{i,\text{in}}$ $(i = 1, 2, 3)$	1.762	mm
Initial crack density, $\epsilon_{i,\text{in}}$ $(i = 1, 2, 3)$	0.138	

* calculated from 28-day cubic compressive strength (Eurocode 2, 2005).

concrete, respectively. A uniform initial distribution of the cracks is assumed for the undamaged concrete, imposing that the three orthogonal crack families have identical initial radii ($a_{\text{in}} = a_{1,\text{in}} = a_{2,\text{in}} = a_{3,\text{in}}$ and $c = c_1 = c_2 = c_3$) and volume fractions ($\phi_{\text{c,in}} = \phi_{\text{c1,in}} = \phi_{\text{c2,in}} = \phi_{\text{c3,in}}$). The cracks are embedded in the solid matrix, which is an isotropic medium due to the modelling of the aggregates as spherical inclusions. As a consequence, the elastic modulus of concrete is equal in the three global directions ($Y_{11} = Y_{22} = Y_{33}$) and it can be associated to the one of the undamaged concrete Y_{in}. As a results, it can be adopted to calibrate the initial aspect ratio X_{in} of the cracks. The crack radius a_{in} and the number of cracks per unit of volume n can be calculated by Equation (5.1). The initial damage state ϵ_{in} is defined by Equation (5.41). Figure 6.2 shows the variation of the elastic modulus Y and of the Poisson ratio ν in the 1-2 plane, as a function of the angular coordinate θ for different combination of initial aspect ratio X_{in} and volume fraction Φ_{in} of the cracks, all leading to the same initial macroscopic stiffness Y_{in} in the global directions. The overall material can be macroscopically considered as nearly isotropic, with negligible variations of its elastic constants (up to 2 %).

After the determination of the initial micro-structure, the microscopic fracture energy g_{f} is derived by imposing that the cracks of the i-th family, with initial radius $a_{i,\text{in}}$, will propagate in a uniaxial tensile test, for a macroscopic stress equal to the tensile strength of undamaged concrete $f_{\mathrm{t,in}}$:

$$G_i\left(\boldsymbol{E}^{\mathrm{cr,in}} = \mathbb{D}_{\mathrm{in}} : \boldsymbol{\Sigma}^{\mathrm{cr,in}}, P = 0, \epsilon_i = \epsilon_{i,\mathrm{in}}\right) := G_{\mathrm{c}i}\left(\epsilon_i = \epsilon_{i,\mathrm{in}}, g_{\mathrm{f}}\right) \tag{6.15}$$

where $\mathbb{D}_{\mathrm{in}}$ is the compliance tensor for the initial damage state, $\boldsymbol{E}^{\mathrm{cr,in}}$ and $\boldsymbol{\Sigma}^{\mathrm{cr,in}}$ are the critical strain and stress tensors for the initial set of crack density variables ϵ_{in}, respectively. The critical stress tensor $\boldsymbol{\Sigma}^{\mathrm{cr,in}}$ has only one non-zero component that is $\Sigma_{ii}^{\mathrm{cr,in}} = f_{\mathrm{t,in}}$ and it is imposed equal for all the families. Being the initial damage variables identical ($\epsilon_{\mathrm{in},1} = \epsilon_{\mathrm{in},2} = \epsilon_{\mathrm{in},3}$), the critical strain tensor $\boldsymbol{E}^{\mathrm{cr,in}}$ results the same in each global direction. As a consequence, the microscopic fracture energy g_{f} and the fracture properties are nearly isotropically distributed in the concrete.

Table 6.1 lists the input and calibrated parameters of the model evaluated for the reactive mix RR2 studied in Chapter 4. The elastic modulus Y_{in} and tensile strength $f_{\mathrm{t,in}}$ of the undamaged RR2 concrete are calculated from 28-day cubic compressive strength (Eurocode 2, 2005), as reported in Table 4.3. The aggregate elastic modulus Y_{agg} has been determined by nano-indentation test (Anaç, 2013), while the one of the cement paste Y_{cem} has been chosen twice smaller. For both phases, the Poisson ratio $\nu_{\mathrm{cem}} = \nu_{\mathrm{agg}}$ is equal to 0.20. The volume fraction of the aggregates ϕ_{agg} is determined by mixture proportion (Table 4.1). The radius of the cracks in the thickness direction c is assumed constant and equal to 0.10 mm. The total initial volume fraction of the cracks is arbitrary set to 70% of the capillarity porosity calculated by the Power's law ($\Phi_{\mathrm{in}} = 0.70\,\Phi_{\mathrm{in}}^{\mathrm{Power}}$), considering that not all the capillary pores contribute to the damage.

6

6.3 Simulation of Uniaxial Loading Tests

Figure 6.3 shows the modelled non-linear behaviour of concrete subjected to external uniaxial tensile or compressive loading. The load is applied along the x-axis, which here corresponds with the 3-axis in the global coordinate system (x → 3). The model results are compared with the analytical formulations proposed by the Model Codes (CEB-FIP, 1993, 2011), which are based on a statistically large number of experimental tests.

In the case of tension loading along the 3-axis (Figure 6.3a), a softening curve is obtained which resembles the so-called exponential softening curve, frequentlly used in numerical models of concrete at structural level. The damage propagation starts after the maximum load is achieved (Figure 6.3c); only the cracks perpendicular to the load direction are propagating ($a_3 > a_{\mathrm{in}}$, $a_1 = a_2 = a_{\mathrm{in}}$). The damage evolution results stable (Figure 6.3e), indicated by the negative stability coefficient s of the propagating cracks (Equation (5.48)). The peak stress is retrieved equal to the tensile strength of undamaged concrete $f_{\mathrm{t,in}}$ as

Table 6.2: Non-linear behaviour of unaffected concrete under uniaxial loading.

Property	Value	Unit
Concrete properties		
Concrete compressive strength, $f_{\mathrm{c,in}}$	53.21*	MPa
Concrete Young's modulus, Y_{in}	36.3*	GPa
Concrete tensile strength, $f_{\mathrm{t,in}}$	2.97*	MPa
Maximum aggregate diameter, d_{max}	22.00	mm
Calculated values using code standards		
Macroscopic fracture energy		
$G_{\mathrm{f}} = 0.041(f_{\mathrm{c,in}}/10)^{0.7}$	0.131	N/mm
$G_{\mathrm{f}} = 0.073 f_{\mathrm{c,in}}^{0.18}$	0.149	N/mm
Obtained values from the simulation		
Tensile behaviour		
$A_{\mathrm{t}} = \int\limits_0^\infty \Sigma_{33} dE_{33}$	2.33 10^{-3}	MPa
$G_{\mathrm{f}} = 3 d_{\mathrm{max}} A_{\mathrm{t}}$	0.154	N/mm
Compressive behaviour		
$f_{\mathrm{c}} = \lvert\Sigma_{33}^{\mathrm{peak}}\rvert$	53.29	MPa
$\lvert\Sigma_{33}^{\mathrm{prop}}\rvert$	19.66	MPa
$\lvert\Sigma_{33}^{\mathrm{prop}}\rvert/\lvert\Sigma_{33}^{\mathrm{peak}}\rvert$	0.36	
$A_{\mathrm{c}} = \int\limits_0^\infty \Sigma_{33} dE_{33}$	1.96 10^{-1}	MPa
$A_{\mathrm{c}}/A_{\mathrm{t}}$	84.36	

* calculated from 28-day cubic compressive strength (Eurocode 2, 2005).

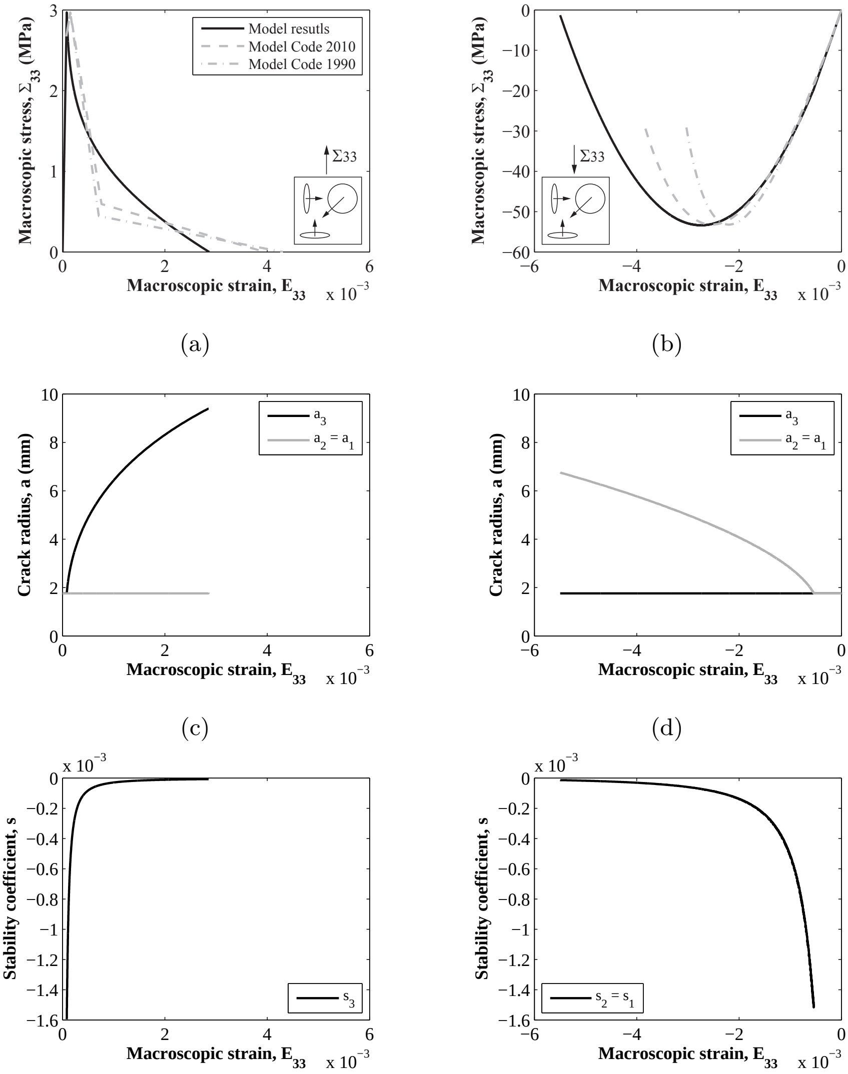

(a) (b)

(c) (d)

(e) (f)

Figure 6.3: Unaffected concrete under uniaxial tensile and compressive loading: (a)-(b) Stress-strain relationship ($\Sigma_{33} - E_{33}$), (c)-(d) Crack propagation, (e)-(f) Stability analysis ($s < 0$).

imposed by the calibration of the microscopic fracture energy g_f (Section 6.2). The macroscopic fracture energy G_f can be estimated, from the simulation, calculating the area underneath the stress-strain curve A_t. Considering that the model represents the behaviour of concrete in the fracture zone, the area A_t is multiplied by three times the maximum aggregate size d_max (Bažant and Oh, 1983), as reported in Table 6.2. The resulting macroscopic fracture energy G_f is close to the estimation provided by the Model Codes (CEB-FIP, 1993, 2011).

In the case of compressive loading along the 3-axis (Figure 6.3a), a stiffening-softening relation is obtained which resembles the well-know parabolic softening curves, prescribed by codes and frequently used in numerical models of concrete at structural level. The cracks are now developing in the two planes perpendicular to the load direction ($a_3 = a_\mathrm{in}$, $a_1 = a_2 > a_\mathrm{in}$); due to the identical initial shape of the cracks, the propagation is similar for the first two families (Figure 6.3d). Figure 6.3e shows the stability of the cracking process. The damage propagation starts at a stress $\Sigma_{33}^\mathrm{prop} = -19.66$ MPa (Table 6.2). The obtained peak stress $\Sigma_{33}^\mathrm{peak} = -53.29$ MPa is close to the compressive strength of concrete. The ratio $\Sigma_{33}^\mathrm{prop}/\Sigma_{33}^\mathrm{peak} = 0.36$ is close to the ratio 1/3 proposed by the Model Codes (CEB-FIP, 1993, 2011). The obtained results in terms of stress-strain curve, are in good agreement with the relationships proposed by the Model Codes (CEB-FIP, 1993, 2011).

Figure 6.4 validates the hypothesis formulated in Section 5.1.3, which assumes that only the positive part of the effective strain $\langle \boldsymbol{E} \rangle$ is controlling the damage evolution (Equation (6.3)). In fact, excluding this assumption the hardening/softening stress-strain relationship in compressive cannot be captured, resulting in the same degradation behaviour observed for tension loading.

In conclusion, the model is able to approximate the known stress-strain relationship of concrete under tensile and compressive loading, with a limited number of input parameters. It is noted that only the elastic branch in tension is a direct result of calibration. The non-linear softening curve in tension and the entire curve in compression are a direct result of the model. The analytical relations have been derived from a large number of experimental campaigns and are worldwide recognized by the scientific community. This proves the validity of the model's hypothesis as well as the calibration procedure.

6.4 Parametric Study

To evaluate the influence of the model input parameters, which are related to the macroscopic properties of undamaged concrete (Y_in, $f_\mathrm{t,in}$), to the solid matrix (Y_cem, Y_agg, $\nu_\mathrm{cem} = \nu_\mathrm{agg}$, ϕ_agg) and to the initial status of cracks (Φ_in, c), a concise sensitivity study is presented.

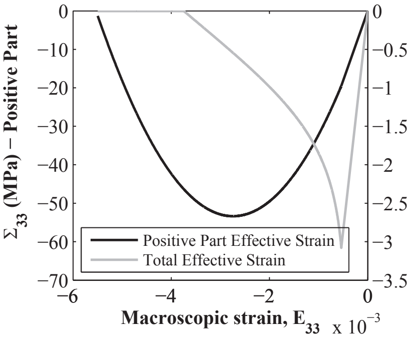

Figure 6.4: Unaffected concrete under uniaxial compressive loading: Effect of the positive part of the macroscopic effective strain $\langle \boldsymbol{E}' \rangle$ as driver for the damage propagation.

The macroscopic properties of undamaged concrete (Y_{in}, $f_{\text{t,in}}$) and the volume fraction of aggregates (ϕ_{agg}) are considered as known and fixed for the analysed case. A parametric study is performed on the remaining variables varying them one by one (Figure 6.5). Each time the calibration procedure is repeated.

The solid matrix is defined by the aggregates embedded in the cement paste. Its properties remain constant during the damage evolution. Thus, rather than the properties of aggregate and cement paste, the elastic constants of the solid matrix are relevant. Its mechanical properties (Y_{m}, ν_{m}) are related to: the volume fraction of the aggregates ϕ_{agg}, the elastic modulus of the cement paste Y_{cem}, the elastic modulus of the aggregates Y_{agg} and the Poisson ratios of both phases $\nu_{\text{cem}} = \nu_{\text{agg}}$. Knowing the amount of aggregates by mix design, the ratio between the elastic moduli of each phase $Y_{\text{cem}}/Y_{\text{agg}}$ and their Poisson ratio $\nu_{\text{cem}} = \nu_{\text{agg}}$ define the stiffness tensor of the solid matrix $\mathbb{C}_{\text{m}}$.

Figure 6.5a and Figure 6.5b present the sensitivity of the model with respect to the ratio between the elastic moduli of cement paste and aggregates $Y_{\text{cem}}/Y_{\text{agg}}$ by varying Y_{cem}. The higher is this ratio, the stiffer is the solid matrix. As a consequence, the calibration against the macroscopic stiffness Y_{in} leads to more elongated penny-shaped initial cracks ($a_{\text{in}} \gg c$). The calibration against the macroscopic strength $f_{\text{t,in}}$ leads to a higher microscopic fracture energy g_{f} (Figure 6.5a). The resulting non-linear behaviour of concrete is strongly affected by the elastic modulus of the solid matrix (Figure 6.5b). In the case of tension loading, the ultimate strain, and consequentially the macroscopic fracture energy G_{f}, results higher for a stiffer solid matrix. In the case of compressive loading, a substantial variation is observed. For a stiffer solid matrix, the cracks propagate

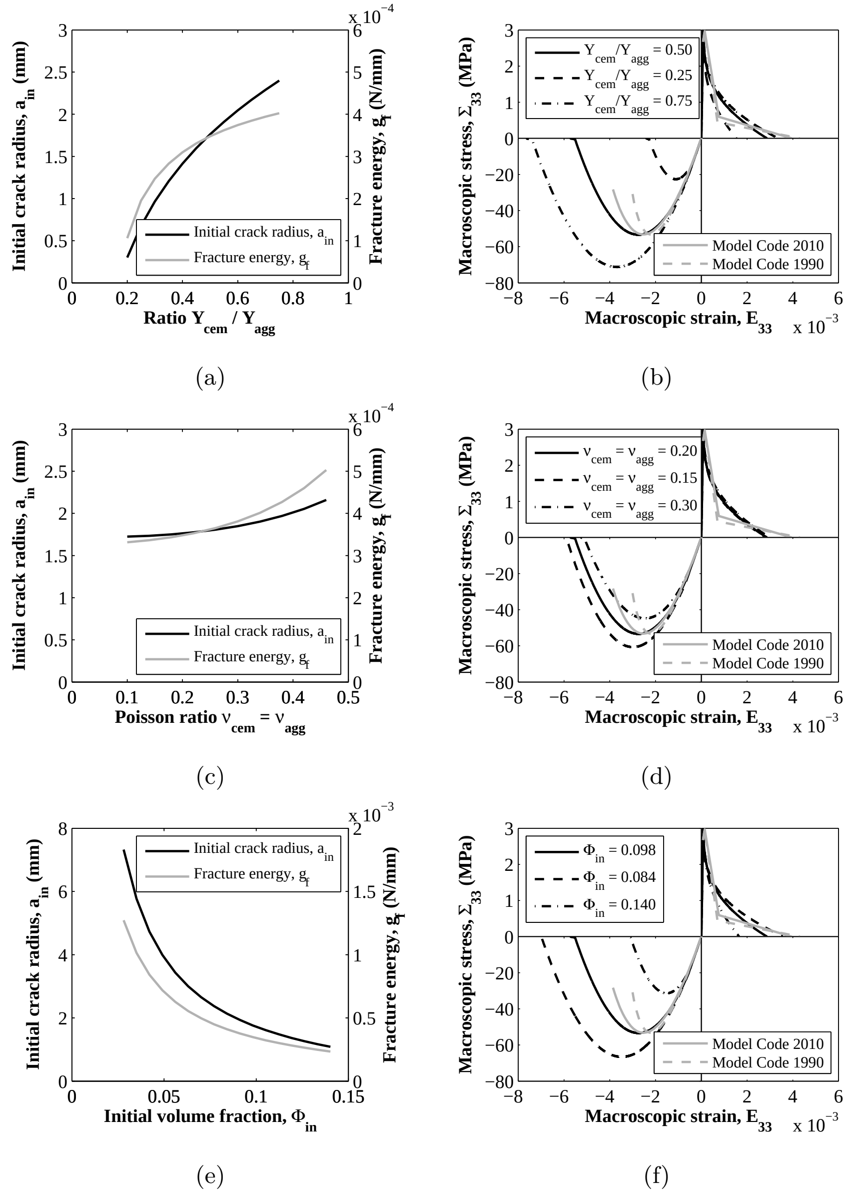

(a) (b)

(c) (d)

(e) (f)

Figure 6.5: Parametric study: (a)-(b) Ratio between the elastic moduli of cement paste and aggregate phases $Y_{\text{cem}}/Y_{\text{agg}}$; (c)-(d) Poisson ratio $\nu_{\text{cem}} = \nu_{\text{agg}}$; (e)-(f) Initial volume fraction of the cracks Φ_{in}. Not scaled Y-axis in figures (b), (d) and (f).

later and the peak stress $f_{\mathrm{c}} = |\Sigma_{33}^{\mathrm{peak}}|$ is higher; furthermore the ratio $\Sigma_{33}^{\mathrm{prop}}/\Sigma_{33}^{\mathrm{peak}}$ decreases.

Figure 6.5c and Figure 6.5d present the influence of Poisson ratios of aggregate and cement paste. Their values are assumed equal. As a consequence of the adopted homogenization method (Equation (5.36)) and of the modelling choices (the aggregates are considered as spherical inclusions), the solid matrix has the same Poisson ratio of its phases ($\nu_{\mathrm{m}} = \nu_{\mathrm{cem}} = \nu_{\mathrm{agg}}$). This elastic constant has a limited influence on both the calibrated parameters and the behaviour of the overall material under uniaxial loading. Its influence can be mainly appreciated for the behaviour of concrete under compressive load, because the Poisson ratio correlates the normal strains.

In Figure 6.5e and Figure 6.5f the attention is focussed on the initial volume fraction of cracks Φ_{in}. Considering the model assumptions, the following correlation holds between the initial aspect ratio X_{in} and the initial volume fraction Φ_{in} for the same overall initial stiffness tensor $\mathbb{C}_{\mathrm{in}}$: the higher is the volume fraction ($\Phi_{\mathrm{in}} \to 1$), the higher is the aspect ratio ($X_{\mathrm{in}} \to 1$); thus the inclusions tend to have a more spheroidal shape ($a_{\mathrm{in}} \to c_{\mathrm{in}}$). If the crack radius c in thickness direction is assumed constant, an inverse relationship is established between the volume fraction and the initial crack radius a_{in} in the major directions (Figure 6.5e). A similar trend is observed for the microscopic fracture energy g_{f}. The initial volume fraction of the cracks Φ_{in} influences the non-linear behaviour of concrete similarly to the ratio between the elastic moduli of cement paste and aggregates $Y_{\mathrm{cem}}/Y_{\mathrm{agg}}$ (compare Figure 6.5b and Figure 6.5f). In fact, an initial lower amount of cracks, which tend to be elongated penny-shaped inclusions ($a_{\mathrm{in}} \gg c$), leads to an overestimation of the compressive strength and of the macroscopic fracture energy.

6

Note that the radius in the thickness direction c affects the initial crack density variable ϵ, but it is not relevant in the damage evolution. In fact, being both the number of cracks per unit of volume n and the radius in the thickness direction c constant parameters during the damage evolution ($c = c_{\mathrm{in}}$ and $n = n_{\mathrm{in}}$), the current crack density variable ϵ, aspect ratio X and the volume fraction ϕ_{c} only depends on their initial values and on the current, a, and initial, a_{in}, crack radius. This can be demonstrated with the help of Equation (5.1) and Equation (5.41):

$$\frac{\epsilon}{\epsilon_{\mathrm{in}}} = \frac{na^3}{na_{\mathrm{in}}^3} = \left(\frac{a}{a_{\mathrm{in}}}\right)^3 \tag{6.16a}$$

$$\frac{X}{X_{\mathrm{in}}} = \frac{c/a}{c_{\mathrm{in}}/a_{\mathrm{in}}} = \frac{a_{\mathrm{in}}}{a} \tag{6.16b}$$

$$\frac{\phi_{\mathrm{c}}}{\phi_{\mathrm{c,in}}} = \frac{4/3\pi cna^2}{4/3\pi c_{\mathrm{in}}na_{\mathrm{in}}^2} = \left(\frac{a}{a_{\mathrm{in}}}\right)^2 \tag{6.16c}$$

Table 6.3: Input parameters for the simulation of biaxial loading tests.

Property	Value	Unit
Input parameters		
Concrete Young's modulus, Y_{in}	30.9*	GPa
Concrete tensile strength, $f_{\mathrm{t,in}}$	2.66*	MPa
Young's modulus of cement paste, Y_{cem}	25.0	GPa
Young's modulus of aggregates, Y_{agg}	70.0	GPa
Poisson ratio, $\nu_{\mathrm{cem}} = \nu_{\mathrm{agg}}$	0.200	
Volume fraction of aggregate, ϕ_{agg}	0.600	
Initial volume fraction of cracks, $\Phi_{\mathrm{in}} = 3\phi_{ci,\mathrm{in}}$	0.076	
Crack thickness, c_i $(i = 1, 2, 3)$	0.100	mm
Calibrated parameters		
Initial aspect ratio, $X_{i,\mathrm{in}}$ $(i = 1, 2, 3)$	0.092	
Microscopic fracture energy, g_{f}	2.71 10^{-4}	N/mm
Dependent parameters		
Young's modulus of solid matrix, Y_{m}	44.9	GPa
Poisson ratio of solid matrix, ν_{m}	0.200	
Nr. of cracks n_i $(i = 1, 2, 3)$	0.051	mm^{-3}
Initial crack radius, $a_{i,\mathrm{in}}$ $(i = 1, 2, 3)$	1.091	mm
Initial crack density, $\epsilon_{i,\mathrm{in}}$ $(i = 1, 2, 3)$	0.066	

* experimental data (Kupfer et al., 1969).

Concluding, the elastic modulus of the solid matrix Y_{m}, expressed as a function of the ratio $Y_{\mathrm{cem}}/Y_{\mathrm{agg}}$, and the initial porosity Φ_{in} can influence the non-linear model behaviour of concrete under uniaxial external loading. The Poisson ratio of the solid matrix ν_{m} has a limited influence, which can be noticed only for the behaviour under compressive loading. On the contrary, the damage process does not depend from the cracks' radius c in the thickness direction.

6.5 Simulation of Biaxial Loading Tests

The model is validated also for the case of unaffected concrete subjected to biaxial loading tests, by simulating the experimental tests performed by Kupfer et al. (1969). The loading is applied along the x- and y-axis, which are aligned with the 1 and 2 global directions.

The input parameters (Table 6.3) are chosen and uniaxial tests along the 2-axis (Figure 6.6a) are performed to determine the compressive strength, which results equal to $f_{\mathrm{c,in}} = |\Sigma_{22}^{\mathrm{peak}}| = 33.00$ MPa. The initial parameters are chosen on the basis of experimental data or literature information; the same calibration procedure described in Section 6.2 is applied. Considering the uniaxial compressive test, the model results able to capture the hardening/softening behaviour, as mentioned in Section 6.3, particularly in the pre-peak stage.

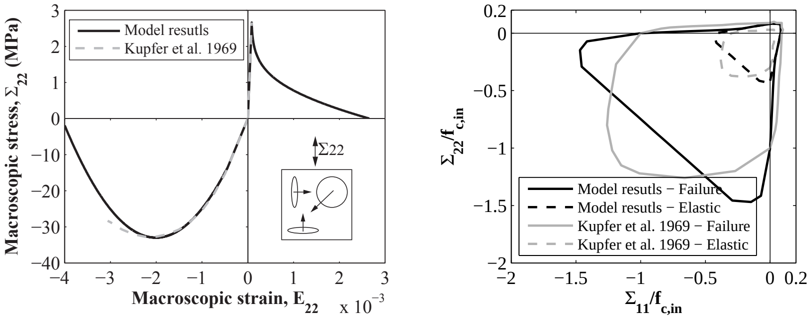

(a) (b)

Figure 6.6: Unaffected concrete under biaxial compressive loading: (a) Uniaxial tensile and compressive loading (Not scaled vertical axis); (b) Biaxial strength of unaffected concrete.

The model results to be insufficient to simulate the behaviour of concrete under a biaxial stress state, as shown in Figure 6.6b. It mainly underestimates the strength of the material by not capturing the beneficial effects of confinement. To better understand the model results, in Figure 6.7, Figure 6.9 and Figure 6.10 the cases of biaxial compressive, biaxial tension and compression-tension loading are analysed, respectively. They are composed by six sub-figures reporting: (a) the elastic and failure strength domains where representative stress ratios are identified; (b) the dissipated energy for different applied stress ratios, in terms of the area underneath the stress-strain curves; (c) the stress-strain relationship along the 2-axis ($\Sigma_{22} - E_{22}$); (d) the evolution of the strain E_{11} as a function of the stress Σ_{22}; (e) and (f) the change in crack radii. The representative stress ratios are chosen for the conditions where the lager stress (in absolute sense) is applied along the 2-axis (x → 2, y → 1, z → 3).

Considering biaxial compressive loading (Figure 6.7a), the strength of the material is overestimated for stress ratios between $0 < -\Sigma_{22}/-\Sigma_{11} \leq 0.4$ and $0 < -\Sigma_{11}/-\Sigma_{22} \leq 0.4$, while it is underestimated in the cases of $0.4 < -\Sigma_{22}/-\Sigma_{11} \leq 1$ and $0.4 < -\Sigma_{11}/-\Sigma_{22} \leq 1$. Figure 6.7 shows the model results for the representative stress ratios $-\Sigma_{22}/-\Sigma_{11}$ equal to 0 (uniaxial compressive loading), 0.1 and 1 (pure compressive biaxial loading).
As shown in Section 6.3, in the case of uniaxial compressive loading ($-\Sigma_{22}/-\Sigma_{11} = 0$), which is the same reported in Figure 6.6a, the know parabolic stress-strain relationship is retrieved (Figure 6.7c) and the Poisson effect can be observed (Figure 6.7d). The cracks with normals perpendicular to the loading direction are propagating at the same rate ($a_1 = a_3 \geq a_{\text{in}}$, Figure 6.7e and Figure 6.7f). Due to the compressive loading along the 2-axis, no crack evolution is occurring in the

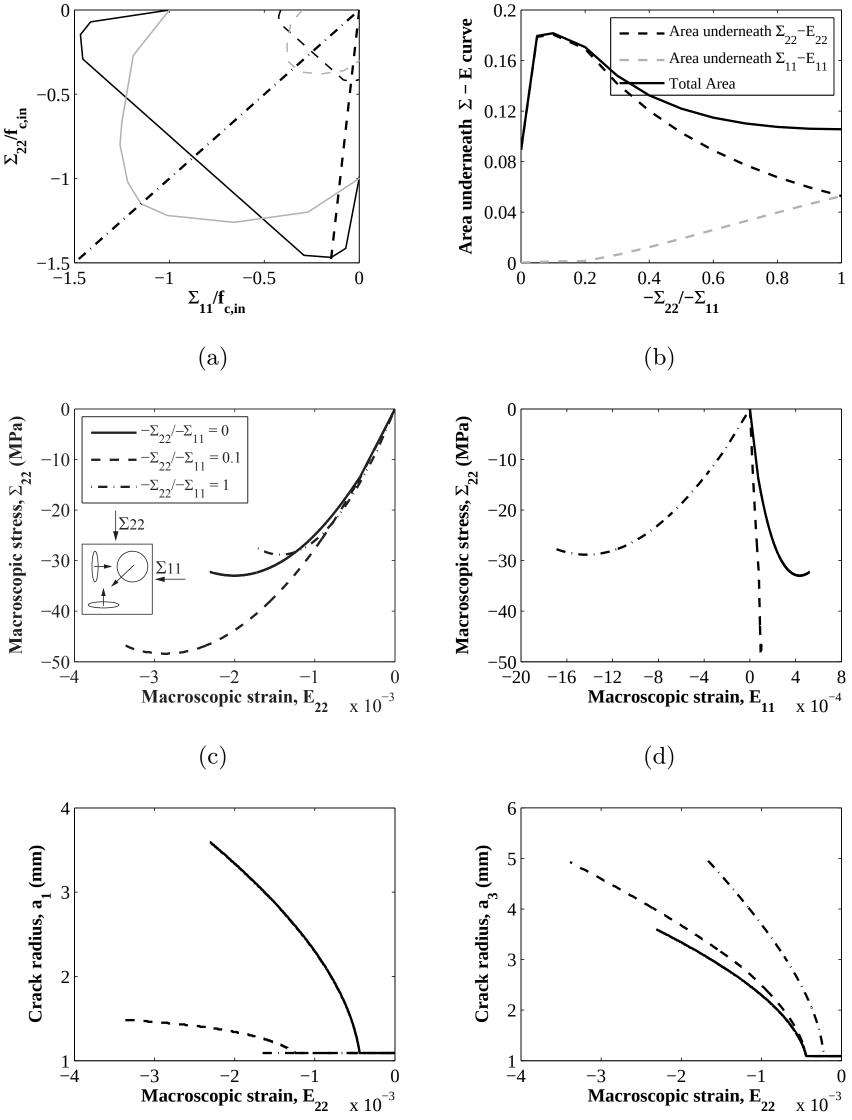

(a) (b)

(c) (d)

(e) (f)

Figure 6.7: Unaffected concrete under biaxial compressive loading: (a) Strength; (b) Area underneath $\Sigma - E$ curves; (c)-(d) Strain in the loading directions (E_{22}, E_{11}); (e)-(f) Crack propagation in 2-3 and 1-2 plane (a_1, a_3).

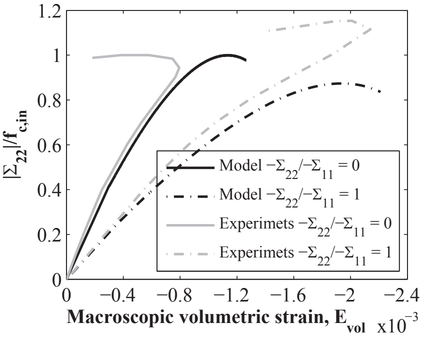

Figure 6.8: Unaffected concrete under biaxial compressive loading: Macroscopic volumetric strain E_{vol}.

1-3 plane ($a_2 = a_{\mathrm{in}}$). The damage starts at a stress level equal to $\Sigma_{22}^{\mathrm{prop}} = -13.60$ MPa, which is $\Sigma_{22}^{\mathrm{prop}} \cong 1/3\Sigma_{22}^{\mathrm{peak}}$.
In the case of pure compressive biaxial loading ($-\Sigma_{22}/-\Sigma_{11} = 1$), the crack propagation is prevented in the two loading directions ($a_1 = a_2 = a_{\mathrm{in}}$, Figure 6.7e), leading to a damage evolution in the 1-2 plane ($a_3 \geq a_{\mathrm{in}}$, Figure 6.7f). The cracking starts earlier than for the uniaxial case, at stress level $\Sigma_{22}^{\mathrm{prop}} = -8.19$ MPa. With only one crack family that is propagating, the peak stress ($\Sigma_{22}^{\mathrm{peak}} = -28.83$ MPa, Figure 6.7c) results lower than the one for the uniaxial compressive loading case. Being the stress and strain in the loading directions evolving similarly and the cracking phenomenon developing only in one plane, the energy dissipated results almost similar to the one of the uniaxial loading case (Figure 6.7b).
To clarify the reasons behind the overestimation of the concrete strength for the cases of $0 < -\Sigma_{22}/-\Sigma_{11} \leq 0.4$ and $0 < -\Sigma_{11}/-\Sigma_{22} \leq 0.4$, the condition $-\Sigma_{22}/-\Sigma_{11} = 0.1$ is analysed. The damaging starts in the 1-2 plane perpendicular to the loading directions ($a_3 \geq a_{\mathrm{in}}$, Figure 6.7f) at circa the same stress level as for the uniaxial loading case ($\Sigma_{22}^{\mathrm{prop}} = -14.01$ MPa). When the stress Σ_{22} equals the uniaxial peak stress, the damage starts also along the less compressed direction, that is the 1-axis ($a_3 > a_1 \geq a_{\mathrm{in}}$, Figure 6.7e), leading to an increase of capacity. The overestimation of the strength follows from the limited energy dissipation along the 1-axis (Figure 6.7b), which is revealed by the snap-back behaviour of the strain E_{11} (Figure 6.7d).

Figure 6.8 reports the evolution of the volumetric strain E_{vol} for the uniaxial ($-\Sigma_{22}/-\Sigma_{11} = 0$) and pure compressive biaxial loading ($-\Sigma_{22}/-\Sigma_{11} = 1$) cases in comparison with the experimental results. The model well represents the pre-peak behaviour, when a decrease of the concrete volume is observed, but

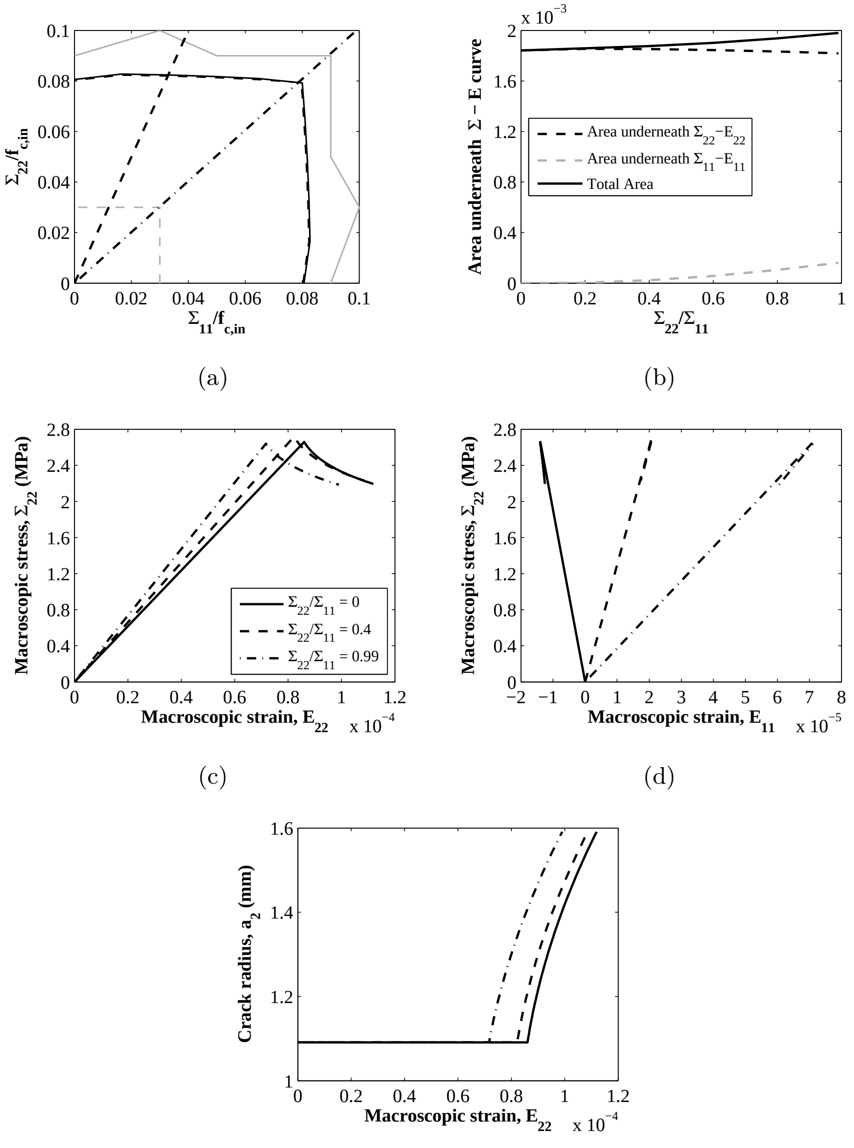

(a)

(b)

(c)

(d)

(e)

Figure 6.9: Unaffected concrete under biaxial tension loading: (a) Strength; (b) Area underneath $\Sigma - E$ curves; (c)-(d) Strain in the loading directions (E_{22}, E_{11}); (e) Crack propagation in 3-1 plane (a_2).

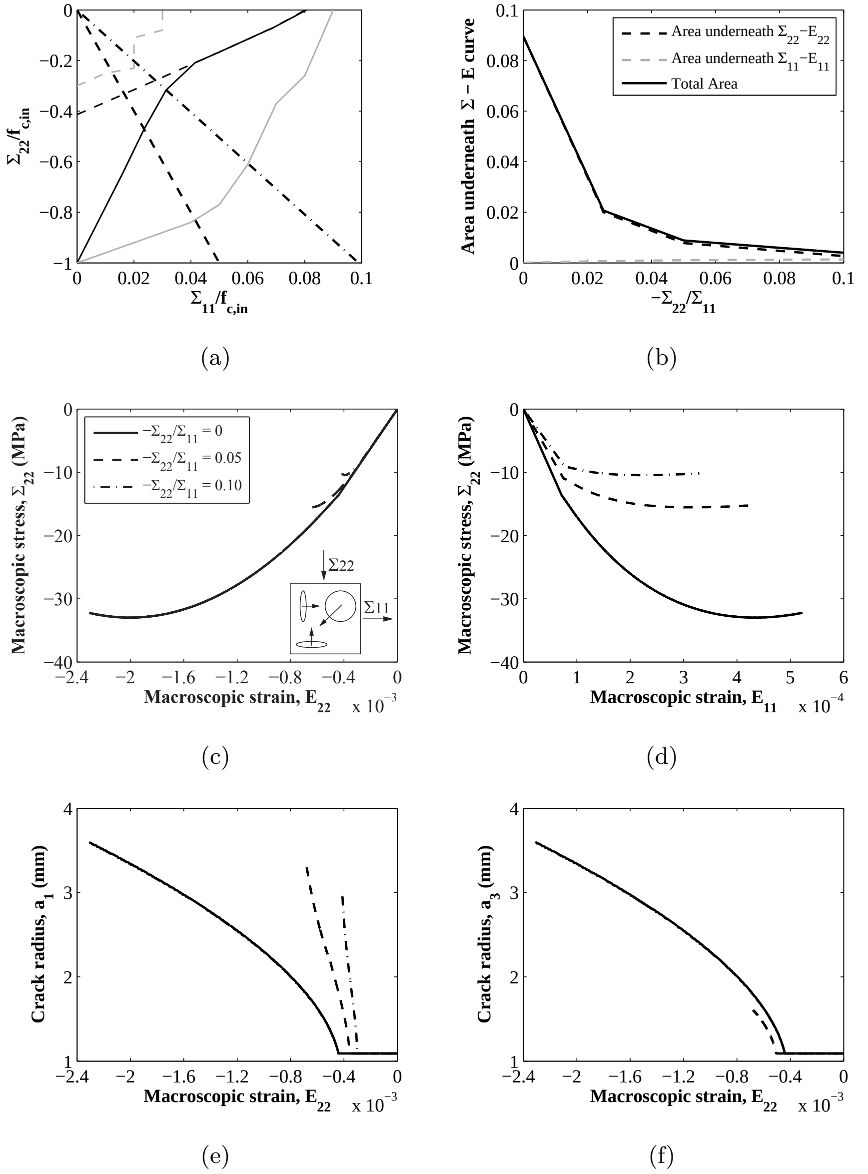

Figure 6.10: Unaffected concrete under combined tension and compressive loading: (a) Strength; (b) Area underneath $\Sigma - E$ curves; (c)-(d) Strain in the loading directions (E_{22}, E_{11}); (e)-(f) Crack propagation in 2-3 and 1-2 plane (a_1, a_3).

cannot capture the subsequent increment of the volumetric strain. Considering the experimental results (Kupfer et al., 1969), it is possible to affirm that high compressive stresses lead to an incompressible behaviour of the concrete governed by an increment of the apparent Poisson ratio. The model is not able to capture this phenomenon due to the assumption of crack propagation in elastic solid matrix. As a consequence, both the model inaccuracies in the estimation of the post-peak behaviour of concrete under uniaxial compressive loading and in the evaluation of concrete strength under biaxial compressive stress state can be addressed to the deficiency of permanent deformation.

In the case of biaxial tensile loading, the model estimate a failure domain similar to the experimental one. Figure 6.9 reports the model results for the representative stress ratios Σ_{22}/Σ_{11} equal to 0 (uniaxial tensile loading), 0.4 and 1 (pure tensile biaxial loading).
For all the cases the behaviour results similar to the uniaxial case, as shown in Section 6.3. The crack propagation occurs only in the plane perpendicular to the loading direction ($a_2 \geq a_{\text{in}}$, Figure 6.9e). The damaging starts when the critical initial stress $\mathbf{\Sigma}^{\text{cr}}$ ($f_{\text{t,in}}$) is reached, as imposed by the calibration procedure against the microscopic fracture energy g_{f} (Equation (6.15)). The energy is mainly dissipated along the 2-axis (Figure 6.9b and Figure 6.9c), leading to a snap-back behaviour for the strain E_{11} (Figure 6.9d).

Experimental findings suggest that the damaging starts at a stress level of approximately one third of the peak stress (Figure 6.9a), even for uniaxial tensile loading. The model is not able to capture this aspect, because the onset of damage also defines the stress at failure (Equation (6.15)).

In the case of combined tension and compressive loading, the model underestimates the strength of the material as a consequence of the elastic behaviour assumed for the solid matrix, as it is concluded for the biaxial compressive loading case. Figure 6.10 reports the model results for the representative stress ratios $-\Sigma_{22}/\Sigma_{11}$, equal to 0 (uniaxial compressive loading), 0.05 and 0.1.
In the case of a tensile loading applied along the 1-axis, the propagation is initiated in the 2-3 plane ($a_1 \geq a_{\text{in}}$, Figure 6.10e). In the case of low applied tensile stresses ($-\Sigma_{22}/\Sigma_{11} = 0.05$) the crack family with a normal along the 2-axis is also evolving ($a_2 \geq a_{\text{in}}$, Figure 6.10f), which is not the case for higher applied tensile stresses ($-\Sigma_{22}/\Sigma_{11} = 0.10$). In any case, the energy is mostly dissipated along the 2-axis (Figure 6.9b). The elastic domain results close to the failure one for stress ratios $-\Sigma_{22}/\Sigma_{11} > 0.10$.

In conclusion, the model is not satisfactory in the simulation of concrete under biaxial stress state, especially in cases which involves biaxial compressive loading. This shortcoming is primarily linked to the assumed elastic behaviour of the solid matrix. In fact, the formation of permanent deformation can be extremely relevant to describe the behaviour of concrete under biaxial stress state. This phenomenon can be associated to the sliding of the cracks. To account for the formation of permanent deformation, the model can be enriched with a plastic formulation for the solid matrix. Alternatively, considering that these deformation can be associate to frictional phenomena, a rough crack model can be considered. In this case, the number of crack families should be increased.

6.6 Concluding Remarks

The micro-poro-fracture-mechanical model, presented in Chapter 5, is validated for the case of unaffected concrete, which results in a drained porous medium subjected to external mechanical loading. The conditions of uniaxial and biaxial loading are analysed adopting a direct solution method.

The initial status of the overall material is determined on the basis of input and calibrated parameters. The former can be divided into three categories related to: the mechanical properties of undamaged concrete (Y_{in}, $f_{\mathrm{t,in}}$), the elastic constants of the solid matrix (Y_{m}, ν_{m}), function of the cement paste and aggregates' characteristics (Y_{cem}, Y_{agg}, $\nu_{\mathrm{cem}} = \nu_{\mathrm{agg}}$, ϕ_{agg}), and the initial status of the cracks (Φ_{in}, c). They can be determined by macro and microscopic investigation, such as mechanical and nano-indentation tests and porosity measurements. A calibration procedure is adopted to determine the initial aspect ratio of the cracks X_{in} and the microscopic fracture energy g_{f} on the basis of the macroscopic stiffness Y_{in} and tensile strength $f_{\mathrm{t,in}}$ of undamaged concrete.

The model results regarding the uniaxial behaviour of unaffected concrete are in good agreement with empirical formulations proposed by the Model Codes (CEB-FIP, 1993, 2011), which are based on a statistically large number of experimental results. The well known stress-strain relationships are approximated in terms of peak stresses, hardening/softening shape and ultimate strains for both tension and compression. Considering that the representative elementary volume is the fracture zone, which size can be estimated as three times the maximum aggregate's diameter (Bažant and Oh, 1983), the model is able to determine the macroscopic fracture energy in tension G_{f}. In case of compressive loading, the peak stress Σ^{peak} and relation between cracking and peak stress $\Sigma^{\mathrm{prop}}/\Sigma^{\mathrm{peak}} \cong 1/3$ are well estimated.

In the case of concrete under biaxial stress state, the model mainly underestimates the strength of the material in the regime of biaxial compression. This is primarily related to the lack, within the model formulation, of permanent deformations, which govern the incompressible behaviour of concrete for high compressive stresses. This phenomenon regards the post-peak behaviour of concrete under uniaxial loading and results essential when modelling the material strength for biaxial stress states.

In conclusion, the model results satisfactory for the evaluation of the mechanical properties (stiffness, uniaxial tensile and compressive strengths) of the overall material, it is further validated in Chapter 7 to determine the deteriorating impact of ASR on concrete material.

Model Validation for ASR-affected Concrete[1]

7

The proposed multiscale material model, which was illustrated in Chapter 5, was validated for the case of unaffected concrete in the previous chapter. The model was able to retrieve, from micro-mechanical quantities, the known macroscopic stress-strain relationships, which are usually adopted as input in structural analyses. In this chapter the problem is extended to the case of ASR-affected concrete by simulating the evolution of expansion and mechanical properties in a unconstrained specimens.

First, the solution method for the case of unconstrained ASR-affected specimens that are subsequently subjected to uniaxial loading is presented (Section 7.1). Afterwards, the evolution of engineering properties during the ASR process is simulated (Section 7.2) for the RR2 concrete presented in Chapter 4. The relation between stiffness and strengths is predicted reasonable well. However, the model overestimates the degradation in stiffness as a function of expansion. As a consequence, various model modifications are explored (Section 7.3). The model (Section 7.4) results a powerful tool for the estimation of the deteriorating impact induced by ASR on concrete, in terms of expansion and stiffness-strengths degradation relationship. It is suggested, similarly to Chapter 5, that the overestimation of the stiffness degradation is related to the lack of permanent deformations within the model formulation.

---

[1] Part of this chapter is based on Esposito and Hendriks (2015)

7.1 Free-expansion and Uniaxial Loading

In the framework of the micro-poro-fracture-mechanical model described in Section 5.1, the ASR-affected concrete is modelled as a porous medium subjected to a macroscopic uniform imposed strain $\boldsymbol{E}$ and saturated by a fluid, which exerts a pressure P.

In the case of specimens stored under free-expansion conditions ($\boldsymbol{\Sigma} = 0$), the pressure P induces a macroscopic expansion strain $\boldsymbol{E} = \boldsymbol{E}^P$ on the external boundaries. The state equations (Equation (5.31)) can be reduced to:

$$\boldsymbol{E} = \boldsymbol{E}^P = \mathbb{D} : \boldsymbol{B} P \tag{7.1a}$$

$$\Phi - \Phi^* = \left(\boldsymbol{B} : \mathbb{D} : \boldsymbol{B} + \frac{1}{N} \right) P \tag{7.1b}$$

where the compliance tensor $\mathbb{D}$ is calculated in agreement with Equation (5.32), the Biot tensor $\boldsymbol{B}$, and modulus $1/N$ are calculated with Equation (5.17) and Equation (5.30), respectively. The damage criterion for the i-th crack family takes the form (Equation (5.44)):

$$G_i - G_{ci} \leq 0; \quad \dot{\epsilon_i} \geq 0; \quad (G_i - G_{ci})\, \dot{\epsilon_i} = 0 \tag{7.2}$$

where the energy release rate G_i (Equation (5.45)) reads:

$$G_i\left(\boldsymbol{E}, P = 0, \epsilon_i\right) = -\frac{1}{2} \langle \boldsymbol{I} : \mathbb{D} P \rangle : \frac{\partial \mathbb{C}}{\partial \epsilon_i} : \langle \boldsymbol{I} : \mathbb{D} P \rangle \tag{7.3}$$

with $\langle \boldsymbol{E}' \rangle = \langle \boldsymbol{I} : \mathbb{D} P \rangle$ the positive part of the macroscopic effective strain tensor. Being the pressure, P, defined as a positive quantity, the operator $\langle \cdot \rangle$ could be skipped in Equation (7.3). The critical energy release rate G_{ci} is evaluated by Equation (5.47):

$$G_{ci}\left(\epsilon_i\right) = \frac{2\pi}{3} g_{\mathrm{f}} \left(\frac{n_i}{\epsilon_i} \right)^{1/3} = \frac{2\pi}{3} \frac{g_{\mathrm{f}}}{a_i} \tag{7.4}$$

The simulation of ASR in concrete under free-expansion conditions, can be performed in terms of crack density variables ϵ similarly to Section 6.1. Being the pressure P an hydrostatic loading and the initial micro-structure defined identical along the three orthogonal directions (Section 6.2), the crack density variables evolve similarly for each crack family ($\epsilon_1 = \epsilon_2 = \epsilon_3$). Not accounting for the nucleation and opening/closing of the cracks, the evolution of the crack density variables ϵ equivalently corresponds to the one of the crack radii a (Section 5.1). Imposing an increment of crack density variables $\epsilon = \epsilon^* + \delta\epsilon$ for each crack family, the critical pressure P^{cr} is calculated imposing that the energy release rate is equal to its threshold value:

$$-\frac{1}{2}\langle \boldsymbol{I} : \mathbb{D}\rangle \frac{\partial \mathbb{C}}{\partial \epsilon}\langle \boldsymbol{I} : \mathbb{D}\rangle \left(P^{\mathrm{cr}}\right)^2 := \frac{2}{3}\pi \frac{g_{\mathrm{f}}}{a} \tag{7.5}$$

The macroscopic strain $\boldsymbol{E} = \boldsymbol{E}^P$ is calculated with Equation (7.1a).

To evaluate the deteriorating impact of ASR on the engineering properties of concrete, a free-expansion test is simulated and subsequently the conditions of uniaxial tension and compressive tests are modelled. During the free-expansion test, the crack system is pressurized and no external mechanical loading is applied. The crack density variables ϵ of each family are evolving similarly and the critical pressure P^{cr} is calculated with Equation (7.5). During the subsequent uniaxial test, two stages can be distinguish: in the first stage the mechanical loading is applied on a pressurized system, while in the second stage the pressure within the cracks vanished due to their increase in size and only the mechanical loading is contributing to the damage. The second stage is characterized by the critical macroscopic strain $\boldsymbol{E}^{\mathrm{cr}}$, which is calculated as described in Section 6.1. In the first stage, where the pressure and the mechanical loading coexist, the current macroscopic strain $\boldsymbol{E}$ is the sum of the applied strain $\boldsymbol{E}^{\mathrm{applied}}$ and of the expansion strain $\boldsymbol{E}^P$, resulting from the pressure P:

$$\boldsymbol{E} = \boldsymbol{E}^{\mathrm{applied}} + \boldsymbol{E}^P = \boldsymbol{E}^{\mathrm{applied}} + \mathbb{D} : \boldsymbol{B} P \tag{7.6}$$

The strain $\boldsymbol{E}^{\mathrm{applied}}$ and the pressure P are correlated to the current crack density variables ϵ. They are expressed as a function of the critical stain $\boldsymbol{E}^{\mathrm{cr}}$ and of the critical pressure P^{cr}:

$$\boldsymbol{E}^{\mathrm{applied}} = \gamma_{\boldsymbol{E}} \boldsymbol{E}^{\mathrm{cr}} \tag{7.7a}$$

$$P = \gamma_P P^{\mathrm{cr}} \tag{7.7b}$$

where $\gamma_{\boldsymbol{E}}$ and γ_P are the loading coefficients, which values vary between 0 and 1. For the current crack density variables ϵ, the critical stain $\boldsymbol{E}^{\mathrm{cr}}$ is calculated with Equation (6.11) considering that only the external mechanical loading is acting on the system, while the critical pressure P^{cr} is evaluated with Equation (7.5) for the case of unconstrained affected concrete. Considering the general damage criterion in Equation (5.45), the effective strain can be expressed as:

$$\boldsymbol{E}' = \boldsymbol{E} + \boldsymbol{I} : \mathbb{D}_{\mathrm{M}} P = \gamma_{\boldsymbol{E}} \boldsymbol{E}^{\mathrm{cr}} + \boldsymbol{I} : \mathbb{D}_{\mathrm{M}} \gamma_P P^{\mathrm{cr}} \tag{7.8}$$

Comparing Equation (7.8) with the expression of the effective strain in Equation (6.3) and Equation (7.3), it results that no further damage is observed in this first stage, which can thus be considered as a transition stage. In fact, the external mechanical loading can create further damage only after that it compensate the effect of the pressure, which was previously developed in the free-expansion test. The direct solution method can be applied thanks to the linear elastic formulation of the model.

In conclusion, the deteriorating impact of ASR on concrete can be simulated by employing a direct solution method based on the evolution of the crack density variables of the three orthogonal families. The evolution of concrete expansion and its mechanical properties, that are elastic modulus, tensile and compressive strength, is determined by simulating first free-expansion conditions and subsequently uniaxial loading tests.

7.2 Simulation of the Deteriorating Impact of ASR

The micro-poro-fracture-mechanical model is applied to reproduce the experimental findings of Chapter 4. The RR2 concrete is chosen, being the most expansive in the experimental campaign. The input and calibrated parameters, listed in Table 7.1, are the same as adopted in Chapter 5.

Figure 7.1 shows the relationship between the crack radius a the macroscopic strain $\boldsymbol{E}^P$ and the pressure P in case of free-expansion conditions. The radii of the three crack families and the main strain components vary equally in the three direction, due to the initial status of the cracks and the isotropic loading condition. In the initial state the cracks are empty and the alkali-silica gel does not pressurize the concrete porosity ($P = 0$) resulting in zero macroscopic deformation ($\boldsymbol{E} = 0$). The saturation of the porous medium is assumed instantaneous resulting in an increase of pressure P and macroscopic strain $\boldsymbol{E}$ for the initial crack radius (Figure 7.1). While the damage process evolves, thus for increasing values of crack radius a the stiffness decreases and the effect of the pressure increases (see Equation (5.32), Equation (5.17) and Equation (5.30)). As a consequence the pressure P, needed for further damaging the system (Equation (7.5)), decreases and the macroscopic expansion strain $\boldsymbol{E}^P$ increases (Equation (7.1)).

To study the effect of ASR on the material deterioration, uniaxial tests have been simulated at eight levels of expansion. Figure 7.2, Figure 7.3 and Figure 7.4 report the main results. For clarity, the figures show only the results for the uniaxial tests; however all the variables are expressed in the total form accounting for the results obtained during the free-expansion test (Figure 7.1). In this case, the macroscopic strain $\boldsymbol{E}$ is the sum of the expansion strain $\boldsymbol{E}^P$ and of the applied one during the uniaxial tests. The case of unaffected concrete ($P = 0$), is the same as presented in Figure 6.3.

The stress-strain curves are shifted on the horizontal axis of a quantity equal to the expansion strain $\boldsymbol{E}^P$ (Figure 7.2a and Figure 7.2b). The curves present a similar shape, composed by a linear and softening/hardening branches. A linear stage is observed as a results of the transition phase between saturated porous medium under free-expansion conditions and drained material under external mechanical loading (Equation (7.8)). Due to the damage induced by the pressure P the stiffness in the linear stage is lower with respect to the one of unaffected concrete. Consequently, the peak stress is reduced both in tension and compression, because the system has already partially dissipated the fracture energy in the free-expansion test. In the case of uniaxial tension loading, the cracks with normal parallel to the loading direction are evolving (Figure 7.2c), while the other cracks stop their propagation and their crack radius is the same observed at the end of the free-expansion test (Figure 7.2e). In the case of compressive loading, the opposite situation is observed (Figure 7.2d and Figure 7.2f). The damage evolutions result stable (Figure 7.3), being the stability coefficient s negative (Equation (5.48)).

Figure 7.4 shows that the crack radius in the thickness direction c^{d} slightly varies as a function of the macroscopic strain $\boldsymbol{E}$ during uniaxial compressive testing; limited variation is observed for the uniaxial tensile tests. Its value has been post-processed as a function of the local strain in the inclusions as proposed by Deude et al. (2001):

$$c_i^{\mathrm{d}} = c_{i,\mathrm{in}} \left(1 + \boldsymbol{n}_i \cdot \boldsymbol{\varepsilon}_i \cdot \boldsymbol{n}_i\right) = c_{i,\mathrm{in}} \left(1 + \boldsymbol{n}_i \cdot \mathbb{A}_i : \boldsymbol{E} \cdot \boldsymbol{n}_i\right) \leq c_{i,\mathrm{in}} \qquad (7.9)$$

in which $c_{i,\mathrm{in}}$ is the initial value of the crack radius in the thickness direction (Table 7.1). The results indicate that the cracks are far from a complete closure, thus including the opening/closing phenomenon of the cracks in the model will not show any appreciable difference.

Figure 7.5 compares the model and experimental results in terms of mechanical properties degradation. The property values are normalized with respect to their initial value for the model results; the normalization procedure for the experimental results has been presented in Chapter 4. The model overestimates the degradation of all the properties, in correlation with the expansion (Figure 7.5a). The model is able to simulate the degradation rate between stiffness and strengths, as shown in Figure 7.5b.

The micro-poro-fracture-mechanical model, which appears successfully in the evaluation of concrete behaviour under external load and correctly approximates the relationship between stiffness and strength degradation in ASR affected concrete, requires improvement to correctly estimate the relationship between expansion and stiffness degradation. In the next section, possible modifications of the proposed model are explored.

Table 7.1: Input parameters for the simulation of the deteriorating impact of ASR.

Property	Value	Unit
Input parameters		
Concrete Young's modulus, Y_{in}	36.3*	GPa
Concrete tensile strength, $f_{\mathrm{t,in}}$	2.970*	MPa
Young's modulus of cement paste, Y_{cem}	43.3	GPa
Young's modulus of aggregates, Y_{agg}	86.5	GPa
Poisson ratio, $\nu_{\mathrm{cem}} = \nu_{\mathrm{agg}}$	0.200	
Volume fraction of aggregate, ϕ_{agg}	0.680	
Initial volume fraction of cracks, $\Phi_{\mathrm{in}} = 3\phi_{ci,\mathrm{in}}$	0.098	
Crack thickness, c_i $(i = 1, 2, 3)$	0.100	mm
Calibrated parameters		
Initial aspect ratio, $X_{i,\mathrm{in}}$ $(i = 1, 2, 3)$	0.057	
Microscopic fracture energy, g_{f}	3.48 10^{-4}	N/mm
Dependent parameters		
Young's modulus of solid matrix, Y_{m}	68.6	GPa
Poisson ratio of solid matrix, ν_{m}	0.200	
Nr. of cracks n_i $(i = 1, 2, 3)$	0.025	
Initial crack radius, $a_{i,\mathrm{in}}$ $(i = 1, 2, 3)$	1.762	mm
Initial crack density, $\epsilon_{i,\mathrm{in}}$ $(i = 1, 2, 3)$	0.138	

* calculated from 28-days cubic compressive strength (Eurocode 2, 2005).

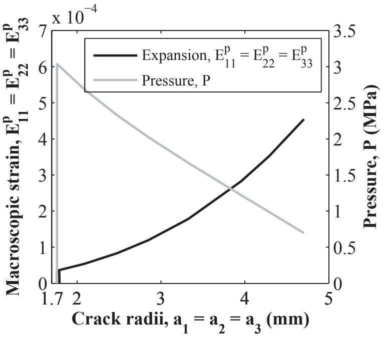

Figure 7.1: ASR-affected concrete under free-expansion conditions: Relation between crack propagation a, pressure P, and macroscopic strain $\boldsymbol{E} = \boldsymbol{E}^{\mathrm{p}}$.

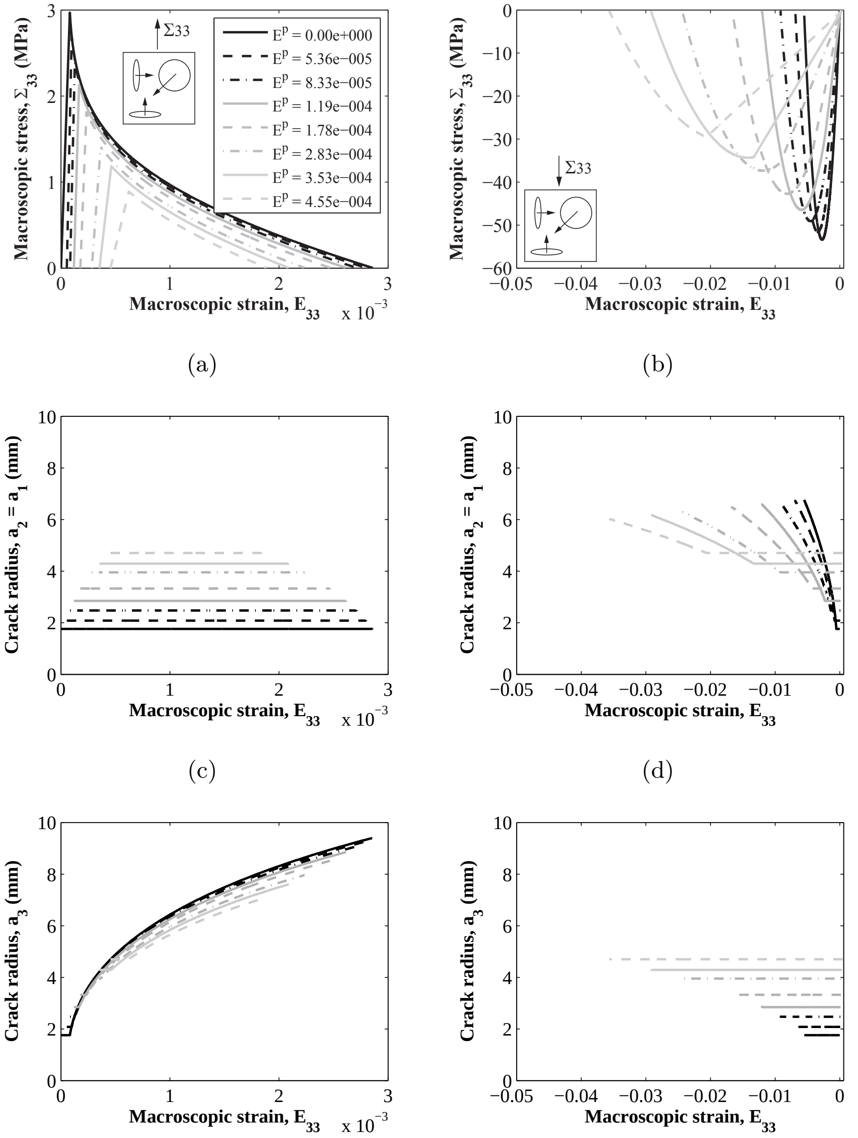

(a) (b)

(c) (d)

(e) (f)

Figure 7.2: Uniaxial tests on unconfined affected concrete: (a)-(b) Stress-strain relationships ($\Sigma_{33} - E_{33}$), (c)-(d) Cracking in 1-3 and 2-3 planes ($a_1 = a_2$), (e)-(f) Cracking in 1-2 plane (a_3).

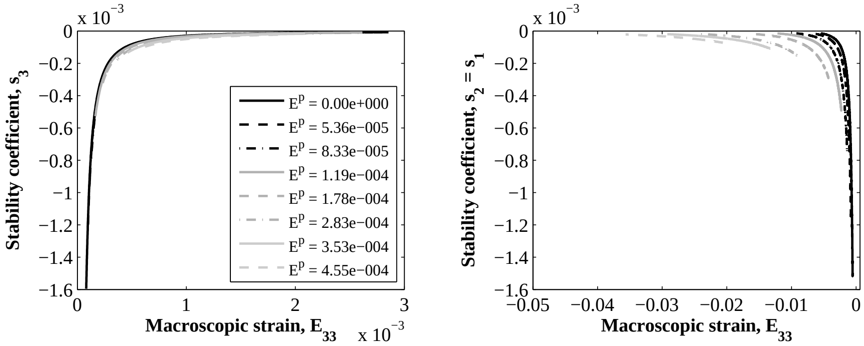

(a) (b)

Figure 7.3: Uniaxial tests on unconfined affected concrete: Stability analysis ($s < 0$) for (a) uniaxial tensile and (b) compressive tests.

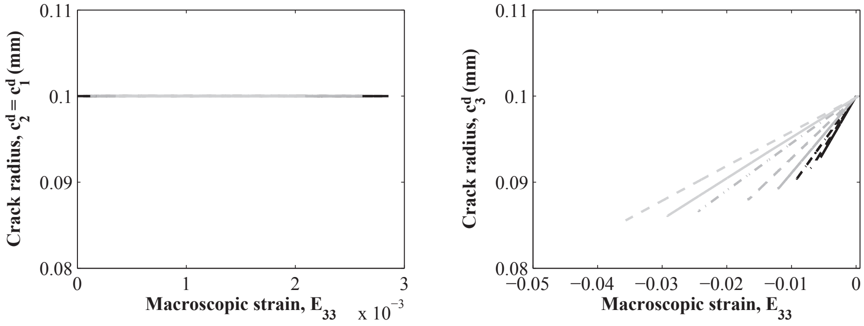

(a) (b)

Figure 7.4: Uniaxial tests on unconfined affected concrete: Post-processing of crack closing for (a) uniaxial tensile and (b) compressive tests (legend in Figure 7.3).

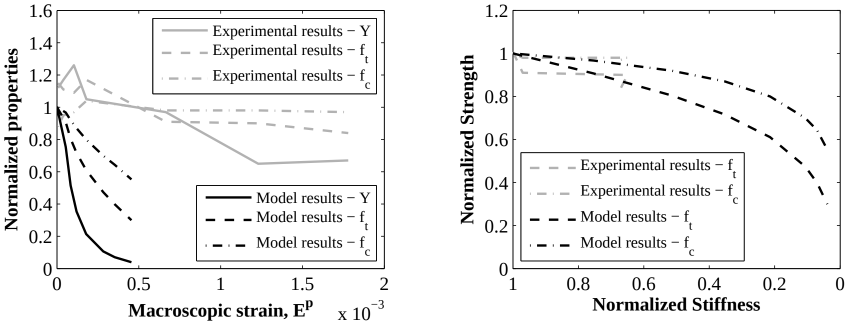

(a) (b)

Figure 7.5: ASR-affected concrete under free-expansion conditions: (a) Degradation of Young's modulus, tensile strength and compressive strength as a function of expansion; (b) Ratio between stiffness and strengths degradation.

7.3 Effects of Model Modifications

In Section 7.2 the micro-poro-fracture-mechanical model, based on a single porosity system, was employed to simulate the ASR-affected concrete behaviour. The concrete is composed by three penny-shaped crack families embedded into a solid matrix, which constituents are aggregates and cement paste (Section 5.1).

Section 6.3 showed that the model is able to predict the behaviour of unaffected concrete under uniaxial tensile and compressive loads, capturing not only the peaks stress, but also its main nonlinear characteristics such as the softening/hardening shape, ultimate strain and macroscopic fracture energy G_f.

When applied to the case of ASR-affected concrete, the model is able to determine the correlation between pressure P and expansion strains $\boldsymbol{E}^P$. The degradation of mechanical properties in ASR-affected concrete under free-expansion conditions, are determined by simulating subsequent uniaxial tests. The relation between stiffness and strengths is predicted reasonable well. However, the model overestimates the degradation in stiffness as a function of expansion.

Three model modifications are explored. The attention is first focussed on a critical re-evaluation of the input parameters. Subsequently, the two-scale double porosity model and the solidification model presented in Section 5.2 are adopted.

7.3.1 Re-evaluation of Input Parameters

The microscopic fracture energy g_f and the crack density variables ϵ govern the fracture process. The latter is a state variable, while the former is a constant. In

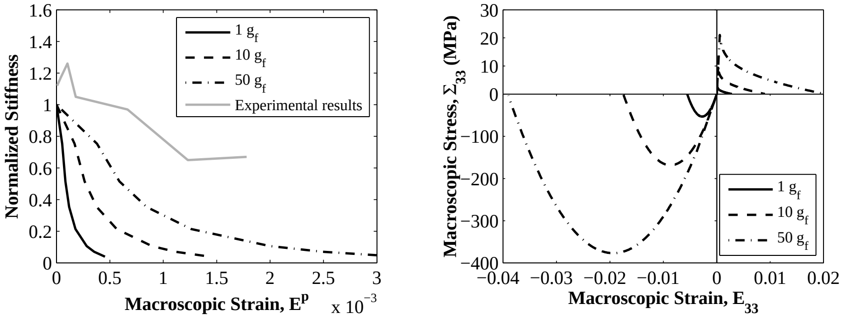

(a) (b)

Figure 7.6: Re-evaluation of input parameters: (a) Stiffness degradation due to pressure P; (b) Uniaxial test of unaffected concrete. Not scaled vertical axis in Figure (b).

Section 6.2, the microscopic fracture energy g_{f} was calibrated imposing that at onset of cracking the macroscopic stress is the same as observed experimentally in a uniaxial tensile test (Equation (6.15)).

Charpin and Ehrlacher (2012) propose to consider the microscopic fracture energy as an input parameter not linked to the tensile properties of the undamaged concrete. Their scope is to model the behaviour of ASR-affected concrete in confined conditions. Their model explains the coupling between internal swelling and external mechanical loading in terms of concrete expansion. High degradation of concrete stiffness for limited expansion values is reported, but a comparison with experimental findings is not made.

The proposed model is modified by adopting a similar approach. The results are obtained by calibrating only the initial aspect ratio X_{in} and considering multiples of the calibrated microscopic fracture energy g_{f}.

This approach shows an improvement in terms of expansion versus stiffness degradation (Figure 7.6), but it presents an undesired drawback in the estimation of the strengths. Figure 7.6a shows that the higher is the input microscopic fracture energy, the lower is the stiffness degradation for the same expansion level. However, a sensible difference with experimental results is still noticeable. Figure 7.6b reveals the major disadvantage of the method. It compares simulations of uniaxial tests performed for unaffected concrete. For high values of the input microscopic fracture energy, the peak stress and the ultimate strain reach unrealistic values, both in tension and compression.

In conclusion, this approach does not show any improvement and highlights once more the link between microscopic damage processes and macroscopic material degradation.

Table 7.2: Complementary initial parameters for the two-scale double porosity model (see also Table 7.1).

Property	Unit	Value		
Volume fraction of pores ϕ_p		0	0.10	0.20
Initial aspect ratio, $X_{i,\mathrm{in}}$ $(i = 1, 2, 3)$	mm	0.057	0.057	0.057
Microscopic fracture energy, g_f	N/mm	3.48 10^{-4}	4.23 10^{-4}	5.20 10^{-4}
Nr. of cracks n_i $(i = 1, 2, 3)$		0.025	0.016	0.007
Initial crack density, $\epsilon_{i,\mathrm{in}}$ $(i = 1, 2, 3)$		0.138	0.085	0.041

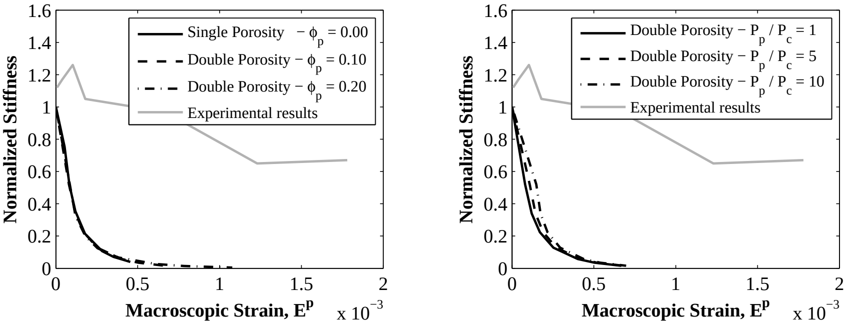

(a) (b)

Figure 7.7: Two-scale double porosity model: (a) Influence of the volume fraction of pores ϕ_p $(P_\mathrm{p} = P_\mathrm{c})$; (b) Influence of the ratio between the pressure in the pores P_p and in the cracks P_c $(\phi_\mathrm{p} = 0.10)$.

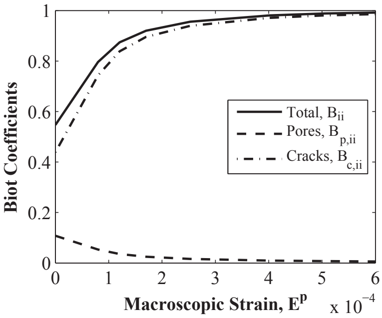

Figure 7.8: Two-scale double porosity model: Evolution of Biot moduli.

7.3.2 Two-Scale Double Porosity

The hierarchical structure of concrete can influence the ASR process and consequently its impact on the material. The influence on the concrete behaviour of a second porosity system, at lower scale than the cracks, is investigated by adopting the two-scale double porosity model illustrated in Section 5.2.1. At lower scale (level I) spherical pores are embedded in the solid matrix, which is composed by aggregates and cement paste. At higher scale (level II) the cracks are propagating in the porous matrix.

To compare the results obtained with the single porosity model (Section 7.2) and the two-scale double porosity model, the calibration procedure has been slightly modified for the latter case by imposing that the initial aspect ratio of the cracks is the same adopted in the former model ($X_{i,\mathrm{in}} = 0.057$, see Table 7.1). Consequently, the initial volume fraction $\phi_{\mathrm{c,in}} = \phi_{\mathrm{c1,in}} = \phi_{\mathrm{c2,in}} = \phi_{\mathrm{c3,in}}$ of the cracks has been calibrated to match the initial elastic modulus Y_{in} of the overall material (Table 7.2). The microscopic fracture energy g_{f} is determined with Equation (6.15), as described in Section 6.2. The volume fraction of spherical pores ϕ_{p} is an input parameter, but its value is limited by the initial volume fraction of cracks Φ_{in} and by the overall initial stiffness Y_{in}.

Figure 7.7a compares the results obtained for different values of the volume fraction of spherical pores ϕ_{p}, while Figure 7.7b considers different ratios between the pressures $P_{\mathrm{p}}/P_{\mathrm{c}}$ in the two porosities. The two-scale double porosity model does not show appreciable difference with respect to the single porosity model. This can be explained by the evolution of Biot tensor $\boldsymbol{B}_{\mathrm{p}}$ (Figure 7.8), which can be directly related to the evolution of the volume fractions. In fact, the volume fraction of spherical pores at level I f_{p} is linked to the one of the cracks Φ at level II (Equation (5.52)):

$$f_{\mathrm{p}} = \phi_{\mathrm{p}} \left(1 - \Phi\right) \tag{7.10}$$

As a consequence, both the stiffness tensor $\mathbb{C}_{\mathrm{pm}}$ and the Biot tensor $\boldsymbol{B}_{\mathrm{pm}}^{\mathrm{m}}$ of the porous matrix decrease leading to a substantial reduction of $\boldsymbol{B}_{\mathrm{p}}$ (Equation (5.53a)). This explains the marginal influence of the pressure in the spherical pores (level I) on the macroscopic expansion (level II).

7.3.3 Solidification

The expansion of concrete is the major effect induced by the ASR process. It is a direct consequence of the swelling of the gel in a confined environment. However, the deterioration of concrete appears to be associated with a more complex phenomenon. Previous sections showed that considering only the effect of an internal pressure P is not sufficient to correctly link the macroscopic expansion and degradation of concrete.

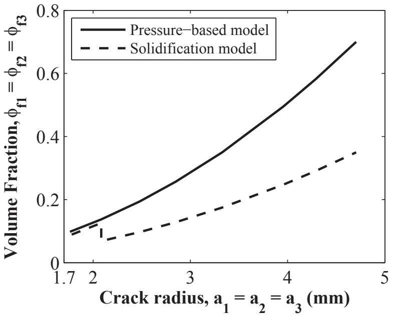

Figure 7.9: Comparison between the pressure-based and the solidification model: Evolution of pressurized cracks' space ϕ_f (solidification ratio $\rho_\mathrm{s} = 0.5$).

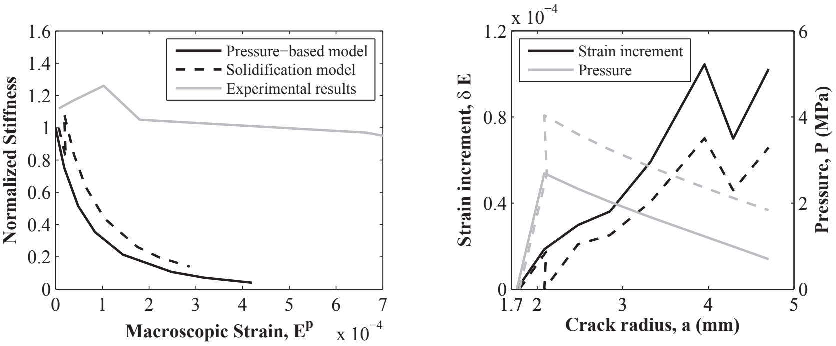

(a) (b)

Figure 7.10: Comparison between the pressure-based and the solidification model: (a) Relation between expansion and stiffness degradation; (b) Evolution of strain increment $\delta \boldsymbol{E} = \delta \widehat{\boldsymbol{E}} - \delta \boldsymbol{E}^*$ and pressure P.

Experimental investigations revealed that the viscoelastic properties of the gel play an important role in the phenomena (Hagelia, 2010; Kawamura and Iwahori, 2004). It can be hypothesized that during the process the gel is changing in phase and increasing its mechanical contribution to the overall concrete material. Furthermore, in structures with major signs of deterioration, expulsion of a dense material was found on their surfaces.

Inspired by the work of Coussy (2005) for freezing materials, the solidification model presented in Section 5.2.2 is adopted to describe the possible contribution of coexisting fluid and solid gel phases to the overall stiffness of the material. The ASR damage process is simulated by means of two subsequent phenomena: swelling and solidification of the gel. The first process defines the macroscopic expansion of concrete, while the second delays the deterioration. The solidification model is compared with the pressure-based model of Section 7.2, adopting the same initial parameters (Table 7.1). The solidification starts at crack radius $a = 2.08$ mm and evolves with a constant ratio $\rho_\mathrm{s} = \phi_\mathrm{cs}/\phi_\mathrm{c} = 0.50$. Both are relatively arbitrary values. The elastic modulus of the solid gel phase is assumed equal to $Y_\mathrm{g} = 45.0$ GPa (Leemann and Lura, 2013).

Figure 7.9 shows the evolution of pressurized cracks space ϕ_f for each crack family as a function of the crack radius a. If the solidification starts, this space is suddenly reduced in agreement with the ratio ρ_s. In the case of the pressure-based model the pressurized cracks space is equivalent to the volume fraction of the cracks $\phi_{\mathrm{f}i} = \phi_{\mathrm{c}i}$.

At onset of solidification, the overall material results stiffer due to the presence of solid gel phase, as shown in Figure 7.10a. As a consequence, the pressure P increases due to the confinement effect exerting by the solid gel on the fluid (Figure 7.10b). No increment of strain ($\delta \boldsymbol{E} = 0$, Equation (5.68)) occurs due to assumption of a stress-free process (Equation (5.70)).

However, as the damaging proceeds, the stiffness drastically decreases because the pressurizing effect becomes more important then the solidification one. In comparison with the pressure-based approach, the solidification model provides lower strain increments for the same crack radius a (Figure 7.10b). In fact, if the cracks are saturated by a fluid and subjected to an increase of internal pressure, P, the increment in strain is $\delta \boldsymbol{E} = \delta \widehat{\boldsymbol{E}}$ (Equation (5.68)). At the contrary, in presence of solidification, the incremental strain is reduced by the quantity $\delta \boldsymbol{E}^*$ ($\delta \boldsymbol{E} = \delta \widehat{\boldsymbol{E}} - \delta \boldsymbol{E}^*$). Consequently, the two approaches provide similar results in terms of degradation versus expansion and no improvement is observed in comparison with experimental results.

7.4 Concluding Remarks

The micro-poro-fracture-mechanical model, presented in Chapter 5, is validated for the case of ASR-affected concrete, which results in a saturated porous medium subjected to pressure, exerted by the fluid on the micro-structure, and to external mechanical loading. The evolution of mechanical properties of ASR-affected concrete is evaluated by simulating first a free-expansion test and subsequently uniaxial loading tests. The boundary value problem is solved by adopting a direct solution method.

A comparison with experimental findings (Chapter 4) shows that the model overestimates the degradation of mechanical properties as a function of the expansion. On the contrary, the relationship between stiffness and strength deterioration is correctly approximated.

To improve the model performances regards the relation between swelling and stiffness reduction of affected concrete, three alternative approaches have been adopted.

First, initial parameters are re-evaluated by considering the microscopic fracture energy as an input parameter (Charpin and Ehrlacher, 2012), rather than a calibrated one linked to the tensile strength of the material. This solution provides a delay in the stiffness reduction for substantially higher values of the microscopic fracture energy. However, the resulting strengths properties are unrealistic. This remarks the link between the microscopic damage process induced by external and internal loads.

Second, a hierarchical distribution of pores is modelled adopting a two-scale double porosity system. The cracks, which represent the capillarity porosity, are propagating in a porous matrix. This medium is composed by the solid matrix and spherical inclusions, representing the C-S-H gel porosity. The influence of a pore system on a lower scale than the cracks, does not sufficiently delay the stiffness degradation.

Eventually, the ASR is simulated by means of two processes; the swelling and the solidification. A simplified transformation of the gel phase is assumed, being first a fluid and subsequently a solid, which contributes to the overall stiffness of the material. A noticeable improvement is observed at onset of solidification. However, further cracking of the partially solidified medium produces a degradation trend similar to the one obtained with the pressure-based model.

In conclusion, both the micro-poro-fracture-mechanical model and its modifications do not provide satisfactory results regarding the relation between swelling and stiffness reduction of affected concrete. This is a consequence of lack of permanent deformation as already observed for the case of unaffected concrete. As shown in Chapter 6, the modelling approach was not able to capture the behaviour of unaffected concrete under biaxial loading. In particular, the model was not

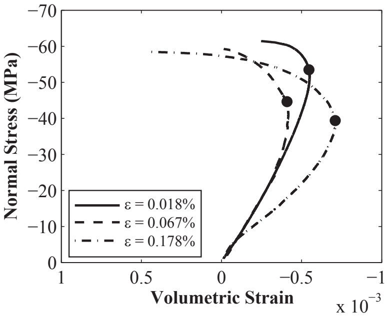

Figure 7.11: Experimental results for uniaxial compressive tests: Volumetric strain for RR2 concrete stored in accelerated conditions for 91, 182, 364 days.

able to describe dilatancy effects, which can be associated with the presence of inelastic deformations. This problem could be overcome with the introduction of a micro-rough cracking model, as already suggested by Mihai and Jefferson (2011), Mihai (2012). The formulation of a model accounting for permanent deformation results even more important for the case of ASR-affected concrete. Recalling the experimental results presented in Chapter 4 and here reported in Figure 7.11, it is observed that the ASR-affected concrete in uniaxial compression shows an earlier change of sign of the volumetric strain compared to the unaffected concrete. This observation may suggest the presence of permanent deformation induced by the alkali-silica gel swelling (e.g. creep deformation). The lack of a nonlinear formulation in the current modelling approach thus results in an overestimation of the expansion-stiffness relationship.

Conclusions

8

The assessment of concrete structures affected by alkali-silica reaction (ASR) is a complex problem due to the interdependency between the reaction, its expansive products, ambient influences, local and structural confinement and loading. The reaction starts within concrete constituents and induces expansion and degradation of concrete, with consequent loss in capacity of the structure.

To better understand this phenomenon, this research aimed to study the deteriorating impact of alkali-silica reaction considering the correlation between expansion and mechanical degradation of concrete. Both experimental and modelling approaches were followed, analysing the phenomenon at concrete level within the perspective of structural assessments. This chapter summarizes the initial assumptions of the research (Section 8.1), its scientific contributions (Section 8.2) and possibility for further research developments (Section 8.3).

8.1 Initial Assumptions

The research presented in this thesis is based on the following considerations:

- *The ASR in concrete structures is considered as a multiscale phenomenon.* The phenomenon, which is trigged within the concrete constituents (reaction product level), forms an expansive alkali-silica gel that induces micro-cracking (aggregate level) and consequently expansion and degradation of the material (concrete level), compromising the performance of structures in terms of both capacity and durability (structural level). The interaction of the various phenomena at the different scales results in a complex behaviour of ASR-affected concrete structures.

- *In the framework of structural assessment, the deteriorating impact of ASR on concrete should be considered in terms of both expansion and degradation of mechanical properties.* Due to the high number of influencing factor, such as boundary and environmental conditions, the problem is too complex to be studied directly at structural level. This requires a profound understanding of the ASR-affected concrete behaviour, which cannot only be associated to the induced concrete expansion. The correlation between expansion and degradation of mechanical properties need to be investigated.

- *The damage effects at concrete level associated to the ASR, which starts at reaction product level, and to the external mechanical loading, acting at structural level, can be both related to the micro-cracking phenomenon at aggregate level.* The swelling of the alkali-silica gel results as an internal loading source for concrete, which triggers a chain of damaging effects. In unaffected structures, the cracking phenomenon, which can be observed and phenomenologically described at material level, has its origin at aggregate level. As a consequence, the damage mechanism at aggregate level results as the common denominator between the internal swelling of ASR gel and the external mechanical loading.

- *An analytically solved multiscale modelling approach, which can bridge the gap between micro- and macro-mechanical models, is needed for the material characterization of ASR-affected concrete structures.* A multiscale micro-poro-fracture-mechanical model allows to describe the interaction between ASR and external mechanical loading at aggregate level, by linking it to the micro-cracking phenomenon. The approach fits in well with a possible down- and up-scaling to reaction product and structural level, respectively.

8.2 Scientific Contributions

The experimental observations of the relation between expansion and degradation of mechanical properties under free-expandable ASR-affected concrete concludes that (Chapter 4):

- *A statistically relevant relationship could be established between the expansion and the degradation of mechanical properties.* Experimental investigations as well as literature data were collected to form a data set based on 52 different concrete mixes. The evolution of stiffness and tensile strength was captured by a S-shaped curve, while for the compressive strength a piecewise linear relationship was chosen. Even thought the data comprised a great variety of concrete mixes and storage conditions, the establishment of such a relationship appeared to be possible.
- *Rather than the compressive strength, the elastic modulus is the best indicator of ASR signs in concrete.* The elastic modulus shows a relevant degradation already at small expansion values, while the compressive strength presents an initial increment.
- *In the case of ASR-affected concrete, the relations between stiffness and strengths cannot be predicted by the known stiffness-strength relationships derived for unaffected concrete.* This results from the different degradation rate of the stiffness and strengths. Consequently, at concrete level unaffected and ASR-affected concrete appear as substantially different materials.

The research shows that the multiscale micro-poro-fracture-mechanical model (Chapter 5) results as an advantageous method for the material characterization of concrete:

- *For the case of unaffected concrete, the model is able to approximate the stress-strain relationship that are usually adopted as input parameters in numerical analyses of structures (Chapter 6).* The behaviour of concrete under uniaxial tension and compression loading is well captured in terms of peak stresses, hardening/softening shape and ultimate strains.
- *For the case of affected concrete under free-expansion condition, the model is able to reproduce the relationship between stiffness and strengths degradation (Chapter 7).* As a consequence, it is able to capture the difference between unaffected and affected concrete at concrete level.
- *The absence of permanent deformation in the model formulation results as limitation (Chapters 6 and 7).* This emerges from the strength underestimation of unaffected concrete under biaxial loading and from the overestimation of the stiffness degradation in ASR-affected concrete.

8.3 Future Research

Considering the scientific contributions, the following experimental investigations are of interest:

- *Systematic laboratory investigations focussed on the correlation between, microscopic damage, concrete expansion and degradation of mechanical properties for concrete under various stress states are recommended (aggregate-to-concrete level).* Due to the multiscale nature of the phenomenon, microscopic damage, material degradation and stress-induced anisotropic behaviour cannot longer be studied as independent aspects of the induced expansion. A combined effort is needed to correlate laboratory to field behaviour.

- *Laboratory observations focussed on the structural component behaviour in relation to the concrete expansion and mechanical degradation of the material are of interest (concrete-to-structural level).* As shown in this research, at material level, unaffected ASR-affected concrete appears as substantially different materials. This difference can have a relevant impact on the structural behaviour. By including the ASR-induced structural effects as part of the multiscale picture, it would be possible to identify a common denominator for the assessment of unaffected and affected structures.

- *Full-scale in-situ experiments on ASR-affected structures can be considered to develop an assessment strategy.* Monitoring strategies and proof loading tests can provide information on the change in behaviour of an ASR-affected concrete structures within its natural environment.

The following enhancements are foreseen for the multiscale material model:

- *To overcome the observed limitations, it is suggested to accounts for permanent deformations within the model formulation.* The presence of high compressive stresses or prolonged loading can induce permanent deformations, which can be explained by the frictional behaviour related to sliding and interlocking of partially closed cracks. To account for this phenomenon a plastic formulation can be adopted for the solid matrix or a rough microcrack model can be formulated. This should be brought in connection with the modelling of long-term processes, such as creep.

- *A multi-direction damage model allows for a better description of the mircocracking phenomenon in concrete and thus of its overall behaviour.* At the moment, the model considers only three orthogonal crack families. This appeared sufficient for the current formulation. However, when accounting for permanent deformations with the description of frictional phenomena, a higher number of crack families is necessary.

- *As ASR in concrete structures is a long-term process, the formulation of a kinetic law is required to describe the evolution of its deteriorating impact in time.* A phenomenological law can be adopted and calibrated against the free-expansion behaviour. Alternatively, a deeper study can be performed by modelling the phenomena between reaction products and aggregate level.

- *The model can be evaluated for unaffected and ASR-affected concrete under various loading configurations.* The model couples ASR and mechanical loading in terms of micro-cracking. It is thus suitable to describe the expansion redistribution effect observed for ASR-affected concrete under compressive stresses. The study of unaffected concrete can be expanded by investigating its behaviour under triaxial stress state.

- *The model can be implemented in a finite element framework.* Redistribution effects, e.g. within a cross section of a structural element could then be evaluated. The strain-driven formulation of the model relates well with the standard displacement-based finite element method.

Bibliography

Ahmed, T., Burley, E., Rigden, S., and Abu-Tair, A. (2003). The effect of alkali reactivity on the mechanical properties of concrete. *Construction and Building Materials*, 17(2):123–144.

Alnaggar, M., Cusatis, G., and Di Luzio, G. (2013). Lattice Discrete Particle Modeling (LDPM) of Alkali Silica Reaction (ASR) deterioration of concrete structures. *Cement and Concrete Composites*, 41:45–59.

American Society for Testing and Materials (2001). *ASTM C1293 - Standard Test Method for Determination of Length Change of Concrete Due to Alkali-Silica Reaction.* West Conshohocken, PA, United States.

American Society for Testing and Materials (2012a). *ASTM C127 - Standard Test Method for Density, Relative Density (Specific Gravity), and Absorption of Coarse Aggregate.* West Conshohocken, PA, United States.

American Society for Testing and Materials (2012b). *ASTM C128 - Standard Test Method for Density, Relative Density (Specific Gravity), and Absorption of Fine Aggregate.* West Conshohocken, PA, United States.

Anaç, C. (2013). Personal communiation.

Anaç, C., Esposito, R., Çopuroğlu, O., Schlangen, E., and Hendriks, M. (2012a). A tool for concrete performance assessment for ASR affected structures: an outlook. In *the 14th International Conference on Alkali Aggregate Reaction (ICAAR14)*, Austin, Texas.

Anaç, C., Schlangen, E., and Çopuroğlu, O. (2012b). Lattice model implementation on alkali silica reaction gel expansion in a reacted concrete medium. In *the*

3^{rd} international conference on concrete repair, rehabilitation and retrofitting (ICCRRR-3), Cape Town, South Africa.

Andic-Cakir, O., Copuroglu, O., and Ramyar, K. (2009). Evaluation of alkali-silica reaction by concrete microbar test. *ACI Materials Journal*, 106(2):184–191.

Bangert, F., Kuhl, D., and Meschke, G. (2004). Chemo-hygro-mechanical modelling and numerical simulation of concrete deterioration caused by alkali-silica reaction. *International Journal for Numerical and Analytical Methods in Geomechanics*, 28(7-8):689–714.

Bažant, Z. and Oh, B.-H. (1983). Crack band theory for fracture of concrete. *Matariaux et Construction*, 16(3):155–177.

Bažant, Z. and Oh, B.-H. (1996). Microplane model for fracture analysis of concrete structures. In *Symposium on Interaction of NonNuclear Munitions with Structures*, pages 49–53, Colorado, United States. U.S. Air Force Academy, Springs.

Bažant, Z. and Steffens, A. (2000). Mathematical model for kinetics of alkali-silica reaction in concrete. *Cement and Concrete Research*, 30(3):419–428.

Bažant, Z., Zi, G., and Meyer, C. (2000). Fracture mechanics of ASR in concretes with waste glass particles of different sizes. *ASCE Journal of Engineering Mechanics*, 126(3):226–232.

Ben Haha, M. (2006). *Mechanical effects of alkali silica reaction in concrete studied by SEM-image analysis*. PhD thesis, Èncole Polytechnique Fèdèrale de Lusanne, Lusanne, Switzerland.

Benveniste, Y. (1987). A new approach to the application of Mori-Tanaka theory in composite materials. *Mechanics of Materials*, 6(2):147–157.

Berra, M., Faggiani, G., Mangialardi, T., and Paolini, A. (2010). Influence of stress restraint on the expansive behaviour of concrete affected by alkali-silica reaction. *Cement and Concrete Research*, 40(9):1403–1409.

Böhm, H. (2015). A short introduction to basic aspects of continuum micromechanics. Technical report, ILSB Report 206.

Budiansky, B. and O'Connell, R. (1976). Elastic moduli of a cracked solid. *International Journal of Solids and Structures*, 12(2):81–97.

Capra, B. and Bournazel, J.-P. (1998). Modeling of induced mechanical effects of alkali-aggregate reactions. *Cement and Concrete Research*, 28(2):251–260.

Capra, B. and Sellier, A. (2003). Orthotropic modelling of alkali-aggregate reaction in concrete structures: numerical simulations. *Mechanics of materials*, 35(8):817–830.

CEB-FIP (1993). *Model Code 1990 (MC90).* Thomas Telford, London, United Kingdom.

CEB-FIP (2011). *Model Code for Concrete Structures (MC2010).* International Federation for Structural Concrete (fib), Lausanne, Switzerland.

Charlwood, R. (1994). A review of alkali aggregate in hydro-electric plants and dams. *Hydropower Dams*, 5:31–62.

Charpin, L. (2013). *Modèle micromécanique pour l'étude de l'anisotropie de la réaction alcali-silice.* PhD thesis, Université Paris-Est, Paris, France.

Charpin, L. and Ehrlacher, A. (2012). A computational linear elastic fracture mechanics-based model for alkali-silica reaction. *Cement and Concrete Research*, 42(4):613–625.

Charpin, L. and Ehrlacher, A. (2014). Microporomechanics study of anisotropy of ASR under loading. *Cement and Concrete Research*, 63:143–157.

Clark, L. and Ng, K. (1989). The effects of alaki-silica reaction on the punching shear strength of reinforced concrete slab. In *the 8th International Conference on Alkali Aggregate Reaction (ICAAR8)*, Kyoto, Japan.

Comby-Peyrot, I., Bernard, F., Bouchard, P.-O., Bay, F., and Garcia-Diaz, E. (2009). Development and validation of a 3D computational tool to describe concrete behaviour at mesoscale. application to the alkali-silica reaction. *Computational Materials Science*, 46(4):1163–1177.

Comi, C., Fedele, R., and Perego, U. (2009). A chemo-thermo-damage model for the analysis of concrete dams affected by alkali-silica reaction. *Mechanics of Materials*, 41(3):210–230.

Çopuroğlu, O. (2010). Effect of silica dissolution on the mechanical characteristics of alkali-reactive aggregates. *Journal of Advanced Concrete Technology*, 8(1):5–14.

Çopuroğlu, O. and Schlangen, E. (2007). Modelling of effect of ASR on concrete microstructure. *Key Engineering Materials*, 348:809–812.

Coussy, O. (2005). Poromechanics of freezing materials. *Journal of the Mechanics and Physics of Solids*, 53(8):1689–1718.

De Jong, M., Belletti, B., Hendriks, M., and Rots, J. (2009). Shell elements for sequentially linear analysis: lateral failure of masonry structures. *Engineering Structures*, 31(7):1382–1392.

den Uijl, J., Kaptijn, N., and Walraven, J. (2000). Shear resistance of flat slab bridges affected by ASR. In *the 11th International Conference on Alkali Aggregate Reaction (ICAAR11)*, pages 1129–1138, Québec City, Canada.

Dent-Glasser, L. and Kataoka, N. (1981). The chemistry of alkali-aggregate reactions. In *the 5th International Conference on Alkali-Aggregate Reaction in Concrete (ICAAR5)*, volume S252/23, pages 66–75, Cape Town, South Africa.

Deude, V., Dormieux, L., Lemarchand, E., Maghous, S., and Kondo, D. (2001). A micromechanical approach to the nonlinear elastic behaviour of rocks. In *DC Rocks 2001 the 38th US Symposium on Rock Mechanics (USRMS)*. American Rock Mechanics Association.

Diamond, S., Berneyback, R., and Struble, L. (1981). On the physics and chemistry of alkali-silica reactions. In *the 5th International Conference on Alkali-Aggregate Reaction in Concrete (ICAAR5)*, volume S252/22, pages 1–11, Cape Town, South Africa.

Dormieux, L., Kondo, D., and Ulm, F.-J. (2006). *Microporomechanics*. John Wiley & Sons, Chichester, United Kingdom.

Dormieux, L., Lemarchand, E., Kondo, D., and Fairbairn, E. (2004). Elements of poro-micromechanics applied to concrete. *Materials and Structures*, 37(265):31–42.

Dunant, C. (2009). *Experimental and modelling study of the alkali-silica-reaction in concrete*. PhD thesis, École Polytechnique Fédérale de Lausanne, Lausanne, Switzerland.

Dunant, C. and Scrivener, K. (2010). Micro-mechanical modelling of alkali-silica-reaction induced degradation using the AMIE framework. *Cement and Concrete Research*, 40(4):517 – 525. Special Issue: ICAAR 13, Trondheim, Norway, June 16-20, 2008.

Esposito, R., Anaç, C., Hendriks, M., and Çopuroğlu, O. (2015). The influence of alkali-silica reaction on the mechanical degradation of concrete. Accepted for publication in ASCE Journal of Materials in Civil Engineering.

Esposito, R. and Hendriks, M. (2012). Degradation of the mechanical properties in ASR-affected concrete: overview and modeling. In *Numerical Modeling Strategies for Sustainable Concrete Structures (SSCS 2012)*, Aix-en-Provence, France.

Esposito, R. and Hendriks, M. (2015). Simulating the deteriorating effect of the alkali-silica reaction in concrete via a micro-poro fracture mechanical model. In *Conference of Mechanics and Physics of Creep, Shrinkage, and Durability of Concrete and Concrete Structures (CONCREEP 10)*, pages 118–127. ASCE Proceedings.

Esposito, R., Hendriks, M., Lilliu, G., and Schreppers, G.-J. (2011). Numerical silulation of concrete structure affected by AAR: The case study of Kariba dam. In *XI ICOLD Benchmarck Workshop on Numerical Analysis of Dams*, Valencia, Spain.

Eurocode 2 (2005). *EN 1992-1-1: Eurocode 2 - Design of concrete structures-Part 1-1: General rules and rules for buildings.*

Fairbairn, E., Ribero, F., Toledo-Filho, R., Lopes, L., and Silvoso, M. (2004). Smeared cracking FEM simulation of alkali silica expansion using a new macroscopic coupled model. In *the 12th International Conference on Alkali-Aggregate Reaction (ICAAR)*, Beijing, China.

Farage, M., Alves, J., and Fairbairn, E. (2004). Macroscopic model of concrete subjected to alkali-aggregate reaction. *Cement and Concrete Research*, 34(3):495–505.

Galli, M. (2014). Modelling of the damage due to alkali-silica reaction in a concrete element. Master's thesis, University of Bologna (in cooperation with delft Universisty of Technology).

Garcia-Diaz, E., Riche, J., Bulteel, D., and Vernet, C. (2006). Mechanism of damage for the alkali-silica reaction. *Cement and Concrete Research*, 36(2):395–400.

Giaccio, G., Zerbino, R., Ponce, J., and Batic, O. (2008). Mechanical behavior of concretes damaged by alkali-silica reaction. *Cement and Concrete Research*, 38(7):993–1004.

Giannini, E. (2012). *Evaluation of concrete structures affected alkali-silica reaction and delayed ettringite formation.* PhD thesis, The University of Texas at Austin, Austin, Texas.

Giannini, E. and Folliard, K. (2012). Stiffness damage and mechanical testing of cores specimens for the evaluation of structures affected by ASR. In *the 14th International Conference on Alkali Aggregate Reaction (ICAAR14)*, Austin, Texas.

Giorla, A. (2013). *Modelling of alkali-silica reaction under multi-axial load.* PhD thesis, École Polytechnique Fédérale de Lausanne, Lausanne, Switzerland.

Giorla, A., Scrivener, K., and Dunant, C. (2015). Influence of visco-elasticity on the stress development induced by alkali-silica reaction. *Cement and Concrete Research*, 70(0):1–8.

Glasser, F. (1992). *The alkali silica reaction in concrete*, chapter Chemistry of the alkali–aggregate reaction, pages 30–53. Blackie and Son Ltd.

Grimal, E., Sellier, A., Le Pape, Y., and Bourdarot, E. (2008a). Creep, shrinkage, and anisotropic damage in alkali-aggregate reaction swelling mechanism-Part I: A constitutive model. *ACI Materials Journal*, 105(3):227–235.

Grimal, E., Sellier, A., Le Pape, Y., and Bourdarot, E. (2008b). Creep, shrinkage, and anisotropic damage in alkali-aggregate reaction swelling-Part II: Identifications of model parameters and applications. *ACI Materials Journal*, 105(3):236–242.

Hagelia, P. (2010). Chemistry of ASR-gels and pore fluids in ultra-accellerated mortar bars: evidence for Si-control on gel expansion properties. In Broekmans, M. and Wigum, B., editors, *the 13th International Conference on Alkali-Aggregate Reactions in Concrete (ICAAR13)*, pages 697–707, Trondheim, Norway.

Hobbs, D. and Gutteridge, W. (1979). Particle size of aggregate and its influence upon the expansion caused by the alkali-silica reaction. *Magazine of Concrete Research*, 31(109):235–242.

Ichikawa, T. and Miura, M. (2007). Modified model of alkali-silica reaction. *Cement and Concrete Research*, 37(9):1291–1297.

Inoue, A., Mikata, Y., Takahashi, Y., and Inamasu, K. (2012). Residual shear capacity of ASR damaged reinforced concrete beams with ruptured stirrups. In *the 14th International Conference on Alkali Aggregate Reaction (ICAAR14)*, Austin, Texas.

International Organization for Standardization (2010). *ISO 1920-10:2010(E) Testing of concrete - Part 10: Determination of static modulus of elasticity in compression.* Geneva, Switzerland.

ISE (1992). *Structural effects of alkali-silica reaction. Technical guidance on the appraisal of existing structures.* SETO Ltd, London, United Kingdom.

Jennings, H., Thomas, J., Rothstein, D., and Chen, J. (2008). *Cements as porous materials*, chapter 6.11, pages 2971–3028. Wiley-VCH Verlag GmbH.

Kagimoto, H., Yasuda, Y., and Kawamura, M. (2014). ASR expansion, expansive pressure and cracking in concrete prisms under various degrees of restraint. *Cement and Concrete Research*, 59:1–15.

Kawamura, M. and Iwahori, K. (2004). ASR gel composition and expansive pressure in mortars under restraint. *Cement and Concrete Composites*, 26(1):47–56.

Klusemann, B. and Svendsen, B. (2010). Homogenization methods for multi-phase elastic composites: Comparisons and benchmarks. *Technische Mechanik*, 30(4):374–386.

Kupfer, H., Hilsdorf, H., and Rusch, H. (1969). Behavior of concrete under biaxial stresses. In *ACI Journal proceedings*, volume 66.

Larive, C. (1998). *Apports combinès de l expèrimentation et de la modèlesllisation á la comprehènsion de l'alcali-rèaction et de ses effets mècaniques.* PhD thesis, Èncole Nationale des Ponts et Chaussèes, Paris, France.

Leemann, A., Le Saout, G., Winnefeld, F., Rentsch, D., and Lothenbach, B. (2011). Alkali-silica reaction: the influence of calcium on silica dissolution and the formation of reaction products. *Journal of the American Ceramic Society*, 94(4):1243–1249.

Leemann, A. and Lura, P. (2013). E-modulus of the alkali-silica-reaction product determined by micro-indentation. *Construction and Building Materials*, 44:221–227.

Léger, P., Côté, P., and Tinawi, R. (1996). Finite element analysis of concrete swelling due to alkali-aggregate reactions in dams. *Computers & Structures*, 60(4):601–611.

Lemarchand, E. (2001). *Contribution de la Micromécanique à l'étude des phénomènes de transport et de couplage poromécanique dans les milieux poreux: Application aux phénomènes de gonflement des géomatériaux.* PhD thesis, Ecole des Ponts ParisTech, Paris, France.

Lemarchand, E., Dormieux, L., and Kondo, D. (2003). A micromechanical analysis of the observed kinetics of ASR-induced swelling in concrete. In Bicanic, N., De Borst, R., Mang, H., and Meschke, G., editors, *Computational Modelling of Concrete Structures (EURO-C)*, pages 483–490, St. Johann im Pongau, Austia. A A Balkema Publisher, Rotterdam.

Lemarchand, E., Dormieux, L., and Ulm, F.-J. (2005). Micromechanics investigation of expansive reactions in chemoelastic concrete. *Philosophical Transactions of the Royal Society A-Mathematical Physical and Engineering Sciences*, 363(1836):2581–2602.

Li, K. and Coussy, O. (2002). Concrete ASR degradation: from material modelling to structure assessment. *Concrete science engineering*, 4(13):35–46.

Lindgård, J. (2013). *Alkali-silica reaction (ASR) - Performance testing.* PhD thesis, Norwegian University of Science and Technology, Trondheinm, Norway.

Liuaudat, J., López, C., and Carol, I. (2014). Diffusion-reaction model for ASR: Formulation and 1D numerical implementation. In Bićanić, N., Mang, H., Meschke, G., and de Borst, R., editors, *Computational Modelling of Concrete Structures (EURO-C)*, St Anton am Alberg. CRC Press, Taylor & Francis Group.

Malla, S. and Wieland, M. (1999). Analysis of an arch-gravity dam with a horizontal crack. *Computers & Structures*, 72:267–278.

Mazars, J. (1986). A description of micro- and macroscale damage of concrete structures. *Engineering Fracture Mechanics*, 25(5):729–737.

Mihai, I. (2012). *Micromechanical constitutive models for cementitious composite materials.* PhD thesis, Cardiff University, Cardiff, United Kindom.

Mihai, I. and Jefferson, A. (2011). A material model for cementitious composite materials with an exterior point Eshelby microcrack initiation criterion. *International Journal of Solids and Structures*, 48(24):3312–3325.

Moesen, M. (2011). MMTensor package documentation - version 1. http://nl.mathworks.com/matlabcentral/fileexchange/32891-mmtensor-1-0.

Monette, L. (1997). Effects of the alkali-silica reaction on unloaded, statically loaded and dynamically loaded reinforced concrete beams. Master's thesis, University of Ottawa, Ottawa, Canada.

Multon, S. (2004). *Evaluation expèrimental et thèorique des effets mècaniques de l'alcali-rèaction sur des structures modéles.* PhD thesis, Universitè de Marne-la-Vallèe (in collaboration with LCPC-EDF), Champs sur Marne, Frace.

Multon, S., Cyr, M., Sellier, A., Diederich, P., and Petit, L. (2010). Effects of aggregate size and alkali content on ASR expansion. *Cement and Concrete Research*, 40(4):508–516.

Multon, S., Sellier, A., and Cyr, M. (2009). Chemo-mechanical modeling for prediction of alkali silica reaction (ASR) expansion. *Cement and Concrete Research*, 39(6):490–500.

Mura, T. (1987). *Micromechanics of defects in solids.* Martinus Nijhoff Publishers.

Nederlands Normalisatie-instituut (2002). *NEN-EN 12390-3 Testing hardened concrete - Part 3: Compressive strength of test specimens.* Delft, The Netherlands.

Nederlands Normalisatie-instituut (2009). *NEN-EN 12390-6 Testing hardened concrete - Part 6: Tensile splitting strength of test specimens.* Delft, The Netherlands.

Nguyen, M., Timothy, J., and Meschke, G. (2014). Numerical analysis of multiple ion species diffusion and alkali-silica reaction in concrete. In Bićanić, N., Mang, H., Meschke, G., and de Borst, R., editors, *Computational Modelling of Concrete Structures (EURO-C)*, St Anton am Alberg. CRC Press, Taylor & Francis Group.

Noret, C., Carrere, A., Molin, X., and Meriott, P.-Y. (2011). Synthesis report on ICOLD benchmarck theme A: effect of concrete swelling on the equilibrium and displacement of an arch dam. In *XI ICOLD Benchmarck Workshop on Numerical Analysis of Dams*, Valencia, Spain.

Pan, J., Feng, Y., Wang, J., Sun, Q., Zhang, C., and Owen, D. (2012). Modeling of alkali-silica reaction in concrete: a review. *Frontiers of Structural and Civil Engineering*, 6(1):1–18.

Pantazopoulou, S. and Thomas, M. (1999). Modeling stress-strain behavior of concrete damaged by alkali-aggregate reaction (AAR). *ACI Structural Journal*, 96(5):790–798.

Pesavento, F., Gawin, D., Wyrzykowski, M., Schrefler, B., and Simoni, L. (2012). Modeling alkali-silica reaction in non-isothermal, partially saturated cement based materials. *Computer Methods in Applied Mechanics and Engineering*, 225:95–115.

Pichler, B. and Hellmich, C. (2011). Upscaling quasi-brittle strength of cement paste and mortar: A multi-scale engineering mechanics model. *Cement and Concrete Research*, 41(5):467–476.

Pierard, O., Friebel, C., and Doghri, I. (2004). Mean-field homogenization of multi-phase thermo-elastic composites: a general framework and its validation. *Composites Science and Technology*, 64:1587–1603.

Pignatelli, R., Comi, C., and Monteiro, P. (2013). A coupled mechanical and chemical damage model for concrete affected by alkali–silica reaction. *Cement and Concrete Research*, 53:196–210.

Poyet, S., Sellier, A., Capra, B., Foray, G., Torrenti, J.-M., Cognon, H., and Bourdarot, E. (2007). Chemical modelling of alkali silica reaction: Influence of the reactive aggregate size distribution. *Materials and Structures*, 40(2):229–239.

Puatatsananon, W. and Saouma, V. (2013). Chemo-mechanical micromodel for alkali-silica reaction. *ACI Materials Journal*, 110(1):67–77.

Reinhardt, H. and Mielich, O. (2011). A fracture mechanics approach to the crack formation in alkali-sensitive grains. *Cement and Concrete Research*, 41(3):255–262.

RILEM TC 219-ACS Alkali-Silica Reaction in Concrete Structures (2011). *RILEM Recommended Test Method: AAR-3 - Detection of potential alkali-reactivity - 38^{o}C test method for aggregate combinations using concrete prisms (Final draft).*

Rivard, P., Ollivier, J.-P., and Ballivy, G. (2002). Characterization of the ASR rim: application to the Potsdam sandstone. *Cement and Concrete Research*, 32(8):1259–1267.

Sanchez, L., Fournie, B., Jolin, M., and Duchesne, J. (2015). Reilable quantification of AAR damage through assessment of Damage Rating Index (DRI). *Cement and Concrete Research*, 67:74–92.

Sanchez, L., Fournier, B., Jolin, M., and Bastien, J. (2014a). Evaluation of the stiffness damage test (SDT) as a tool for assessing damage in concrete due to ASR: Test loading and output responses for concretes incorporating fine or coarse reactive aggregates. *Cement and Concrete Research*, 56:213–229.

Sanchez, L., Multon, S., Sellier, A., Cyr, M., Fournier, B., and Jolin, M. (2014b). Comparative study of a chemo-mechanical modeling for alkali silica reaction (ASR) with experimental evidences. *Construction and Building Materials*, 72:301–315.

Saouma, V. (2013). *Numerical Modeling of AAR.* CRC Press.

Saouma, V. and Perotti, L. (2006). Constitutive model for alkali-aggregate reactions. *ACI Materials Journal*, 103(3):194–202.

Saouma, V. and Xi, Y. (2004). Literature review of alkali aggregate reactions in concrete dams. Technical Report CU/SA-XI-2004/001, Swiss Federal Office for Water and Geology FOWG.

Sargolzahi, M., Kodjo, S., Rivard, P., and Rhazi, J. (2010). Effectiveness of nondestructive testing for the evaluation of alkali silica reaction in concrete. *Construction and Building Materials*, 24(8):1398 – 1403.

Schlangen, E. and Copuroğlu, O. (2010). Modeling of expansion and cracking due to ASR with a 3D lattice model. In *Fracture Mechanics of Concrete and Concrete Structures (FramCos7)*, Seoul, Korea. Korea Concrete Institute.

Schlangen, E. and Van Breugel, K. (2005). Prediction of tensile strength reduction of concrete due to ASR. In *Third international conference on construction materials, performance, innovations and structural implications (ConMat'5)*, Vancouver, Canada.

Schlangen, E. and Van Mier, J. (1992). Experimental and numerical analysis of micromechanisms of fracture of cement-based composites. *Cement and Concrete Composites*, 14(2):105–118.

Sims, I. and Nixon, P. (2003). RILEM recommended test method AAR-0: Detection of alkali-reactivity potential in concrete - outline guide to the use of RILEM methods in assessments of aggregates for potential alkali-reactivity. *Materials and Structures*, 36(7):472–479.

Stemland, H. (2013). Nautesund bru. Technical Report 3D0593, SINTEF, Richard Birkelands vei 3, 7465 Trondheim, Norway. Translated in English by Rodum, E.

Suwito, A., Jin, W., Xi, Y., and Meyer, C. (2002). A mathematical model for the pessimum size effect of ASR in concrete. *Concrete Science and Engineering*, 4(13):23–34.

Swamy, R. and Al-Asali, M. (1988). Engineering properties of concrete affected by alkali-silica reaction. *ACI Materials Journal*, 85(5):367–374.

Swamy, R. N. (1992). *The alkali-silica reaction in concrete.* CRC Press.

Thompson, G., Charlwood, R., Steele, R., and Curtis, D. (1994). Mactaquac generating station intake and spillway remedial measures. In *the 18th International Congress on Large Dams*, volume 1, pages 347–368, Durban, South Africa.

Tirabassi, A. (2013). Numerical assessment of concrete bridge elements suffering from alkali-silica reaction. Master's thesis, University of L'Aquila (in cooperation with delft Universisty of Technology).

Todorovic, M. (2013). Numerical and analytical homogenization approaches in the framework of multi-scale analyses of heterogeneous materials. Master's thesis, University of Bologna (in cooperation with delft Universisty of Technology).

Ulm, F.-J. (2014). Micro-poro-fracture-mechanics. Personal comunication MIT/CEE/1-263.

Ulm, F.-J., Abuhaikal, M., Petersen, T., and Pellenq, R. (2014). Poro-chemo-fracture-mechanics… bottom-up: Application to risk of fracture design of oil and gas cement sheath at early ages. In *Computational Modelling of Concrete Structures (EURO-C)*, volume 1, page 61, St. Anton am Arlberg, Austria. CRC Press.

Ulm, F.-J., Coussy, O., Li, K., and Larive, C. (2000). Thermo-chemo-mechanics of ASR expansion in concrete structures. *ASCE Journal of Engineering Mechanics*, 126(3):233–242.

Ulm, F.-J., Petrson, M., and Lemarchand, E. (2002). Is ASR-expansion caused by chemoporoplastic dilatation? *Computer Science and Engineering*, 4(13):47–55.

Wang, H. and Gillott, J. (1991). Mechanism of alkali-silica reaction and the significance of calcium hydroxide. *Cement and Concrete Research*, 21(4):647–654.

Weiberger, C., Cai, W., and Barnett, D. M. (2005). Elastic of microscopic structures. Stanford University.

Winnicki, A. and Pietruszczak, S. (2008). On mechanical degradation of reinforced concrete affected by alkali-silica reaction. *Journal of Engineering Mechanics*, 134(8):611–627.

Winnicki, A., Seręga, S., and Norys, F. (2014). Chemoplastic modelling of alkali-silica reaction (ASR). In *Computational Modelling of Concrete Structures (EURO-C)*, volume 2, pages 765–774, St. Anton am Arlberg, Austria. CRC Press.

Wu, T., Temizer, I., and Wriggers, P. (2014). Multiscale hydro-thermo-chemo-mechanical coupling: Application to alkali-silica reaction. *Computational Materials Science*, 84:381–395.

Zhang, C., Wang, A., Tang, M., Wu, B., and Zhang, N. (1999). Influence of aggregate size and aggregate size grading on asr expansion. *Cement and Concrete Research*, 29(9):1393–1396.

Applications of Models Based on Concrete Expansion

A

To investigate the behaviour of ASR-affected concrete structures, a concrete expansion-based model was first selected in this thesis work. These preliminary analyses the subsequent work on the pressure-based multiscale material model as presented in the core part of the thesis (Chapter 5). The model ranges between concrete to structural level and uses the induced concrete expansion as starting point. The evolution the imposed expansion in time is described with the kinetic law propose by Ulm et al. (2000). The expansion redistribution effect, consequence of the coupling between the induced expansion and the external mechanical loading, is captured following Saouma and Perotti (2006). The induced expansion is considered as a stress-free deformation and no damage is associated to it. The model was implemented in the finite element software DIANA.

Two case studies are analysed: the Kariba arch dam (Appendix A.1) and the Nautesund bridge (Appendix A.2). In the first case, linear finite element analyses are performed to simulate the structural behaviour. In the second case, non-linear finite element analyses are employed to model the behaviour of affected concrete elements, which were sawn from the bridge and subsequently subject to three point bending testing. The Nautesund bridge represents also the main focus of the experimental campaign developed within the PAT-ASR project.

The case studies highlight the complex behaviour of ASR-affected structures. It results necessary to investigate the phenomenon at concrete level.

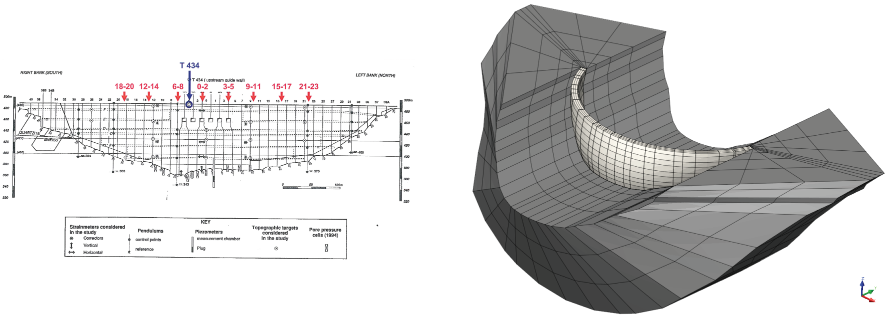

(a) (b)

Figure A.1: The case study of Kariba arch dam: (a) Geometry and monitoring system; (b) Adopted finite element mesh;

A.1 The Case Study of Kariba Arch Dam

The Kariba arch dam is a widely studied benchmark thanks to the large number of monitoring data. The long double curvature arch dam, which was built across the Zambezi river between 1956 and 1959, presented signs of expansion soon after the starting of its operation. A monitoring system was installed to observe the vertical and radial displacement of the dam crest (Figure A.1a).

The structural behaviour is studied by employing finite element analysis (FEA) based on the thermo-chemo-mechanical model (Esposito et al., 2011). A three-dimensional mesh (Figure A.1b) is defined for the dam and the foundation, considering interface elements. A phased analysis is adopted to simulate the construction, the impounding and the operation phases. Due to the limited variation in temperature, the thermal effects are excluded.

Figure A.2 shows the comparison between monitoring data and numerical results in term of vertical and radial displacement of the dam's crest. The former were calibrated to identify the parameters related to the ASR phenomenon, while the latter are model results. The model is not able to capture the global behaviour of the dam; it overestimates the radial displacement.

The adopted approach, which is suitable for practical engineering, is not able to capture the overall behaviour of the structure. The causes can be identified in linear behaviour of the material as well as in the exclusion of long term effects, such as creep (Noret et al., 2011). However, to capture this effects at structural level phenomenological laws are often adopted. These laws employ a large number of input parameters, which calibration requires several experimental observations.

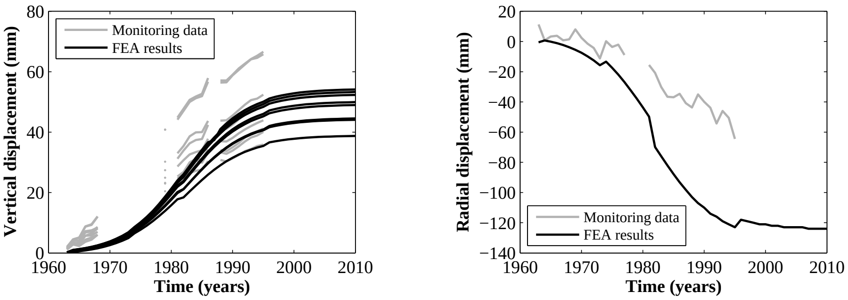

(a) (b)

Figure A.2: Comparison between monitoring data and numerical results for the case study of Kariba arch dam: (a) Vertical crest displacement; (b) Radial crest displacement.

A.2 The Case Study of Nautesund Bridge

The Nautesund bridge, formerly located in Oslo (Norway), was object of several field and laboratory investigations involving micro to macroscopic observations. The structure represented the main object of the PAT-ASR project, which includes this thesis work. Since it was possible to identify the aggregate source, the concrete mix was recovered and subsequently replicated in laboratory (Anaç et al., 2012a). During the bridge demolition in 2009, beam elements (Figure A.3) were sawn cut and tested in laboratory under three-point bending (Stemland, 2013).

The thermo-chemo-mechanical model prosed by Saouma and Perotti (2006) is used to simulate the behaviour of the extracted beam elements. Two- and three-dimensional non-linear FEA are carried out with the DIANA software (Galli, 2014; Tirabassi, 2013). A phased analysis is adopted to simulate first the in-situ phase of the structural element as part of the bridge and second the laboratory test. The imposed concrete expansion is considered both as a isotropic deformation and an anisotropic deformation correlated to the stress state of the material. The input parameters adopted to define the kinetic law are derived by the laboratory experimental results of the replicated concrete mixes design (Chapter 4, Anaç et al. (2012a)). The non-linear behaviour of concrete is captured with a smeared rotating crack model.

Figure A.4 shows the numerical results during the bending test phase. The numerical results are presented in terms of mid-span displacement and the maximum force achieved during the experiment is reported. By considering the expansion redistribution effect, both two- and three-dimensional analyses provide an estimate of the capacity that is closer to the experimental data. No yielding

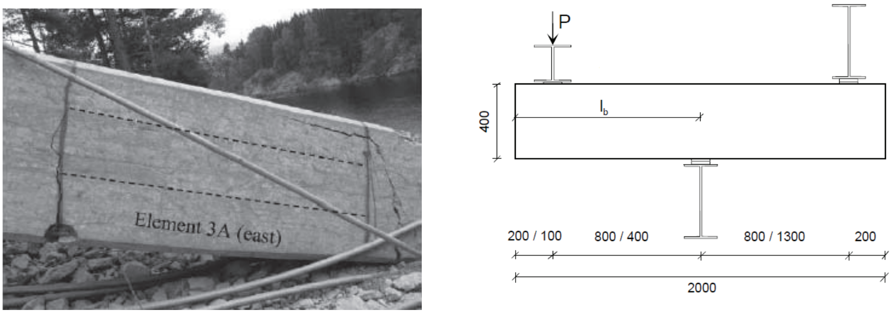

(a) (b)

Figure A.3: The case study of Nautesund bridge: (a) Sawn cut beam element; (b) Three-point bending test configuration.

of the reinforcement is observed in the numerical results, while it was observed in the experiments. As reported in Section 2.3, the yielding of reinforcements may be a sign of ASR in concrete elements, because this phenomenon may occur earlier than in unaffected concrete elements.

For this case study, the adopted approach results satisfactory, but a substantial effort was required for the parameters identification. Several institutes over the years studied the problem from petrographic to the structural point of view. This large amount of information promote the Nautesund bridge as a case study for benchmarks. On the contrary, it shows the limitation of the modelling approach, which results case dependent.

A.3 Concluding Remarks

As the assessment of ASR effects in concrete structures is the primary focus of the thesis work, preliminary analyses to simulate the behaviour of structures and structural elements were carried out by adopting a thermo-chemo-mechanical model based on concrete expansion. The model, inspired by the work of Saouma and Perotti (2006),Ulm et al. (2000), is based on phenomenological relationships. A kinetic law is adopted to define the evolution in time of concrete expansion, which results as an imposed stress-free deformation. The swelling redistribution effects is accounted by considering that the expansion along the principal stress axes depends on the stress state of the material.

The model is adopted to study the behaviour of the Kariba arch dam and of structural elements sawn cut by the Nautesund bridge. These two case studies

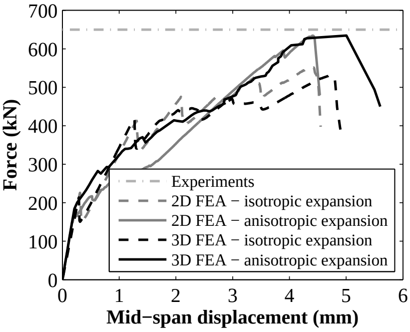

Figure A.4: Comparison between experimental and numerical results for the case study of Nautesund bridge.

allow for the model validation, thanks to the large number of field and laboratory measurements.

The performance of the model results highlights the complex behaviour of ASR-affected structures and rises questions on the applicability of the used phenomenological relationships. As a consequence, the need of a better understanding of the problem at concrete level results necessary. This aspect was further developed within this thesis work as a main objective. Considering the modelling approach, first the 1D expansion-based thermo-chemo-cracking model was developed, as presented in Appendix B. Its focus is on the formulation of a cracking model to describe the damage phenomenon in ASR-affected concrete specimens under free-expansion conditions. By concluding that the multiscale nature of the phenomenon has a large impact on the material behaviour, the attention was moved to the multiscale material model presented in Chapter 5.

1D Expansion-based Thermo-Chemo-Cracking Model[1]

The alkali-silica reaction (ASR) has a large impact on concrete and can generate harmful effects in concrete structures, as described in Chapter 2. During the years engineers and researches developed various modelling approaches to predict the behaviour of affected structures (Chapter 3).

With a focus on the structural assessments, a thermo-chemo-cracking model was first developed in this Ph.D work to correlates the degradation of mechanical properties to the induced expansion. The rheological model is merged within the approach proposed in Appendix A, which adopts the kinetic law proposed by Ulm et al. (2000) to describe the evolution of concrete expansion in time and the relation proposed by Saouma and Perotti (2006) to account for the expansion redistribution effect. The approach aims to describe the mechanical behaviour of both unaffected and affected concretes.

The 1D thinking model consists of two parallel inelastic springs, one of them working in series with the imposed expansion (Appendix B.1). Its parameters are calibrated to predict the evolution of the effective elastic modulus as a function of concrete expansion for the case of specimens stored under free-expansion conditions (Appendix B.2). Subsequently, the approached is adopted to predict the strength degradation for the same case (Appendix B.3). The model results not able to predict sufficiently the deteriorating impact of ASR on concrete (Appendix B.4). To better understand the phenomenon, further investigation is needed at a lower level; thus the viewpoint was moved from the concrete to the aggregate level. These conclusions further motivated the choice of the pressure-based multiscale material model proposed in Chapter 5.

---

[1] This chapter is based on Esposito and Hendriks (2012)

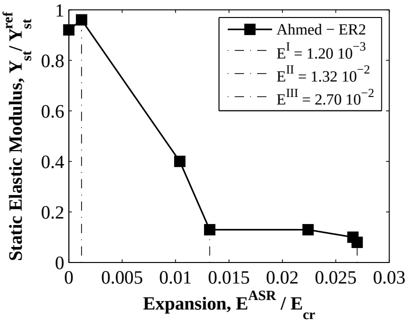

Figure B.1: Considerations regarding the stiffness degradation in unconfined ASR-affected concrete.

B.1 Material Model Description

The model is conceived to work for two main situations: unaffected concrete subjected to mechanical loading and ASR-affected concrete under free-expansion condition. In particular, it is focused on the stiffness degradation and the concrete behaviour in tension. The approach should be able to approximate the known stress-strain relationships observed for unaffected concrete under mechanical loading. In the case of affected concrete, the model should account for the ASR-induced concrete expansion, considering that this mechanism leads only to a partial degradation of the engineering properties (Chapter 4).

To formulate the model for the case of ASR-affected concrete, the mechanical degradation of specimens under free-expansion conditions is analysed. One of the worst case scenario is selected, that is reported by Ahmed et al. (2003). Figure B.1 shows the variation of Young's modulus as a function of expansion strains in terms of normalised values. The stiffness is normalised, as proposed in Chapter 4, with respect to its value at the reference expansion of 0.05% (Table 4.7). The expansion strain is normalised with respect to the cracking strain of undamaged concrete $E_{\mathrm{cr}} = f_{\mathrm{t,in}}/Y_{\mathrm{in}}$. The degradation trend of the stiffness can be summarised in three phases: (1) an initial stage characterised by no expansion and slightly stiffness degradation, (2) a stage of high expansion and degradation rate and (3) a final stage in which both expansion and stiffness reach an asymptotic value.

To describe the deteriorating impact of ASR on concrete in terms of both the expansion and the degradation of mechanical properties, a 1D thermo-chemo-cracking model is adopted. The model (Figure B.2a) consists of two parallel inelastic springs (first and second branch), both possibly subjected to damage. The ASR-induced expansion is modelled using two stress-free expansion cells.

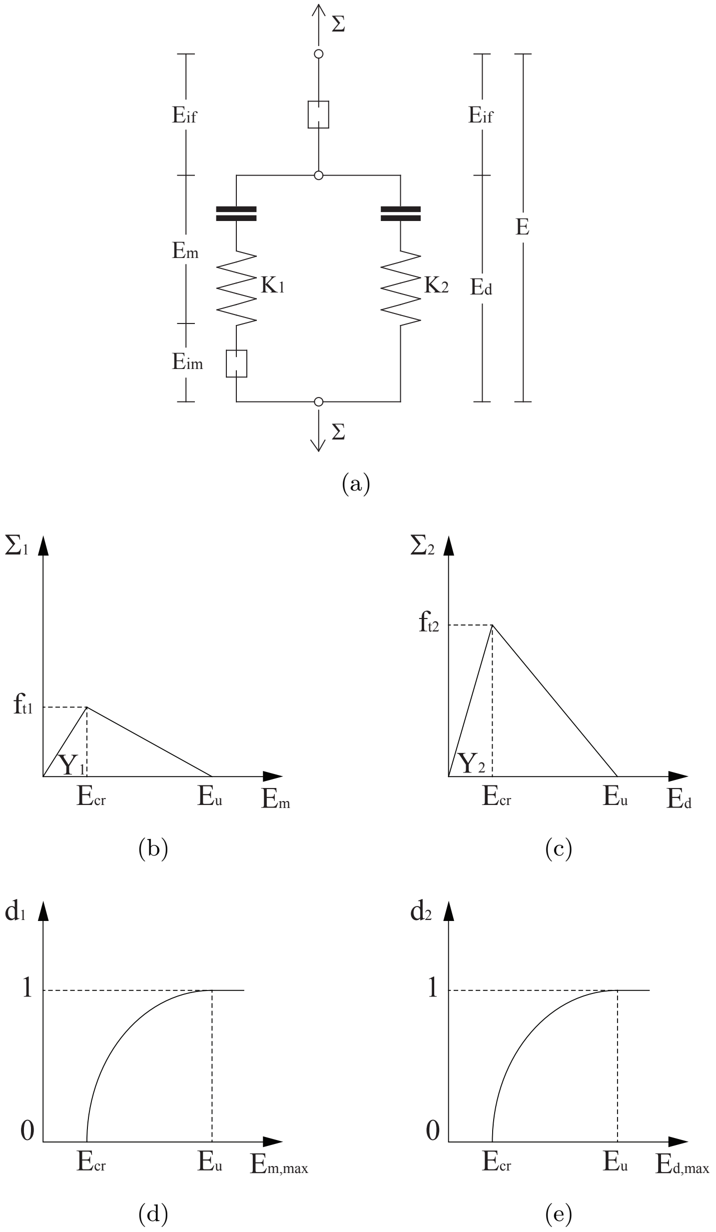

Figure B.2: 1D thermo-chemo-cracking model: (a) Rheological model; (b)-(c) Stress-strain relationship for the first and second branch; (d)-(e) Damage variable in the first and second branch.

One expansion cell (third branch) is placed in series to the two springs. This cell results in expansion without causing internal stresses. The other expansion cell causes internal compression and internal tension stresses in the respective parallel chains. The mechanical effects due to the ASR is considered with a smeared approach. The total strain $\boldsymbol{E}$ is defined as the sum of the strain due to external mechanical loading and the ASR-induced strain. The kinetic law proposed by Ulm et al. (2000) is adopted to define the evolution of the ASR-induced volumetric strain as a function of time and temperature:

$$E_{\mathrm{vol}}^{\mathrm{ASR}} = E_{\mathrm{vol}}^{\infty} \frac{1 - \exp\left(-\frac{t}{t_{\mathrm{c}}}\right)}{1 + \exp\left(\frac{t_{\mathrm{l}} - t}{t_{\mathrm{c}}}\right)} \tag{B.1}$$

where t is the current time, $E_{\mathrm{vol}}^{\infty}$ is the maximum volumetric expansion and t_{c} are t_{l} are the characteristic and the latency time, respectively. The time parameters are defined as a function of the absolute temperature T:

$$t_{\mathrm{c}} = t_{\mathrm{c}}^{\mathrm{ref}} \exp\left[U_{\mathrm{c}}\left(\frac{1}{T} - \frac{1}{T^{\mathrm{ref}}}\right)\right] \tag{B.2a}$$

$$t_{\mathrm{l}} = t_{\mathrm{l}}^{\mathrm{ref}} \exp\left[U_{\mathrm{l}}\left(\frac{1}{T} - \frac{1}{T^{\mathrm{ref}}}\right)\right] \tag{B.2b}$$

with $t_{\mathrm{c}}^{\mathrm{ref}}$ and $t_{\mathrm{l}}^{\mathrm{ref}}$ being respectively the values of the characteristic and the latency time at the reference temperature T^{ref}. The two time variables are correlated to their activation energy U_{c} (5400 ± 500 K) and U_{l} (9400 ± 500 K).

To account for anisotropic behaviour observed for confined affected concrete, the linear expansion along the principal stress directions is defined in agreement with the approach proposed by Saouma and Perotti (2006):

$$E_{ii}^{\mathrm{ASR}} = w_i E_{\mathrm{vol}}^{\mathrm{ASR}} \tag{B.3}$$

where w_i is the weight coefficients along the i-th principal direction, evaluated on the basis of the principal stresses. Here a 1D model is presented, which is evaluated along the i-th direction. For clarity the subscript relative to the principal stress direction is omitted.

The overall stiffness of the model is defined as:

$$Y = (1 - d_1)\, Y_1 + (1 - d_2)\, Y_2 \tag{B.4}$$

where d_1 and d_2 are damage coefficients, which vary between 0 (not damaged system) and 1 (fully damaged system), defined on the basis of the maximum strains during the load history. In both the first and second branch a linear tension softening law is assumed to describe the post-peak behaviour (Figure B.2b and Figure B.2c) and a similar relationship is adopted to describe the evolution of the damage coefficients (Figure B.2d and Figure B.2e):

$$d_1 = d\left(\max E_{\mathrm{m}}\right) \tag{B.5a}$$

$$d_2 = d\left(\max E_{\mathrm{d}}\right) \tag{B.5b}$$

Both the damage coefficients, based on the tension softening law, can be expressed as:

$$d\left(\max E_j\right) = \begin{cases} 0 & E_j \leq E_{\mathrm{cr}} \\ 1 - \frac{E_{\mathrm{cr}}}{E_{\mathrm{u}} - E_{\mathrm{cr}}}\left(\frac{E_{\mathrm{u}}}{E_j} - 1\right) & E_{\mathrm{cr}} < E_j < E_{\mathrm{u}} \\ 1 & E_j \geq E_{\mathrm{u}} \end{cases} \tag{B.6}$$

where E_j is the strain in the j-th branch. The ASR-induced strain is separated in two components: E_{im} associated to the expansion and the damage mechanisms and E_{if} determining only the expansion behaviour:

$$E_{\mathrm{im}} = \alpha E^{\mathrm{ASR}} \tag{B.7a}$$

$$E_{\mathrm{im}} = \left(1 - \alpha + \gamma\right) E^{\mathrm{ASR}} \tag{B.7b}$$

where α is a distribution constant. It is considered that the ASR-induced expansion does not totally contribute to the overall strain, thus the variable γ is introduced. The mechanical strains defining the damage can be expressed as:

$$E_{\mathrm{m}} = E - \left(1 + \gamma\right) E^{\mathrm{ASR}} \tag{B.8a}$$

$$E_{\mathrm{d}} = E - \left(1 - \alpha + \gamma\right) E^{\mathrm{ASR}} \tag{B.8b}$$

The stress-strain relationship results:

$$\begin{aligned} \Sigma &= Y\left(E - E_{\mathrm{if}} - \frac{\left(1 - d_1\right)Y_1}{\left(1 - d_1\right)Y_1 + \left(1 - d_2\right)Y_2} E_{\mathrm{im}}\right) = \\ &= Y\left[E - \left(1 + \gamma - \frac{\left(1 - d_2\right)Y_2}{\left(1 - d_1\right)Y_1 + \left(1 - d_2\right)Y_2}\alpha\right) E^{\mathrm{ASR}}\right] \end{aligned} \tag{B.9}$$

In the case of a specimen under free-expansion condition ($E = E^{\mathrm{ASR}}$ and $\Sigma = 0$), Equation (B.9) leads to the following expression for γ:

$$\gamma = \frac{\left(1 - d_2\right)Y_2}{\left(1 - d_1\right)Y_1 + \left(1 - d_2\right)Y_2}\alpha \tag{B.10}$$

Equation (B.9) combined with Equation (B.4) and Equation (B.10) now defines a damage dependent macroscopic stress-strain relation with an explicit input of the

ASR-induced strain E^{ASR}. The damage evolution is defined by Equation (B.5) and Equation (B.6). In the commonly used displacement-based finite element method, the strains E and E^{ASR} are supposed to be known within each Newton-Raphson iteration. A simple iterative process is needed to solve for the updated damage values (d_1, d_2) in the range $0 \leq d \leq 1$. Eventually, Equation (B.9) defines the stress update.

B.2 Calibration Procedure

To correlate the model's parameters, Y_1, Y_2 and α, to the material properties of concrete, the model is calibrated considering two main situations: unaffected concrete subjected to mechanical load and ASR-affected concrete under free-expansion condition. For both the situations a straightforward relation can be established between the stiffness' value in the first, Y_1, and second, Y_2, branch and the initial value of the Young's modulus, Y_{in}:

$$Y_{\mathrm{in}} = Y_1 + Y_2 \tag{B.11}$$

In the case of unaffected concrete ($E^{\mathrm{ASR}} = 0$), the model is transformed in an equivalent single damaging spring model with initial stiffness Y_{in}. The damage is then controlled by a single damage parameter $d = d_1 = d_2$, which evolution law makes use of the material properties E_{cr} and E_{u} for softening concrete based on a regularized fracture energy.

In the case of affected concrete under free-expansion condition ($E = E^{\mathrm{ASR}}$ and $\Sigma = 0$), the main observations shown in Figure B.1 should be compatible with the proposed damage laws in Figure B.2e. In this case the spring in the first branch is in compression, thus no damage can occur in this branch ($d_1 = 0$). Moreover the stresses in the first and second branch are balanced ($\Sigma = 0$). Two states of the system are considered: when the damage starts and when it is finished. First the case $E^{\mathrm{ASR}} = E^{\mathrm{I}}$ is considered:

$$E = E^{\mathrm{ASR}} = E^{\mathrm{I}} \quad \rightarrow \quad E_{\mathrm{m}}\left(\Sigma = 0, d_2 = 0\right) = E_{\mathrm{cr}} \tag{B.12}$$

Combining Equation (B.12) and Equation (B.8b), the parameter α can be calculated as:

$$\alpha = \frac{Y_1 + Y_2}{Y_1} \frac{E_{\mathrm{cr}}}{E^{\mathrm{I}}} \tag{B.13}$$

Second the case $E^{\mathrm{ASR}} = E^{\mathrm{II}}$ is considered:

$$E = E^{\mathrm{ASR}} = E^{\mathrm{II}} \quad \rightarrow \quad E_{\mathrm{m}}\left(\Sigma = 0, d_2 = 1\right) = E_{\mathrm{u}} \tag{B.14}$$

Combining Equation (B.14) and Equation (B.8b), the parameter α can be calculated as:

$$\alpha = \frac{E_\mathrm{u}}{E^\mathrm{II}} \tag{B.15}$$

Considering Equation (B.13) and Equation (B.15), the residual normalised stiffness $\overline{\beta_\mathrm{Y}}$ can be defined as:

$$\overline{\beta_\mathrm{Y}} = \frac{Y_1}{Y_\mathrm{in}} = \frac{E^\mathrm{II}}{E^\mathrm{I}} \frac{E_\mathrm{cr}}{E_\mathrm{u}} \tag{B.16}$$

Eventually, the material parameters Y_1, Y_2 and α can be expressed as a function of the residual normalised stiffness $\overline{\beta_\mathrm{Y}}$:

$$Y_1 = \overline{\beta_\mathrm{Y}} Y_\mathrm{in} = \frac{E^\mathrm{II}}{E^\mathrm{I}} \frac{E_\mathrm{cr}}{E_\mathrm{u}} \tag{B.17a}$$

$$Y_2 = Y_\mathrm{in} - Y_1 = \left(1 - \overline{\beta_\mathrm{Y}}\right) Y_\mathrm{in} \tag{B.17b}$$

$$\alpha = \frac{E_\mathrm{u}}{E^\mathrm{II}} = \frac{1}{\overline{\beta_\mathrm{Y}}} \frac{E_\mathrm{cr}}{E^\mathrm{I}} \tag{B.17c}$$

B.3 Simulation of Mechanical Degradation due to ASR

The model is adopted to simulate the degradation of stiffness and strength for ASR-affected concrete under free-expansion condition. The case analysed by Ahmed et al. (2003) is chosen. Table B.1 lists the material parameters of the model. The evaluation of the normalised residual stiffness value $\overline{\beta_\mathrm{Y}}$ through Equation (B.16) results in agreement with the experimental observations (Figure B.1).

Figure B.3 shows the comparison between the model results and the experimental findings. The prediction of the stiffness degradation (Figure B.3a), but they are insufficient in the prediction of the strength behaviour (Figure B.3b). This is a direct consequence of assuming the same residual fractional value for the stiffness and the strength ($\overline{\beta_\mathrm{Y}} = \overline{\beta_\mathrm{t}}$).

The results are further compared with the model proposed by Saouma and Perotti (2006), who calculate the degradation of the stiffness and strength with a sinusoidal time-dependent curve. They consider the residual normalised properties $\overline{\beta_\mathrm{Y}}$ and $\overline{\beta_\mathrm{t}}$ as input parameters, which are assumed in this comparison equal to 0.11 and 0.60, respectively. The formulation proposed by Saouma and Perotti (2006) requires the definition of two different residual fractional values for the two parameters, thus the degradation of stiffness and strength is well predicted for expansion strains close to the maximum value. However, this approach cannot predict the initial delay of the degradation and underestimates the degradation during the reaction development.

Table B.1: Input and calibrated parameters for the 1D thermo-chemo-cracking model.

Property	Value	Unit	Reference
Input parameters			
Concrete Young's modulus, Y_{in}	22.1	GPa	Ahmed et al. (2003)
Concrete tensile strength, $f_{\mathrm{t,in}}$	1.42	MPa	Ahmed et al. (2003)
Concrete compressive strength, $f_{\mathrm{c,in}}$	41.2	MPa	Ahmed et al. (2003)
Crack spacing, h	30	mm	Ahmed et al. (2003)
Macroscopic fracture energy, G_{f}	0.143	N/mm	CEB-FIP (2011)
Cracking strain, E_{cr}	$6.43\ 10^{-5}$		$E_{\mathrm{cr}} = f_{\mathrm{t,in}}/Y_{\mathrm{in}}$
Ultimate strain, E_{u}	$6.76\ 10^{-3}$		$E_{\mathrm{u}} = E_{\mathrm{cr}} + (2G_{\mathrm{f}})\,/\,(hf_{\mathrm{t,in}})$
ASR strain at point I, E^{I}	$1.20\ 10^{-3}$		Ahmed et al. (2003)
ASR strain at point II, E^{II}	$1.32\ 10^{-3}$		Ahmed et al. (2003)
Residual normalised stiffness, β_{Y}	0.11		Equation (B.16)
Calibrated parameters			
Stiffness in the first branch, Y_1	2.31	GPa	
Stiffness in the second branch, Y_2	19.8	GPa	
Distribution coefficient, α	0.51		

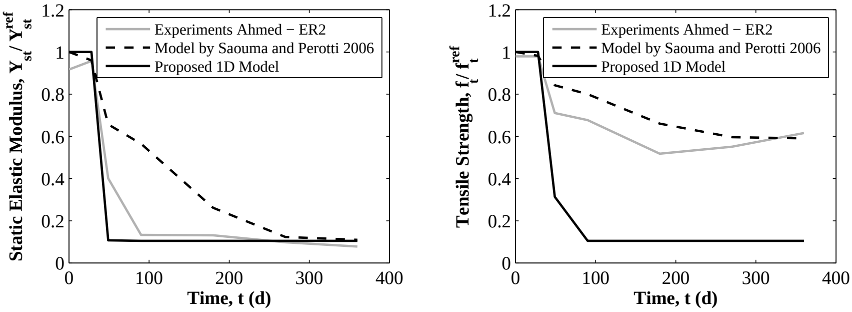

(a) (b)

Figure B.3: Simulation results of 1D thermo-chemo-cracking model: (a) Static elastic modulus degradation; (b) Tensile strength degradation.

B.4 Concluding Remarks

The assessment of ASR-affected concrete structures is often studied via numerical approaches developed at concrete level. In the last decades, several researchers developed practical engineering models to predict the structural behaviour. These models focus on the correlation between ASR-induced expansion, environmental and boundary conditions. In some cases, the chemical reaction is accounted via phenomenological kinetics law.

The practical engineering models primarily consider the deteriorating impact of ASR as an induced expansion without properly accounting for the degradation of mechanical properties. At the contrary, experimental investigations reported a substantial degradation of stiffness and strength properties (Chapter 4).

To account for the correlation between the ASR-induced expansion and the degradation of mechanical properties, a 1D expansion-based thermo-chemo-cracking material model is presented. This model is suitable for both unaffected and affected concrete. The rheological model consists of three branches, two placed in parallel and third one placed in series with the previous two. Stress-free expansion cells are introduced to model the ASR-induced strain. The equilibrium between the gel and the concrete skeleton under free-expansion condition is provided from the two springs placed in parallel. Two damage cells are introduced to define the degradation due to the external mechanical load and the ASR.

To validate the model, the worst case scenario is considered for the ASR-affected concrete. The experimental test performed by Ahmed et al. (2003) are considered. The comparison provides a good results in terms of stiffness. The model cannot predict completely the behaviour in terms of strength degradation, because the same residual fractional value for stiffness and strength is adopted. The comparison with the approach proposed by Saouma and Perotti (2006) suggest that two different values should be taken in account.

This simplified approach results unsatisfactory for the prediction of the deteriorating impact of the ASR on concrete. The phenomenon results to complex to be understood at the material level. For a better understanding, the viewpoint should be moved from the concrete to the aggregate level. However, the new approach should be formulated within the perspective of structural assessments.

Detailed Experimental Results

This appendix reports the main experimental results, presented in Chapter 4, related to RR1 and RR2 concretes, made with Dutch and Norwegian aggregates, respectively. Concrete expansions and mechanical properties are determined after exposure of the specimens for 14, 28, 49, 91, 182, 252 and 364 days to accelerated conditions. Each property is derived as the average of the results on three specimens (Table C.1 and Table C.2).

The accelerated expansion tests (Figure C.1) have been performed on 75x75x280 mm prisms in agreement with RILEM recommendation AAR-3 (2011). The mechanical properties (Figure C.2, Figure C.3, Figure C.4 and Figure C.5) have been determined on 100x100x400 mm prisms and on cubes with 150 mm side in agreement with ISO 1920-10:2010(E) (2010) and EN 13290-6:2009 (2009).

Figure C.7, Figure C.8, Figure C.10 and Figure C.11 show the evolution of normal strain, along the loading axis, and transversal strain, parallel to loading direction, during the uniaxial compressive tests, while Figure C.9 and Figure C.12 report the specimen's volume change.

Table C.1: Experimental results for RR1 concrete (Dutch aggregates).

Expansion, ε (%)							
Time (d)	14	28	49	91	182	252	364
Specimen 1	-0.004	0.000	0.003	0.008	0.030	0.068	0.094
Specimen 2	-0.002	0.002	0.004	0.008	0.042	0.092	0.131
Specimen 3	-0.002	0.003	0.006	0.010	0.036	0.076	0.112
Average	-0.003	0.002	0.005	0.009	0.036	0.079	0.112
Elastic modulus, Y (MPa)							
Time (d)	14	28	49	91	182	252	364
Specimen 1	42605	43388	42910	43119	38292	39502	42151
Specimen 2	41802	41843	42475	43464	41284	40546	39477
Specimen 3	42248	42892	44048	42641	37055	41973	38811
Average	42218	42708	43144	43075	38877	40673	40146
Poisson ratio, ν							
Time (d)	14	28	49	91	182	252	364
Specimen 1	0.19	0.25	0.21	0.19	0.45	0.18	0.18
Specimen 2	0.21	0.17	0.15	0.21	0.18	0.18	0.18
Specimen 3	0.18	0.19	0.43	0.19	0.20	0.17	0.18
Average	0.19	0.20	0.26	0.20	0.28	0.18	0.18
Compressive strength, f_{c} (MPa)							
Time (d)	14	28	49	91	182	252	364
Specimen 1	45.5	48.1	55.4	49.6	61.4	61.8	63.1
Specimen 2	45.2	52.9	52.1	57.4	58.3	61.9	64.7
Specimen 3	46.3	50.8	55.1	53.8	58.2	61.6	61.1
Average	45.7	50.6	54.2	53.6	59.3	61.8	63.0
Compressive peak strain, $\varepsilon^{\mathrm{peak}}$ (‰)							
Time (d)	14	28	49	91	182	252	364
Specimen 1	-1.54	-1.45	-1.72	-1.47	-1.74	-2.03	-1.91
Specimen 2	-1.47	-1.60	-1.57	-1.77	-1.72	-1.89	-2.00
Specimen 3	-1.55	-1.58	-1.63	-1.53	-1.94	-1.97	-1.98
Average	-1.52	-1.54	-1.64	-1.59	-1.80	-1.96	-1.96
Splitting tensile strength, $f_{\mathrm{t,sp}}$ (MPa)							
Time (d)	14	28	49	91	182	252	364
Specimen 1	3.57	3.56	4.26	4.49	3.94	3.60	3.13
Specimen 2	3.85	3.99	3.73	4.13	3.40	3.52	3.36
Specimen 3	4.33	4.01	4.85	4.53	4.20	3.60	3.31
Average	3.92	3.85	4.28	4.38	3.85	3.57	3.27

Table C.2: Experimental results for RR2 concrete (Norwegian aggregates).

Expansion, ε (%)

Time (d)	14	28	49	91	182	252	364
Specimen 1	0.000	0.003	0.010	0.019	0.073	0.128	0.193
Specimen 2	0.000	0.004	0.010	0.017	0.061	0.114	0.168
Specimen 3	0.002	0.005	0.011	0.019	0.066	0.126	0.174
Average	0.001	0.004	0.010	0.018	0.067	0.123	0.178

Elastic modulus, Y (MPa)

Time (d)	14	28	49	91	182	252	364
Specimen 1	28503	30639	33593	27837	23489	16801	17793
Specimen 2	30376	30866	32583	28009	25713	15608	16951
Specimen 3	28610	29886	32941	26432	27180	18581	17553
Average	29163	30464	33039	27426	25460	16997	17433

Poisson ratio, ν

Time (d)	14	28	49	91	182	252	364
Specimen 1	0.21	0.20	0.21	0.23	0.23	0.35	0.24
Specimen 2	0.20	0.21	0.19	0.26	0.26	0.23	0.26
Specimen 3	0.20	0.21	0.48	0.23	0.27	0.24	0.26
Average	0.20	0.21	0.29	0.24	0.25	0.27	0.25

Compressive strength, f_{c} (MPa)

Time (d)	14	28	49	91	182	252	364
Specimen 1	52.6	57.3	59.6	64.5	59.8	58.3	59.9
Specimen 2	53.5	57.9	60.5	65.1	58.4	63.7	57.6
Specimen 3	54.6	60.0	58.9	61.6	61.7	58.1	60.7
Average	53.6	58.4	59.7	63.7	60.0	60.0	59.4

Compressive peak strain, $\varepsilon^{\mathrm{peak}}$ (‰)

Time (d)	14	28	49	91	182	252	364
Specimen 1	-2.50	-2.42	-2.75	-2.92	-2.81	-3.20	-3.47
Specimen 2	-2.53	-2.53	-2.77	-2.89	-2.76	-3.35	-3.62
Specimen 3	-2.75	-2.66	-2.80	-2.52	-2.74	-3.20	-3.90
Average	-2.59	-2.54	-2.77	-2.78	-2.77	-3.25	-3.67

Splitting tensile strength, $f_{\mathrm{t,sp}}$ (MPa)

Time (d)	14	28	49	91	182	252	364
Specimen 1	4.35	4.33	3.33	4.76	3.67	3.78	3.42
Specimen 2	4.33	4.23	4.67	4.16	3.38	3.27	3.13
Specimen 3	4.63	4.27	4.60	4.66	3.47	3.34	3.20
Average	4.44	4.28	4.20	4.53	3.51	3.46	3.25

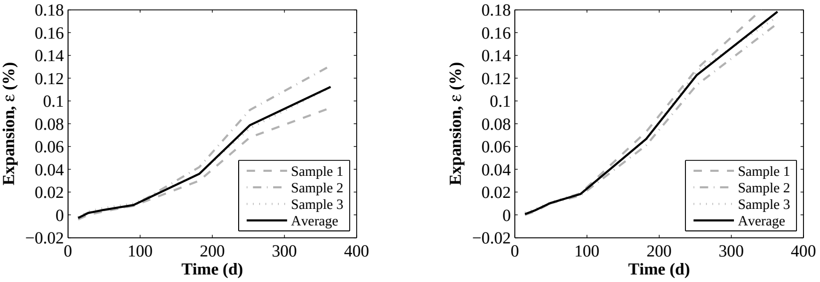

(a) (b)

Figure C.1: Concrete expansion ε: (a) RR1 concrete (Dutch aggregates); (b) RR2 concrete (Norwegian aggregates).

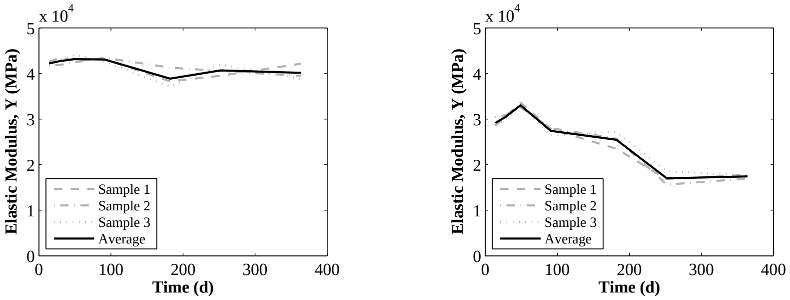

(a) (b)

Figure C.2: Elastic modulus Y: (a) RR1 concrete (Dutch aggregates); (b) RR2 concrete (Norwegian aggregates).

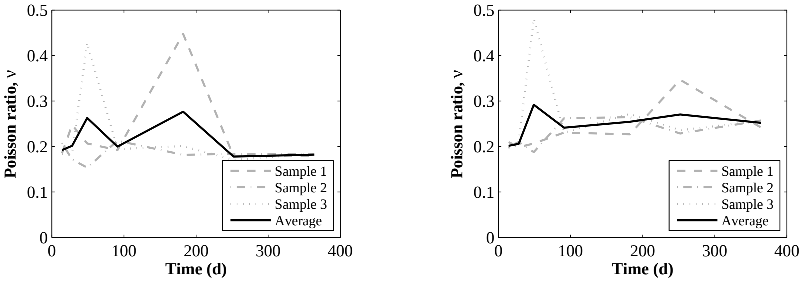

(a)

(b)

Figure C.3: Poisson ratio ν: (a) RR1 concrete (Dutch aggregates); (b) RR2 concrete (Norwegian aggregates).

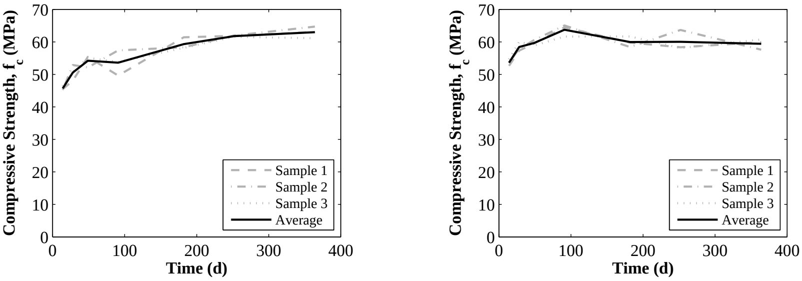

(a)

(b)

Figure C.4: Compressive strength f_c: (a) RR1 concrete (Dutch aggregates); (b) RR2 concrete (Norwegian aggregates).

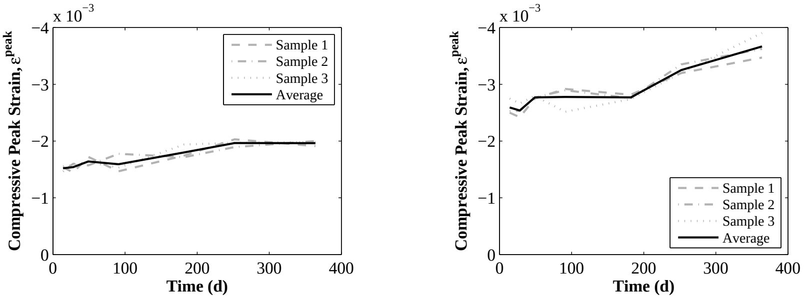

(a) (b)

Figure C.5: Compressive peak strain $\varepsilon^{\text{peak}}$: (a) RR1 concrete (Dutch aggregates); (b) RR2 concrete (Norwegian aggregates).

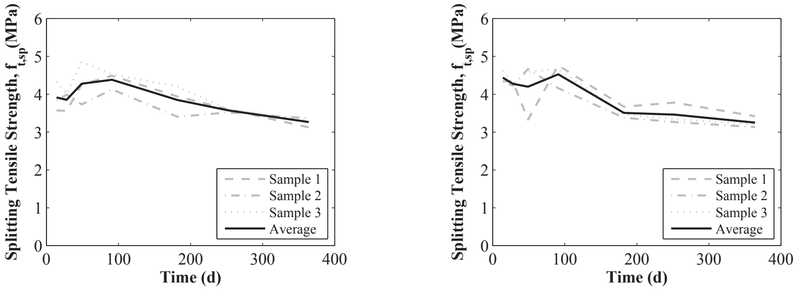

(a) (b)

Figure C.6: Splitting tensile strength $f_{\text{t,sp}}$: (a) RR1 concrete (Dutch aggregates); (b) RR2 concrete (Norwegian aggregates).

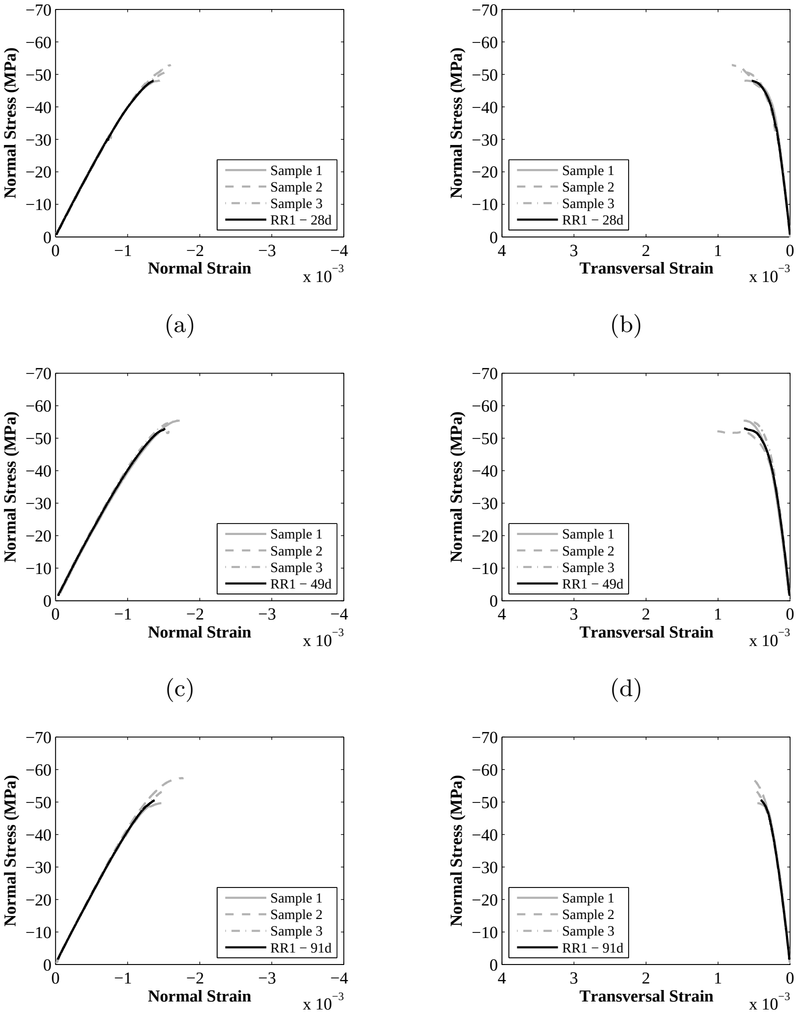

(a) (b)

(c) (d)

(e) (f)

Figure C.7: RR1 mix design (Dutch aggregates): Development of stress and strain in the uniaxial compressive test for specimens exposed to ASR environment for 28 (a)-(b), 49 (c)-(d) and 91 (e)-(f) days.

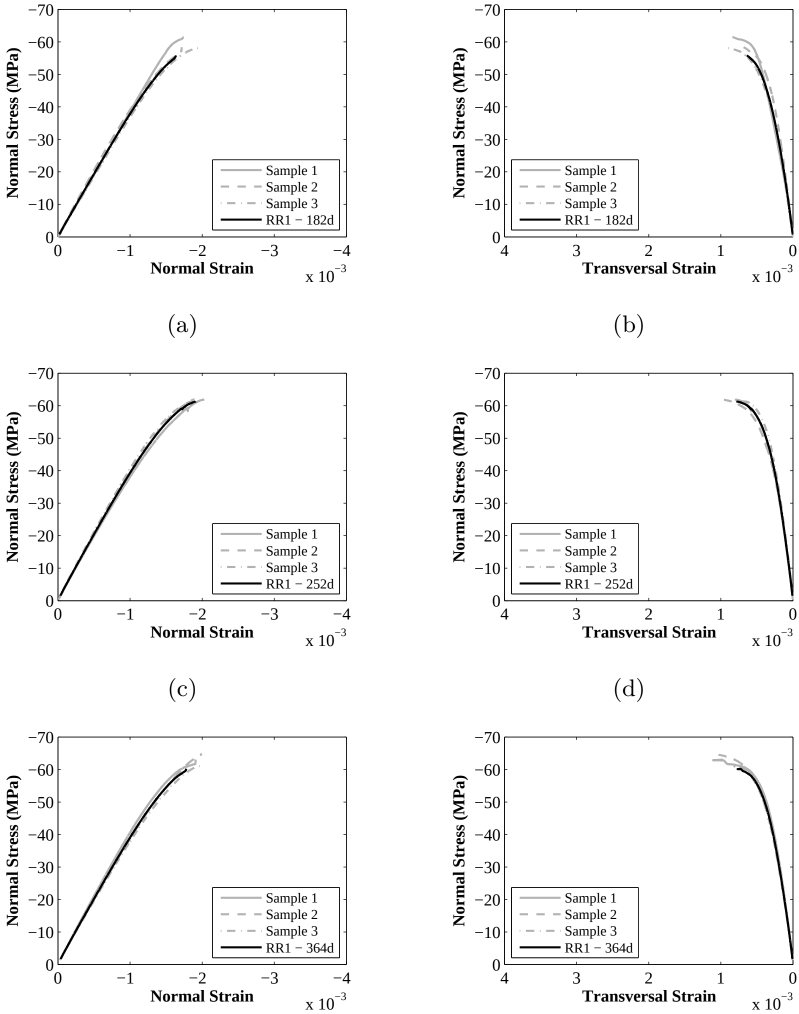

(a) (b)

(c) (d)

(e) (f)

Figure C.8: RR1 concrete (Dutch aggregates): Development of stress and strain in the uniaxial compressive test for specimens exposed to accelerated conditions for 26 (a)-(b), 36 (c)-(d) and 52 (e)-(f) days.

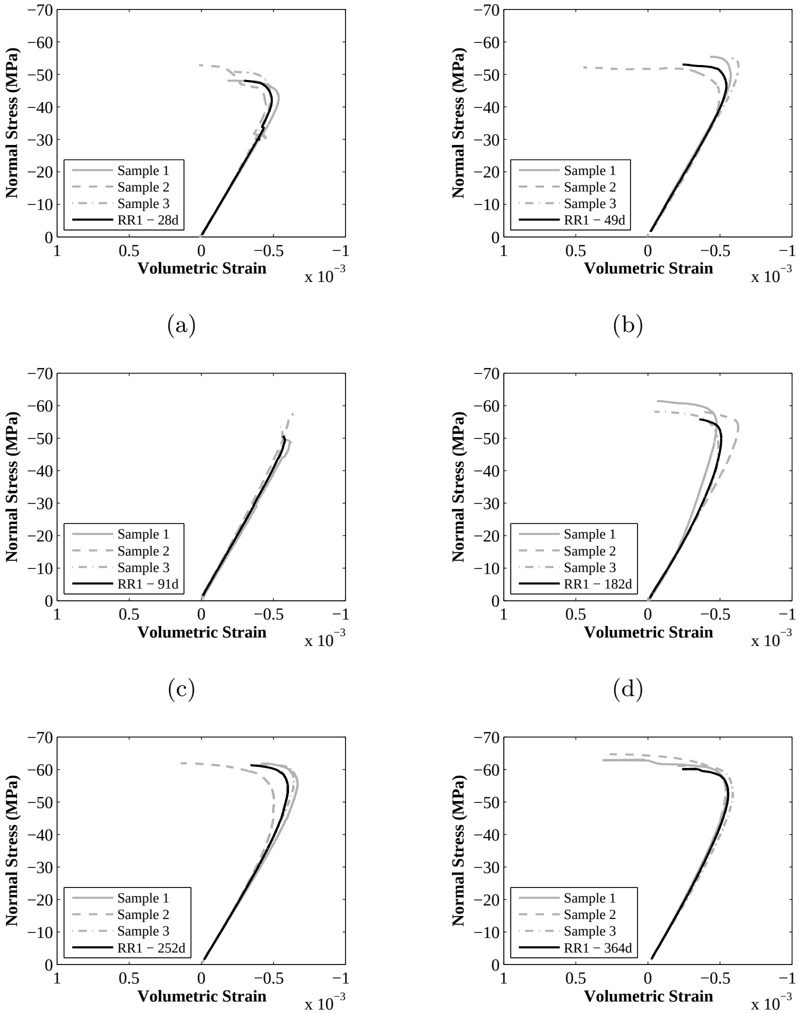

(a) (b)

(c) (d)

(e) (f)

Figure C.9: RR1 concrete (Dutch aggregates): Development of volumetric strain in the uniaxial compressive test for specimens exposed to accelerated conditions for 28 (a), 49 (b), 91 (c), 182 (d), 252 (e) and 364 (f) days.

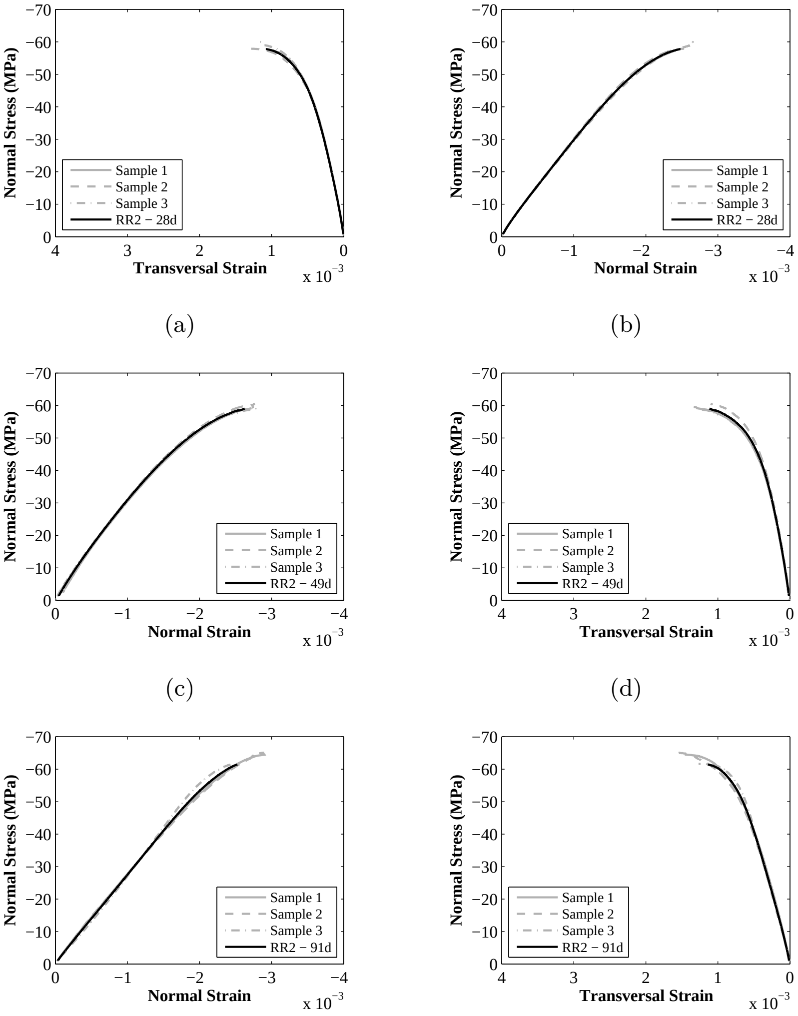

(a) (b)

(c) (d)

(e) (f)

Figure C.10: RR2 concrete (Norwegian aggregates): Development of stress and strain in the uniaxial compressive test for specimens exposed to accelerated conditions for 28 (a)-(b), 49 (c)-(d) and 91 (e)-(f) days.

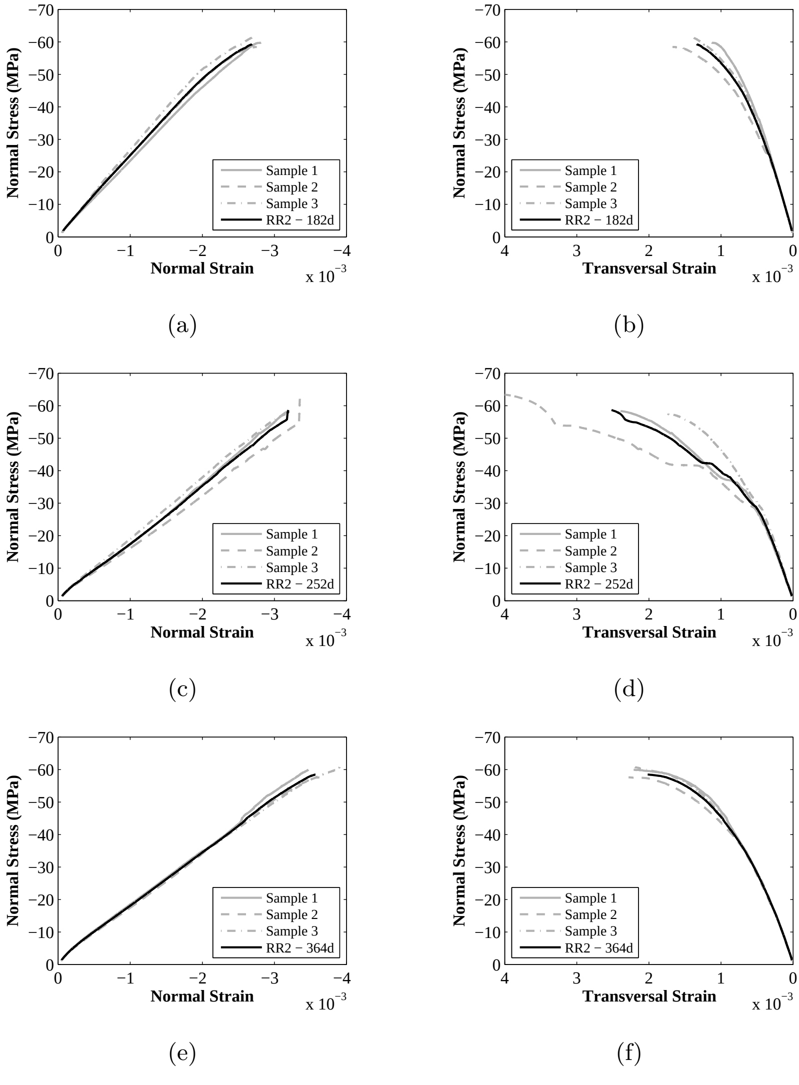

(a) (b)

(c) (d)

(e) (f)

Figure C.11: RR2 concrete (Norwegian aggregates): Development of stress and strain in the uniaxial compressive test for specimens exposed to accelerated conditions for 182 (a)-(b), 252 (c)-(d) and 364 (e)-(f) days.

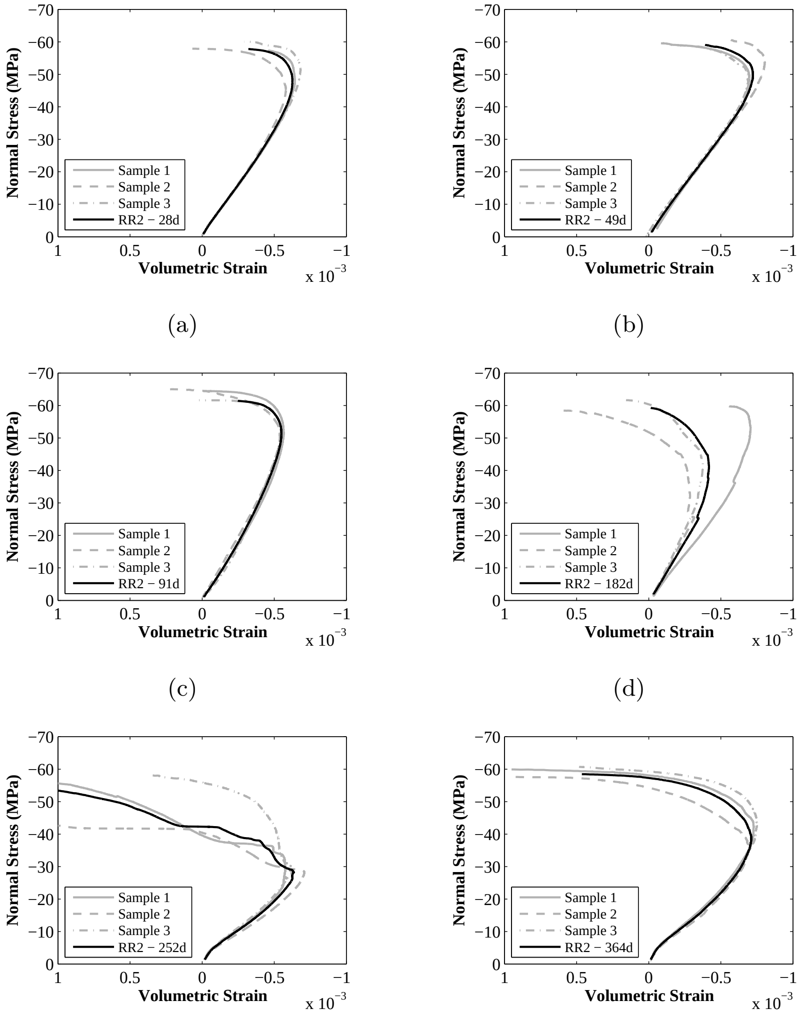

(a) (b)

(c) (d)

(e) (f)

Figure C.12: RR2 concrete (Norwegian aggregates): Development of volumetric strain in the uniaxial compressive test for specimens exposed to accelerated conditions for 28 (a), 49 (b), 91 (c), 182 (d), 252 (e) and 364 (f) days.

Mean-field homogenization methods

D

Engineering, industrial and biological materials (e.g. concrete,composite and bone), which at neked eye appear as homogeneous materials, present inhomogeneity at small length scale. They are composed by dissimilar constituents or phases, which differ in material properties, geometry and topology.

The homogenization theory allows determining the macroscopic effective mechanical properties (e.g. stiffness) of a microscopically heterogeneous material. The complex micro-structure of the material is schematized with a statistically representative elementary volume (REV). The mechanical properties of the material are determined by solving the boundary value problem for the REV.

Mean-field homogenization methods analytically solve the boundary value problem by averaging the local deformation field, determined prior for every inclusion. These methods are characterized by a fast solution method; however, they can be applied only for rather simplified micro-structural arrangements.

Thanks to the technological development, recently numerical homogenization methods were developed. They model both the micro- and macro-structure of the material with the finite element method. These method can describe complex and geometrically irregular micro-structural arrangements; however, they require elevated computational effort and only provide results for the selected micro-structure.

In this appendix the classical mean-field homogenization methods are introduced and subsequently compared with respect to the estimation of the elastic constants of concrete. First, the theoretical background is introduced (Appendix D.1). Afterwards, implementation aspects are described (Appendix D.2). Eventually, a comparison with numerical homogenization methods is addressed (Appendix D.3). This appendix supports the multiscale material model presented in Chapter 5.

D.1 Theoretical Background

Mean-field homogenization methods analytically determine the macroscopic effective property of heterogeneous materials, composed by a regular-shaped inclusions, with a two-stage procedure. They are usually applied to two-phase materials composed by an inclusion phase embedded in a matrix phase. However, they can be extended to multiple-phase materials.

In the first stage, the local (microscopic) problem for a single inclusion is solved by determining the correlation between the microscopic and macroscopic deformations. This problem was solved in closed form by Eshelby for ellipsoidal inclusions (Appendix D.1.1).

In the second stage, the global (macroscopic) field is determined as an average of the local one. Various methods were developed to solve the global problem (Appendix D.1.2), which differ in the study of the interaction between the phases. The dilute scheme assumes that the inclusions are not interacting between themselves, while the Mori-Tanaka scheme allows for a limited interaction between the inclusion phases. The self-consistent scheme accounts for interaction between the inclusions and the matrix phase.

D.1.1 Solution of the Eshelby Problem

Eshelby determined the local deformation field for a single inclusion embedded in a matrix phase (Weiberger et al., 2005). A REV composed by a homogeneous linear elastic material with volume Ω and surface area $\delta\Omega$ is considered (Figure D.1a). The matrix phase is occupying a sub-volume Ω_{m}, while the inclusion phase is located in a sub-volume Ω_i with surface area $\delta\Omega_i$. Both phases are characterized by the same elastic constants. It is assumed that the inclusion is subjected to an uniform permanent (inelastic) deformation, which is characterized by the eigenstrain $\boldsymbol{E}_i^*$

To determine the behaviour of both phases, Eshelby solved an equivalent virtual problem (Figure D.1). First, the inclusions is removed from the system (Figure D.1b), which is described as:

$$\begin{cases} \boldsymbol{E} = 0 \\ \boldsymbol{\Sigma} = 0 \\ \boldsymbol{u} = 0 \end{cases} \tag{D.1a}$$

$$\begin{cases} \boldsymbol{E}_i = \boldsymbol{E}_i^* \\ \boldsymbol{\Sigma}_i = 0 \\ \boldsymbol{u}_i = \boldsymbol{E}^* : \boldsymbol{z} \end{cases} \tag{D.1b}$$

where $\boldsymbol{E}$, $\boldsymbol{\Sigma}$ and $\boldsymbol{u}$ are the strain, stress and displacement in the matrix phase, respectively, while $\boldsymbol{E}_i$, $\boldsymbol{\Sigma}_i$ and $\boldsymbol{u}_i$ refer to the inclusion. The vector $\boldsymbol{z}$ identifies the

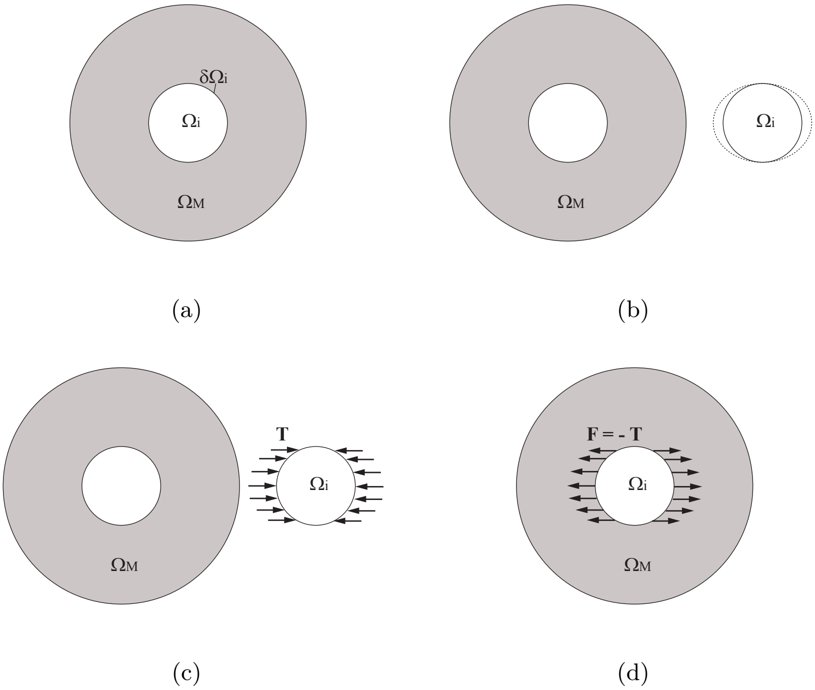

(a) (b)

(c) (d)

Figure D.1: Virtual problem adopted by Eshelby (adapted from Weiberger et al. (2005)).

position inside the volume Ω. Afterwards, a traction $\boldsymbol{T}$ is applied on the inclusion surface $\delta\Omega_i$ to contrast with the eigenstrain $\boldsymbol{E}^*$, (Figure D.1c). The strain, stress and displacement fields read:

$$\begin{cases} \boldsymbol{E} = 0 \\ \boldsymbol{\Sigma} = 0 \\ \boldsymbol{u} = 0 \end{cases} \tag{D.2a}$$

$$\begin{cases} \boldsymbol{E}_i = \boldsymbol{E}_i^{\mathrm{el}} + \boldsymbol{E}_i^* \\ \boldsymbol{\Sigma}_i = \mathbb{C} : \boldsymbol{E}_i^{\mathrm{el}} = -\mathbb{C} : \boldsymbol{E}_i^* = -\boldsymbol{\Sigma}_i^* \\ \boldsymbol{u}_i = 0 \end{cases} \tag{D.2b}$$

Subsequently, the inclusion, which is subjected to the traction $\boldsymbol{T}$, is re-inserted into the system, without provoking any change to the state of both phases. The traction force $\boldsymbol{T}$ is then removed. The constrained displacement field $\boldsymbol{u}_i^{\mathrm{c}}\,(x)$ can be determined by solving the problem of a material subjected to a body force

$\boldsymbol{F} = -\boldsymbol{T}$ on the surface $\delta\Omega_i$ (Figure D.1d). The strain, stress and displacement fields can be expressed in terms of the constrained displacement field $\boldsymbol{u}_i^{\mathrm{c}}\left(\boldsymbol{z}\right)$:

$$\begin{cases} \boldsymbol{E} = \boldsymbol{E}^{\mathrm{c}} \\ \boldsymbol{\Sigma} = \boldsymbol{\Sigma}^{\mathrm{c}} \\ \boldsymbol{u} = \boldsymbol{u}^{\mathrm{c}} \end{cases} \tag{D.3a}$$

$$\begin{cases} \boldsymbol{E}_i = \boldsymbol{E}_i^{\mathrm{el}} + \boldsymbol{E}_i^{*} \\ \boldsymbol{\Sigma}_i = \boldsymbol{\Sigma}^{\mathrm{c}} - \boldsymbol{\Sigma}^{*} = \mathbb{C} : \left(\boldsymbol{E}_i^{\mathrm{c}} - \boldsymbol{E}_i^{*}\right) \\ \boldsymbol{u}_i = \boldsymbol{u}_i^{\mathrm{c}} \end{cases} \tag{D.3b}$$

To link the constrained strain $\boldsymbol{E}_i^{\mathrm{c}}$ to the eigenstrain $\boldsymbol{E}_i^{*}$, the 4th order tensor $\mathbb{S}$ is introduced:

$$\boldsymbol{E}_i^{\mathrm{c}} = \mathbb{S} : \boldsymbol{E}_i^{*} \tag{D.4}$$

The Eshelby's tensor $\mathbb{S}$, like the stiffness tensor $\mathbb{C}$, results minor symmetric

$$S_{ijkl} = S_{jikl} = S_{ijlk} \tag{D.5}$$

It has been proved that *for an ellipsoidal inclusion in a homogeneous infinite matrix, the Eshelby tensor* $\mathbb{S}$ *is a constant tensor. Hence the stress-strain fields inside the inclusion are uniform.*

Mura (1987) derived the formulation of the Eshelby's tensor $\mathbb{S}_i$ for a family of ellipsoidal inclusions in an isotropic medium. In the case of a family of identical penny-shaped inclusions with normal $\boldsymbol{n}_i$ aligned along the 3-axis and characterized by major radii $a = b$ in the inclusion's plane and minor radius c along the thickness direction, it results:

$$\begin{aligned}
&S_{1111} = S_{2222} = \frac{\pi\,(13-8\nu)}{32\,(1-\nu)}\frac{c}{a}\\
&S_{3333} = 1 - \frac{\pi\,(1-2\nu)}{4\,(1-\nu)}\frac{c}{a}\\
&S_{1122} = S_{2211} = \frac{\pi\,(8\nu-1)}{32\,(1-\nu)}\frac{c}{a}\\
&S_{1133} = S_{2233} = \frac{\pi\,(2\nu-1)}{8\,(1-\nu)}\frac{c}{a}\\
&S_{3311} = S_{3322} = \frac{\nu}{1-\nu}\left(1 - \frac{\pi\,(4\nu+1)}{8\nu}\frac{c}{a}\right)\\
&S_{1212} = S_{2112} = S_{1221} = S_{2121} = \frac{\pi\,(7-8\nu)}{32\,(1-\nu)}\frac{c}{a}\\
&S_{1313} = S_{3113} = S_{1331} = S_{3131} = \frac{1}{2}\left(1 + \frac{\pi\,(\nu-2)}{4\,(1-\nu)}\frac{c}{a}\right)\\
&S_{2323} = S_{3223} = S_{2332} = S_{3232} = \frac{1}{2}\left(1 + \frac{\pi\,(\nu-2)}{4\,(1-\nu)}\frac{c}{a}\right)
\end{aligned} \tag{D.6}$$

In the case of spherical inclusions ($a = b = c$), the Eshelby's tensor, $\mathbb{S}_i$, results:

$$S_{ijkl} = \frac{5\nu-1}{15\,(1-\nu)} I_{ij} I_{kl} + \frac{4-5\nu}{15\,(1-\nu)} \left(I_{ik} I_{jl} + I_{il} I_{jk}\right) \tag{D.7}$$

where the 2$^{\text{nd}}$ order tensor $\boldsymbol{I}$ is the Kronecker delta equal to:

$$I_{ij} = \begin{cases} 0 & i \neq j \\ 1 & i = j \end{cases} \tag{D.8}$$

The solution of the Eshelby problem provide the local (microscopic) field behaviour, which is subsequently averaged to determine the global (macroscopic) field behaviour. Various mean-field homogenization methods are available in literature.

D.1.2 Classical Analytical Homogenization Methods

The dilute, the Mori-Tanaka and the self-consistent schemes are the classical mean-field homogenization methods. They estimate the global (macroscopic) field behaviour as an average of the local (microscopic) one, which is obtained by following Eshelby's solution.

The solution of these method is here provided for a two-phase material, with overall stiffness tensor $\mathbb{C}$, composed by inclusions embedded in a matrix phase. The REV is subjected to homogeneous boundary conditions, which can be displacements or tractions. The effective stiffness tensor $\mathbb{C}$ and its inverse the compliance tensor $\mathbb{D}$ are evaluated as:

$$\mathbb{C} = \mathbb{C}_{\mathrm{m}} + \phi_i \left(\mathbb{C}_i - \mathbb{C}_{\mathrm{m}}\right) : \mathbb{X}_i \tag{D.9a}$$

$$\mathbb{D} = \mathbb{D}_{\mathrm{m}} + \phi_i \left(\mathbb{D}_i - \mathbb{D}_{\mathrm{m}}\right) : \mathbb{Y}_i \tag{D.9b}$$

where the subscriptions m and i refers to the matrix and inclusions' quantities, respectively. The volume fraction ϕ_i is defined as the ratio between the volume occupied by the inclusions and the total volume. The tensors $\mathbb{X}_i$ and $\mathbb{Y}_i$ are the average strain and stress concentration tensors, which link the strain $\boldsymbol{E}_i$ and the stress $\boldsymbol{\Sigma}_i$ in the inclusions to the macroscopic applied one:

$$\boldsymbol{E}_i = \mathbb{X}_i : \boldsymbol{E} \tag{D.10a}$$

$$\boldsymbol{\Sigma}_i = \mathbb{Y}_i : \boldsymbol{\Sigma} \tag{D.10b}$$

The difference between the three methods lays in the interaction degree between the various phases. This is expressed by a different estimate for the average strain, $\mathbb{X}_i$, and stress, $\mathbb{Y}_i$, concentration tensors.

The dilute scheme assumes that the inclusions, which are perfectly embedded in the matrix, do not interact between themselves. The dilute average strain, $\mathbb{T}_i = \mathbb{X}_i^{\mathrm{dilute}}$, and stress, $\mathbb{W}_i = \mathbb{Y}_i^{\mathrm{dilute}}$, concentration tensors are obtained by embedding a single inclusions in an all-matrix medium:

$$\mathbb{T}_i = \left[\mathbb{I} + \mathbb{S}_i : \mathbb{C}_{\mathrm{m}}^{-1} : \left(\mathbb{C}_i - \mathbb{C}_{\mathrm{m}}\right)\right]^{-1} \tag{D.11a}$$

$$\mathbb{W}_i = \mathbb{C}_i : \mathbb{T}_i : \mathbb{D}_i \tag{D.11b}$$

where $\mathbb{I}$ is the 4th order symmetric identity tensor defined as:

$$I_{ijkl} = \frac{1}{2} \left(I_{ik} I_{jl} + I_{il} I_{jk}\right) \tag{D.12}$$

with $\boldsymbol{I}$ the 2nd order identity tensor (Equation (D.8)).

The Mori-Tanaka scheme allows for slightly interaction of the inclusions, by assuming that "each inclusion behaves like an isolated inclusion in the matrix phase seeing the matrix deformation as a far-field strain" (Benveniste, 1987). The average strain, $\mathbb{A}_i = \mathbb{X}_i^{\mathrm{MT}}$, and stress, $\mathbb{B}_i = \mathbb{Y}_i^{\mathrm{MT}}$, concentration tensors can be determined as:

$$\mathbb{A}_i = \mathbb{T}_i : \left(\phi_{\mathrm{m}} \mathbb{I} + \phi_i \mathbb{T}_i\right)^{-1} \tag{D.13a}$$

$$\mathbb{B}_i = \mathbb{W}_i : \left(\phi_{\mathrm{m}} \mathbb{I} + \phi_i \mathbb{W}_i\right)^{-1} \tag{D.13b}$$

with $\mathbb{T}_i$ and $\mathbb{W}_i$ their dilute estimations (Equation (D.11a),Equation (D.11b)).

The self-consistent method (Klusemann and Svendsen, 2010) approximates the interaction between the phases by assuming that each component is embedded in an infinite volume made of an effective medium, which has as mechanical characteristics the one of the overall material. The average strain, $\mathbb{Z}_i = \mathbb{X}_i^{\mathrm{SC}}$, and stress, $\mathbb{V}_i = \mathbb{Y}_i^{\mathrm{SC}}$, concentration tensors can be determined as:

$$\mathbb{Z}_i = \left[\mathbb{I} + \mathbb{S}_i : \mathbb{C}^{-1} : (\mathbb{C}_i - \mathbb{C})\right]^{-1} \tag{D.14a}$$

$$\mathbb{V}_i = \mathbb{C}_i : \mathbb{Z}_i : \mathbb{D}_i \tag{D.14b}$$

Further information regarding these and other analytical homogenization methods can be found in literature, e.g. Böhm (2015); Pierard et al. (2004).

D.2 Implementation

The homogenization theory is adopted in the multiscale material model presented in Chapter 5. The theory and the model are implemented in the MATLAB software. The MMtensor package (Moesen, 2011) is adopted to calculate the Eshelby and stiffness tensors. To compute the stiffness tensor, mapping techniques are adopted to transform tensors into matrix form. In this section an overview of mapping techniques is presented.

D.2.1 Tensor Operations

In tensor notation, z represents a scalar, $\boldsymbol{z}$ denote a 1st order tensor, $\boldsymbol{Z}$ represents a 2nd order tensor and $\mathbb{Z}$ represents a 4th order tensor. Table D.1 lists the main tensor operations for (minor) symmetric tensors. A 2nd order tensor $\boldsymbol{Z}$ is defined symmetric if $Z_{ij} = Z_{ji}$. A 4th order tensor is defined minor symmetric if $Z_{ijkl} = Z_{jikl} = Z_{ijlk}$ and is major symmetric if $Z_{ijkl} = Z_{lkji}$.

D.2.2 Mapping Techniques

A mapping technique allows representing a (minor) symmetric tensor in matrix form by keeping unaltered its properties. Equation (D.15a) and Equation (D.15b) represent the concept for a 2nd and 4th order tensor.

$$A = A_{ij} = \begin{bmatrix} A_{11} & A_{12} & A_{13} \\ A_{21} & A_{22} & A_{23} \\ A_{31} & A_{32} & A_{33} \end{bmatrix} \rightarrow \boldsymbol{a} = a_m = \begin{Bmatrix} h_n A_{11} \\ h_n A_{22} \\ h_n A_{23} \\ h_t A_{23} \\ h_t A_{31} \\ h_t A_{12} \end{Bmatrix} \tag{D.15a}$$

Table D.1: Tensor operations for (minor) symmetric tensors.

Dyadic product	
$\mathbb{Z} = \boldsymbol{X} \otimes \boldsymbol{Y}$	$Z_{ijkl} = X_{ij} Y_{kl}$
Double dot product	
$z = \boldsymbol{x} \cdot \boldsymbol{y}$	$z = x_m y_m = \sum_m x_m y_m$
$\boldsymbol{z} = \boldsymbol{X} \cdot \boldsymbol{y}$	$z_i = x_{im} y_m = \sum_m x_{im} y_m$
$\boldsymbol{Z} = \boldsymbol{X} \cdot \boldsymbol{Y}$	$Z_{ij} = X_{im} Y_{mj} = \sum_m X_{im} Y_{mj}$
Inner product	
$\mathbb{Z} = \mathbb{X} : \mathbb{Y}$	$Z_{ijkl} = X_{ijmn} Y_{mnkl} = \sum_m \sum_n X_{ijmn} Y_{mnkl}$
$\boldsymbol{Z} = \mathbb{X} : \boldsymbol{Y}$	$Z_{ij} = X_{ijmn} Y_{mn} = \sum_m \sum_n X_{ijmn} Y_{mn}$
$z = \boldsymbol{X} : \boldsymbol{Y}$	$z = X_{mn} Y_{mn} = \sum_m \sum_n X_{mn} Y_{mn}$

$$
\begin{aligned}
\mathbb{A} = A_{ijkl} \rightarrow \boldsymbol{A} = A_{mn} = & \\
= \begin{bmatrix}
H_n A_{1111} & H_n A_{1122} & H_n A_{1133} & 0 & 0 & 0 \\
H_n A_{2211} & H_n A_{2222} & H_n A_{2233} & 0 & 0 & 0 \\
H_n A_{3311} & H_n A_{3322} & H_n A_{3333} & 0 & 0 & 0 \\
0 & 0 & 0 & H_t A_{2323} & 0 & 0 \\
0 & 0 & 0 & 0 & H_t A_{3131} & 0 \\
0 & 0 & 0 & 0 & 0 & H_t A_{1212}
\end{bmatrix} &
\end{aligned}
\tag{D.15b}
$$

where h_t, h_n, H_t, H_n are the mapping coefficients which depends from the adopted techniques.

These techniques are often used in engineering to represent the stress, strain, stiffness and compliance tensors in matrix form. Following the elasticity theory, stress and strain are defined as 2^{nd} order tensors with 3x3 = 9 components, while the stiffness and compliance tensors are defined as a 4^{th} tensors with 3x3x3x3 = 81 components. Due to symmetry, the former tensors are constituted by 6 non-zero components, while the latter tensors are constituted by 21 non-zero components.

Voigt mapping is the most adopted technique in the engineering field and ensures that the deformation energy is equally computed in tensor and matrix notation:

$$\frac{1}{2}\boldsymbol{\Sigma} : \boldsymbol{E} = \boldsymbol{\sigma}^T \cdot \boldsymbol{\varepsilon} \tag{D.16}$$

Following the notation in Equation (D.15), the coefficients for the Voigt mapping result equal to:

$$h_n = \begin{cases} 1 & \text{stress} \\ 1 & \text{strain} \end{cases} \tag{D.17a}$$

$$h_t = \begin{cases} 1 & \text{stress} \\ 2 & \text{strain} \end{cases} \tag{D.17b}$$

$$H_n = \begin{cases} 1 & \text{stiffness} \\ 1 & \text{compliace} \end{cases} \tag{D.17c}$$

$$H_t = \begin{cases} 1 & \text{stiffness} \\ 4 & \text{compliace} \end{cases} \tag{D.17d}$$

The Voigt mapping has the advantage that it does not modified the stress and stiffness components in matrix notation. However, it modifies the components of strain and compliance tensors in matrix notation, thus all advantages of tensor algebra cannot be used. In particular, the inverse operation is not applicable.

A more consistent techniques is the Kelvin mapping, which ensure the equivalence between tensor and matrix operation. The mapping coefficients are:

$$h_n = \;2 \quad 2^{\text{nd}} \text{ order tensors} \tag{D.18a}$$

$$h_t = \;\sqrt{2} \quad 2^{\text{nd}} \text{ order tensors} \tag{D.18b}$$

$$H_n = \;1 \quad 4^{\text{th}} \text{ order tensors} \tag{D.18c}$$

$$H_t = \;2 \quad 4^{\text{th}} \text{ order tensors} \tag{D.18d}$$

Kelvin mapping technique solves all the limitations presented by the Voigt mapping and it is adopted in this work.

D.3 Comparison with Numerical Homogenization

To provide closed form solution, analytical homogenization methods adopt a simplified description of the REV. The inclusions are described as regular geometrical shapes and their interaction is limited. The REV phases are usually assumed as linear elastic materials.

Numerical homogenization methods provide a more refined description of the REV by adopting the finite element method (FEM). More complex inclusions shapes and interaction phenomena can be captured by this techniques. However, the computational effort required is elevated, especially if employed in multiscale approaches.

This section presents a comparison between analytical and numerical homogenization estimates for a two-phase material. A REV composed by zero-stiffness inclusions and embedded in a linear elastic matrix is considered. The elastic modulus Y_{m} and Poisson ratio ν_{m} of the matrix are chosen equal to 25000 MPa and 0.2, respectively. The various methods are compared in terms of normalized

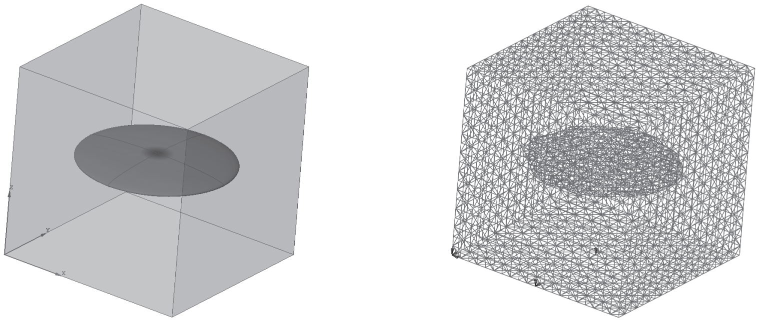

(a) (b)

Figure D.2: Numerical homogenization for a single inclusion system: (a) REV representation; (b) Finite element discretization (reproduced from Todorovic (2013)).

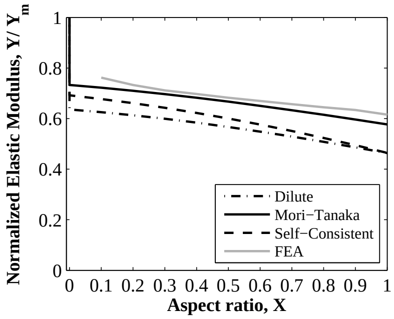

Figure D.3: Comparison of stiffness estimation obtained by analytical and numerical homogenization methods for a single inclusion system (adapted from Todorovic (2013)).

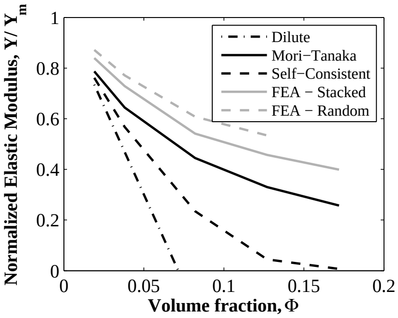

Figure D.4: Comparison of stiffness estimation obtained by analytical and numerical homogenization methods for one family of penny-shaped inclusions ($X = 0.1$), (adapted from Todorovic (2013)).

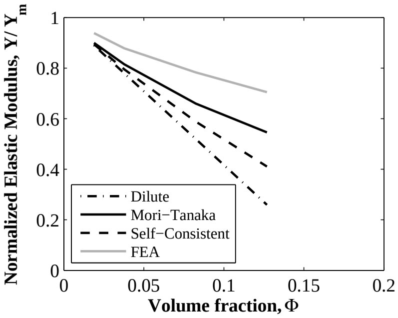

Figure D.5: Comparison of stiffness estimation obtained by analytical and numerical homogenization methods for three orthogonal families of penny-shaped inclusions ($X = 0.1$), (adapted from Todorovic (2013)).

elastic modulus, which is the ratio between the elastic modulus of the homogenized material Y and of the matrix phase Y_{m}.

In the case of numerical homogenization, finite element analysis (FEA) is carried out to simulate an uniaxial tensile test on the two-phase material (Todorovic, 2013). The REV is modelled in three-dimensions with 4-noded isoparametric solid pyramid elements (Figure D.2). Periodic boundary conditions are applied to simulate an uniform stress distribution.

Figure D.3 shows the comparison between analytical and numerical homogenization methods for the case of a single inclusion for various aspect ratio X. Among the analytical methods, the Mori-Tanaka scheme closely approximate the numerical estimates with an average error of 4%.

Figure D.4 shows the comparison for one family of multiple aligned penny-shaped inclusions with aspect ratio $X = 0.1$. The elastic modulus is evaluated in the direction parallel to the normal inclusion axis. Conversely to the analytical methods, the numerical approach allows investigating the influence of inclusions' position on the overall stiffness. For this case a stacked and a random distribution of inclusions is considered. The latter results stiffer than the former. The difference in stiffness between the two estimates increases by incrementing the volume fraction of the inclusions. Among the analytical methods, the Mori-Tanaka scheme shows a similar trend than the numerical estimates. On the contrary, the dilute and the self-consistent schemes substantially differ from the numerical estimates by reaching a percolation threshold.

Figure D.5 shows the comparison for three orthogonal families of penny-shaped inclusions with aspect ratio $X = 0.1$. The number of inclusions, thus the volume fraction, is kept equal between the families. The total volume fraction Φ, thus results as the sum of the volume fraction of the three families. Comparing the analytical and numerical homogenization method results, the considerations observed for one inclusion family apply. The Mori-Tanaka scheme results the closest to the numerical estimates, while the dilute and self-consistent scheme tend to deviate.

D.4 Concluding Remarks

In this chapter the main aspects of mean-field homogenization methods are presented. This theory has been adopted in the multiscale material model presented in Chapter 5. It allows determining the macroscopic effective mechanical properties (e.g. stiffness) of a microscopically heterogeneous material. The micro-structure is schematized within the framework of a representative elementary volume and the boundary value problem is analytically solved by averaging the local deformation field.

The classical analytical homogenization methods take advantage of the Elshelby's solutions, which allows determining the local deformation field for a single inclusion embedded in a matrix phase. By considering various averaging techniques different estimates can be retrieved. The most simple one is the dilute scheme, which assumes no interaction between the inclusions. A higher interaction degree is instead accounted by the Mori-Tanaka and self-consistent scheme.

The implementation of mean-field homogenization methods requires the mapping of tensors into matrix form. This technique is often used in engineering to represent the stress, strain, stiffness and compliance tensors in matrix form. They can be applied thanks to the minor symmetric form of the stiffness and compliances tensors. Two techniques are available in literature, the Voigt and the Kelvin mapping. The former ensures that the deformation energy is equally computed in tensor and matrix notation, while the latter provide a correspondence between the tensor and matrix operations. Even if the Voigt mapping is the most common used techniques in engineering, it presents several drawback when employed in the analytical homogenization framework. This can be easily overcome by the Kelvin mapping.

The classical analytical homogenization methods have been compared with a numerical homogenization approach based on finite element method. Three-dimensional numerical analysis have been carried out to simulate an uniaxial tensile test on two-phase material. The case of penny-shaped inclusions with zero-stiffness has been studied. The comparison promotes the Mori-Tanaka scheme as the best estimate among the classical analytical methods for the given cases. However, an underestimation of the stiffness with respect to the numerical approach has been observed.

Acknowledgements

The research described in this thesis was developed within the STW project *Performance Assessment Tool for Alkali-Silica Reaction* (PAT-ASR) (code No. 10977), which is part of the STW program *Integral Solutions for Sustainable Construction* (IS2C). The project was mainly financed by the Dutch National Foundation STW and by Rijkswaterstraat, which is part of the Dutch Ministry of Infrastructures and the Environment. I thank all the people working in this program, from the people involved in the proposal stage to the Ph.D. candidates who developed it, because they created a synergistic group in which it was a pleasure to work.

I want to express my gratitude to Prof. Max A.N. Hendriks for the guidance and the support that I received along my Ph.D. journey. He was always open and enthusiastic in embracing my ideas, giving me the freedom that every Ph.D. student deserves. I want to thank Prof. Jan G. Rots, who welcomed me in the group of Structural Mechanics. I am thankful to Dr. Oguzhan Çopuroğlu and Prof. Erik Schlangen for initiating the PAT-ASR project. During this project, I very much appreciated our discussions, which always included a variety of different points of view, because they made me thinking out-of-the-box. A warm thanks goes to Caner Anaç, with whom I shared all the joys and the troubles of this project. I would like to thank Guðbjartur Jón Einarsson and Marc Ottelé for their help in the experimental work.

I would like to acknowledge Per Hagelia and Eva Rodum from the Norwegian Public Road Administration (NPRA) and Hans Stemland and Jan Lindgård from SINTEF for their collaboration and for providing the PAT-ASR team with a great case study: the Nautesund bridge. I want to express my gratitude to Prof. Joop Den Uijl for sharing with me all his experience on the topic at the beginning of my Ph.D studies. I am thankful to Dr. Ane De Boer for involving me in the project concerning the proof loading of the Vlijmen Oost bridge. I want to express my gratitude to Prof. Franz-Josef Ulm for the interesting discussion on the micro-poro-mechanics theory. My gratitude goes to Prof. François Toutlemonde, Prof. Stéphane Multon and Prof. Jean-François Seignol to provide me with data and dissertations from their group. I will never forget the first time I met Dr. Laurent Charpin; he stood up at the ICAAR14 conference in 2012 to agree with my ideas. At that time, we were both young Ph.D. students and (almost) the only researchers applying micro-poro-mechanics to model ASR in concrete. Thank you very much for our conversations and discussions.

I would like to acknowledge all the committee members for the comments and discussions, which contributed to the final version of my dissertation. I am thankful to Zahid Hossin for drawing the beautiful cover of this thesis.

During this work, experimental tests were performed in the Stevin II Laboratory of the Delft University of Technology. This would have been not possible without the help of Gerrit Nagtegaal and Fred Schilperoort.

I am certainly in debt with my officemates Anne van de Graaf, Arthur Slobbe and Giorgia Giardina for sharing opinions, troubles, chatting and coffee. My warm thanks goes to my lunch group, whose size changed over the years, for being every day with me. I am thankful to Alessandra Tirabassi, Marko Todorovick and Mauro Galli for their contribution to this thesis during their graduation project. I would like to thank all the colleagues and friends of the department of Structural Engineering. It was a lot of fun running through the building of the Civil Engineering faculty.

I want to express my gratitude to Prof. Beatrice Belletti for having been my mentor and for introducing me to the group of Structural Mechanics at Delft University of Technology. I will never forget all the work that we did for my MSc. graduation project, together with Prof. Joost Walraven. Everything I learned with you helped me in my Ph.D. career.

I am eternally grateful to all my friends; thank you very much for never let me down. A particular word goes to Alieh, Eleonora, Eugenia, Laura, Francesca, Maria, Sayeda, Rosanna and Valentina, who shared with me all the adventures of this Ph.D. journey from the very first day.

Last but not least, I would like to thank my parents Giovanni and Franca and my brother Camillo Fabio for the support and love that they bring in my life. A special thanks goes to Giorgio for sharing life with me.

Curriculum Vitæ

Personal information

Name	**Rita Esposito**
Email	r.esposito@tudelft.nl rita.esposito85@gmail.com
Date of Birth	25 June 1985
Nationality	Italian

Work experience and education

Jan 2015 - present	Post-doctoral Researcher Department of Structural Engineering, Delft University of Technology, Delft, The Netherlands
Jan 2011 - Jan 2016	Ph.D. Candidate Department of Structural Engineering, Delft University of Technology, Delft, The Netherlands
Apr 2010 - Dec 2010	Assistant Researcher Department of Civil Engineering (DICATeA) University of Parma, Parma, Italy
Sep 2004 - Mar 2010	Degree in Civil Engineering University of Parma, Parma, Italy
Sep 1999 - Jun 2004	Scientific High School High School G. Aselli, Cremona, Italy

List of Publications

Journal publications

5. **R. Esposito**, C. Anaç, M.A.N. Hendriks and O. Çopuroğlu *The Influence of Alkali-Silica Reaction on the Mechanical Degradation of Concrete*, Accepted for publication in ASCE Journal of Materials.

4. **R. Esposito** and M.A.N. Hendriks *Simulating the Deteriorating Effect of the Alkali-Silica Reaction in Concrete via a Micro-Poro Fracture Mechanical Model*, Proceeding of the International Conference on Mechanics and Physics of Creep, Shrinkage, and Durability of Concrete and Concrete Structures (CONCREEP 10), Vienna, Austria. ASCE Proceedings, 118-127 (2015).

3. C. Damoni, B. Belletti and **R. Esposito** *Numerical prediction of the response of a squat shear wall subjected to monotonic loading*, European Journal of Environmental and Civil Engineering, **18**(7), 754-769 (2014).

2. B. Belletti **R. Esposito** and J.C. Walraven *Shear capacity of normal, lightweight, and high-strength concrete beams according to Model Code 2010. II: Experimental results versus nonlinear finite element program results*, , Journal of Structural Engineering, ASCE, **139**(9), 1600-1607 (2012).

1. J.C. Walraven, B. Belletti and **R. Esposito** *Shear capacity of normal, lightweight, and high-strength concrete beams according to Model Code 2010. I: Experimental Results versus Analytical Model Results*, , Journal of Structural Engineering, ASCE, **139**(9), 1593-1599 (2012).

Conference publications

10. **R. Esposito** and M.A.N. Hendriks *Ageing effects of alkali-silica reaction in concrete structures*,Proceedings of the 1st International Conference on Ageing of Materials and Structures, Delft, The Netherlands. 347-356 (2014).

9. **R. Esposito** and M.A.N. Hendriks *Modeling of Alkali-Silica Reaction in concrete: A multiscale approach for structural analysis*,Proceedings of the International Conference on Computational Modelling of Concrete Structures (EURO-C), St. Anton am Alberg, Austria. CRC Press, 1, 87-96 (2014).

8. **R. Esposito** and M.A.N. Hendriks *Towards Structural Modelling of Alkali-Silica Reaction in Concrete*, Proceedings of the International Conference on Durability of Reinforced Concrete from Composition to Protection, Springer International Publishing, 179-188 (2015).

7. **R. Esposito** and M.A.N. Hendriks *Structural modelling of ASR-affected concrete: The approach developed in the PAT-ASR project*, The Nordic Concrete Federation, **11**, 95-104 (2014).

6. **R. Esposito** and M.A.N. Hendriks *Multiscale material model for ASR-affected concrete structures*,Proceedings of the 12th International Conference on Computational Plasticity: Fundamentals and Applications (COMPLAS), Barcelona, Spain. CIMNE, (2013).

5. B. Belletti, **R. Esposito** and C. Damoni *Numerical prediction of the response of a squat shear wall subjected to monotonic loading through PARCCL model*, Proceedings of the VIII International Conference on Fracture Mechanics of Concrete and Concrete Structures (FramCos-8), Toledo, Spain. CIMNE, (2013).

4. **R. Esposito** and M.A.N. Hendriks *Degradation of the mechanical properties in ASR-affected concrete: overview and modeling*,Proceedings of the International Conference on Numerical Modeling Strategies for Sustainable Concrete Structures (SSCS), Aix en Provence, France. (2012).

3. **R. Esposito** and M.A.N. Hendriks *A review of ASR modeling approaches for finite element analysis of dams and bridges*,Proceedings of the 14th International Conference on Alkali-Aggregate Reaction in Concrete (ICAAR) Austin, Texas. (2012).

2. C. Anaç, **R. Esposito**, O. Çopuroglu, E. Schlangen and M.A.N. Hendriks *A tool for concrete performance assessment for ASR affected structures: An outlook*,Proceedings of the 14th International Conference on Alkali-Aggregate Reaction in Concrete (ICAAR) Austin, Texas. (2012).

1. B. Belletti and **R. Esposito** *Un modello costitutivo per elementi in CA soggetti ad azioni cicliche*,Proceedings of the 18th CTE Conference Bresca, Italy. (2010) (In Italian).

Propositions

accompanying the dissertation

The Deteriorating Impact of Alkali-Silica Reaction on Concrete

Expansion and Mechanical Properties

by

Rita Esposito

1. From the view point of structural assessment, the deteriorating impact of ASR in concrete should be considered not only in terms of induced expansion, but also with respect to the mechanical degradation.
2. Only measuring the compressive strength of cores extracted from affected structures has a limited value for the assessment perspective.
3. The combined deteriorating impact of ASR and external mechanical loading on concrete can be explained by the micro-cracking phenomenon.
4. To model the mechanical degradation of ASR-affected concrete in free-expansion conditions, a multiscale material model should account for permanent deformation.
5. If material sciences experts and structural engineers would have the patience to accept their differences and unifying their language, insights on structural performances could be gained faster
6. As a researcher, one should dream the impossible and plan the possible.
7. Conventions are adopted to achieve simplified and practical solutions; however, the ideas behind them should be understood.
8. A good supervisor should deal with constraints and give freedom to Ph.D. students.
9. The law of action-reaction does not ensure the equilibrium of a tango dancing couple.
10. Life is like concrete, it is the binder that gives the quality.

These propositions are regarded as opposable and defendable, and have been approved as such by the promotor Prof. dr. ir. M.A.N. Hendriks.

Stellingen

behorende bij het proefschrift

The Deteriorating Impact of Alkali-Silica Reaction on Concrete

Expansion and Mechanical Properties

door

Rita Esposito

1. Vanuit het oogpunt van de beoordeling van de constructieve veligheid, moet het schadelijke effect van ASR op beton niet alleen in termen van geïnduceerde expansie worden beschouwd, maar ook met betrekking tot de mechanische degradatie
2. Het alleen meten van de druksterkte van boorkernen van een aangetaste constructie, heeft een beperkte waarde vanuit het perspectief van een constructieve beoordeling.
3. De gecombineerde negatieve invloed van ASR en externe mechanische belasting op beton, kan door het fenomeen van micro-scheuren verklaard worden.
4. Om de mechanische degradatie van ASR-aangetast beton te modelleren, moet een meerschalig materiaalmodel rekening houden met blijvende vervorming.
5. Als materiaalkundigen en constructeurs het geduld zouden hebben om hun verschillen te accepteren en hun taal te unificeren, kunnen inzichten over het gedrag van constructies sneller verkregen worden.
6. Als onderzoeker, moet je het onmogelijke dromen en het mogelijke plannen.
7. Conventies worden gebruikt om te komen tot vereenvoudigde en praktische oplossingen; echter, de achterliggende ideeën moeten begrepen worden.
8. Een goede begeleider bewaakt de randvoorwaarden en geeft vrijheid aan promovendi.
9. De actie-reactie-wet garandeert geen evenwicht van een tango-dansend paar.
10. Leven is als beton, het is het bindmiddel dat de kwaliteit geeft.

Deze stellingen worden opponeerbaar en verdedigbaar geacht en zijn als zodanig goedgekeurd door de promotor Prof. dr. ir. M.A.N. Hendriks.